

59

**Threshold Electrodisintegration of the Deuteron at High
Momentum Transfer**

by

William Michael Schmitt

B.A., Physics and Chemistry
University of Missouri-Saint Louis
June 1987

Submitted to the Department of Physics
in partial fulfillment of the requirements for the degree of

Doctor of Philosophy

at the

MASSACHUSETTS INSTITUTE OF TECHNOLOGY

June 1993

© Massachusetts Institute of Technology 1993

Signature Redacted

Signature of Author

Department of Physics
May 13, 1993

Signature Redacted

Certified by

Dr. Claude F. Williamson
Senior Research Scientist
Thesis Supervisor

Signature Redacted

Accepted by

Professor George F. Koster
Chairman of the Graduate Committee

ARCHIVES

MASSACHUSETTS INSTITUTE
OF TECHNOLOGY

JUN 02 1993

Threshold Electrodisintegration of the Deuteron at High Momentum Transfer

by

William Michael Schmitt

Submitted to the Department of Physics
on May 13, 1993, in partial fulfillment of the
requirements for the degree of
Doctor of Philosophy

Abstract

This thesis presents the results of an experiment at the Bates Linear Accelerator Center in which cross section measurements for deuteron electrodisintegration near threshold were made at high momentum transfer with good energy resolution. The experiment was performed at a constant scattering angle of 160° at bombarding energies of 347, 576, 754, 820 and 913 MeV. The corresponding measured Q^2 values were 8.7, 20.5, 31.6, 36.0, and 42.4 fm^{-2} . Threshold cross sections averaged over 0-3 MeV and 0-10 MeV in E_{np} were calculated. Measurements were also obtained for elastic electron-deuteron scattering and elastic electron-hydrogen scattering (the latter only at 913 MeV).

The analysis of the data involved accurately determining the elastic line shape. Landau straggling, external Bremsstrahlung radiation, and internal Bremsstrahlung radiation (both from the scattered electron and target nucleus) were included. A Monte Carlo simulation was written to include the geometry of the target cell, target collimating slits and model the acceptance of the electron spectrometer. The elastic line shape and spectrometer acceptances agreed very well with the data.

The averaged threshold cross sections were compared with existing data in the region of overlap. Good agreement was seen with the Saclay data which was averaged over 0-3 MeV in E_{np} . And comparison to the poorer resolution SLAC measurement which was averaged over 0-10 MeV in E_{np} also showed good agreement.

Comparisons of the data were made with theoretical calculations. The standard nonrelativistic meson-exchange calculations agree only qualitatively with trend of the data. These calculations are very model dependent since a fully relativistic theory is not yet present. Hybrid quark-hadron calculations which put quark degrees of freedom in the deuteron wave functions at small distances agree with the overall magnitude of the data.

Thesis Supervisor: Dr. Claude F. Williamson
Title: Senior Research Scientist

Acknowledgements

The work presented in this thesis would not have been possible without the large support that I've received during my time here at MIT. I'd like to thank the people that have affected and shaped my life for the last 6 years.

First, I'd like to thank my advisor, Claude Williamson, for showing me patience throughout this work from its inception to its completion. Claude has inspired me to grow as a person and physicist, and I'm grateful for all the knowledge he has given me. Even days when things were tough Claude always found the right things to say to bring my motivation back. I thank Claude and his wife, Delaine, for the wonderful dinners and their warm hospitality.

I'd like to thank the collaborators on this experiment without whom this experiment would not have happened. The University of Massachusetts-Amherst group for providing the new horizontal drift chambers and the ongoing discussions with Rory Miskimen and KyongSei Lee were always helpful. Peter Bosted from American University for providing the lead-glass blocks for the shower array. Saclay for providing the gas Cherenkov detector.

I'd also like to thank the Bates staff for getting the experiment going and running smoothly. Joe Dzengeleski was invaluable for fixing the cryogenic refrigerator when it started have problems. John Zumbro and Karen Dow for all their help with the data acquisition software. And Christine Twiss for handling all of my calls to Bates and her cheerful personality made Bates a fun place to work.

I'd like to thank the many fellow graduate students that I've had the pleasure of knowing. Each one has enriched my life in some intangible way. Mark Yuly was one of my first friends here at MIT. I was lucky to have such a great friend during my stay here. I will indeed miss the lunches, Christmas shopping, guitar playing, baseball throwing, and, oh yeah, the Krunch Koats! Terry Yates was my advisors only other student when I arrived here. Terry help me out a lot during the initial years of getting acquainted with the Bates laboratory and the Q data acquisition system. I'd also like to mention Wilson Fong, Tom McIlvain, Vipul Bhushan, Dave Jordan, Mark Wang (Whao! Whao!), Hojoon Park, Jeff Grandy, John Morrison, Marla Dowell, Maurik Holtrop and Kevin Lee. They've all enriched my life.

I'd like to thank the former graduate students who helped make MIT fun during my early years. Don Pham for his companionship. Eric Kronenberg for his easy-going nature and his love

for a good physics problem along with leather woven objects hurled at 97 mph. Jon Glickman for having such a great sense of humor. He could always make me laugh. And Kristina Isakovich for making the penthouse a fun place to be.

I'd also like to thank the people of the TCC for enriching my life. Without the friendships of Tony Bogner, Paula Waschbusch, Mark Vandevoorde, Mark Mozgowiec, and John Nguyen my life at MIT would not have been as fulfilling.

Lastly, I'd like to thank my family for their love and support. Mom, Dad, Paul, Tom, Theresa, Sue, grandpa and the memory of my grandma.

Dedicated to my family

Contents

1	Introduction	19
1.1	Electron-Deuteron Scattering	19
1.2	Kinematics and Definitions	26
2	Experimental Apparatus and Procedure	29
2.1	Overview	29
2.2	Electron Beam	31
2.3	Liquid Deuterium Target System	31
2.3.1	Overview	32
2.3.2	The Target Cell	32
2.4	ELSSY Spectrometer System	35
2.4.1	ELSSY Spectrometer	35
2.4.2	Focal Plane Instrumentation	37
2.4.3	VDC	38
2.4.3.1	Vertical-distance Lookup Table Calibration	38
2.4.3.2	Vertical-distance Correction	43
2.4.3.3	VDC Sag Correction	46
2.4.3.4	Vertical-distance Sum Cuts	47
2.4.4	HDC	49
2.4.4.1	Drift-distance Lookup Table Calibration	53
2.4.4.2	Drift-distance Sum Cuts	54
2.4.5	Gas Cherenkov Detector	55
2.4.6	Lead-Glass Cherenkov Detector	58
2.5	Data Acquisition	60

3	Elastic Line Shape	63
3.1	Energy Loss Processes	64
3.1.1	Collision and Ionization Losses	64
3.1.2	Bremsstrahlung Losses	68
3.1.2.1	External Bremsstrahlung	68
3.1.2.2	Internal Bremsstrahlung	70
3.2	The Convolution	76
3.2.1	Scattering Geometry and Definitions	77
3.2.2	Elastic Line Shape	81
3.2.2.1	Full Line Shape	81
3.2.2.2	Normalization	83
3.2.2.3	Near Elastic Peak	85
3.2.2.4	Most Probable Energy Loss	93
3.2.3	Target-Averaged Elastic Line Shape	95
3.3	Approximate Formulas for the Line Shape Near the Elastic Peak	96
3.3.1	Large Negative λ Expansion	97
3.3.2	Small T Expansion	98
3.3.3	Large Positive λ Expansion	99
3.3.4	Comparison with Numerical Evaluation	103
3.4	Equivalent Radiator Method	106
4	Monte Carlo Model	109
4.1	Event Modeling	109
4.2	Reverse Matrix Elements	115
4.3	Results	116
4.3.1	Integrated Solid Angle	117
4.3.2	Scattering Vertex Reconstruction	118
4.3.3	Target-Averaged Line Shape, $D^{\text{TA}}(E, \omega)$	119
4.3.4	Inelastic Radiative Correction Factor, \mathcal{R}_{inel}	121
5	Data Analysis	125
5.1	Overview	125
5.2	Monte Carlo Comparisons	126
5.3	Experimental Cross Sections	126
5.3.1	Integrated Solid Angle	133
5.3.2	Incident Electron Flux	133
5.3.3	Target Density	133

5.3.4	Detection Efficiencies	134
5.3.5	Radiative Correction Factor	135
5.4	Radiative Unfolding	136
5.5	Beam Energy	140
5.6	Systematic Errors	141
6	Results and Discussion	143
6.1	Results	143
6.2	Comparison with Existing Data	144
6.3	Comparison with Theory	144
6.4	Conclusions	149
A	The ELSSY Focal Surface	153
B	The Target Collimating Slits	161
C	Table of the Landau Functions $\phi(\lambda)$ and $\psi(\lambda)$	165
D	Density Effect Correction	167
E	Elastic Line Shape with Cross Section Dependence	171
F	The ELSSY Matrix Elements	177
G	Monte Carlo Code	183
H	Threshold Cross Sections	197

List of Figures

1-1	Isospin states for a two nucleon system.	20
1-2	The spectrum of scattered electrons from deuterium at 155 degrees.	22
1-3	The kinematics of the electrodisintegration reaction.	22
1-4	Meson-exchange current diagrams and an isobar-current diagram. a) Interaction with a π in flight. b) Pair creation term. c) Excitation of a Δ -isobar resonance.	24
1-5	Threshold electrodisintegration cross section evaluated at $E_{np} = 1.5$ MeV	25
2-1	A schematic diagram of the Bates liquid deuterium target loop.	33
2-2	The target cell geometry including the target collimating slits and the ELSSY horizontal solid angle defining slits.	34
2-3	The ELSSY spectrometer is shown with rays of three different values of energy loss and vertical scattering angle. The curved line connecting the focal points in the rear of the spectrometer is the approximate location of the focal surface. Also shown is the ELSSY detector package.	36
2-4	The focal plane detection system. The dashed curve illustrates the approximate location of the focal surface. The axes, Y_f and Y_{VDC} , point out of the page.	39
2-5	The VDC drift cells along with a typical track.	40
2-6	A VDC drift-time histogram.	41
2-7	A VDC vertical-distance histogram.	42
2-8	A close-up view of an idealized VDC drift cell. Each of the two pairs of rays is shown with its minimum drift-path.	44
2-9	The vertical-distance sum histograms for the VDC. The dashed lines are the cuts that were used to define acceptable values for the sums.	48
2-10	The difference between the VDC drift-time histograms when the vertical-distance sum cuts are included. The dashed histogram includes the sum cuts the solid histogram does not.	50
2-11	The wire geometry of the HDC illustrating the signal wires and the drift-cells. A typical particle track is also shown with a transverse angle ϕ_f . This track intercepts the chamber at an angle of $45^\circ - \theta_f$	51

2-12	The two HDCs and a typical particle track with a transverse angle of ϕ_f . This track intercepts the chambers at an angle of $45^\circ - \theta_f$. Y_{VDC} is located at the VDC.	52
2-13	An HDC drift-time histogram.	53
2-14	An HDC drift-distance histogram.	55
2-15	The drift-distance sum histogram for an HDC chamber. The dashed lines is the cut that was used to define acceptable values for the sum.	56
2-16	The difference between the HDC drift-time histograms when the drift-distance sum cut is included. The dashed histogram includes the sum cut the solid histogram does not.	57
2-17	The lead-glass normalized response to electrons and cosmic ray muons. The solid histogram is the electron spectrum. The dashed histograms are the cosmic ray muon spectra evaluated at two different normalization energies.	60
2-18	The effectiveness of the lead-glass detectors at reducing the cosmic ray background.	61
3-1	The Landau ϕ and ψ distributions.	66
3-2	The first order Feynman diagrams for external bremsstrahlung processes in matter.	68
3-3	The first order Feynman diagrams for internal bremsstrahlung processes in matter: a) Radiation from the electron current. b) Radiation from the nuclear current.	71
3-4	Corrections to elastic scattering to order α^4 . a) Pure elastic scattering (1γ exchange diagram.) b) 2γ exchange diagrams. c) Vacuum polarization diagram. d) Vertex correction diagrams.	71
3-5	Elastic peak with no straggling. Δ is the experimental energy cutoff used when computing the cross section.	72
3-6	The target cell and scattering geometry indicating the various pieces that the electron has to travel through before it exits the cell.	77
3-7	a) Schematic picture of the various energy losses as an electron traverses the target cell. b) An energy diagram indicating the energy losses.	79
3-8	Contour used in evaluating the inverse Laplace transform integral.	90
3-9	Comparing $\Phi(\lambda, T)$ for $T = 0$ and $T = 0.1$.	91
3-10	The line shape for elastic scattering from liquid hydrogen evaluated for $E = 900$ MeV, $\theta = 160^\circ$, and scattering from the center of the target cell, \mathcal{X}_{center} .	92
3-11	The line shape for elastic scattering from liquid deuterium evaluated for $E = 900$ MeV, $\theta = 160^\circ$, and scattering from the center of the target cell, \mathcal{X}_{center} .	93
3-12	The target cell and collimating slits illustrating the target averaging that occurs.	95
3-13	The angle, ζ , used in the large positive λ expansion.	101
3-14	Plots of the equation relating λ and κ for $T = 0$, $T = 0.2$, and $T = 0.4$.	102

3-15	Comparison of the numerical evaluation of $\Phi(\lambda, T)$ with the approximate expansion formulas. For $-3 \leq \lambda < 5$ the small T expansion was used and for $\lambda \geq 5$ the large positive λ expansion was used. The arrow indicates where the change occurs.	105
3-16	Schematic diagram indicating the placement of the equivalent radiator, t_{eq} , used to account for internal bremsstrahlung.	107
4-1	The focal plane coordinate system for the forward matrix elements and the VDC coordinate system which is inclined at a nominal angle of 45°	114
4-2	The solid angle acceptance function, $\Omega(z)$	118
4-3	The ELSSY target angle reconstructions. The solid histograms are the actual distributions and the dashed histograms are the reconstructions.	120
4-4	The ELSSY target position reconstruction. The solid histogram is the actual distribution and the dashed histogram is the reconstruction.	121
4-5	Monte Carlo calculation of the target-averaged line shape for elastic scattering from liquid deuterium evaluated for $E = 900$ MeV, $\theta = 160^\circ$. The dashed curve is the line shape, D^{nep} , for scattering at the center of the target cell, \mathcal{X}_{center}	122
5-1	The plot θ_{target} versus x_{VDC} for a quasi-elastic data run with 12 inch vertical slits and a similar Monte Carlo run.	127
5-2	Spectrum of 347 MeV scattered electrons from deuterium at 160° . The histogram is the experimental data and the solid circles are the Monte Carlo calculation for the elastic line shape.	128
5-3	Spectrum of 913 MeV scattered electrons from hydrogen at 160° . The histogram is the experimental data and the solid circles are the Monte Carlo calculation for the elastic line shape.	128
5-4	Scattering within a small volume element of the extended target.	129
5-5	Comparison of two methods used to unfold the 347 MeV threshold data. The first plot was generated without using either smoothing or Chauvenet's criterion. The second plot included these additions and is the final result.	140
6-1	Comparison of the new threshold electrodisintegration cross section measurements with existing data.	145
6-2	Threshold electrodisintegration cross sections averaged over $E_{np} = 0 - 3$ MeV compared with Paris potential calculations evaluated at $E_{np} = 1.5$ MeV	147
6-3	Threshold electrodisintegration cross sections compared with Argonne v_{14} potential calculations.	148

6-4	Threshold electrodisintegration cross sections averaged over $E_{np} = 0 - 3$ MeV compared with hybrid quark-hadron models evaluated at $E_{np} = 1.5$ MeV	150
6-5	Radiative unfolded threshold spectra.	151
A-1	Sketch of the focal surface curvature in the dispersion plane. The central ray is shown along with two rays with the same δ but different θ 's at the target. Their intersection defines a point on the focal surface.	154
A-2	Sketch of the focal surface curvature perpendicular to the dispersion plane. Two off-axis ($\phi_t \neq 0$) central rays are shown with different θ_t . Their intersection defines a point on the focal surface.	157
B-1	A flat quasi-elastic response.	163
E-1	Schematic diagram illustrating the scattering process.	172
E-2	Elastic line shapes for scattering from ^1H showing the effect of including the energy dependence of the elastic cross section.	175

List of Tables

2.1	The target collimating slit coordinates.	35
3.1	The external bremsstrahlung parameter b	89
3.2	Values for λ_{peak} corresponding to the maximum of the function $\Phi(\lambda, T)$	94
3.3	Comparison of large positive λ expansions with the exact result for the function $\Phi(\lambda, T)$ when $T = 0$	104
5.1	Detector efficiencies.	134
5.2	\mathcal{R}_{el} radiative correction factors.	135
5.3	Estimated systematic errors.	141
6.1	Experimental cross sections measured in the thesis.	144
A.1	The curvature of the ELSSY focal surface in the dispersion plane compared with a flat focal surface at an angle of 43.5°	156
B.1	Estimated cross sections for the deuterium threshold electrodisintegration and aluminum quasi-elastic reactions at the kinematics of this experiment.	162
B.2	Count rate estimates per beam burst for the deuterium threshold electrodisintegration and aluminum quasi-elastic reactions at the kinematics of this experiment.	162
B.3	The minimum electron slit traversal thicknesses needed effectively to eliminate the quasi-elastic aluminum background.	164
C.1	Table of the Landau functions $\phi(\lambda)$ and $\psi(\lambda)$	166
D.1	The independent density effect correction parameters.	168
D.2	Density effect correction parameters.	169
F.1	The first order ELSSY forward matrix elements for $R = 2.23$ meters. Units are that of Raytrace: distances in [cm], angles in [mr], and δ in %.	179
F.2	The second order ELSSY forward matrix elements for $R = 2.23$ meters. These are for a focal plane tilt angle of 0° . Units are that of Raytrace: distances in [cm], angles in [mr], and δ in %.	179

F.3	Some important third and fourth order ELSSY forward matrix elements for $R = 2.23$ meters. These are for a focal plane tilt angle of 0° . Units are that of raytrace: distances in [cm], angles in [mr], and δ in %.	180
F.4	The ELSSY reverse matrix elements generated from the Monte Carlo Model. These express the target coordinates in terms of the VDC coordinates. Units are that of Raytrace: distances in [cm], angles in [mr], and δ in %.	181
H.1	Unfolded threshold cross sections.	198
H.2	Unfolded threshold cross sections.	199
H.3	Unfolded threshold cross sections.	199
H.4	Unfolded threshold cross sections.	200

Chapter 1

Introduction

This thesis presents new measurements of deuteron threshold electrodisintegration at high momentum transfer. These measurements were made with good momentum resolution which allowed the threshold cross sections to be averaged over 0 to 3 MeV in E_{np} for comparison with previous measurements from Saclay [1]. The Q^2 of the measured points ranged from 8 to 42 fm^{-2} extending the previous Saclay measurements which ended at 27 fm^{-2} . The data were also averaged over 0 to 10 MeV in E_{np} for comparison with a poorer resolution SLAC measurement [2].

This thesis is divided into six chapters. The first chapter discusses the physics of the electrodisintegration reaction and defines the kinematic variables used throughout this thesis. The second chapter describes the experimental setup and the procedures used to acquire the data. Chapters three, four, and five are devoted to data analysis. The last Chapter presents the results and makes comparisons with other data and theoretical calculations.

1.1 Electron-Deuteron Scattering

In any experiment where one wishes to learn more about a particular phenomenon (e.g. nuclear structure), it is desirable to use a well understood interaction to probe the object under study. Thereby one can hope to achieve a clean theoretical separation of the phenomenon from the interaction. The electromagnetic interaction (QED) satisfies this criterion, and electron scattering experiments have aided us tremendously in our fundamental understanding of the

This peak results from the M1 transition from the deuteron ground state to the unbound isovector scattering state 1S_0 illustrated in Figure 1-1. By performing the measurement at large scattering angles this transition is enhanced. This can be shown from the general formula for unpolarized single-arm electron scattering

$$\frac{d^2\sigma}{d\Omega d\omega} = \frac{\sigma_M}{\eta} [V_L(\theta)R_L + V_T(\theta)R_T], \quad (1.1)$$

where σ_M is the Mott cross section, η is the recoil factor, R_L and R_T are the longitudinal and transverse nuclear response functions, and V_L and V_T are their corresponding kinematic factors.

$$V_L = \frac{Q_\mu^4}{q^4} \quad (1.2)$$

$$V_T = \frac{Q_\mu^2}{2q^2} + \tan^2 \frac{\theta}{2} \quad (1.3)$$

Since the M1 transition from the deuteron ground state is purely transverse, the breakup cross section is very nearly proportional to $V_T R_T$. Therefore, at backward angles the cross section is enhanced by transverse kinematic factor due to the V_T term. For 155° the enhancement factor is roughly 20. The experiment presented in this thesis measured the cross section at 160° where the enhancement factor is 32.

Near threshold the cross section is dominated by this transition at this bombarding energy. For higher values of excitation energy larger angular momentum scattering states contribute to the cross section. It turns out that this transition is an ideal place to study the meson-exchange current aspects of the nucleon-nucleon interaction.

Illustrated in Figure 1-3 is the electrodisintegration reaction. An incident electron of energy E transfers a virtual photon to the deuteron and scatters at an angle θ with energy E' . The deuteron absorbs the virtual photon and reacts to the interaction. If the energy transferred by the virtual photon is large enough, the interaction can cause the deuteron to break apart. Since the deuteron is weakly bound this happens for energy transfers greater than 2.225 MeV. The variable E_{np} is the resulting relative energy of the emerging neutron-proton system, and just at breakup $E_{np} = 0$. Since the nuclear binding is believed to result from virtual meson exchange, electron scattering experiments which are sensitive to the charge and current structure, can provide information on the currents resulting from such processes. Notice that in Figure 1-3 it was left unclear how the virtual photon actually coupled to the deuteron. Since the deuteron is composed of nucleons, the simplest picture is that the virtual photon couples only to the

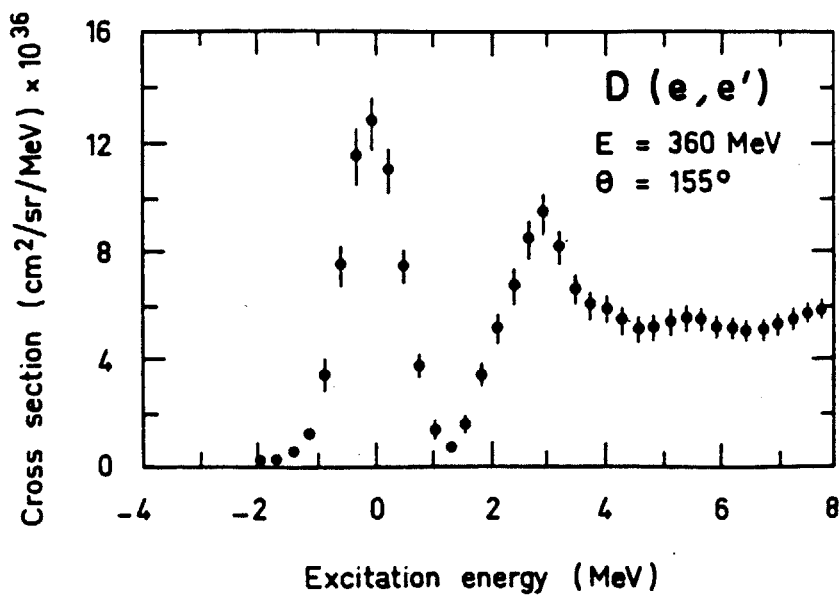


Figure 1-2: The spectrum of scattered electrons from deuterium at 155 degrees. Taken from reference [1].

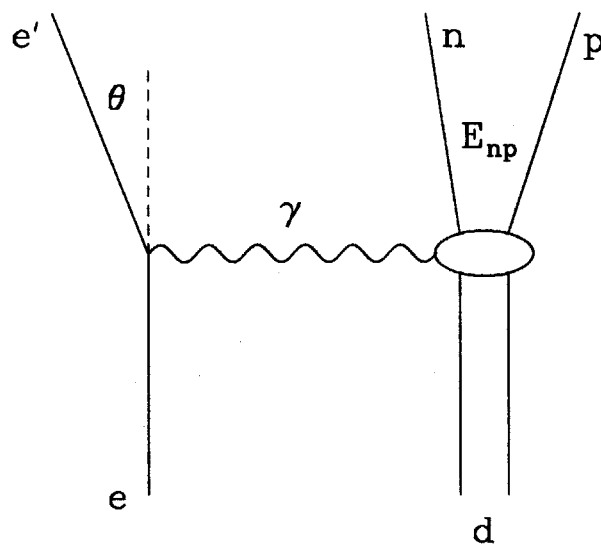


Figure 1-3: The kinematics of the electrodisintegration reaction.

nucleon currents (one-body current). This is called the impulse approximation (IA) and the scattering amplitude for this process is proportional to the following matrix element,

$$\langle {}^1S_0 | \hat{T}_{1\text{-body}}^{M1} | {}^3S_1 + {}^3D_1 \rangle \quad (1.4)$$

which can be separated as follows,

$$\langle {}^1S_0 | \hat{T}_{1\text{-body}}^{M1} | {}^3S_1 \rangle + \langle {}^1S_0 | \hat{T}_{1\text{-body}}^{M1} | {}^3D_1 \rangle, \quad (1.5)$$

where $\hat{T}_{1\text{-body}}^{M1}$ is the one-body operator for the M1 transition. The first matrix element is the amplitude for the ${}^3S_1 \rightarrow {}^1S_0$ transition and the second is the amplitude for the ${}^3D_1 \rightarrow {}^1S_0$ transition. However, due to the presence of mediating virtual mesons the photon can also couple to the meson-exchange currents (MEC) which is a two-body current. These are illustrated in Figure 1-4a-b. The first graph represents a coupling of the virtual photon to a mediating pion in flight. The second graph is a nucleon-antinucleon pair excitation process. In Figure 1-4c the virtual photon excites a nucleon isobar resonance, the lowest mass being the $\Delta(1232)$ resonance. This is a one-body Δ -isobar current (IC). The contribution from these processes to the scattering amplitude is expressed by the following matrix elements,

$$\langle {}^1S_0 | \hat{T}_{\text{pion}}^{M1} | {}^3S_1 + {}^3D_1 \rangle + \langle {}^1S_0 | \hat{T}_{\text{pair}}^{M1} | {}^3S_1 + {}^3D_1 \rangle + \langle {}^1S_0 | \hat{T}_{\Delta}^{M1} | {}^3S_1 + {}^3D_1 \rangle. \quad (1.6)$$

At high momentum transfers where the spatial resolution of the virtual photon becomes smaller than the size of the deuteron the effects of the MEC should become more apparent. Using the value 4 fm for the size of the deuteron we obtain a rough estimate that MEC should become more prominent for $Q^2 > 2.5 \text{ fm}^{-2}$. This is indeed the case as can be seen in Figure 1-5 [3]. The dotted curve is the impulse approximation calculation (IA), the dashed curve includes pion-exchange currents, the dot-dashed includes rho-exchange currents and finally the solid curve includes the effect of isobar currents (IC) (see Figure 1-4). The open squares are data from a measurement made at Saclay where the threshold cross sections have been averaged over 0 to 3 MeV in E_{np} [1]. The calculations used the Paris potential to generate the ground state and scattering state wave functions and are evaluated at $E_{np} = 1.5 \text{ MeV}$. As can be seen in Figure 1-5, the result from the IA calculation disagrees strongly with the trend of the data for even modest values of Q^2 . In particular, the IA calculation predicts a large minimum in the threshold cross section at $Q^2 \sim 12 \text{ fm}^{-2}$ which is not present in the data. The IA minimum is due to a destructive interference between the amplitudes for the ${}^3S_1 \rightarrow {}^1S_0$ and

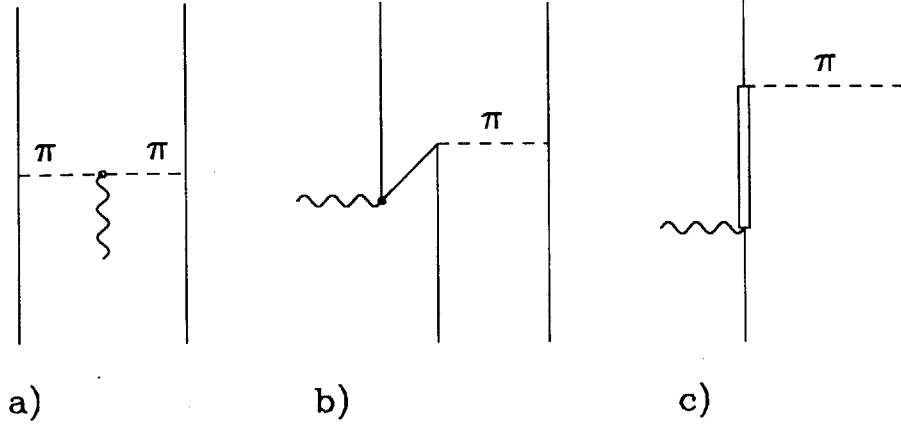


Figure 1-4: Meson-exchange current diagrams and an isobar-current diagram. a) Interaction with a π in flight. b) Pair creation term. c) Excitation of a Δ -isobar resonance.

${}^3D_1 \rightarrow {}^1S_0$ transitions (see Equation 1.5). Because of the cancellation of one-body currents almost the entire strength at $Q^2 \sim 12 \text{ fm}^{-2}$ is due to non-nucleonic degrees of freedom. Indeed, including MEC and IC brings the theory into good agreement with the Saclay data. This agreement is a striking example of the necessity of including mesonic degrees of freedom in order to obtain agreement of theory to experiment. Above a momentum transfer of about 25 fm^{-2} the theoretical curves calculated with different meson-exchange potentials diverge sharply, reflecting the sensitive cancellation of the one-body and two-body amplitudes. This region ($25 \text{ fm}^{-2} < Q^2 < 40 \text{ fm}^{-2}$) is accessible at the Bates facility, and the motivation for this experiment was to provide accurate data in this range of momentum transfer where there is great model sensitivity to the two-body currents. At even higher momentum transfers, such as will be available at the CEBAF facility, shorter range components of the nucleon-nucleon interaction can be probed. Eventually, a more appropriate description in terms of the constituent quarks and gluons should be given and measurement of deuteron threshold electrodisintegration at very high Q^2 may provide such information.

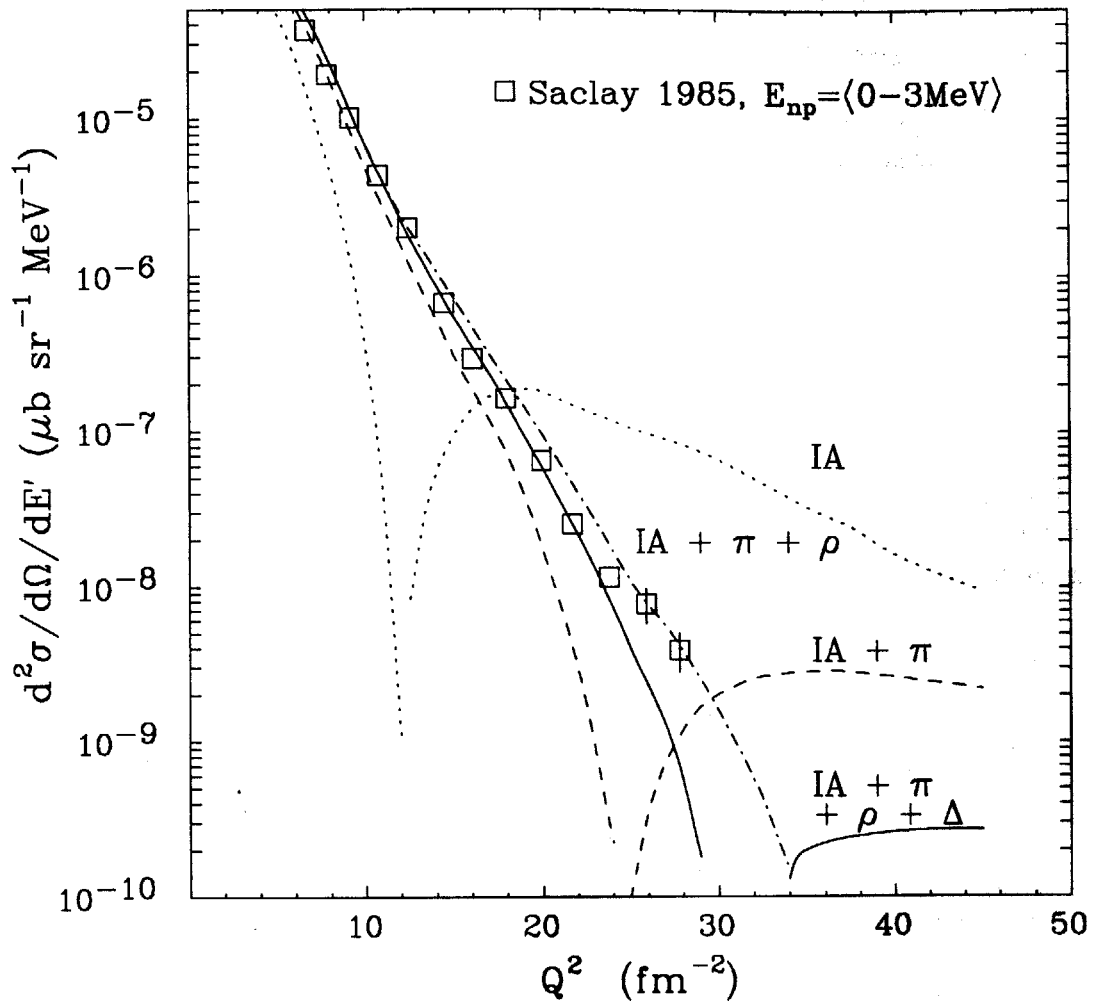


Figure 1-5: Threshold electrodisintegration cross section evaluated at $E_{np} = 1.5 \text{ MeV}$ [3]. The dotted curve is the impulse approximation, the dashed curve includes pion-exchange currents, the dot-dashed includes rho-exchange currents and finally the solid curve includes the effect of isobar components in the wave function.

1.2 Kinematics and Definitions

The variables used to define the kinematics of deuteron electrodisintegration are presented in this section. These notations will be used throughout the thesis.

Illustrated in Figure 1-3 is the electrodisintegration reaction. From the figure the following 4-momenta are defined as follows:

$$P_e = (E, \vec{p}) \quad (1.7)$$

$$P_d = (M_d, 0) \quad (1.8)$$

$$P'_e = (E', \vec{p}') \quad (1.9)$$

$$P'_d = (E'_d, \vec{p}'_d) \quad (1.10)$$

where E (E') is the initial (scattered) electron energy and \vec{p} (\vec{p}') its 3-momentum and M_d is the mass of the deuteron where it is taken to be initially at rest. The 4-momentum transferred, Q , is given by the expression

$$Q = P_e - P'_e = (E - E', \vec{p} - \vec{p}'). \quad (1.11)$$

From conservation of 4-momentum we have the following relation

$$P_e + P_d = P'_e + P'_d \quad (1.12)$$

which can be rewritten as

$$P_e - P'_e + P_d = P'_d. \quad (1.13)$$

Squaring the above equation gives the expression

$$P_e^2 + P_e'^2 + P_d^2 - 2P_e \cdot P'_e + 2P_e \cdot P_d - 2P'_e \cdot P_d = P_d'^2 \quad (1.14)$$

where the inner products are defined as follows

$$P \cdot P' = EE' - \vec{p} \cdot \vec{p}' \quad (1.15)$$

$$P^2 = M_{rest}^2. \quad (1.16)$$

For the deuteron final momentum, P'_d , the square of the 4-momentum is written as follows:

$$P_d'^2 = (M_n + M_p + E_{np})^2 \quad (1.17)$$

where the kinematic variable E_{np} is the relative separation energy of the final neutron-proton system when the deuteron breaks apart. Since $M_n + M_p = M_d + 2.225$ this result can be re-expressed in terms of an excitation energy, E_{exc} , where $E_{exc} = 2.225 + E_{np}$.

$$P_d'^2 = (M_d + E_{exc})^2 \quad (1.18)$$

Solving Equation 1.14 for the scattered electron energy, E' , we obtain the well known formula for ultra-relativistic electron scattering,

$$E' = \frac{1}{\eta} \left(E - E_{exc} - \frac{E_{exc}^2}{2M_d} \right) \quad (1.19)$$

where the recoil factor, η , and excitation energy are given by the expressions

$$\eta = 1 + \frac{2E}{M_d} \sin^2\left(\frac{\theta}{2}\right) \quad (1.20)$$

$$E_{exc} = 2.23 + E_{np} . \quad (1.21)$$

The square of the 4-momentum transfer can be also evaluated to yield the following result for ultra-relativistic electrons.

$$Q^2 = -4EE' \sin^2(\theta/2) \quad (1.22)$$

Chapter 2

Experimental Apparatus and Procedure

2.1 Overview

The experiment to measure the threshold electrodisintegration of the deuteron was performed at the MIT-Bates Linear Accelerator Center which is located in Middleton, Massachusetts. The experimental run started on April 12, 1990, and was completed May 26, 1990. During this period, the threshold measurements were made at five different incident electron energies, 347, 576, 754, 820, and 913 MeV, with a scattering angle of 160° . Our highest energy, 913 MeV, was also the highest energy achieved to that time at the Bates LINAC. The incident electrons scattered from a liquid deuterium target and were momentum analyzed with the high resolution spectrometer, ELSSY, located in the North Experimental Hall. The corresponding Q^2 points were as follows: 8.7, 20.5, 31.6, 36.0, and 42.4 fm^{-2} .

Because the threshold cross sections were expected to be as small as $10^{-40} \text{ cm}^2/\text{sr}/\text{MeV}$ at the highest Q^2 point, considerable effort had to be devoted to the design of the experiment. In particular, the count rate which is given by luminosity, \mathcal{L} , times cross section, σ , times solid angle, Ω , had to be made as large as possible in order to make the measurement feasible. Good resolution ($< 1.5 \text{ MeV FWHM}$) was also required to separate the elastic peak from the breakup threshold (2.2 MeV). Unfortunately, all of these experimental constraints are coupled and in the end one must arrive at an acceptable compromise. For example, a liquid deuterium target was used in this experiment, and the usable thickness had to be limited to less than 5 centimeters due to the energy resolution constraint. The liquid deuterium target was cooled by a 200 Watt

cryogenic helium refrigerator. The capacity of the refrigerator limited the intensity of beam current that we could use ($< 50 \mu\text{A}$). In the end, the counting rate at the highest Q^2 point was only expected to be 2 counts per day. This put stringent limits on the level of background that we could accept (< 2 counts/day).

The sources of background can be grouped into two categories: beam dependent and beam independent. The beam dependent source comes from having an electron beam on a target and is also called target related background. The beam independent source comes from cosmic rays triggering the detection system. Making the measurement near the deuterium elastic peak helped to eliminate some sources of target related background due to kinematics. Other more exotic multi-step processes such as π^0 production quickly followed by its decay, $\pi^0 \rightarrow \gamma\gamma$, and then pair production, $\gamma \rightarrow e^+e^-$, could generate electrons within our acceptance. This contribution was estimated to be too small. The largest source of target related background was electron scattering from the aluminum target cell. These electrons were effectively eliminated by designing target collimating slits which blocked electrons scattered from the target cell entrance and exit windows from entering the spectrometer acceptance. Unfortunately, electrons from the beam halo could scatter from the sides of the target cell and be accepted into the spectrometer. Therefore, beam halo monitors (phototubes upstream and downstream of the target) were used to monitor the quality of the beam. Secondary emission monitors (SEM) were also used to shut down the experiment if the beam drifted significantly from its predetermined line.

The beam independent source was reduced by making improvements to the existing ELSSY focal plane detection system. To provide better transverse angle (ϕ_f) resolution two new horizontal drift chambers (HDC) were designed and constructed. This allowed a cut to be placed on the angular distribution to help separate real electron events from cosmic rays with large transverse angles (ϕ_f). A new gas Cherenkov detector was also designed and constructed to separate pions from electrons. Unfortunately, cosmic muons with energies greater than 2 GeV could still trigger the Cherenkov detector and therefore appear as an electron. This small fraction of events was reduced by using lead-glass shower-counter blocks. These separate the cosmic muons from the electrons based on the difference in their electromagnetic shower development. A muon is inefficient in generating an electromagnetic shower and will therefore deposit little of its energy inside the detector. However, an electron will generate a large shower and deposit most or all of its energy in the detector.

The improvements made to the focal plane detection system allowed us to measure cross sections as small as $10^{-40} \text{ cm}^2/\text{sr}/\text{MeV}$ with good resolution. Our measurements also represent the smallest cross sections that had been measured at that time at the Bates laboratory.

2.2 Electron Beam

The Bates LINAC provided an electron beam with energies ranging from 350 to 900 MeV. The average beam current used in this experiment was 25 μA with a 1% duty factor. The energy spread in the incident beam was 0.3% and was dispersed on the target. This dispersion when coupled to the ELSSY spectrometer dispersion provides a condition known as dispersion matching [4]. In this mode resolutions in momentum loss, $\delta P/P$, of the order of 10^{-4} (0.01%) are achievable in the ELSSY focal plane. This is more than an order of magnitude better than the resolution of the incident electron beam. When the system is fully dispersion matched the dispersion of the beam, $(x|\delta)_{\text{Beam}}$, and its height are given by the following expressions for elastic scattering [5],

$$(x|\delta)_{\text{Beam}} = -\frac{1}{\eta} \frac{(x|\delta)_{\text{ELSSY}}}{(x|x)_{\text{ELSSY}}} = \frac{6.70}{\eta} [\text{cm}/\%], \quad (2.1)$$

$$\text{Beam Height} = \frac{2.0}{\eta} [\text{cm}], \quad (2.2)$$

where $(x|\delta)_{\text{ELSSY}}$ and $(x|x)_{\text{ELSSY}}$ are the spectrometer first-order matrix elements (see Appendix F), and η is the recoil factor,

$$\eta = 1 + \frac{2E_{\text{Beam}}}{M_t} \sin^2(\beta/2). \quad (2.3)$$

In this experiment we tried to run fully dispersion matched when possible. However, since our peak widths were very broad, of the order of 1.5 MeV FWHM due to energy straggling, this was not an important factor in the resolution.

2.3 Liquid Deuterium Target System

The Bates high power liquid deuterium target system was used in this experiment. This system is capable of producing either a liquid deuterium or a liquid hydrogen target. Targets of both isotopes were used in this experiment. The design, operation, and safety of the system is discussed in detail elsewhere [6] [7]. In the following sections only a brief description is given of this system.

2.3.1 Overview

The liquid deuterium target system consisted of three main parts: a 200 Watt cryogenic helium refrigerator, a target loop, and a gas handling valve panel. The 200 Watt refrigerator was used to supply cryogenic helium to a counterflow heat exchange located inside the target loop to provide liquefaction. The gas handling valve panel was used to direct the flow of the target gas from a 3100 gallon reservoir to the target loop. A schematic diagram of the target loop is shown in Figure 2-1 illustrating some of its features. The target loop is roughly one meter high and a half a meter wide and contains 10 liters of liquid target when full. The liquid was circulated in the loop by two vaneaxial fans to speeds of the order of 2 m/s. The heater currents were modulated by the beam current so as to maintain a constant heat load on the target at all times. Not indicated in the target loop figure were several temperature sensors. These consisted of both diode and thermocouple temperatures sensors. These were monitored during the experiment, as well as the target loop pressure, for safety considerations and accurate liquid density information. The information from the various sensors was also written to magnetic tape as part of the data acquisition system. The electron beam passes through the section illustrated in the figure as the removable target piece. This is discussed in more detail in the following section. The target loop was mounted inside the North Hall scattering chamber assembly with feedthroughs at the top for the cryogenic helium and gaseous deuterium.

2.3.2 The Target Cell

The geometry of the target cell is shown in Figure 2-2. The cell was made of aluminum and the wall thickness was .037 inches. The equation describing the inner and outer cell shapes was modeled as

$$\left(\frac{|z|}{a}\right)^m + \left(\frac{|y|}{b}\right)^m = 1, \quad (2.4)$$

and the following parameters for the inner and outer shapes were determined, $a_i = 4.671$ cm, $b_i = 1.606$ cm, $m_i = 2.295$, and $a_o = 4.765$ cm, $b_o = 1.700$ cm, $m_o = 2.310$ respectively.

The target collimating slits indicated in the figure were attached to a metal strut which was mounted from the top of the scattering chamber. The purpose of the slits was effectively to eliminate the electrons which scattered from the entrance and exit window of the target cell, and their design is discussed in Appendix B. These slits also define the usable target length and were accurately aligned using the theodolite mounted at the back of the ELSSY spectrometer. In Table 2.1 the coordinates for each of the slit edges are given. The ELSSY horizontal slits

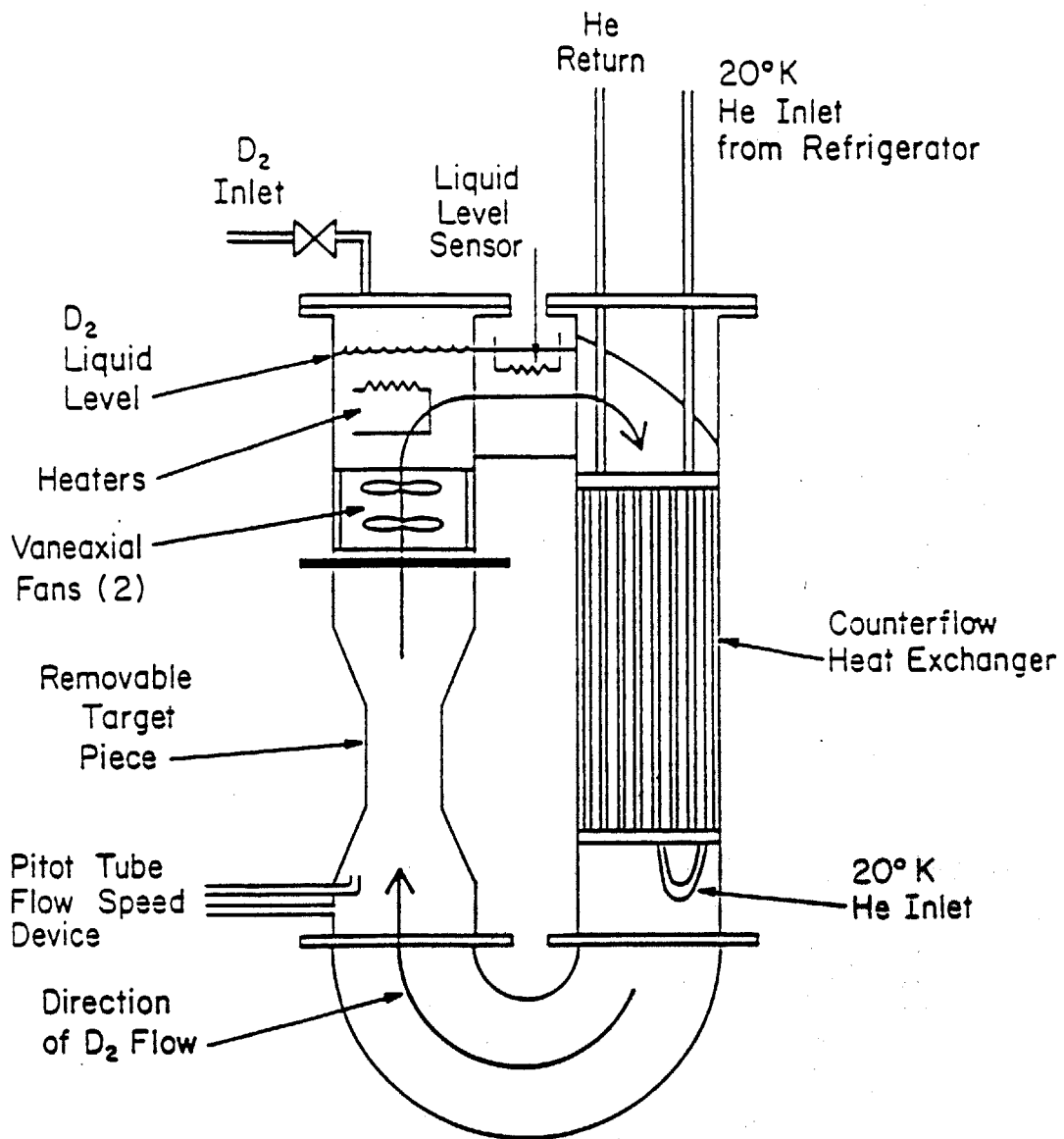


Figure 2-1: A schematic diagram of the Bates liquid deuterium target loop.

Edge	Coordinates
a	$y = -4.79$ cm $z = -11.04$ cm
b	$y = -2.25$ cm $z = -3.63$ cm
c	$y = -3.94$ cm $z = -12.16$ cm
d	$y = -1.40$ cm $z = -5.59$ cm

Table 2.1: The target collimating slit coordinates.

which are indicated in the figure are 194 cm away the pivot point and the vertical slits are at a distance of 200 cm.

2.4 ELSSY Spectrometer System

2.4.1 ELSSY Spectrometer

The Energy Loss Spectrometer System (ELSSY) is the Bates high resolution 900 MeV/c magnetic spectrometer [4]. When the system is fully dispersion matched resolutions of the order of 10^{-4} in $\delta P/P$ are achievable. The principle behind dispersion matching is to focus all beam particles with the same energy loss at the same point on the focal surface. A diagram of the spectrometer is shown in Figure 2-3 along with nine representative rays. The nine rays emerge from the target with three values of θ_t and three values of δ . For each value of δ the rays are focused at the rear of the spectrometer. The curve connecting the points illustrates the approximate location of the focal surface. In Appendix A the shape of the ELSSY focal surface is discussed in detail. The focal plane detection system is also shown at the rear of the spectrometer. The spectrometer is a split dipole design with a 90° vertical bend. The design value for the bending radius, R , for the central ray ($\delta = 0$ and $\theta_f = 0$) is 2.23 meters. The

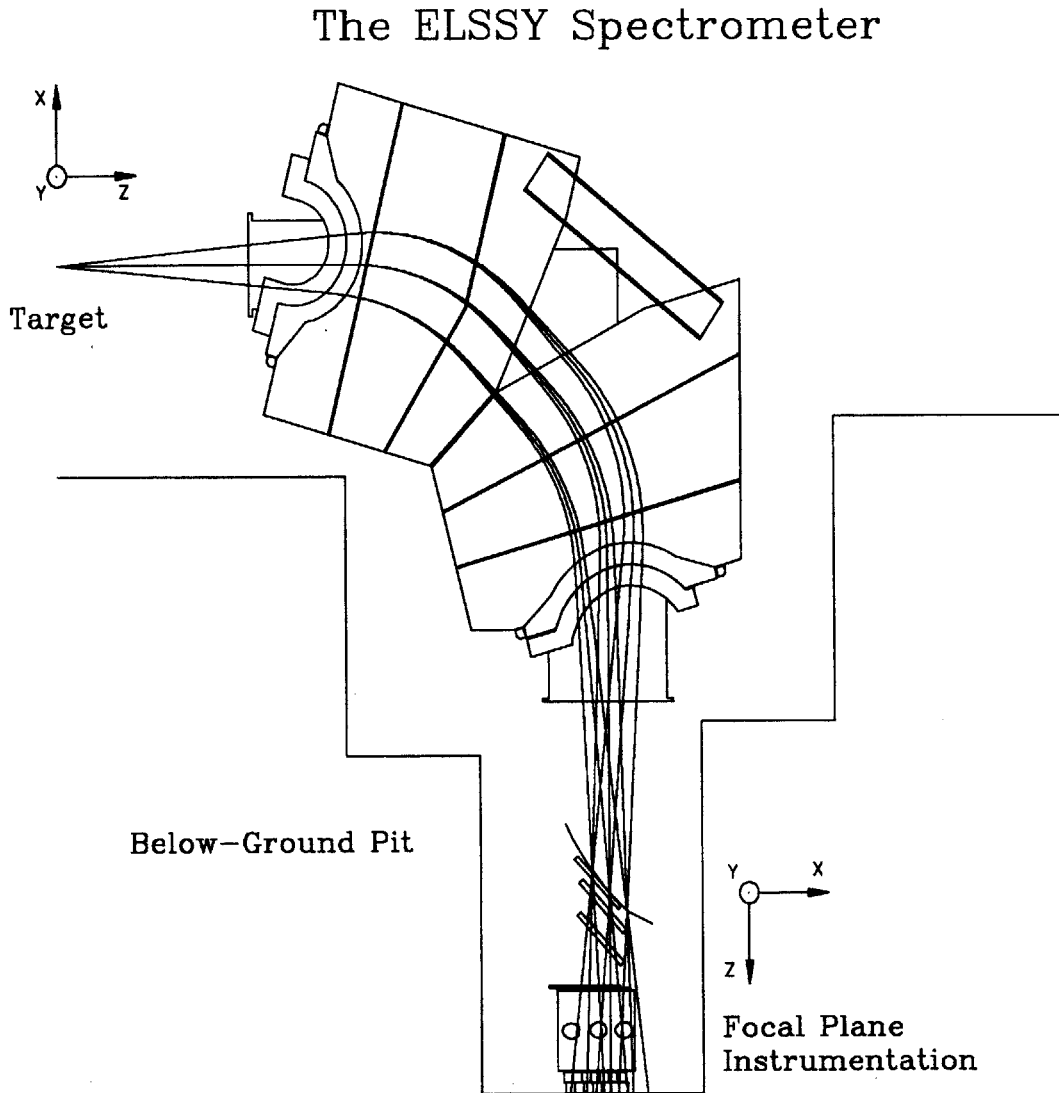


Figure 2-3: The ELSSY spectrometer is shown with rays of three different values of energy loss and vertical scattering angle. The curved line connecting the focal points in the rear of the spectrometer is the approximate location of the focal surface. Also shown is the ELSSY detector package.

force experienced by the central ray is given by the Lorentz equation:

$$\vec{F} = \frac{e}{c} \vec{v} \times \vec{B}. \quad (2.5)$$

This can be reduced as follows:

$$\frac{\gamma m v^2}{R} = \frac{e}{c} v B, \quad (2.6)$$

$$\frac{P_{\text{cent}}}{B} = \frac{eR}{c}, \quad (2.7)$$

where P_{cent} is the momentum of the central ray. The quantity P_{cent}/B is often referred to as the spectrometer constant. Evaluating this constant, eR/c , for ELSSY gives us the design value for the spectrometer constant.

$$\frac{P_{\text{cent}}}{B} = 66.85 \text{ MeV}/c/\text{kG}. \quad (2.8)$$

The forward and reverse transfer matrix elements for the spectrometer are presented in Appendix F.

2.4.2 Focal Plane Instrumentation

Shown in Figure 2-4 is a close-up view of the focal plane detection system. The detection system consisted of a vertical drift chamber (VDC), two horizontal drift chambers (HDC), a pair of scintillators, a gas Cherenkov detector, and an array of 14 lead-glass Cherenkov detectors. The VDC was inclined at a nominal angle of 45° to coincide as nearly as possible with the focal surface which is indicated by the dashed line in the figure (see Appendix A). The HDCs were also inclined at 45° .

The VDC was used to measure the focal plane coordinates x_{VDC} and θ_f of the scattered electrons in the rear of the spectrometer. x_{VDC} is the x -displacement along the VDC. The dotted line shown inside of the VDC chamber illustrates the orientation of the signal wires: perpendicular to the plane of the page. The offset, x_o , of the central ray from the center of the VDC needs to be calibrated. This was done in the energy calibration. The two horizontal drift chambers were used to measure y_{VDC} and ϕ_f where y_{VDC} is the y -displacement at the VDC and ϕ_f is the transverse angle. The lines shown inside of the HDC chambers illustrates the orientation of their signal wires: in the plane of the page. The scintillators were used for

timing. The gas Cherenkov and lead-glass blocks were used for particle identification. The experimental trigger consisted of a good scintillator and a good Cherenkov or lead-glass signal. In the following sections the salient features of each of the detector's operation and analysis is discussed.

2.4.3 VDC

In the paper by Bertozzi *et al.* [8] the design, operation, and analysis of the VDC is discussed at some length. This will not be repeated here. But some corrections that were made to the existing VDC analysis will be presented. These corrections are primarily for the reconstruction of the focal plane angle, θ_f . They were necessary in order to obtain agreement with the Monte Carlo simulation for the focal plane angle. In this sense the Monte Carlo was a valuable tool for finding many subtle errors in the VDC analysis.

2.4.3.1 Vertical-distance Lookup Table Calibration

Shown in Figure 2-5 is a typical electron track incident on the VDC with angle θ and the hit pattern illustrating the drift-paths which follow the field lines. The spacing between the signal wires, u , is 0.250 inches (6.35 mm). The dotted circles represent the approximate extent of the radial field region for each drift cell. The measured drift-times in each cell come from the shortest drift-paths and are calculated from the delay line readouts as follows:

$$t_d = \frac{1}{2}(t_L + t_R) + \text{offset} , \quad (2.9)$$

where t_L and t_R are the TDC stop times from the opposite ends of the delay line. Since the VDC used three delay lines in the readout, only three drift-times could be obtained per event. The wire numbers, n_1 , n_2 , and n_3 , of the triggered cells are given by the difference, $t_L - t_R$, for each delay line. The vertical distances, y_1 , y_2 , and y_3 , shown in the figure are the distances from the signal wire to the intersection of the ray with the center of the cell. These distances need to be reconstructed in order to calculate the focal plane variables, x_{VDC} and θ_f ($\theta_f = 45^\circ - \theta$). This is accomplished by using a drift-time to vertical-distance lookup table; $y = y(t_d)$. The lookup table is constructed using the integral-drift-time method [9].

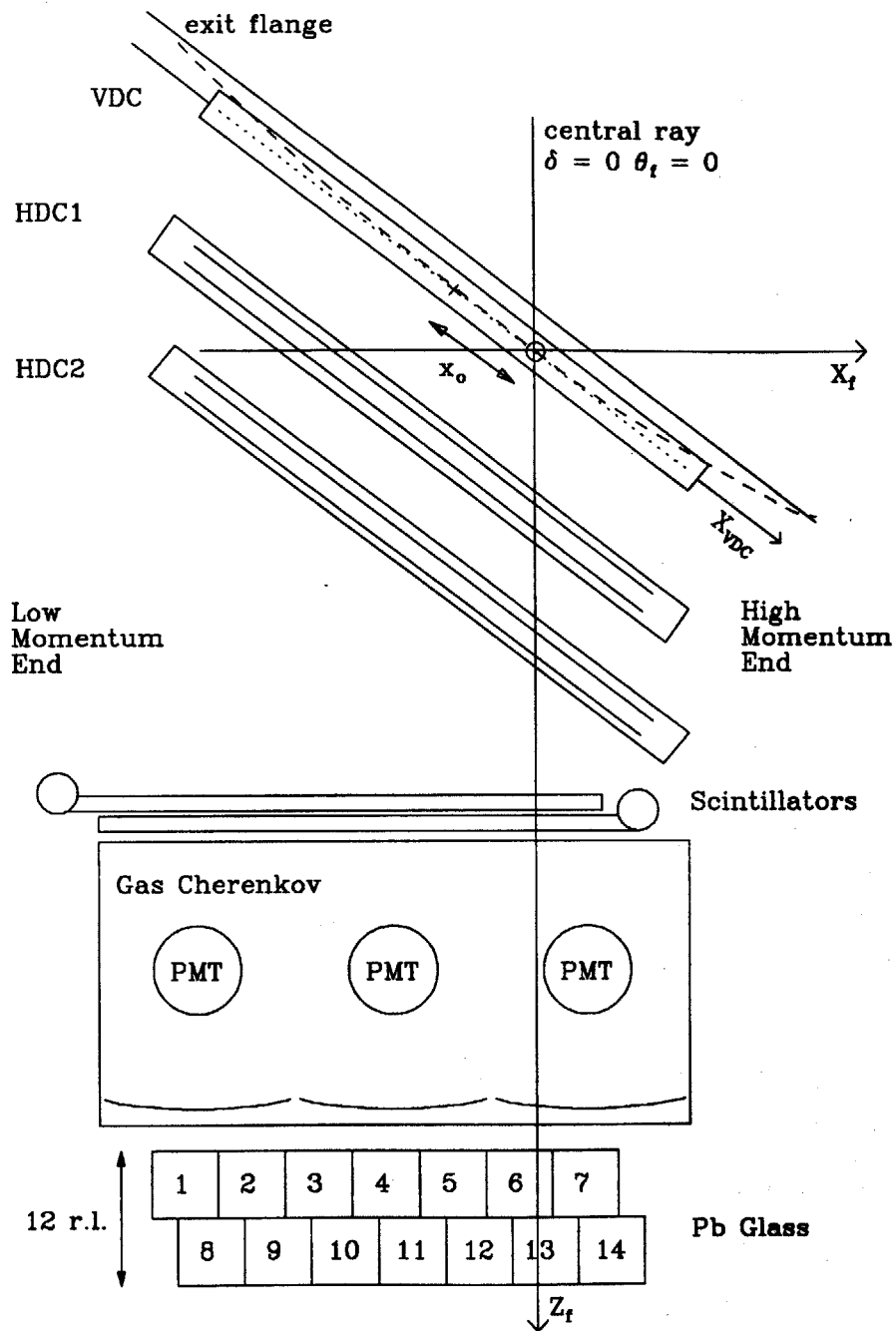


Figure 2-4: The focal plane detection system. The dashed curve illustrates the approximate location of the focal surface. The axes, Y_f and Y_{VDC} , point out of the page.

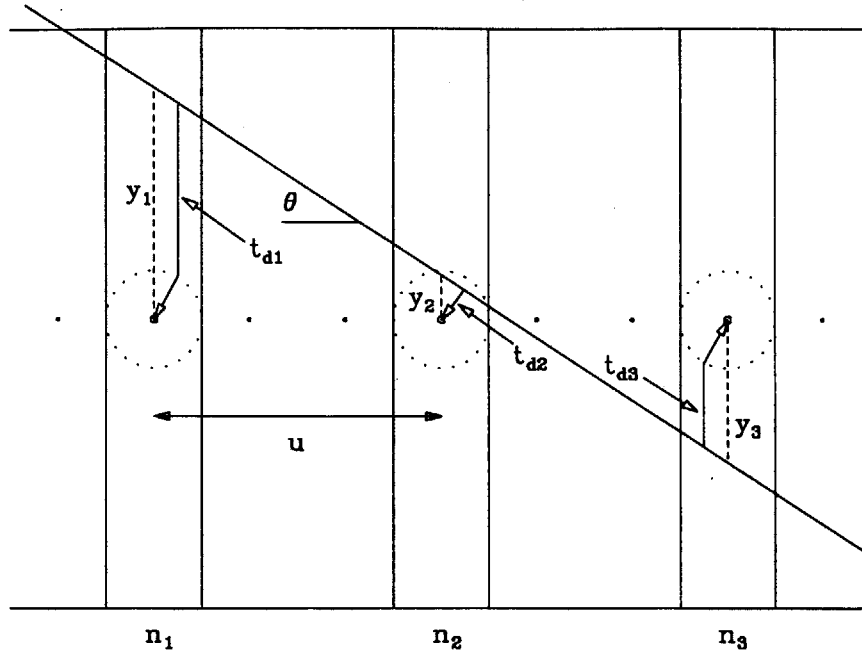


Figure 2-5: The VDC drift cells along with a typical track.

In Figure 2-6 a drift-time histogram for a quasi-elastic spectrum is shown. Mathematically this histogram can be expressed by the quantity, dN/dt_d , the number of counts per unit drift-time channel. This can be separated as follows:

$$\frac{dN}{dt_d} = \frac{dN}{dy} \frac{dy}{dt_d} = \frac{dN}{dy} v_d, \quad (2.10)$$

where dN/dy is the number of counts per unit vertical-distance and v_d is the drift velocity. Therefore, if the drift-cell has been uniformly illuminated ($dN/dy = \text{constant}$), the shape of the drift-time histogram reflects the drift velocity. For the VDC this is misleading for two reasons. First, because of the three delay line readout system there is a maximum allowable vertical-distance for each angle of incidence. This maximum distance is found from geometry by setting the vertical-distances on adjacent cells of the same delay line equal. The result is as follows:

$$y_{max}(\theta) = \frac{3u}{2} \tan \theta. \quad (2.11)$$

The finite vertical angle acceptance, $\pm\Delta\theta$, then causes a spread in the maximum vertical-distances which leads to the drop off at large drift-times even though the drift velocity is well

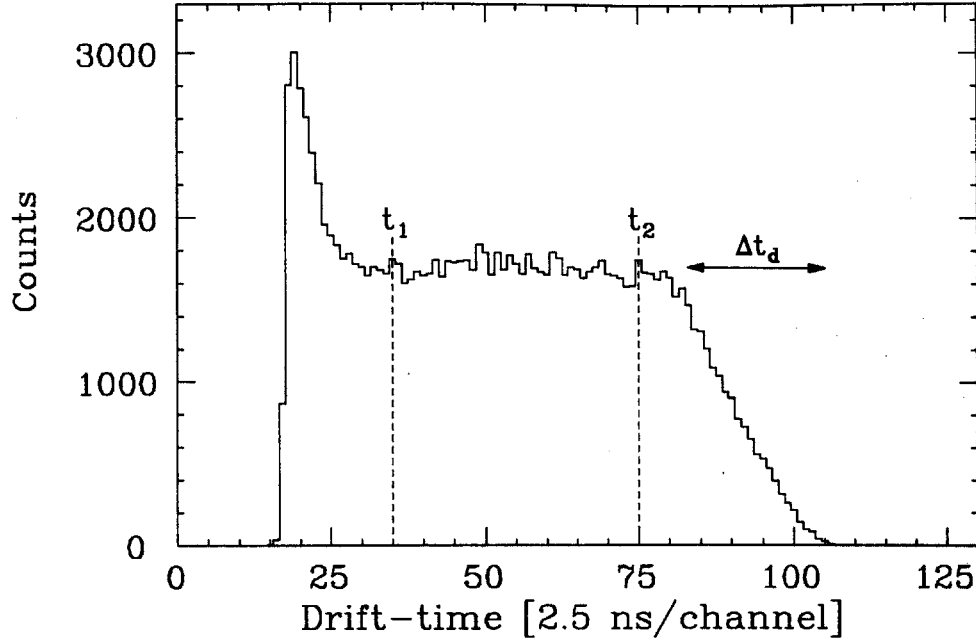


Figure 2-6: A VDC drift-time histogram.

saturated (see Figure 2-6). The width of the falloff, Δt_d , is given by the following formula for small $\Delta\theta$:

$$\Delta t_d = \frac{\Delta y_{max}}{v_d} = \frac{3u}{v_d} \sec^2(\theta) \Delta\theta, \quad (2.12)$$

where $\langle\theta\rangle$ is the average angle.

Secondly, the sharp peak at the beginning of the histogram is mostly an effective increase in drift velocity due to the change in the geometry of the field lines near the wire [8]. The magnitude of this increase is proportional to the angle of the inclined track. The more normal it is with respect to the VDC signal plane, the larger this peak becomes, and the converse is also true. However, the lookup table for the VDC can still be constructed.

From Equation 2.10 we obtain the following equation provided that dN/dy is a constant.

$$y(t_d) = \frac{1}{dN/dy} \int_0^{t_d} \frac{dN}{dt} dt. \quad (2.13)$$

For the VDC the quantity dN/dy will be constant for $t_d < t_2$ as indicated in the drift-time histogram. Therefore this equation is valid only in this range. The constant, dN/dy , can then

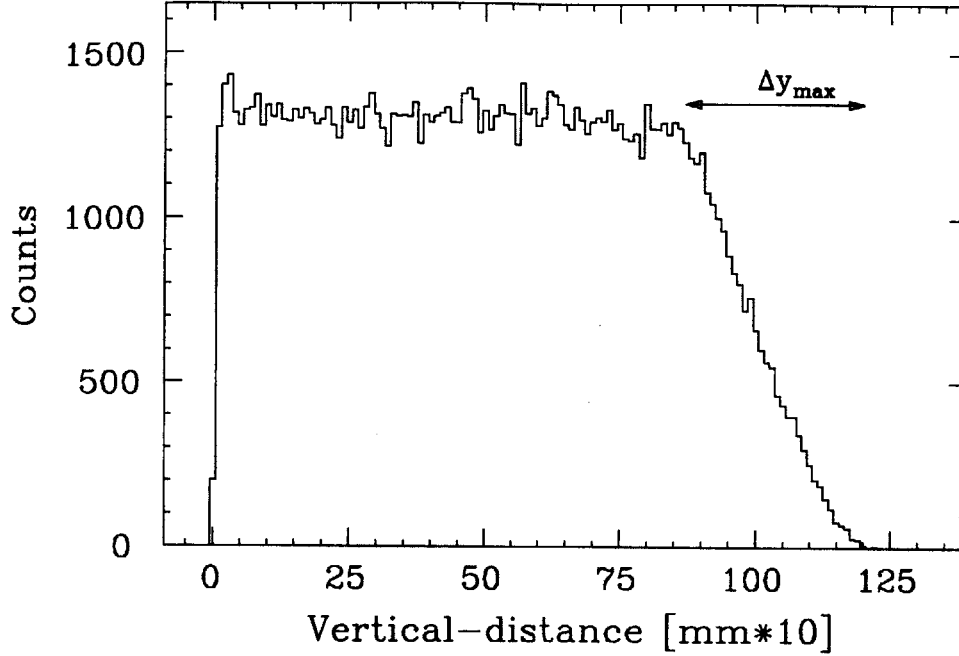


Figure 2-7: A VDC vertical-distance histogram.

be determined from the drift velocity. For drift times between t_1 and t_2 the drift velocity and dN/dy should be constant. Therefore we have the following equality,

$$\frac{dN}{dy} = \frac{1}{v_d} \frac{d\langle N \rangle_{flat}}{dt}, \quad (2.14)$$

where $d\langle N \rangle_{flat}/dt$ is the average number of counts per unit channel between t_1 and t_2 where the histogram is flat. The drift velocity for the VDC is roughly $50 \mu\text{m/ns}$. Therefore, a lookup table of vertical-distance as a function of drift-time can be generated from Equation 2.13 for $t_d < t_2$ as follows:

$$y(t_d) = \frac{v_d}{d\langle N \rangle_{flat}/dt} \int_0^{t_d} \frac{dN}{dt} dt. \quad t_d < t_2. \quad (2.15)$$

For drift-times greater than t_2 , the equation for $y(t_d)$ can then be extrapolated linearly using the drift velocity. The result of this procedure generates a complete lookup table of vertical-distance as a function of drift-time. Shown in Figure 2-7 is the vertical-distance histogram generated from the VDC drift-time histogram, Figure 2-6, using this lookup table.

2.4.3.2 Vertical-distance Correction

For the VDC, tracks with different incident angles have different drift-time spectra. Specifically, the peak at small drift times in the drift-time histogram becomes larger or smaller for steeper or shallower tracks respectively. Therefore, different incident angles will have different lookup tables. This presents a problem since we do not have drift-time spectra for each incident angle but an averaged histogram as shown in Figure 2-6. However, for small vertical angle acceptances the resultant drift-time histogram is a good representation of the drift-time histogram for the average angle, $\langle\theta\rangle$. Therefore, the lookup table constructed from this histogram is correct only for the average angle. If the central ray passes through the middle of the VDC this average angle is 45° ($\langle\theta_f\rangle = 0$). For angles, $\theta \neq \langle\theta\rangle$, the lookup table vertical-distances need to be corrected due to the incident angle dependence. The problem is illustrated in Figure 2-8 where two pairs of incident rays and their shortest drift-paths are shown for an idealized field shape geometry. The radius of the radial field region for the VDC is $R \cong 0.1$ cm.

Suppose we have calibrated a lookup table for ray₀ (the ray with $\theta_0 = \langle\theta\rangle$) and consider the arbitrary ray with $\theta \neq \theta_0$. Since their shortest drift-paths are the same they will have the same drift-time. Therefore, the lookup table will assign them the same value of vertical-distance, y_0 . But clearly from the figure this is not correct since they intersect the Y-axis at different points. Ray₀ intersects the Y-axis at y_0 and the arbitrary ray at y . In order to obtain the correct value of the vertical-distance for the arbitrary ray a correction, Δy , needs to be added to the lookup distance, y_0 . This is accomplished as follows.

First, consider the case where the drift-path, d , is greater than or equal to the radius of the radial field region: $d \geq R$. Then an equation for the shortest drift-path, d_{min} , can be obtained from the geometry shown in Figure 2-8 by setting the slope of the ray equal to the slope of the circle. The point on the circle which satisfies this condition is where the electron drift changes direction and is illustrated in the figure. The resulting expression for the shortest drift-path is as follows:

$$d_{min}(y, \theta) = y + R(1 - \sec \theta), \quad d \geq R. \quad (2.16)$$

Using this relation we can re-express the condition $d \geq R$ in terms of the vertical-distance y for ray₀.

$$d_{min}(y_0, \theta_0) \geq R \geq y_0 + R(1 - \sec \theta_0) \quad (2.17)$$

$$\Rightarrow y_0 \geq R / \cos \theta_0. \quad (2.18)$$

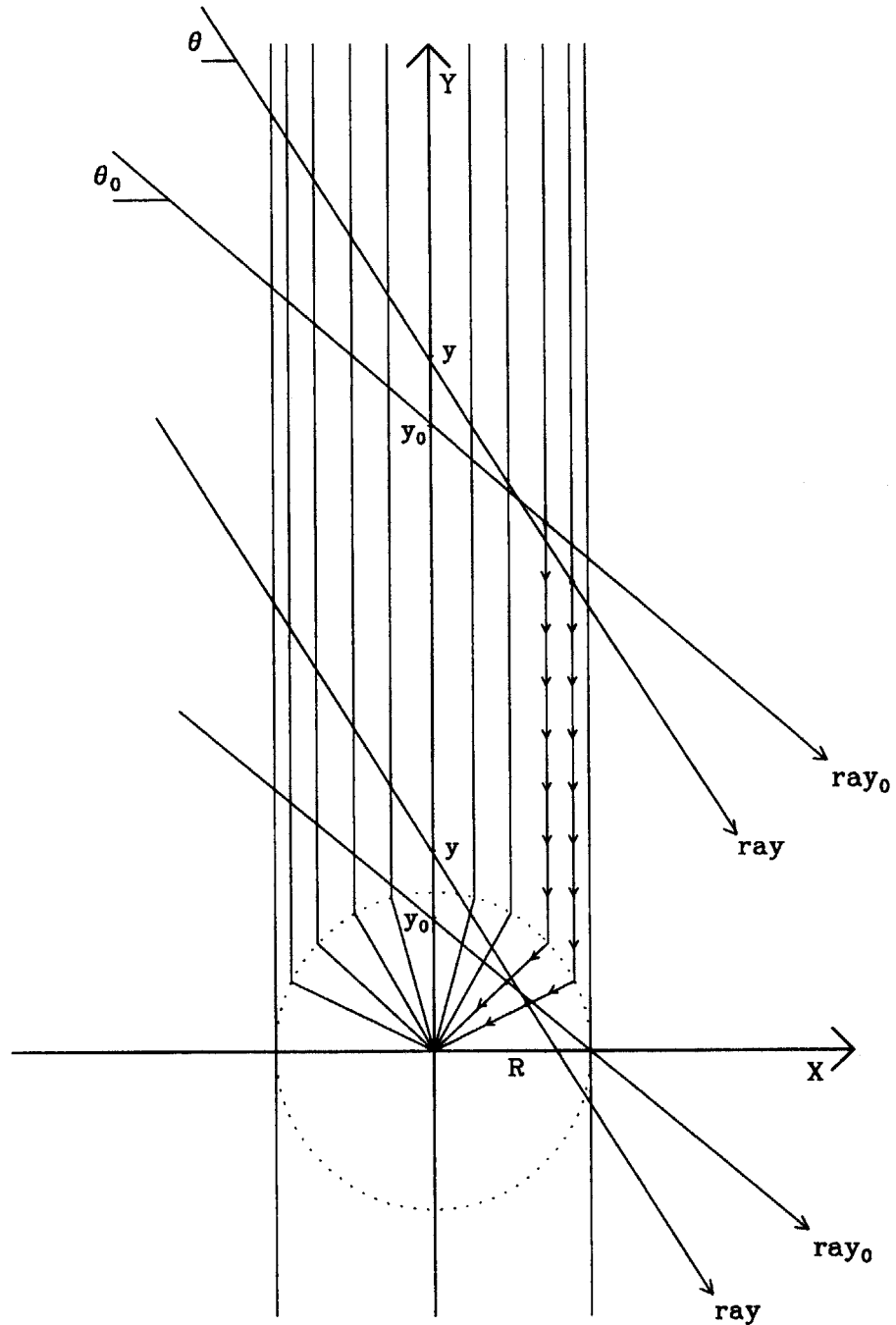


Figure 2-8: A close-up view of an idealized VDC drift cell. Each of the two pairs of rays is shown with its minimum drift-path.

Let us assume that we have a correct lookup table of vertical-distances for ray₀ and consider an arbitrary ray (see Figure 2-8). The minimum drift-paths are given as follows:

$$d_0 = y_0 + R(1 - \sec \theta_0), \quad (2.19)$$

$$d = y + R(1 - \sec \theta). \quad (2.20)$$

When $d = d_0$ both rays will be assigned the same vertical-distance from the lookup table. The correction, Δy , for the arbitrary ray is obtained by setting $d = d_0$.

$$\Delta y = y - y_0 = R(\sec \theta - \sec \theta_0), \quad y_0 \geq R / \cos \theta_0. \quad (2.21)$$

Therefore, vertical-distances from the lookup table should be corrected according to their angles as follows:

$$y_{\text{corr}} = y_{\text{lookup}} + R(\sec \theta - \sec \theta_0), \quad y_{\text{lookup}} \geq R / \cos \theta_0, \quad (2.22)$$

where $y_{\text{lookup}} \equiv y_0$. Notice that for $\theta = \theta_0$ the correction term goes to zero.

The same procedure can be done for drift-paths less than R . The minimum drift-path is given by,

$$d_{\text{min}}(y, \theta) = y \cos \theta, \quad d < R, \quad (2.23)$$

and the correction, Δy , is given as follows:

$$\Delta y = y - y_0 = y_0 \left(\frac{\cos \theta_0}{\cos \theta} - 1 \right), \quad y_0 < R / \cos \theta_0. \quad (2.24)$$

The corrected vertical-distance from the lookup table is expressed as follows:

$$y_{\text{corr}} = y_{\text{lookup}} \frac{\cos \theta_0}{\cos \theta}, \quad y_{\text{lookup}} < R / \cos \theta_0. \quad (2.25)$$

A typical range for the angles, θ , is $45^\circ \pm 80$ mr. Using Equation 2.21 the size of the vertical-distance correction is of the order of 100 μm .

In order to use this correction when analyzing the VDC, the angle, θ , needs to be known. This is accomplished as follows. Consider Figure 2-5 with an arbitrary track of angle θ . The lookup table will give us the vertical-distances, y_1 , y_2 , and y_3 for each cell. The corrections to

the vertical-distances, Δy_1 , Δy_2 , and Δy_3 depend on the angle θ . Using the outer two cells to construct the angle θ we have the following self consistent equation for the angle:

$$\theta = \tan^{-1} \left[\frac{y_1 + \Delta y_1(\theta) + y_3 + \Delta y_3(\theta)}{2u} \right]. \quad (2.26)$$

Using Equation 2.21 for the vertical-distance corrections ($d \geq R$), this can be rewritten as follows:

$$\frac{\sin \theta}{\cos \theta} = \frac{y_1 + y_3 + 2R(\sec \theta - \sec \theta_0)}{2u}. \quad (2.27)$$

Solving this equation gives us the expression for the corrected angle:

$$\cos \theta = \frac{-YZ + \sqrt{1 + Y^2 - Z^2}}{1 + Y^2}, \quad (2.28)$$

where

$$Y = \frac{y_1 + y_3 - 2R \sec \theta_0}{2u}, \quad (2.29)$$

$$Z = \frac{R}{u}. \quad (2.30)$$

The focal plane angle is then given by the expression, $\theta_f = 45^\circ - \theta$, where 45° is the nominal angle of incline for the VDC.

This correction depends only on two parameters, R and θ_0 : the radius of the radial field region and the average angle respectively. The radius R was determined from the design of the VDC to be $R = 0.1$ cm (ideal case). The average angle depends on the momentum and angular acceptances of the spectrometer. For a uniform angular acceptance with position on the VDC, this is given by the average angle passing the center of the VDC. For this experiment the center of the VDC was located at a $\delta \sim -2\%$. Therefore, using the matrix element $(\theta|\delta) = 11.648$ (Appendix F) the average angle chosen was $\theta_0 \sim 46^\circ$. The correction to the focal plane angle was then ~ 10 mr. This was a 10% systematic effect.

2.4.3.3 VDC Sag Correction

The VDC was inclined at a nominal angle of 45° at the rear of the spectrometer and was supported only at its ends. The weight of the chamber induced a small amount of vertical sag whose shape can be roughly approximated as parabolic. This sagging affected the measurement

of the focal plane angle θ_f , $\theta_f = 45^\circ - \theta$ (see previous section), since the angle of the local plane (45°) will change from one end of the VDC to the other end. This was corrected for as follows.

The maximum amount of vertical sag at the center of the chamber was measured to be $s = 1.9 \pm 0.1$ mm and the total length $L = 813$ mm. Since the amount of sagging was small it can be described approximately as parabolic.

$$y = s \left(\frac{x_{\text{VDC}}}{L/2} \right)^2. \quad (2.31)$$

The correction to the focal plane angle is then expressed as follows:

$$\frac{dy}{dx} = \frac{8s}{L^2} x_{\text{VDC}} \equiv \sin \theta_{\text{sag}} \cong \theta_{\text{sag}}, \quad (2.32)$$

$$\theta_{\text{sag}} [\text{mr}] = 0.231 x_{\text{VDC}} [\text{cm}], \quad (2.33)$$

$$\theta_f = \theta_f + \theta_{\text{sag}}. \quad (2.34)$$

At the ends of the VDC's active area, $x_{\text{VDC}} = \pm 30$ cm, the correction is of the order of 7 milliradians.

2.4.3.4 Vertical-distance Sum Cuts

For events which had three consecutive cell wire hits, the vertical-distances (see Figure 2-5), y_1 , y_2 , and y_3 , were then added together as follows:

$$S12 = y_1 + y_2,$$

$$S13 = y_1 + y_3,$$

$$S23 = y_2 + y_3.$$

Since the electron track through the VDC is a straight line these summed distances are given by geometry. For example, a 45° track would have $S13 = 2u$. Shown in Figure 2-9 are histograms of the summed distances. The summed distance, $y_1 + y_3$, is roughly centered at $2u$ and the width is proportional to the vertical angle acceptance, $\Delta\theta$, of the spectrometer.

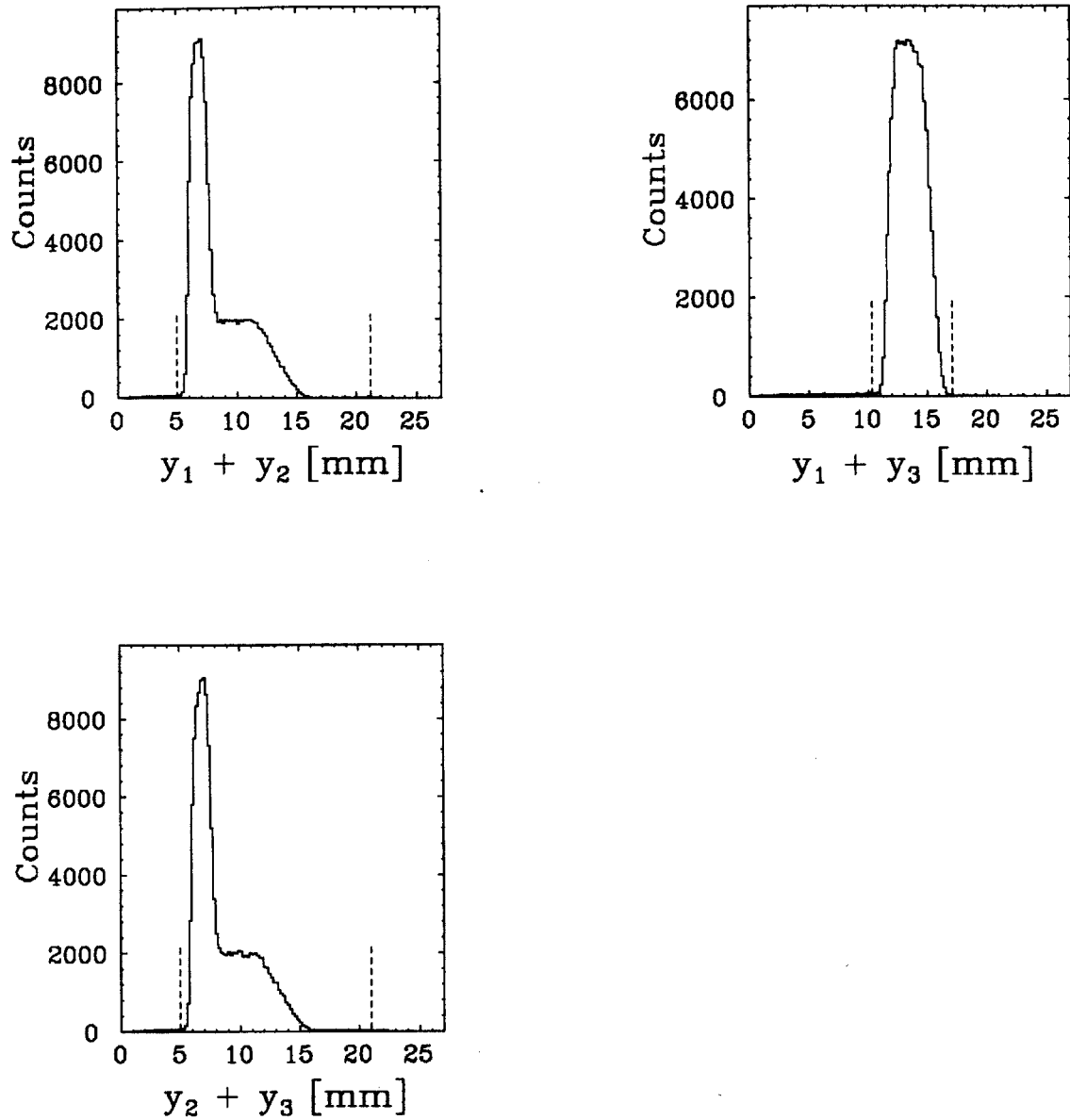


Figure 2-9: The vertical-distance sum histograms for the VDC. The dashed lines are the cuts that were used to define acceptable values for the sums.

Any very small or very large vertical-distance sum corresponds to focal plane angles which are not in the vertical angle acceptance. As shown in the figure only small anomalous drift-sums exist in the spectrum. These are believed to be caused by pre-empted stops in the VDC drift cells from Møller scattering inside the chamber. The idea is as follows: Of the two Møller scattered electrons, one must continue to move very nearly in the original direction ($\sim 0^\circ$) in order to create a trigger while the other ($\sim 90^\circ$) passes near a cell wire. In order to eliminate these events, cuts were placed on the vertical-distance sum histograms (see Figure 2-9). The lost events were included in the VDC inefficiency correction. This correction was of the order of 1.4%.

These pre-empted stops also affect the drift-time spectrum by increasing the number of shorter drift times. This is shown in Figure 2-10 where the dashed histogram includes the vertical-distance sum cuts and the solid histogram does not. The vertical-distance sum cuts affect the drift-time histogram differentially, more counts are lost at shorter drift-times. The dashed histogram thus reflects the true drift-time spectrum. Therefore, when generating the vertical-distance lookup table the dashed histogram was used.

2.4.4 HDC

The design, operation, and construction of the horizontal drift chambers (HDCs) is discussed in detail elsewhere [10] and will not be repeated here. In this section only the features relevant to its analysis are presented.

The two horizontal drift chambers which are shown in Figure 2-4, HDC1 and HDC2, are identical in design. Each chamber contains two signal planes and each signal plane is read out with one delay line. A signal plane consists of 8 anode wires (20 μm gold-plated tungsten) spaced at 1.2 inch intervals. The drift-time and wire number for each plane are given by the sum and difference between the TDC stop times from the opposite ends of the delay line. A cross sectional view of a chamber is shown in Figure 2-11 where only half of the active area is illustrated. This represents an end-on view for each HDC chamber (see Figure 2-4). The two signal planes are separated by 3/4 inch and staggered by half the wire spacing. Between the signal wires are located field shaping wires (20 μm beryllium-copper). These wires are also located symmetrically above and below the signal plane (1/8 inch) with a spacing of 0.1 inches and define the drift cell. The maximum drift-distance for each cell is 0.6 inches (15.24 mm).

Also illustrated in Figure 2-11 is a typical electron track and the associated drift-distances for each signal plane: d_1 and d_2 . Since the focal plane angle ϕ_f is small (~ 10 mr), the

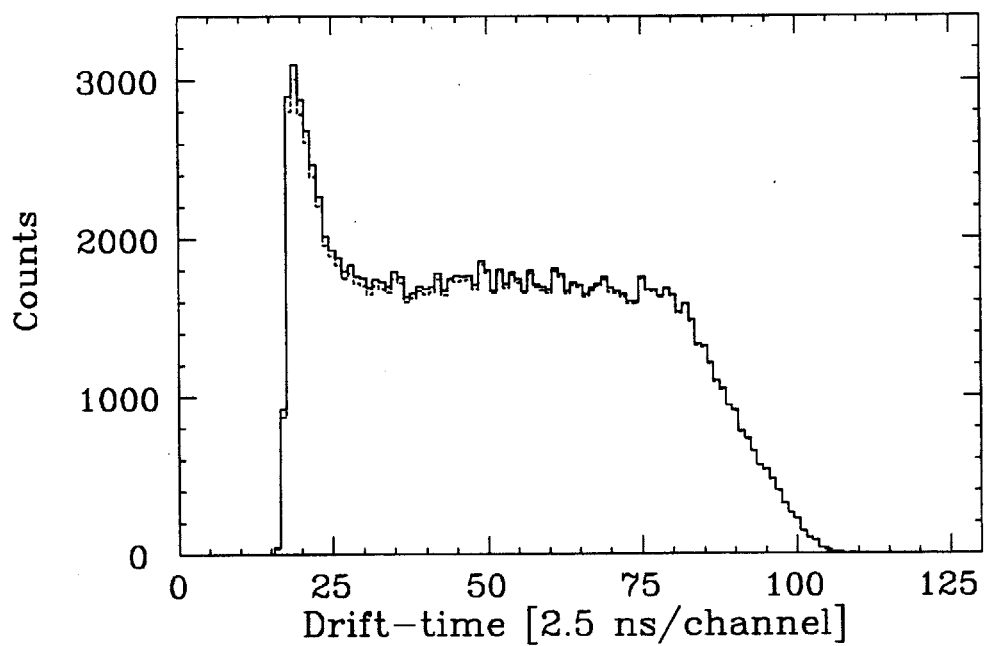


Figure 2-10: The difference between the VDC drift-time histograms when the vertical-distance sum cuts are included. The dashed histogram includes the sum cuts the solid histogram does not.

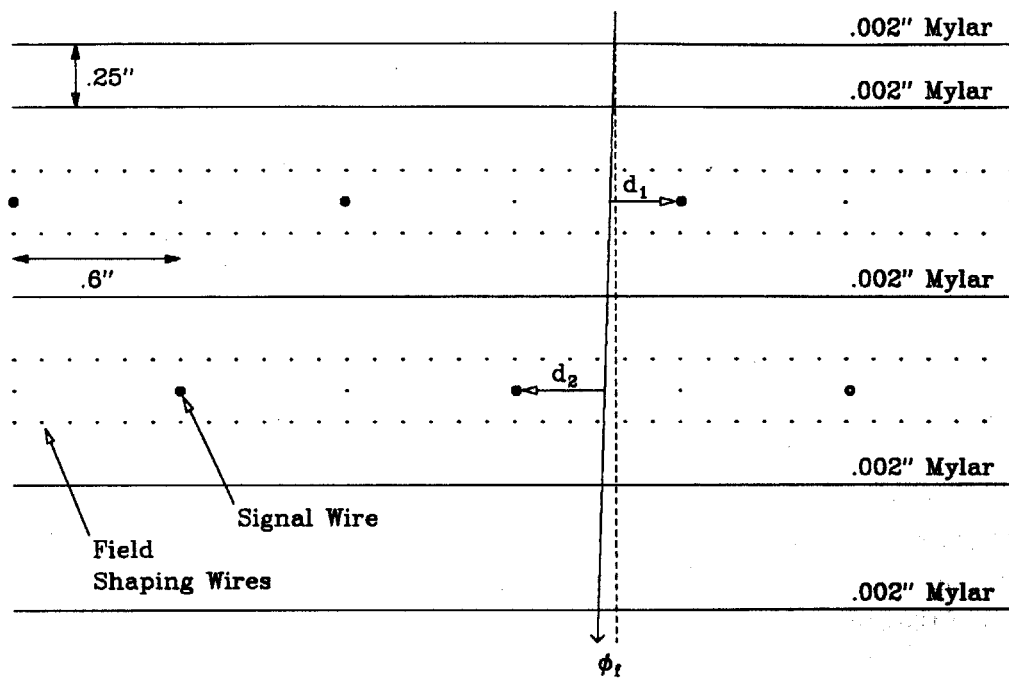


Figure 2-11: The wire geometry of the HDC illustrating the signal wires and the drift-cells. A typical particle track is also shown with a transverse angle ϕ_f . This track intercepts the chamber at an angle of $45^\circ - \theta_f$.

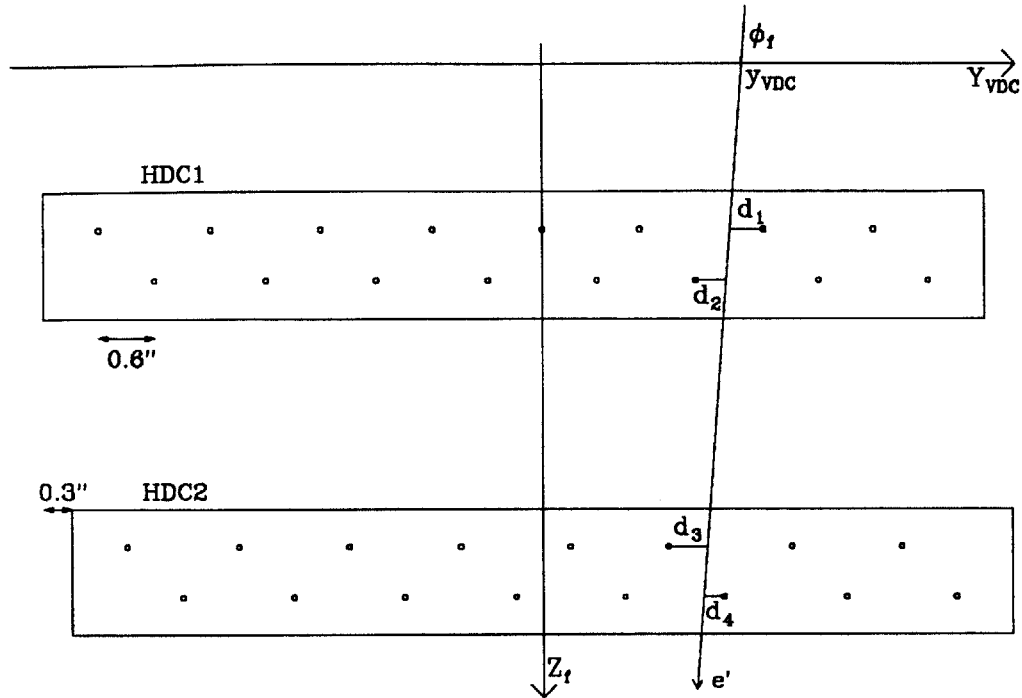


Figure 2-12: The two HDCs and a typical particle track with a transverse angle of ϕ_f . This track intercepts the chambers at an angle of $45^\circ - \theta_f$. Y_{VDC} is located at the VDC.

drift-distance sum, $d_1 + d_2$, should be roughly half the wire spacing, 15.24 mm. The chamber resolution for the drift-distances is $\cong 150 \mu\text{m}$. This gives us an angular resolution for each chamber of the order of 8 mr.

The second chamber, HDC2, was separated vertically from HDC1 by 18.1 centimeters. This chamber was also displaced a quarter of a wire spacing from HDC1 to completely stagger the four signal plane wires symmetrically and is illustrated in Figure 2-12. A typical electron track is also shown along with the corresponding drift-distances for each signal plane: d_1 , d_2 , d_3 , and d_4 .

When decoding the drift-distance information there is an ambiguity as to the possible orientation of the drift-distances for each plane, whether it should point to the right or left of the signal wire. Since the angle ϕ_f is less than 38° the orientation of one drift-distance in each plane can be determined unambiguously. Constructing a line between these two points allows the other two drift-distance orientations to be determined. Hence, all four drift-distance orientations can be determined exactly. From the drift-distances and the distances the particle traverses between the signal planes the angle ϕ_f and the y -coordinate at the VDC, y_{VDC} , can

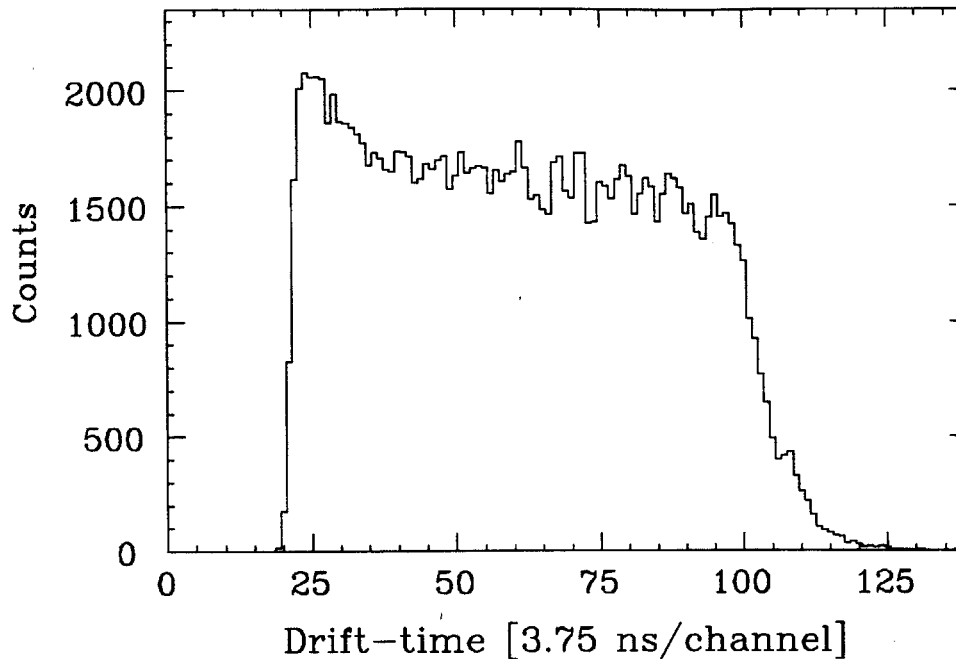


Figure 2-13: An HDC drift-time histogram.

be constructed. Since the distances the particle traverses between the signal planes depends on the angle θ_f , this must be done after the VDC processing. Using both chambers the angular resolution in ϕ_f was better than 1 mr. The resolution in x_{VDC} was $\cong 150 \mu\text{m}$.

A small relative twist of HDC1 and HDC2 was discovered and corrected for in the HDC analysis software. This was identified by examining a two-dimensional plot of x_{VDC} versus ϕ_f . When the chambers are twisted, the centroid of ϕ_f will appear to be correlated with x_{VDC} .

2.4.4.1 Drift-distance Lookup Table Calibration

The drift-distance lookup table was constructed using the integral-drift-time method [9]. This calibration differs from the VDC calibration (see Section 2.4.3) in two important ways. First, since the particle tracks are inclined roughly perpendicular to the HDC drift-cells there is no need to make a distinction between the drift-distance and vertical-distance as in the case for the VDC. Secondly, since the ϕ_f acceptance is small there is no need for an angle dependent drift-distance correction as was necessary for the VDC.

Shown in Figure 2-13 is a typical drift-time spectrum for one of the HDC delay lines. Equation 2.10 expresses the relationship between the number of counts per channel and the drift velocity:

$$\frac{dN}{dt_d} = \frac{dN}{dy} \frac{dy}{dt_d} = \frac{dN}{dy} v_d, \quad (2.35)$$

where dN/dy is the number of counts per unit drift-distance. For the HDC, dN/dy is a constant over the length of a drift-cell. Therefore, we can construct the following relation for the drift-distance, y .

$$y(t_d) = \frac{1}{dN/dy} \int_0^{t_d} \frac{dN}{dt} dt. \quad (2.36)$$

Using the maximum length for the drift-distance, the length of the drift-cell ($L = 15.24$ mm), dN/dy can be calibrated as follows:

$$L = \frac{1}{dN/dy} N_{\text{tot}}, \quad (2.37)$$

where N_{tot} is the total number of counts in the drift-time spectrum. The drift-distance lookup table is then given by Equation 2.36. A program called DRT [11] was used to perform the calibration, and a typical drift-distance spectrum is shown in Figure 2-14.

2.4.4.2 Drift-distance Sum Cuts

For each chamber which had adjacent wire hits, the following drift sum was computed:

$$S_{\text{drift}} = y_1 + y_2, \quad (2.38)$$

where y_1 and y_2 are the drift-distances corresponding to each signal plane. Since the focal plane angle ϕ_f is small (~ 10 mr) this sum should be roughly equal to half the signal wire spacing (15.24 mm) based on the HDC geometry. Shown in Figure 2-15 is a typical drift-distance sum histogram. The sharp peak in the histogram corresponds to half the signal wire spacing. Any very short or very large drift-distance sums correspond to focal plane angles which are not in the acceptance. As shown in the figure only small anomalous drift-sums exist in the spectrum. These are believed to be caused by pre-empted stops in the HDC drift-cells from Møller scattering inside the chamber (see Section 2.4.3). In order to eliminate these events, a cut was placed on the drift-distance sum histogram for each chamber. The dashed lines in

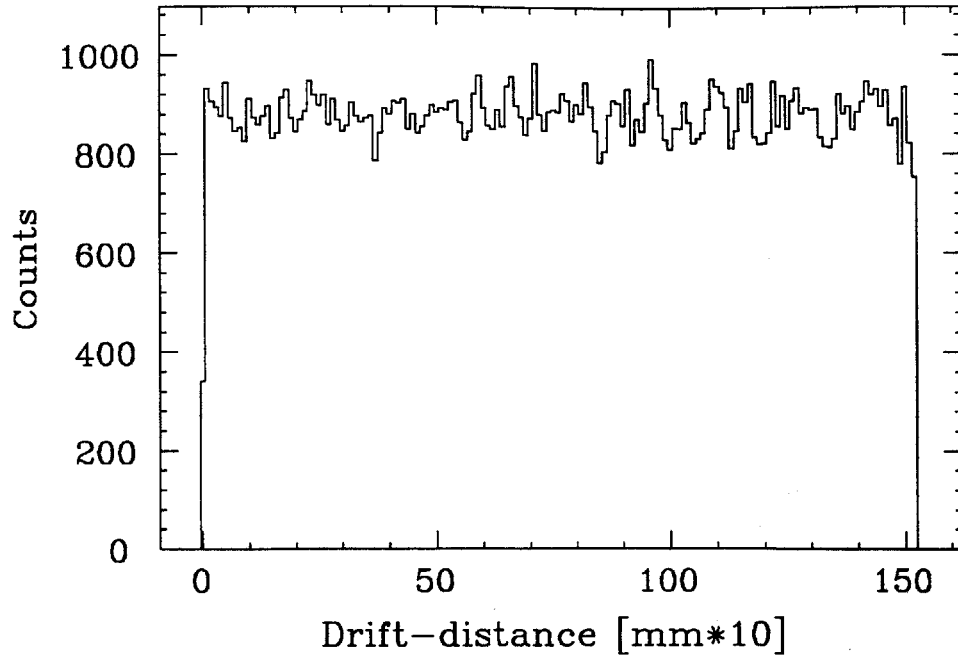


Figure 2-14: An HDC drift-distance histogram.

Figure 2-15 is the cut that was used. The lost events were included in the HDC inefficiency correction. This was of the order of 3% for each chamber.

These pre-empted stops also affect the drift-time spectrum by increasing the number of shorter drift-times. This effect is illustrated in Figure 2-16 where the dashed histogram includes the drift-distance sum cut and the solid histogram does not. When generating the drift-distance lookup table the dashed histogram was used since it reflects the true drift-time spectrum.

2.4.5 Gas Cherenkov Detector

Shown in Figure 2-4 is the gas Cherenkov detector that was in this experiment. The operating gas was isobutane at atmospheric pressure and room temperature. The index of refraction, n , of isobutane is 1.00127 [12]. Therefore, the threshold charged particle velocity, β_{thresh} , for producing Cherenkov radiation is [13]

$$\beta_{\text{thresh}} > \frac{1}{n} = 0.99873, \quad (2.39)$$

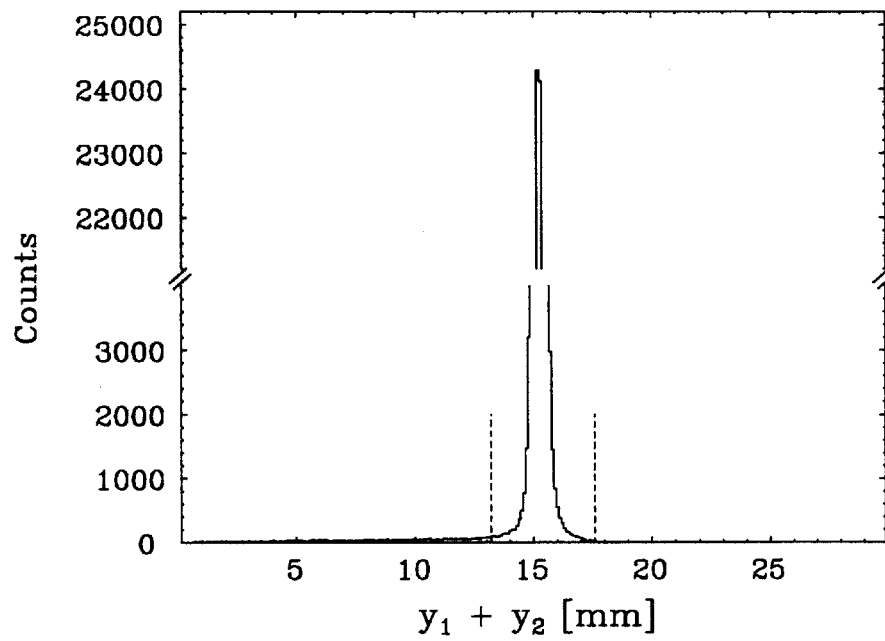


Figure 2-15: The drift-distance sum histogram for an HDC chamber. The dashed lines is the cut that was used to define acceptable values for the sum.

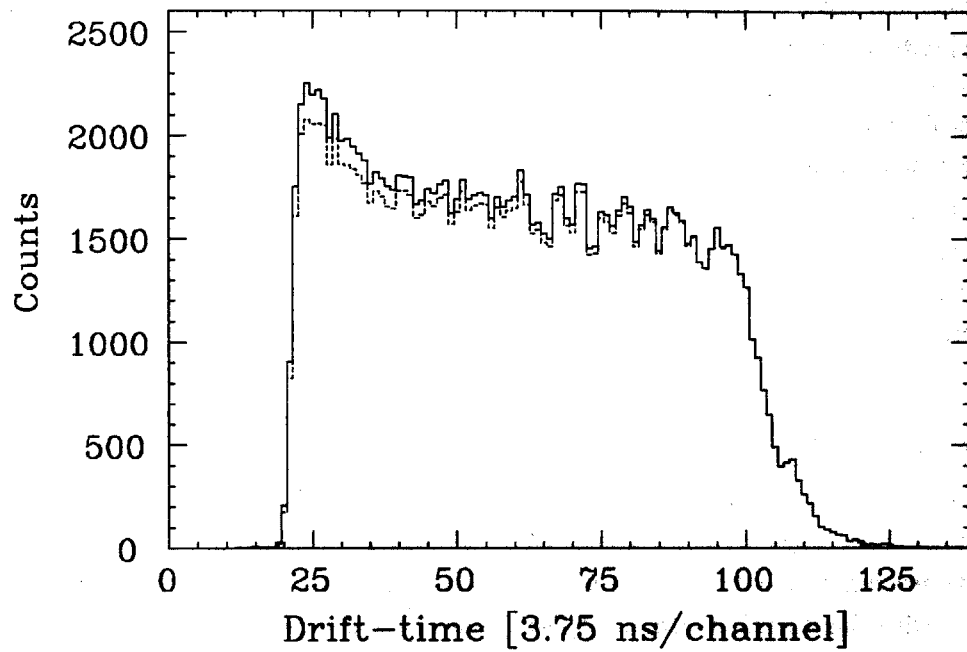


Figure 2-16: The difference between the HDC drift-time histograms when the drift-distance sum cut is included. The dashed histogram includes the sum cut the solid histogram does not.

and the corresponding momentum threshold is given by the expression

$$P_{\text{thresh}} = m \frac{\beta_{\text{thresh}}^2}{\sqrt{1 - \beta_{\text{thresh}}^2}} . \quad (2.40)$$

The angle of the emitted radiation with respect to the charge particle direction is given by the expression:

$$\theta_{\text{Cher}} = \cos^{-1} \frac{1}{\beta n} . \quad (2.41)$$

Since the index of refraction is almost unity the radiation is emitted in the forward direction with an angle less than 3° . At the bottom of the gas Cherenkov detector were 3 paraboloidal mirrors which focused the radiation on three five-inch photomultipliers.

The momentum thresholds for electrons, muons, and pions are 10 MeV/c, 2.0 GeV/c, 2.8 GeV/c respectively. Since pions at the focal plane had momenta less than 500 MeV/c, this allowed us to separate cleanly the electron events from pion events. However, a small fraction of cosmic ray muons will have sufficiently large momenta to trigger the detector. These were eliminated with lead-glass Cherenkov detectors (see below). The overall efficiency of this detector was determined to be better than 99.5% (see Section 5.3.4).

2.4.6 Lead-Glass Cherenkov Detector

The lead-glass Cherenkov detector consisted of a segmented array of 14 individual lead-glass blocks that were placed underneath the gas Cherenkov detector. This array is shown in Figure 2-4 in relation with the other detectors. The lead-glass blocks were divided into a top and bottom layer of seven blocks each and were staggered to get complete coverage. The dimension of each block was $10 \times 10 \text{ cm}^2$ at the face and 25 cm long. At the end of each block a photomultiplier tube (PMT) was attached. The lead glass had a density of 5.18 g/cm^3 , index of refraction 1.804, and a unit radiation length of 1.68 cm. The minimum ionizing energy loss, dE/dx , for a charged particle passing through the lead glass is roughly 1.5 MeV/g/cm^2 . The two layers illustrated in Figure 2-4 represent a total thickness of about 12 radiation lengths. The scattered electrons passing through them generate an electromagnetic shower and the two layers were adequate for containing 98% of the longitudinal development.

The purpose of these detectors was to reduce the amount of beam-independent related background due to cosmic rays. Specifically, the highly energetic cosmic muons that could

trigger the gas Cherenkov detector ($P_\mu > 2 \text{ GeV}/c$) and hence appear as a good electron event. These detectors were only efficient at separating the cosmic muons from the electrons at the highest beam energies. This is explained below.

The lead-glass detectors measure the amount of Cherenkov light produced by a passing charged particle. The measured signal, S , is then proportional to the total amount of Cherenkov light which is proportional to the total radiator length, L_{tot} [14].

$$S_{\text{PbG}} \propto L_{\text{tot}} . \quad (2.42)$$

Using the index of refraction, $n = 1.802$, we obtain the following momentum thresholds for generating Cherenkov light in lead glass: electrons $0.34 \text{ MeV}/c$ and muons $70 \text{ MeV}/c$. When an electron passes through the lead-glass detector it generates a large electromagnetic shower and loses almost all of its energy inside the detector. The shower is composed primarily of electrons, positrons, and photons. In this case the lead-glass signal is going to be proportional to the total radiator lengths of all the charged particles generated in the shower. This total length is given by conservation of energy assuming that all the energy eventually appears as ionization loss [15]:

$$S_{e^-} \propto L_{\text{tot}} \approx \frac{E_e}{\epsilon} , \quad (2.43)$$

where ϵ is the minimum ionization energy loss expressed per unit radiation length and for lead glass is $13 \text{ MeV}/\text{r.l.}$. Since the lead-glass signal for electrons scales with the energy it is useful to create a normalized signal which factors out this dependence. The normalized signal is then given as follows:

$$S_{\text{Norm}} = \frac{S}{E_e} , \quad (2.44)$$

and is independent of energy for electrons. However, since muons are inefficient at generating an electromagnetic shower their signal in the lead-glass Cherenkov detectors is simply proportional to their total path length. For muons with enough energy to pass completely through the detector this is the total length of the detector, 12 radiation lengths. Therefore, the normalized lead-glass signal for the cosmic muons shifts to lower values as $1/E_e$. This effect is illustrated in Figure 2-17. The solid histogram is the normalized electron signal and is arbitrarily centered at channel 100. The two dashed histograms are the normalized cosmic ray signals for E_e equal to 255 MeV and 450 MeV. These are the scattered electron energies corresponding to the lowest and highest beam energies used in this experiment, 347 MeV and 913 MeV respectively. As can be seen in the figure the cosmic ray muon separation was only efficient at the highest energies in this experiment. However, the elimination of the cosmic ray background was important only at

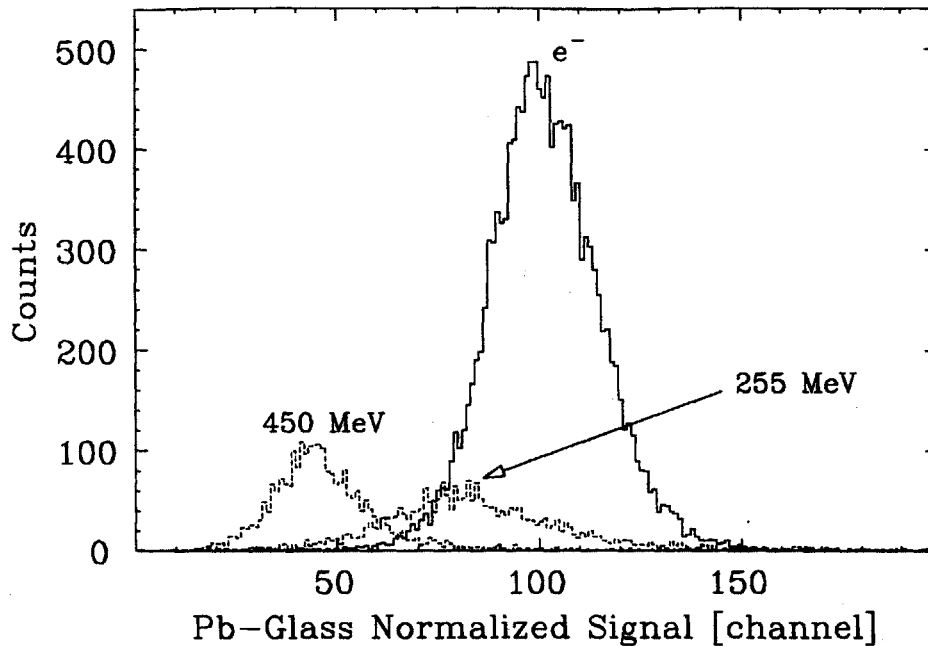


Figure 2-17: The lead-glass normalized response to electrons and cosmic ray muons. The solid histogram is the electron spectrum. The dashed histograms are the cosmic ray muon spectra evaluated at two different normalization energies.

the highest energies where the electrodisintegration cross sections were very small. This system proved to be very effective in reducing the beam-unrelated background to negligible levels and is shown explicitly for the 913 MeV raw data in Figure 2-18. The top histogram was made with a cut on the lead-glass normalized spectrum to define good electron events. The bottom histogram did not include this cut. The effectiveness of the lead glass blocks can be seen by the elimination of the counts in the “superelastic” region where the deuterium elastic peak is located at 0 MeV of excitation.

2.5 Data Acquisition

The raw signals from each of the detectors illustrated in Figure 2-4 were processed by the electronics in the experimental counting-bay room. This involved the following: The raw delay line signals from each of the drift chambers were amplitude discriminated and sent to time-to-digital

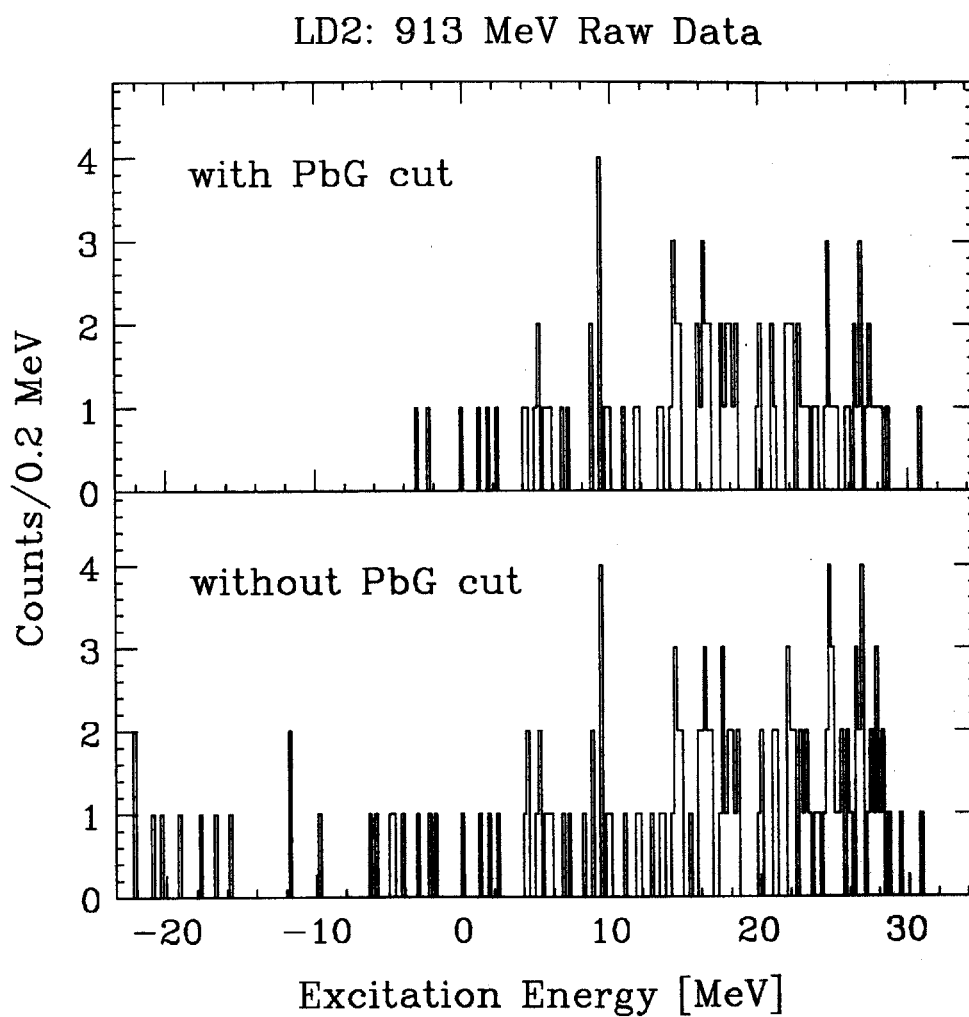


Figure 2-18: The effectiveness of the lead-glass detectors at reducing the cosmic ray background.

converters (TDCs). The raw signals from the scintillators, gas Cherenkov, and lead-glass blocks went to analog-to-digital converters (ADCs) and were also amplitude discriminated. The experimental trigger consisted of the following coincidence: A good scintillator signal with a good Cherenkov signal and/or a good lead-glass signal. For each trigger that occurred, the information from all the detectors was written to magnetic tape for an off-line analysis. A portion of these events was also analyzed on-line so that problems could be identified and corrected during the experiment. The Los Alamos Q system was used for both the data acquisition and analysis of the data [16] [17].

Chapter 3

Elastic Line Shape

When an electron traverses matter it undergoes multiple interactions with the atoms of the medium. These interactions cause the incident electron to lose energy. Two of the major energy loss processes are collision losses (Møller scattering) and the radiating of real photons (bremsstrahlung). These energy loss processes will affect the spectrum of scattered electrons observed in an electron scattering experiment. Specifically, they will tend to shift and broaden the scattering peaks to some characteristic line shape with a large tail toward lower momenta. When analyzing electron scattering data this line shape needs to be known in order to calculate accurate cross sections. In this chapter, the method described by Bergstrom [18] will be used to obtain this line shape for the elastic peak. However, there are significant differences in the present development. For the radiative correction factor, Bergstrom used the result derived for potential scattering [19]. This does not include radiative corrections from the nuclear current nor does it include the effect of kinematic recoil. For the light targets (deuterium and hydrogen) that were used in this experiment these effects cannot be ignored, especially kinematic recoil. Tsai [20] derived the radiative correction factor for elastic scattering from hydrogen including these effects, and it is this formula which we used to obtain the line shape.

This chapter is divided into four main sections. The first section deals with the two major energy loss processes affecting the line shape. The second treats the convolution of these processes. The third section develops approximate formulas for the line shape near the elastic peak. And finally, the fourth section relates this convolution method to the equivalent radiator method as described in Mo and Tsai [21].

3.1 Energy Loss Processes

3.1.1 Collision and Ionization Losses

When a charged particle traverses matter, it undergoes many collisions with the atomic electrons in the medium. These collisions lead to ionization and excitation of the atoms in the medium. Following Landau [22], we seek the distribution $D_I(E, \Delta, x)$ where $D_I(E, \Delta, x)d\Delta$ is the probability that an incident particle of energy E , after traveling a distance x , will have energy loss in the range $[\Delta, \Delta + d\Delta]$ due to these collisions.

A refinement of the Landau development was to include the Sternheimer density effect correction [23] which takes account of the polarizability of the medium. Therefore, we used the following formula for the mean ionization loss for a maximum energy transfer E_{\max} [24]:

$$-\left. \frac{dE}{dx} \right|_{\leq E_{\max}} = \frac{2\pi n e^4}{m_e c^2 \beta^2} \left[\ln \left(\frac{2m_e c^2 \beta^2 E_{\max}}{I^2 (1 - \beta^2)} \right) - \beta^2 - \delta \right], \quad (3.1)$$

where

n is the electron density of the target medium,

m_e is the mass of the electron,

e is the charge of the electron,

I is the mean ionization potential for the electrons of the medium,

δ is the density effect correction parameter, and

β is the ratio of the particle velocity to the speed of light, v/c .

The only difference between this formula and the one used by Landau is the inclusion of the density effect correction. The parameterization used for the density effect correction is presented in detail in Appendix D.

The Landau result for $D_I(E, \Delta, x)$ including this correction is expressed in terms of a universal function $\phi(\lambda)$ shown in Figure 3-1 and defined by the following formulas:

$$D_I(E, \Delta, x) = \frac{1}{\xi} \phi(\lambda), \quad (3.2)$$

$$\phi(\lambda) = \frac{1}{\pi} \int_0^{\infty} e^{-\lambda r - r \ln r} \sin \pi r \, dr, \quad (3.3)$$

$$\xi = x \frac{2\pi n e^4}{m_e c^2 \beta^2}, \quad (3.4)$$

$$\lambda(\Delta) = \frac{\Delta}{\xi} - \left(\ln \frac{\xi}{\epsilon'} + 1 - C \right), \quad (3.5)$$

$$\ln \epsilon' = -\ln \left(\frac{2m_e c^2 \beta^2}{I^2 (1 - \beta^2)} \right) + \beta^2 + \delta, \quad (3.6)$$

$$C = 0.5772... \text{ (Euler's constant)}. \quad (3.7)$$

The energy dependence of this distribution is expressed in terms of the variable β which is given by:

$$\beta = \frac{\sqrt{E^2 - m_e^2}}{E}. \quad (3.8)$$

For relativistic electrons ($E \gg m_e$) we have $\beta \approx 1$. In this case the energy dependence of the distribution, neglecting the density effect correction, is dominated by the $\ln[1/(1 - \beta^2)]$ term which can be re-expressed as $\ln[E^2/m_e^2]$. This energy dependence rises logarithmically with energy and is therefore weak. Including the density effect correction parameter, δ , actually cancels this rise above some energy eliminating the logarithmic increase.

Another universal function used by Landau is $\psi(\lambda)$, the integral probability of observing $\lambda' \geq \lambda$. It is defined as follows and also shown in Figure 3-1:

$$\psi(\lambda) = \int_{\lambda}^{\infty} \phi(\lambda') \, d\lambda'. \quad (3.9)$$

which can be re-expressed using Equation 3.3 to give the following integral

$$\psi(\lambda) = \int_0^{\infty} e^{-\lambda r - r \ln r} \frac{\sin \pi r}{\pi r} \, dr. \quad (3.10)$$

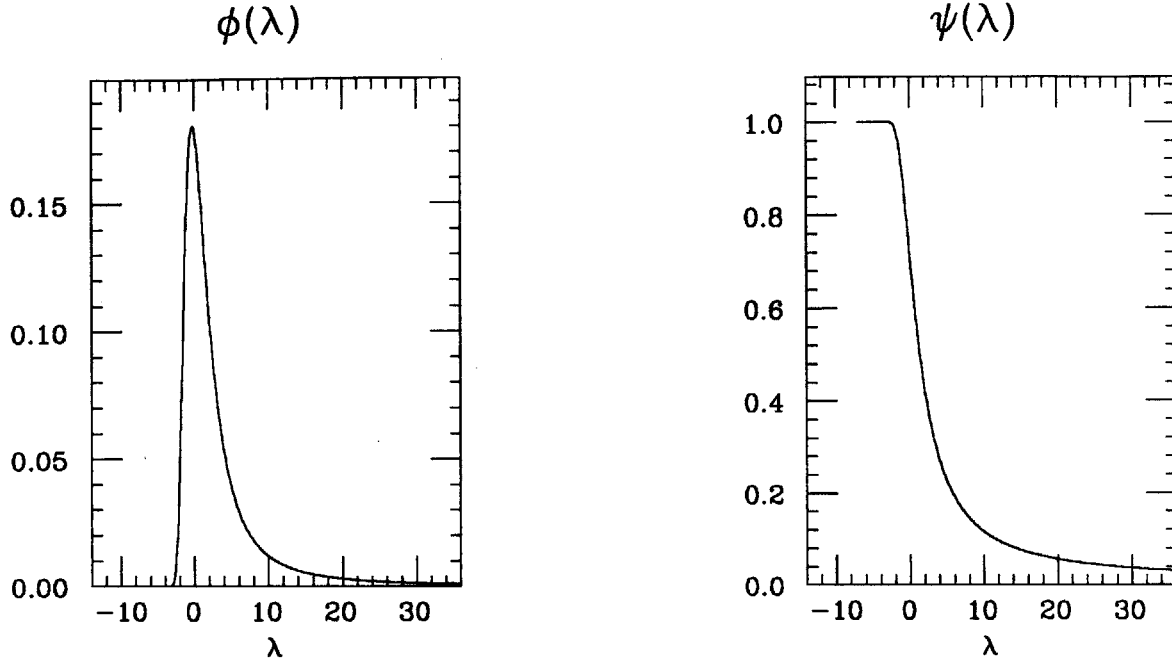


Figure 3-1: The Landau ϕ and ψ distributions.

From the peak of the Landau ϕ distribution, a formula for the most probable energy loss can be obtained. Landau's result is:

$$\Delta_{\text{mp}} = \xi \left[\ln \frac{\xi}{e'} + 1 - C + \lambda_{\text{peak}} \right], \quad (3.11)$$

where λ_{peak} corresponds to the maximum of $\phi(\lambda)$: $\lambda_{\text{peak}} \approx -0.225$ [25].

The overall normalization of D_I is given by

$$\int_0^E D_I(E, \Delta, x) d\Delta = \int_{\lambda(0)}^{\lambda(E)} \phi(\lambda') d\lambda'. \quad (3.12)$$

Since $\phi(\lambda)$ vanishes rapidly for large lambda, we can replace the upper limit in the integral with infinity with negligible error. Then our normalization can be written in terms of the Landau ψ distribution evaluated at $\lambda(0)$.

$$\int_0^E D_I(E, \Delta, x) d\Delta \approx \psi(\lambda(0)). \quad (3.13)$$

From the plot of $\phi(\lambda)$ shown in Figure 3-1, the value of $\lambda(0)$ must be less -2.5 since an energy loss of zero must lie to the left of the peak. Using Table C.1 we find that for $\lambda < -2.5$, $\psi(\lambda) \approx 1$. Therefore, we obtain the following normalization for D_I :

$$\int_0^E D_I(E, \Delta, x) d\Delta \approx \psi(\lambda(0)) \approx 1. \quad (3.14)$$

For the method used in finding the line shape the Laplace transform of D_I is needed. From Landau [22], including the density effect correction, the Laplace transform is given by:

$$\begin{aligned} d_I(E, s, x) &\equiv \mathcal{L}[D_I(E, \Delta, x)] = \int_0^\infty d\Delta e^{-s\Delta} D_I(E, \Delta, x) \\ &= e^{-s\xi[1-C-\ln(se')]} , \end{aligned} \quad (3.15)$$

where a small d is used to denote the Laplace transform of the distribution and the other quantities are as defined previously. From the Laplace transform it is easy to show that $D_I(E, \Delta, x)$ has the correct limit as $x \rightarrow 0$. When $x = 0$ we also have $\xi = 0$ (see Equation 3.4). Therefore

$$d_I(E, s, 0) = 1 , \quad (3.16)$$

and since $\mathcal{L}[\delta(\Delta)] = 1$, we must have

$$D_I(E, \Delta, 0) = \delta(\Delta) . \quad (3.17)$$



Figure 3-2: The first order Feynman diagrams for external bremsstrahlung processes in matter.

3.1.2 Bremsstrahlung Losses

In addition to the ionization energy loss, a charged particle also loses energy by radiating real photons while passing through matter. This radiation is called bremsstrahlung radiation and occurs as the passing particle is accelerated in the coulomb field of a nearby atom. Most of these collisions result in small angle deflections of the incident particle. The radiation associated with this is called “external” bremsstrahlung. The radiation coming from the collision that results in the main large angle scattering event that one is observing is called “internal” bremsstrahlung.

3.1.2.1 External Bremsstrahlung

In Figure 3-2 the first order Feynman diagrams associated with external bremsstrahlung are shown. We seek the distribution $D_{B_{\text{ext}}}(E, \Delta, x)$ where $D_{B_{\text{ext}}}(E, \Delta, x)d\Delta$ is the probability that an incident electron of energy E , after traversing a thickness x , will have energy loss in the range $[\Delta, \Delta + d\Delta]$ due to external bremsstrahlung. From Tsai [26] [27] we have the formula,

$$D_{B_{\text{ext}}}(E, \Delta, x) = \frac{1}{E\Gamma(bt)} \left(\frac{\Delta}{E}\right)^{bt-1} \left[1 - \frac{\Delta}{E} + \frac{3}{4} \left(\frac{\Delta}{E}\right)^2\right], \quad \Delta < 0.8E, \quad (3.18)$$

$$t < 0.05 \text{ r. l.},$$

where t is the thickness in radiation lengths, x/X_{rad} , and X_{rad} is the unit radiation length (r. l.) of the material. The parameter b is a function of the atomic number, Z , of the target medium

and is given by the following formula [27].

$$b = \frac{4}{3} \left(1 + \frac{1}{12} \frac{Z^2 + Z}{Z^2 L_{\text{rad}} + Z L'_{\text{rad}}} \right), \quad (3.19)$$

$$\begin{aligned} L_{\text{rad}} &= \ln(184.15Z^{-1/3}) \quad Z \geq 5, \\ &= 5.31 \quad Z = 1, \\ L'_{\text{rad}} &= \ln(1194Z^{-2/3}) \quad Z \geq 5, \\ &= 6.144 \quad Z = 1. \end{aligned}$$

The normalization is expressed as follows:

$$\int_0^E D_{B_{\text{ext}}}(E, \Delta, x) d\Delta = 1. \quad (3.20)$$

Near the elastic peak, $\Delta/E \ll 1$, we can simplify our expression for $D_{B_{\text{ext}}}(E, \Delta, x)$ and only keep the leading term in the expansion. From Equation 3.18 we obtain the distribution for external bremsstrahlung near the elastic peak (abbreviated nep).

$$D_{B_{\text{ext}}}^{\text{nep}}(E, \Delta, x) = \frac{1}{E\Gamma(bt)} \left(\frac{\Delta}{E} \right)^{bt-1}, \quad \Delta/E \ll 1, \quad (3.21)$$

$t < 0.05$ r. l.

This expression has the same form as that used by Bergstrom in his analysis [18]. The only difference is the value chosen for the parameter b . Since Bergstrom used the distribution given by Heitler [28] for external bremsstrahlung, his value for b was $1/\ln 2$. Our value is expressed by Equation 3.19 and is only weakly dependent on Z . For $Z = 13$ Equation 3.19 gives 1.358 for b . The difference between the two values is $\sim 6\%$. The energy dependence of this distribution can be explored by considering $D_{B_{\text{ext}}}^{\text{nep}}$ evaluated at $E + \delta E$.

$$D_{B_{\text{ext}}}^{\text{nep}}(E + \delta E, \Delta, x) = D_{B_{\text{ext}}}^{\text{nep}}(E, \Delta, x) \left[1 - \frac{\delta E}{E} \right]^{-bt}. \quad (3.22)$$

When $bt \ll 1$, the factor on the right hand side is ~ 1 . For this case $D_{B_{\text{ext}}}$ is weakly dependent on the incident energy E .

The Laplace transform of this distribution is,

$$\begin{aligned} d_{B_{\text{ext}}}^{\text{nep}}(E, s, x) &\equiv \mathcal{L}[D_{B_{\text{ext}}}^{\text{nep}}(E, \Delta, x)] = \int_0^\infty d\Delta e^{-s\Delta} D_{B_{\text{ext}}}^{\text{nep}}(E, \Delta, x) \\ &= \frac{1}{(Es)^{bt}}, \end{aligned} \quad (3.23)$$

where a small d is used to denote the Laplace transform of this distribution and the other quantities are as defined previously. From the Laplace transform it is easy to show that $D_{B_{\text{ext}}}^{\text{nep}}(E, \Delta, x)$ has the correct limit as $x \rightarrow 0$. When $x = 0$ ($t = 0$) we have

$$d_{B_{\text{ext}}}^{\text{nep}}(E, s, 0) = 1, \quad (3.24)$$

and since $\mathcal{L}[\delta(\Delta)] = 1$, we must have

$$D_{B_{\text{ext}}}^{\text{nep}}(E, \Delta, 0) = \delta(\Delta). \quad (3.25)$$

3.1.2.2 Internal Bremsstrahlung

In Figure 3-3 the first order Feynman diagrams associated with internal bremsstrahlung are shown. We seek the distribution $D_{B_{\text{int}}}(E, \Delta, \theta)$ where $D_{B_{\text{int}}}(E, \Delta, \theta)d\Delta$ is the probability that an incident particle of energy E , after scattering with angle θ , will have energy loss in the range $[\Delta, \Delta + d\Delta]$ due to internal bremsstrahlung. In order to obtain this distribution we will use the radiative correction factor derived by Tsai [21] [26] for electron-proton scattering: $\delta_{\text{Tsai}}(\Delta)$. Included in this correction are the inelastic diagrams of Figure 3-3 and also corrections to lowest order elastic scattering shown in Figure 3-4. The inelastic diagrams are responsible for the energy loss during the scattering process and therefore directly affect the line shape. The higher order elastic diagrams do not affect the line shape since there is no energy loss. Instead they only affect the overall measured cross section. As far as the line shape is concerned these Δ independent terms are not important. But we must keep them in order to get the correct radiation correction factor. We also will use the correction factor derived for electron-proton scattering for electron-deuteron scattering, although this is not exactly correct. The nuclear differences between the proton and deuteron will affect the amplitudes for the nuclear radiation diagrams. Unfortunately there appear to be no calculations for radiative corrections to electron scattering from the deuteron.

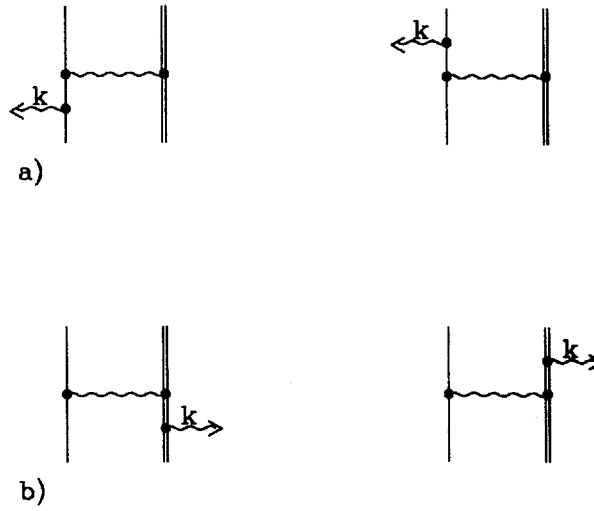


Figure 3-3: The first order Feynman diagrams for internal bremsstrahlung processes in matter: a) Radiation from the electron current. b) Radiation from the nuclear current.

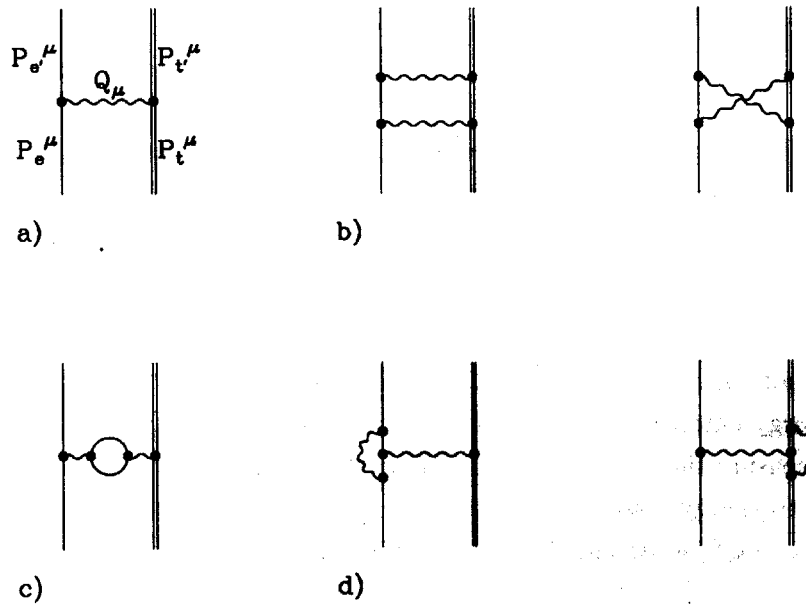


Figure 3-4: Corrections to elastic scattering to order α^4 . a) Pure elastic scattering (1γ exchange diagram.) b) 2γ exchange diagrams. c) Vacuum polarization diagram. d) Vertex correction diagrams.

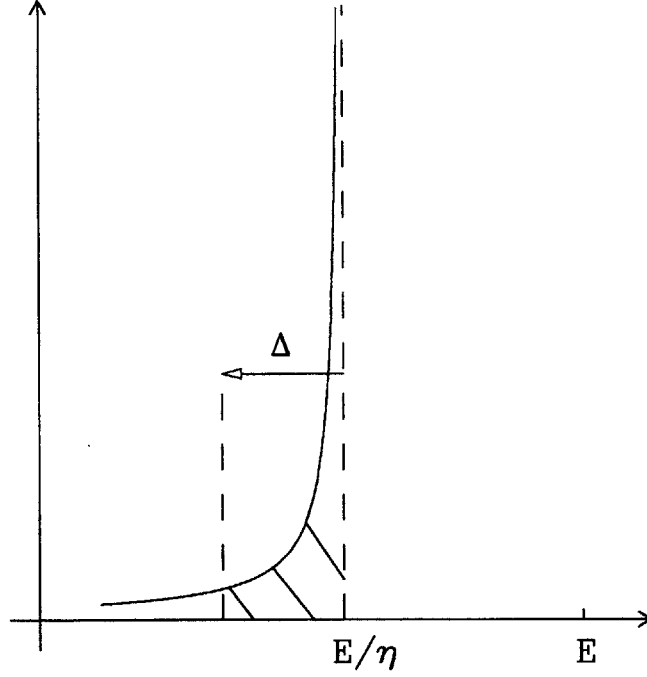


Figure 3-5: Elastic peak with no straggling. Δ is the experimental energy cutoff used when computing the cross section.

We have the following relationship between the pure one-photon exchange cross section and the experimentally measured cross section:

$$\left(\frac{d\sigma}{d\Omega}\right)_{\text{meas.}} = \left(\frac{d\sigma}{d\Omega}\right)_{1\gamma} \times \{1 + \delta_{\text{Tsaï}}(\Delta)\}, \quad (3.26)$$

where Δ is the soft photon cutoff limit and is illustrated in Figure 3-5. This cutoff is the experimental energy cutoff that is used when extracting the measured cross section since it is not feasible to measure the whole tail. The factor $\{1 + \delta_{\text{Tsaï}}(\Delta)\}$ corrects for the fraction that will be lost due to energy losses greater than Δ . The expression for $\delta_{\text{Tsaï}}(\Delta)$ is given by the following formula ($-Q^2 \gg m_e^2$ and $E, E' \gg m_e$):

$$\delta_{\text{Tsaï}}(\Delta) = -\frac{\alpha}{\pi} \left\{ (2\mathcal{A} + Z^2\mathcal{B}) \ln \left(\frac{E}{\eta\Delta} \right) + \Xi \right\}, \quad \text{for } \Delta(1 + 2E/M_i) \ll E', \quad (3.27)$$

where

$$Z = +1 \quad (\text{electron-target scattering}), \quad (3.28)$$

$$A = \ln \frac{-Q^2}{m_e^2} - 1 + 2Z \ln \eta, \quad (3.29)$$

$$B = \frac{1}{\beta'_t} \ln \left[\frac{1 + \beta'_t}{1 - \beta'_t} \right] - 2, \quad (3.30)$$

$$\Xi = \frac{28}{9} - \frac{13}{6} \ln \frac{-Q^2}{m_e^2} - 3A \ln \eta + (2A + Z^2 B) \ln \eta \quad (3.31)$$

$$\begin{aligned} & -\Phi\left(\frac{E' - E}{E'}\right) - Z^2 \ln \frac{E'_t}{M_t} + Z^2 B \ln\left(\frac{M_t}{\eta E}\right) \\ & + \frac{Z^2}{\beta'_t} \left[\frac{1}{2} \ln \frac{1 + \beta'_t}{1 - \beta'_t} \ln \frac{E'_t + M_t}{2M_t} - \Phi\left(-\left(\frac{E'_t - M_t}{E'_t + M_t}\right)^{1/2} \left(\frac{1 + \beta'_t}{1 - \beta'_t}\right)^{1/2}\right) \right] \\ & + Z \left[\Phi\left(\frac{-(M_t - E')}{E}\right) - \Phi\left(\frac{M_t(M_t - E')}{2E'E'_t - M_t E}\right) + \Phi\left(\frac{2E'(M_t - E')}{2E'E'_t - M_t E}\right) \right. \\ & \quad \left. + \ln \left| \frac{2E'E'_t - M_t E}{E(M_t - 2E')} \right| \ln\left(\frac{M_t}{2E'}\right) \right] \\ & - Z \left[\Phi\left(\frac{-(E'_t - E')}{E'}\right) - \Phi\left(\frac{M_t(E'_t - E')}{2EE'_t - M_t E'}\right) + \Phi\left(\frac{2E(E'_t - E')}{2EE'_t - M_t E'}\right) \right. \\ & \quad \left. + \ln \left| \frac{2EE'_t - M_t E'}{E'(M_t - 2E)} \right| \ln\left(\frac{M_t}{2E}\right) \right] \\ & - Z \left[\Phi\left(\frac{-(M_t - E)}{E}\right) - \Phi\left(\frac{M_t - E}{E}\right) + \Phi\left(\frac{2(M_t - E)}{M_t}\right) \right. \\ & \quad \left. + \ln \left| \frac{M_t}{2E - M_t} \right| \ln\left(\frac{M_t}{2E}\right) \right] \\ & + Z \left[\Phi\left(\frac{-(M_t - E')}{E'}\right) - \Phi\left(\frac{M_t - E'}{E'}\right) + \Phi\left(\frac{2(M_t - E')}{M_t}\right) \right. \\ & \quad \left. + \ln \left| \frac{M_t}{2E' - M_t} \right| \ln\left(\frac{M_t}{2E'}\right) \right] \\ & + \frac{Z^2}{\beta'_t} \Phi\left(\left(\frac{E'_t - M_t}{E'_t + M_t}\right)^{1/2} \left(\frac{1 - \beta'_t}{1 + \beta'_t}\right)^{1/2}\right) \\ & - \Phi\left(\frac{E - E'}{E}\right) + \frac{Z^2}{\beta'_t} \left[-\Phi\left(\left(\frac{E'_t - M_t}{E'_t + M_t}\right)^{1/2}\right) + \Phi\left(-\left(\frac{E'_t - M_t}{E'_t + M_t}\right)^{1/2}\right) \right], \end{aligned}$$

and Φ is the Spence function defined by the integral:

$$\Phi(x) \equiv \int_0^x \frac{-\ln|1-y|}{y} dy. \quad (3.32)$$

The other quantities are given by the kinematics for elastic electron-target scattering. From 4-momentum conservation we have (see Figure 3-4a)

$$P_e^\mu + P_t^\mu = P_{e'}^\mu + P_t'^\mu, \quad (3.33)$$

where

$$P_e^\mu = (E, \vec{p}),$$

$$P_t^\mu = (M_t, 0),$$

$$P_{e'}^\mu = (E', \vec{p}'),$$

$$P_t'^\mu = (E_t', \vec{p}_t').$$

Assuming the electrons are relativistic we obtain the following expressions:

$$Q^2 = (P_e^\mu - P_{e'}^\mu)^2 = -4EE' \sin^2(\theta/2), \quad (3.34)$$

$$E' = \frac{E}{\eta}, \quad (3.35)$$

$$\eta = 1 + \frac{2E}{M_t} \sin^2(\theta/2) \quad (\text{recoil factor}), \quad (3.36)$$

$$E_t' = E + M_t - E', \quad (3.37)$$

$$\beta_t' = \frac{v_t'}{c} = \frac{\sqrt{E_t'^2 - M_t^2}}{E_t'}. \quad (3.38)$$

This correction as it stands has one major flaw; as $\Delta \rightarrow 0$ the correction factor, $\{1 + \delta_{\text{Tsaï}}(\Delta)\}$, becomes negative. This is unphysical since cross sections are positive numbers. To remedy this we shall use Schwinger's prescription [29] of exponentiating the correction.

$$\{1 + \delta_{\text{Tsaï}}(\Delta)\} \Rightarrow e^{\delta_{\text{Tsaï}}(\Delta)}.$$

This exponentiated form now has the correct physical limit as $\Delta \rightarrow 0$, the correction also goes to zero. Which says that pure elastic scattering does not exist in the real world due to the higher order radiative processes.

The relationship between the measured and one-photon exchange cross sections then becomes:

$$\begin{aligned} \left. \frac{d\sigma}{d\Omega} \right)_{\text{meas.}} &= \left. \frac{d\sigma}{d\Omega} \right)_{1\gamma} e^{\delta_{\text{Tsal}}(\Delta)} \\ &= \left. \frac{d\sigma}{d\Omega} \right)_{1\gamma} e^{\delta_2} \left(\frac{\eta\Delta}{E} \right)^{\delta_1}, \end{aligned} \quad (3.39)$$

where

$$\delta_1 = +\frac{\alpha}{\pi} (2\mathcal{A} + Z^2\mathcal{B}), \quad (3.40)$$

$$\delta_2 = -\frac{\alpha}{\pi} \Xi. \quad (3.41)$$

Taking the derivative of this expression with respect to Δ gives us the doubly differential cross section, $d^2\sigma/d\Omega/d\Delta$, which is the spectrum of scattered electrons shown in Figure 3-5.

$$\left. \frac{d^2\sigma}{d\Omega d\Delta} \right)_{\text{meas.}} = \left. \frac{d\sigma}{d\Omega} \right)_{1\gamma} e^{\delta_2} \frac{\eta\delta_1}{E} \left(\frac{\eta\Delta}{E} \right)^{\delta_1-1}. \quad (3.42)$$

From this the distribution $D_{B_{\text{int}}}$ can be obtained since $D_{B_{\text{int}}} \propto d^2\sigma/d\Omega/d\Delta$. Requiring the following normalization,

$$\int_0^{E/\eta} D_{B_{\text{int}}}(E, \Delta, \theta) d\Delta = 1, \quad (3.43)$$

we find

$$D_{B_{\text{int}}}(E, \Delta, \theta) = \frac{\eta\delta_1}{E} \left(\frac{\eta\Delta}{E} \right)^{\delta_1-1}, \quad (3.44)$$

with

$$\delta_1 = +\frac{\alpha}{\pi} \left[2 \left(\ln \frac{-Q^2}{m_e^2} - 1 \right) + 4Z \ln \eta + Z^2 \left(\frac{1}{\beta'_t} \ln \frac{1 + \beta'_t}{1 - \beta'_t} - 2 \right) \right]. \quad (3.45)$$

We can interpret the various pieces of δ_1 as it contributes to $D_{B_{\text{int}}}$ in the following way (see Figure 3-3). The Z independent term is the contribution from the electron radiation diagrams. The term proportional to Z is the interference between the electron and target radiation diagrams. The Z^2 term is just the contribution from the target radiation diagrams. Notice that even though the Z^2 contribution may be small, the interference term can be quite significant and cannot be neglected.

The energy dependence of this distribution can be explored by considering $D_{B_{\text{int}}}$ evaluated at $E + \delta E$.

$$D_{B_{\text{int}}}(E + \delta E, \Delta, \theta) = D_{B_{\text{int}}}(E, \Delta, \theta) \left[1 - \frac{\delta E}{E} \right]^{-\delta_1}. \quad (3.46)$$

When $\delta_1 \ll 1$, the factor on the right hand side is ~ 1 . For this case $D_{B_{\text{int}}}$ is weakly dependent on the incident energy E .

Rewriting our doubly differential cross section in terms of $D_{B_{\text{int}}}$ we obtain the following expression.

$$\left. \frac{d^2\sigma}{d\Omega d\Delta} \right)_{\text{meas.}} = \left. \frac{d\sigma}{d\Omega} \right)_{1\gamma} e^{\delta_2} D_{B_{\text{int}}}(E, \Delta, \theta). \quad (3.47)$$

Where the factor e^{δ_2} adjusts the overall magnitude of the one-photon exchange cross section due to the higher order scattering processes.

The Laplace transform of this distribution is given by the following expression,

$$\begin{aligned} d_{B_{\text{int}}}(E, s, \theta) &\equiv \mathcal{L}[D_{B_{\text{int}}}(E, \Delta, \theta)] = \int_0^\infty d\Delta e^{-s\Delta} D_{B_{\text{int}}}(E, \Delta, \theta) \\ &= \Gamma(\delta_1 + 1) \left(\frac{\eta}{Es} \right)^{\delta_1}, \end{aligned} \quad (3.48)$$

where a small d is used to denote the Laplace transform of this distribution and the other quantities are as defined previously. From the Laplace transform we can check to see if $D_{B_{\text{int}}}$ has the correct limit as $\theta \rightarrow 0$ ($-Q^2 \rightarrow 0$). We should have $d_{B_{\text{int}}}(E, \Delta, 0) = 1$ which implies that $D_{B_{\text{int}}}(E, \Delta, 0) = \delta(\Delta)$. This requires $\delta_1 \rightarrow 0$. From Equation 3.45 only one term fails to go to zero as $\theta \rightarrow 0$. This is the Z independent term which diverges logarithmically as Q^2 . This term comes from the electron radiation diagram and was derived in the extreme relativistic region where $-Q^2 \gg m_e^2$. From Schwinger (Equation 2.102 [29]), we find that the general expression indeed vanishes as $\theta \rightarrow 0$ ensuring that $D_{B_{\text{int}}}(E, \Delta, 0)$ would be a $\delta(\Delta)$ if the extreme relativistic limit were not used.

3.2 The Convolution

In the previous section we presented the distributions that govern the energy loss of an electron as it passes through matter. What we seek to find is the energy loss distribution for electrons

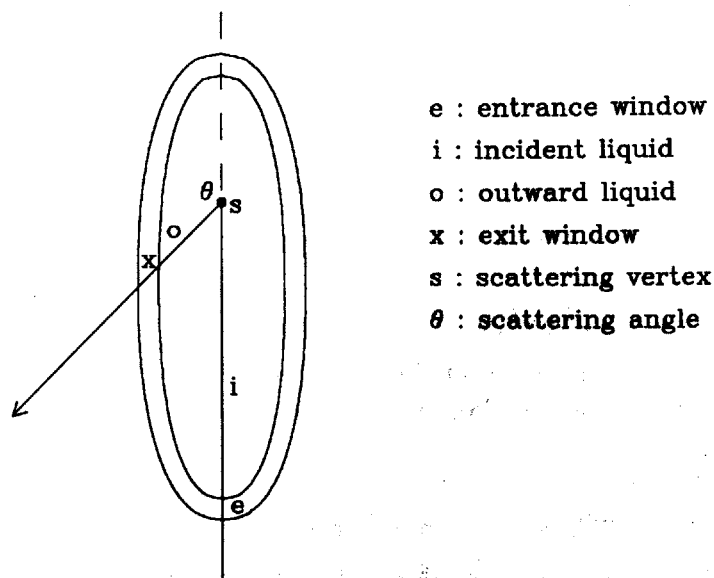


Figure 3-6: The target cell and scattering geometry indicating the various pieces that the electron has to travel through before it exits the cell.

traversing the target cell and the line shape which describes the shape of the spectrum of scattered electrons observed. The energy loss distribution is used to calculate the fraction of electrons that will lose enough energy to fall outside of the experimental acceptance. This represents part of the radiative correction, and the elastic line shape is used to subtract the contribution of the elastic tail from the inelastic electron spectrum.

The target cell consists of either liquid deuterium or hydrogen in an aluminum casing. Finding the energy loss distribution **requires** convoluting the various energy loss distributions for each segment of the target cell. This energy loss distribution is a probability distribution. The elastic line shape is also given by such a convolution except that the cross section for scattering needs to be included in the convolution.

3.2.1 Scattering Geometry and Definitions

In Figure 3-6 the target cell geometry is shown along with a representative scattered electron path. We divide this total path into four pieces. The electron first passes through an aluminum entrance window of thickness x_e . Then before it undergoes the main scattering event it passes through some amount of incident liquid of thickness x_i . After the scattering, it then passes through some amount of outward liquid of thickness x_o . Finally upon leaving the target cell it

passes through some amount of the aluminum exit window of thickness x_x . Throughout this traversal the electron loses energy as it passes through x_e , x_i , x_o , and x_x due to ionization and external bremsstrahlung and also at the scattering vertex due to internal bremsstrahlung. For convenience we shall define the following energy loss distribution $F_{IB_{ext}}(E, \Delta, x)$:

$$F_{IB_{ext}}(E, \Delta, x) = \int_0^{\Delta} D_I(E, \epsilon, x) D_{B_{ext}}(E, \Delta - \epsilon, x) d\epsilon. \quad (3.49)$$

This distribution is a convolution of the fundamental energy loss distributions D_I and $D_{B_{ext}}$, and $F_{IB_{ext}}(E, \Delta, x)d\Delta$ is the probability that an incident particle of energy E , after traveling a distance x , will have energy loss in the range $[\Delta, \Delta + d\Delta]$ due to ionization and external bremsstrahlung.

Shown in Figure 3-7a is a schematic diagram representing the various energy losses that occur as the electron traverses the target cell. Δ_e , Δ_i , Δ_o , and Δ_x are the energy losses that occur as the electron traverses t_e , t_i , t_o , and t_x respectively. The t 's are the thicknesses expressed in terms of their radiation lengths,

$$t_e = \frac{x_e}{X_{rad}^e}, \quad (3.50)$$

$$t_i = \frac{x_i}{X_{rad}^i}, \quad (3.51)$$

$$t_o = \frac{x_o}{X_{rad}^o}, \quad (3.52)$$

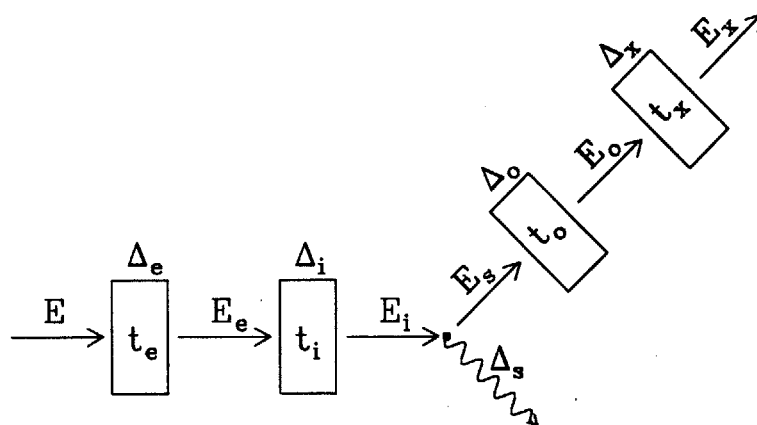
$$t_x = \frac{x_x}{X_{rad}^x}, \quad (3.53)$$

where the X_{rad} 's are their associated unit radiation lengths. These energy losses are governed by the distribution $F_{IB_{ext}}(E, \Delta, x)$. Δ_s is the energy loss that occurs due to internal bremsstrahlung at the scattering vertex and is governed by $D_{B_{int}}(E, \Delta, \theta)$. Also shown are the electron energies E_e , E_i , E_s , E_o , and E_x as it passes through the target cell. Shown in Figure 3-7b is an energy diagram indicating the various pieces of the energy losses that occur as the electron traverses the target cell. From this figure we have the following relationships for the electron energy as it passes through the cell. If E is the incident energy we have:

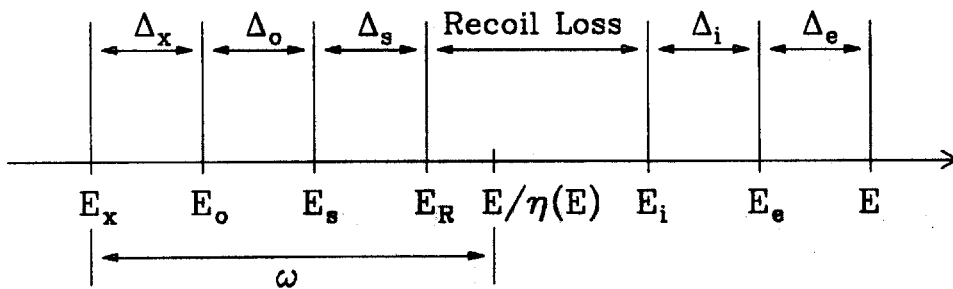
$$E_e = E - \Delta_e, \quad (3.54)$$

$$E_i = E_e - \Delta_i, \quad (3.55)$$

$$E_R = \frac{E_i}{\eta(E_i)} \quad (\text{elastic scattering}), \quad (3.56)$$



a)



b)

Figure 3-7: a) Schematic picture of the various energy losses as an electron traverses the target cell. b) An energy diagram indicating the energy losses.

$$E_s = E_R - \Delta_s, \quad (3.57)$$

$$E_o = E_s - \Delta_o, \quad (3.58)$$

$$E_x = E_o - \Delta_x, \quad (3.59)$$

where

$$\eta(E_i) = 1 + \frac{2E_i}{M_t} \sin^2(\theta/2), \quad (3.60)$$

with M_t being the target mass and θ the scattering angle. Eliminating the intermediate energies and solving for E_x as a function of the energy losses, Δ , and the incident energy, E , gives the following expression:

$$E_x = \frac{E - \Delta_e - \Delta_i}{\eta(E - \Delta_e - \Delta_i)} - \Delta_s - \Delta_o - \Delta_x. \quad (3.61)$$

From this figure we also define a new energy loss variable ω as follows,

$$\omega = \frac{E}{\eta(E)} - E_x, \quad (3.62)$$

where $E/\eta(E)$ is the pure recoil scattered energy with no energy losses and E_x is the exiting electron energy; hence ω is the energy loss not due to recoil and has the range $[0, E/\eta(E)]$. Substituting Equation 3.61 for E_x gives ω as a function of the energy losses, Δ , and the incident energy, E :

$$\omega = \frac{E}{\eta(E)} - \frac{E - \Delta_e - \Delta_i}{\eta(E - \Delta_e - \Delta_i)} + \Delta_s + \Delta_o + \Delta_x. \quad (3.63)$$

The energy loss variable, ω , is related to the excitation energy, E_{exc} , by the following equation,

$$E_x = \frac{E - E_{exc} - E_{exc}^2/(2M_t)}{\eta(E)} = \frac{E}{\eta(E)} - \omega, \quad (3.64)$$

which gives the following equality:

$$E_{exc} + \frac{E_{exc}^2}{2M_t} = \eta\omega. \quad (3.65)$$

For small values of E_{exc}/M_t the quadratic term can be neglected to yield:

$$E_{exc} \cong \eta\omega. \quad (3.66)$$

For small values of energy loss before, Δ_{bef} , and after, Δ_{aft} , scattering (see Equation 3.61) ω can be expressed as follows:

$$\omega \cong \Delta_{\text{aft}} + \frac{\Delta_{\text{bef}}}{\eta^2}. \quad (3.67)$$

3.2.2 Elastic Line Shape

3.2.2.1 Full Line Shape

We seek the distribution $D(E, \omega, \mathcal{X})$ where $D(E, \omega, \mathcal{X})d\omega$ is the probability that an electron of energy E , after traversing the target cell following a path described by the coordinates $\mathcal{X} \equiv (x_e, x_i, x_o, x_x, \theta)$, will have energy loss in the range $[\omega, \omega + d\omega]$ due to ionization, external bremsstrahlung, and internal bremsstrahlung. This distribution is given by convoluting the various energy loss distributions for each segment of the target cell and is expressed as follows:

$$\begin{aligned} D(E, \omega, \mathcal{X}) = & \int_0^{\Delta_e^{\text{max}}(\omega)} d\Delta_e \int_0^{\Delta_i^{\text{max}}(\omega, \Delta_e)} d\Delta_i \int_0^{\Delta_s^{\text{max}}(\omega, \Delta_e, \Delta_i)} d\Delta_s \quad (3.68) \\ & \times \int_0^{\Delta_o^{\text{max}}(\omega, \Delta_e, \Delta_i, \Delta_s)} d\Delta_o F_{IB_{\text{ext}}}(E, \Delta_e, x_e) \\ & \times F_{IB_{\text{ext}}}(E_e, \Delta_i, x_i) D_{B_{\text{int}}}(E_i, \Delta_s, \theta) F_{IB_{\text{ext}}}(E_s, \Delta_o, x_o) \\ & \times F_{IB_{\text{ext}}}(E_o, \Delta_x^{\text{max}}(\omega, \Delta_e, \Delta_i, \Delta_s, \Delta_o), x_x). \end{aligned}$$

The elastic line shape is then given by the following expression,

$$\begin{aligned} \left. \frac{d^2\sigma}{d\Omega d\omega} \right)_{\text{meas.}} = & \int_0^{\Delta_e^{\text{max}}(\omega)} d\Delta_e \int_0^{\Delta_i^{\text{max}}(\omega, \Delta_e)} d\Delta_i \int_0^{\Delta_s^{\text{max}}(\omega, \Delta_e, \Delta_i)} d\Delta_s \quad (3.69) \\ & \times \int_0^{\Delta_o^{\text{max}}(\omega, \Delta_e, \Delta_i, \Delta_s)} d\Delta_o F_{IB_{\text{ext}}}(E, \Delta_e, x_e) \\ & \times F_{IB_{\text{ext}}}(E_e, \Delta_i, x_i) \left. \frac{d\sigma(E_i)}{d\Omega} \right)_{1\gamma} e^{\delta_2} D_{B_{\text{int}}}(E_i, \Delta_s, \theta) \\ & \times F_{IB_{\text{ext}}}(E_s, \Delta_o, x_o) F_{IB_{\text{ext}}}(E_o, \Delta_x^{\text{max}}(\omega, \Delta_e, \Delta_i, \Delta_s, \Delta_o), x_x), \end{aligned}$$

where the dependence of the cross section at the time of scattering on the electron energy has been included (see Equation 3.47). The effect of this dependence is to increase the size of the elastic tail at large energy losses. This is due to the increase of the cross section at low incident scattering energies, E_i . Ignoring this dependence, the cross section can be brought outside of

the multiple convolution and the elastic line shape can be expressed in terms of the energy loss distribution, $D(E, \omega, \mathcal{X})$.

$$\left. \frac{d^2\sigma}{d\Omega d\omega} \right)_{\text{meas.}} = \left. \frac{d\sigma}{d\Omega} \right)_{1\gamma} e^{\delta_2} D(E, \omega, \mathcal{X}). \quad (3.70)$$

The validity of this relation is justified near the elastic peak where the energy loss are small and the change in the scattering cross section is small (see Appendix E). For the rest of this chapter this equality is used.

The Δ^{max} 's present in the multiple convolution can be obtained from Equation 3.63 using conservation of energy. To get Δ_e^{max} we set Δ_i , Δ_s , Δ_o , and Δ_x equal to zero. This gives us the equation for Δ_e^{max} :

$$\omega = \frac{E}{\eta(E)} - \frac{E - \Delta_e^{\text{max}}}{\eta(E - \Delta_e^{\text{max}})}. \quad (3.71)$$

Solving for Δ_e^{max} yields,

$$\Delta_e^{\text{max}} = \frac{\eta^2 \omega}{1 + (\eta - 1)\eta\omega/E}, \quad (3.72)$$

where

$$\eta \equiv \eta(E) = 1 + \frac{2E}{M_t} \sin^2(\theta/2). \quad (3.73)$$

Carrying out the same operations for Δ_i^{max} but keeping Δ_e in the expression and setting the rest of the energy losses Δ_s , Δ_o , and Δ_x equal to zero gives:

$$\Delta_i^{\text{max}} = \Delta_e^{\text{max}} - \Delta_e. \quad (3.74)$$

Similarly for the remaining losses we obtain:

$$\Delta_s^{\text{max}} = \omega - \frac{(\Delta_e + \Delta_i)}{\eta^2} \left[1 - \left(\frac{\eta - 1}{\eta} \right) \left(\frac{\Delta_e + \Delta_i}{E} \right) \right]^{-1}, \quad (3.75)$$

$$\Delta_o^{\text{max}} = \Delta_s^{\text{max}} - \Delta_s, \quad (3.76)$$

$$\Delta_x^{\text{max}} = \Delta_s^{\text{max}} - \Delta_s - \Delta_o. \quad (3.77)$$

One simplification that can be made to the above convolution is to eliminate the Δ dependence for the incident energies in Equations 3.54 through 3.58. This gives the following

relations:

$$E_e \approx E, \quad (3.78)$$

$$E_i \approx E, \quad (3.79)$$

$$E_s \approx E/\eta, \quad (3.80)$$

$$E_o \approx E/\eta. \quad (3.81)$$

The validity of this step rests on the assumption that either the distributions are weakly dependent on the incident energy or the energy losses are small compared to the incident energy.

3.2.2.2 Normalization

The normalization of $D(E, \omega, \mathcal{X})$ is expressed as follows:

$$\begin{aligned} \int_0^{E/\eta} d\omega D(E, \omega, \mathcal{X}) &= \int_0^{E/\eta} d\omega \int_0^{\Delta_s^{\max}} d\Delta_e^{\max} \int_0^{\Delta_s^{\max} - \Delta_e} d\Delta_i \int_0^{\Delta_s^{\max}} d\Delta_s \quad (3.82) \\ &\times \int_0^{\Delta_s^{\max} - \Delta_s} d\Delta_o F_{IB_{ext}}(E, \Delta_e, x_e) F_{IB_{ext}}(E, \Delta_i, x_i) \\ &\times D_{B_{int}}(E, \Delta_s, \theta) \\ &\times F_{IB_{ext}}(E/\eta, \Delta_o, x_o) F_{IB_{ext}}(E/\eta, \Delta_s^{\max} - \Delta_s - \Delta_o, x_x), \end{aligned}$$

where the approximations, Equations 3.78 through 3.81, were used for the distributions incident energies.

To evaluate this multiple integral we make the following change of variable:

$$\begin{aligned} y_1 &= \Delta_e, \\ y_2 &= \Delta_i, \\ y_3 &= \Delta_s, \\ y_4 &= \Delta_o, \\ y_5 &= \Delta_s^{\max} - \Delta_s - \Delta_o. \end{aligned}$$

The normalization then becomes:

$$\begin{aligned}
\int_0^{E/\eta} d\omega D(E, \omega, \mathcal{X}) &= \int dy_1 \int dy_2 \int dy_3 \int dy_4 \int dy_5 \\
&\times J\left(\frac{\Delta_e, \Delta_i, \Delta_s, \Delta_o, \omega}{y_1, y_2, y_3, y_4, y_5}\right) \\
&\times F_{IB_{\text{ext}}}(E, y_1, x_e) F_{IB_{\text{ext}}}(E, y_2, x_i) D_{B_{\text{int}}}(E, y_3, \theta) \\
&\times F_{IB_{\text{ext}}}(E/\eta, y_4, x_o) F_{IB_{\text{ext}}}(E/\eta, y_5, x_x),
\end{aligned} \tag{3.83}$$

where

$$J\left(\frac{\Delta_e, \Delta_i, \Delta_s, \Delta_o, \omega}{y_1, y_2, y_3, y_4, y_5}\right) = 1,$$

is the Jacobian of the transformation. The new limits of integration over the five-dimensional space $(y_1, y_2, y_3, y_4, y_5)$ can be obtained by considering conservation of energy. The result is as follows:

$$\begin{aligned}
\int_0^{E/\eta} d\omega D(E, \omega, \mathcal{X}) &= \int_0^E dy_1 \int_0^{E-y_1} dy_2 \int_0^{E/\eta-(y_1+y_2)/\eta} dy_3 \\
&\times \int_0^{E/\eta-y_3-(y_1+y_2)/\eta} dy_4 \int_0^{E/\eta-y_3-y_4-(y_1+y_2)/\eta} dy_5 \\
&\times F_{IB_{\text{ext}}}(E, y_1, x_e) F_{IB_{\text{ext}}}(E, y_2, x_i) \\
&\times D_{B_{\text{int}}}(E, y_3, \theta) F_{IB_{\text{ext}}}(E/\eta, y_4, x_o) F_{IB_{\text{ext}}}(E/\eta, y_5, x_x),
\end{aligned} \tag{3.84}$$

and the region of integration is over a corner of a five-dimensional box. Outside of this region the distributions are vanishingly small. Therefore, we can expand the limits of integration over the entire box with negligible error. This leads to five separable one-dimensional integrals for the normalization,

$$\begin{aligned}
\int_0^{E/\eta} d\omega D(E, \omega, \mathcal{X}) &\approx \int_0^E dy_1 F_{IB_{\text{ext}}}(E, y_1, x_e) \int_0^E dy_2 F_{IB_{\text{ext}}}(E, y_2, x_i) \\
&\times \int_0^E dy_3 D_{B_{\text{int}}}(E, y_3, \theta) \\
&\times \int_0^{E/\eta} dy_4 F_{IB_{\text{ext}}}(E/\eta, y_4, x_o) \int_0^{E/\eta} dy_5 F_{IB_{\text{ext}}}(E/\eta, y_5, x_x),
\end{aligned} \tag{3.85}$$

and each separate integral is itself a normalization condition for the individual distributions. $D_{B_{\text{int}}}$ has unit normalization as shown by Equation 3.43. $F_{IB_{\text{ext}}}$ is a convolution of D_I and $D_{B_{\text{ext}}}$ (see Equation 3.49). Using the same technique, it can also be shown that its normalization can

be expressed as a product of the normalizations for D_I and $D_{B_{\text{ext}}}$. Since both of these have unit normalization (see Equations 3.14 and 3.20), the overall normalization of $D(E, \omega, \mathcal{X})$ is unity.

$$\int_0^{E/\eta} d\omega D(E, \omega, \mathcal{X}) \approx \prod (\text{Individual Normalizations}) = 1. \quad (3.86)$$

3.2.2.3 Near Elastic Peak

If we are only interested in the knowing line shape near the elastic peak, the following simplifications can be made to Equation 3.68 for the full line shape. In Equation 3.72 for Δ_e^{max} we make the following small energy loss approximation:

$$\Delta_e^{\text{max}} \approx \eta^2 \omega \quad \text{for} \quad (\eta - 1) \frac{\omega}{E/\eta} \ll 1. \quad (3.87)$$

We can express this condition on ω in terms of the individual energy losses: Δ_e , Δ_i , Δ_s , Δ_o , and Δ_x . Rewriting Equation 3.63 in the following form,

$$(\eta - 1) \frac{\omega}{E/\eta} = (\eta - 1) \left[1 - \left(1 + \frac{\Delta_e + \Delta_i}{E} \right) \left(1 - \frac{\eta - 1}{\eta} \frac{\Delta_e + \Delta_i}{E} \right)^{-1} + \frac{\Delta_s + \Delta_o + \Delta_x}{E/\eta} \right], \quad (3.88)$$

we then must also have for $(\eta - 1)\omega/E/\eta \ll 1$:

$$\frac{\Delta_e + \Delta_i}{E} \ll 1, \quad (3.89)$$

and

$$\frac{\Delta_s + \Delta_o + \Delta_x}{E/\eta} \ll 1. \quad (3.90)$$

Using this small energy loss approximation in Equation 3.75 for Δ_s^{max} gives the following:

$$\Delta_s^{\text{max}} \approx \omega - \frac{(\Delta_e + \Delta_i)}{\eta^2}. \quad (3.91)$$

The convolution for the line shape near the elastic peak (abbreviated nep) then becomes:

$$\begin{aligned}
D^{\text{nep}}(E, \omega, \mathcal{X}) &= \int_0^{\eta^2 \omega} d\Delta_e \int_0^{\eta^2 \omega - \Delta_e} d\Delta_i \int_0^{\omega - (\Delta_e + \Delta_i)/\eta^2} d\Delta_s \\
&\times \int_0^{\omega - \Delta_s - (\Delta_e + \Delta_i)/\eta^2} d\Delta_o F_{IB_{\text{ext}}}^{\text{nep}}(E, \Delta_e, x_e) \\
&\times F_{IB_{\text{ext}}}^{\text{nep}}(E, \Delta_i, x_i) D_{B_{\text{int}}}(E, \Delta_s, \theta) F_{IB_{\text{ext}}}^{\text{nep}}(E/\eta, \Delta_o, x_o) \\
&\times F_{IB_{\text{ext}}}^{\text{nep}}(E/\eta, \omega - \Delta_s - \Delta_o - (\Delta_e + \Delta_i)/\eta^2, x_x),
\end{aligned} \tag{3.92}$$

where

$$F_{IB_{\text{ext}}}^{\text{nep}}(E, \Delta, x) = \int_0^\Delta D_I(E, \epsilon, x) D_{B_{\text{ext}}}^{\text{nep}}(E, \Delta - \epsilon, x) d\epsilon. \tag{3.93}$$

The limits of integration can be understood from the following argument. For elastic scattering we have the relationship $E' = E/\eta(E)$. If one considers differential changes in the energies we obtain $\delta E' = \delta E/\eta^2(E)$. Therefore, before scattering we can lose a multiplicative factor of η^2 more energy than after scattering and still fall into the scattered energy bin ω .

The Laplace transform of this convolution is given by the following expression:

$$\begin{aligned}
d^{\text{nep}}(E, s, \mathcal{X}) &\equiv \mathcal{L}[D^{\text{nep}}(E, \omega, \mathcal{X})] = \int_0^\infty d\omega e^{-s\omega} D^{\text{nep}}(E, \omega, \mathcal{X}) \\
&= \int_0^\infty d\omega \int_0^{\eta^2 \omega} d\Delta_e \int_0^{\eta^2 \omega - \Delta_e} d\Delta_i \int_0^{\omega - (\Delta_e + \Delta_i)/\eta^2} d\Delta_s \\
&\times \int_0^{\omega - \Delta_s - (\Delta_e + \Delta_i)/\eta^2} d\Delta_o e^{-s\omega} F_{IB_{\text{ext}}}^{\text{nep}}(E, \Delta_e, x_e) \\
&\times F_{IB_{\text{ext}}}^{\text{nep}}(E, \Delta_i, x_i) D_{B_{\text{int}}}(E, \Delta_s, \theta) F_{IB_{\text{ext}}}^{\text{nep}}(E/\eta, \Delta_o, x_o) \\
&\times F_{IB_{\text{ext}}}^{\text{nep}}(E/\eta, \omega - \Delta_s - \Delta_o - (\Delta_e + \Delta_i)/\eta^2, x_x),
\end{aligned} \tag{3.94}$$

where a small d is used to denote the Laplace transform of this distribution. To evaluate this we make the following change of variable:

$$\begin{aligned}
y_1 &= \Delta_e, \\
y_2 &= \Delta_i, \\
y_3 &= \Delta_s, \\
y_4 &= \Delta_o, \\
y_5 &= \omega - \Delta_s - \Delta_o - (\Delta_e + \Delta_i)/\eta^2.
\end{aligned}$$

The multiple integral then becomes:

$$\begin{aligned}
 d^{\text{nep}}(E, s, \mathcal{X}) &= \int_0^\infty dy_1 \int_0^\infty dy_2 \int_0^\infty dy_3 \int_0^\infty dy_4 \int_0^\infty dy_5 \\
 &\times J\left(\frac{\Delta_e, \Delta_i, \Delta_s, \Delta_o, \omega}{y_1, y_2, y_3, y_4, y_5}\right) \\
 &\times e^{-s(y_3+y_4+y_5+(y_1+y_2)/\eta^2)} \\
 &\times F_{IB_{\text{ext}}}^{\text{nep}}(E, y_1, x_e) F_{IB_{\text{ext}}}^{\text{nep}}(E, y_2, x_i) D_{B_{\text{int}}}(E, y_3, \theta) \\
 &\times F_{IB_{\text{ext}}}^{\text{nep}}(E/\eta, y_4, x_o) F_{IB_{\text{ext}}}^{\text{nep}}(E/\eta, y_5, x_x),
 \end{aligned} \tag{3.95}$$

where

$$J\left(\frac{\Delta_e, \Delta_i, \Delta_s, \Delta_o, \omega}{y_1, y_2, y_3, y_4, y_5}\right) = 1$$

is the Jacobian of the transformation. This multiple integral can now be expressed as five separate one-dimensional integrals:

$$\begin{aligned}
 d^{\text{nep}}(E, s, \mathcal{X}) &= \int_0^\infty dy_1 e^{-sy_1/\eta^2} F_{IB_{\text{ext}}}^{\text{nep}}(E, y_1, x_e) \\
 &\times \int_0^\infty dy_2 e^{-sy_2/\eta^2} F_{IB_{\text{ext}}}^{\text{nep}}(E, y_2, x_i) \\
 &\times \int_0^\infty dy_3 e^{-sy_3} D_{B_{\text{int}}}(E, y_3, \theta) \\
 &\times \int_0^\infty dy_4 e^{-sy_4} F_{IB_{\text{ext}}}^{\text{nep}}(E, y_4, x_o) \\
 &\times \int_0^\infty dy_5 e^{-sy_5} F_{IB_{\text{ext}}}^{\text{nep}}(E, y_5, x_x),
 \end{aligned} \tag{3.96}$$

where each integral is itself a Laplace transform of a distribution: $F_{IB_{\text{ext}}}^{\text{nep}}$ or $D_{B_{\text{int}}}$. Similarly, for the Laplace transform of $F_{IB_{\text{ext}}}^{\text{nep}}$ (see Equation 3.93) we find:

$$\int_0^\infty dy e^{-sy} F_{IB_{\text{ext}}}^{\text{nep}}(E, y, x) = \int_0^\infty dy_1 e^{-sy_1} D_I(E, y_1, x) \int_0^\infty dy_2 e^{-sy_2} D_{B_{\text{ext}}}^{\text{nep}}(E, y_2, x). \tag{3.97}$$

Therefore our expression for d^{nep} becomes a simple product of the individual Laplace transforms:

$$\begin{aligned}
d^{\text{nep}}(E, s, \mathcal{X}) = & d_I(E, s/\eta^2, x_e) d_{\text{B}_{\text{ext}}}^{\text{nep}}(E, s/\eta^2, x_e) \\
& \times d_I(E, s/\eta^2, x_i) d_{\text{B}_{\text{ext}}}^{\text{nep}}(E, s/\eta^2, x_i) \\
& \times d_{\text{B}_{\text{int}}}(E, s, \theta) \\
& \times d_I(E/\eta, s, x_o) d_{\text{B}_{\text{ext}}}^{\text{nep}}(E/\eta, s, x_o) \\
& \times d_I(E/\eta, s, x_x) d_{\text{B}_{\text{ext}}}^{\text{nep}}(E/\eta, s, x_x),
\end{aligned} \tag{3.98}$$

where these are given by Equations 3.15, 3.23, and 3.48. Substituting the formulas for the individual Laplace transforms we obtain the following:

$$\begin{aligned}
d^{\text{nep}}(E, s, \mathcal{X}) = & \exp[-\xi_e s/\eta^2(1 - C - \ln(\epsilon'_e s/\eta^2))] (Es/\eta^2)^{-b_e t_e} \\
& \times \exp[-\xi_i s/\eta^2(1 - C - \ln(\epsilon'_i s/\eta^2))] (Es/\eta^2)^{-b_i t_i} \\
& \times \Gamma(\delta_1 + 1) (Es/\eta)^{-\delta_1} \\
& \times \exp[-\xi_o s(1 - C - \ln(\epsilon'_o s))] (Es/\eta)^{-b_o t_o} \\
& \times \exp[-\xi_x s(1 - C - \ln(\epsilon'_x s))] (Es/\eta)^{-b_x t_x},
\end{aligned} \tag{3.99}$$

where all quantities are as previously defined. From this expression we can check to see if $D^{\text{nep}}(E, \omega, \mathcal{X})$ has the correct limit as $\mathcal{X} \rightarrow 0$, i.e. as x_e, x_i, x_o, x_x , and $\theta \rightarrow 0$. We should have $d^{\text{nep}}(E, \Delta, 0) = 1$ which implies that $D^{\text{nep}}(E, \omega, 0) = \delta(\omega)$. The only problem with this is associated with Equation 3.48 for $d_{\text{B}_{\text{int}}}$. This has already been mentioned in the section for this distribution and arises because the radiative correction used to derive it is valid only in the extreme relativistic limit ($-Q^2 \gg m_e^2$ and $E, E' \gg m_e$). If the $-Q^2 \ll m_e^2$ limit were used, we would have the correct limit.

In Table 3.1 are shown the values of the parameter b (see Equation 3.19) for the target cell wall, b_e and b_x , and target liquid, b_i and b_o . Since b differs less than 1% between the two, an average value denoted by b is used for simplicity in what follows. Rewriting the expression for d^{nep} we obtain the following:

$$d^{\text{nep}}(E, s, \mathcal{X}) = \Gamma(\delta_1 + 1) \left(\frac{\eta G}{E} \right)^T \eta^{bt_{\text{bet}}} \exp[-Fs - (T - Gs) \ln(Gs)], \tag{3.100}$$

where

$$F = (1 - C)G - \frac{\xi_e}{\eta^2} \ln \left(\frac{\epsilon'_e}{\eta^2 G} \right) - \frac{\xi_i}{\eta^2} \ln \left(\frac{\epsilon'_i}{\eta^2 G} \right) - \xi_o \ln \left(\frac{\epsilon'_o}{G} \right) - \xi_x \ln \left(\frac{\epsilon'_x}{G} \right), \tag{3.101}$$

b_e	b_i	b_o	b_x	average b
Al	LH ₂ or LD ₂	LH ₂ or LD ₂	Al	
Z=13	Z=1	Z=1	Z=13	
1.3584	1.3514	1.3514	1.3584	1.3549

Table 3.1: The external bremsstrahlung parameter b .

$$G = \xi_e/\eta^2 + \xi_i/\eta^2 + \xi_o + \xi_x, \quad (3.102)$$

$$T = bt_{\text{tot}} + \delta_1, \quad (3.103)$$

and t_{tot} is the total number of radiation lengths traversed

$$t_{\text{tot}} = t_e + t_i + t_o + t_x, \quad (3.104)$$

and t_{bef} is the number of radiation lengths traversed before scattering

$$t_{\text{bef}} = t_e + t_i. \quad (3.105)$$

We can obtain the desired distribution, $D^{\text{nep}}(E, \omega, \mathcal{X})$, by performing the inverse Laplace transform of $d^{\text{nep}}(E, s, \mathcal{X})$. This is given by the following integral [30]:

$$\begin{aligned} D^{\text{nep}}(E, \omega, \mathcal{X}) &\equiv \mathcal{L}^{-1}[d^{\text{nep}}(E, s, \mathcal{X})] = \frac{1}{2\pi i} \int_{c-i\infty}^{c+i\infty} ds e^{\omega s} d^{\text{nep}}(E, s, \mathcal{X}) \\ &= \frac{H}{2\pi i} \int_{c-i\infty}^{c+i\infty} ds e^{[(\omega-F)s - (T-Gs)\ln(Gs)]}, \end{aligned} \quad (3.106)$$

where

$$H = \Gamma(\delta_1 + 1) \eta^{bt_{\text{bef}}} \left(\frac{\eta G}{E} \right)^T. \quad (3.107)$$

Making the change of variable,

$$u = Gs,$$

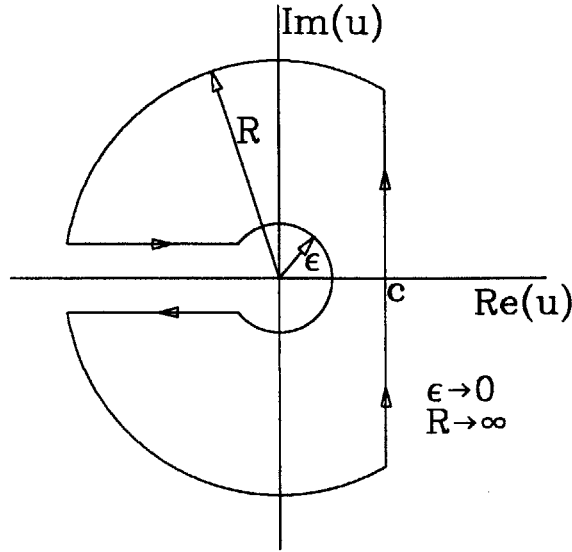


Figure 3-8: Contour used in evaluating the inverse Laplace transform integral.

our expression becomes

$$D^{\text{nep}}(E, \omega, \mathcal{X}) = \frac{H}{G} \Phi(\lambda, T), \quad (3.108)$$

with

$$\Phi(\lambda, T) = \frac{1}{2\pi i} \int_{c-i\infty}^{c+i\infty} du e^{[\lambda u - (T-u) \ln u]}, \quad (3.109)$$

and

$$\lambda = \frac{\omega - F}{G}. \quad (3.110)$$

The integral for $\Phi(\lambda, T)$ can be evaluated by using the contour shown in Figure 3-8 [30]. The result is:

$$\Phi(\lambda, T) = \frac{1}{\pi} \int_0^\infty e^{-[\lambda r + (T+r) \ln r]} \sin \pi(r+T) dr \quad T < 1. \quad (3.111)$$

Notice that when $T = 0$, $\Phi(\lambda, T)$ becomes the Landau $\phi(\lambda)$ distribution (see Equation 3.3):

$$\Phi(\lambda, 0) = \phi(\lambda). \quad (3.112)$$

Therefore, the effect of bremsstrahlung radiation on the line shape is expressed solely through the variable T . Shown in Figure 3-9 is $\Phi(\lambda, T)$ plotted for $T = 0$ and $T = 0.1$. From this figure it can be seen that the overall effect of bremsstrahlung radiation is to increase the strength of the tail, whereas the position of the peak of the distribution, λ_{peak} , is less influenced by it.

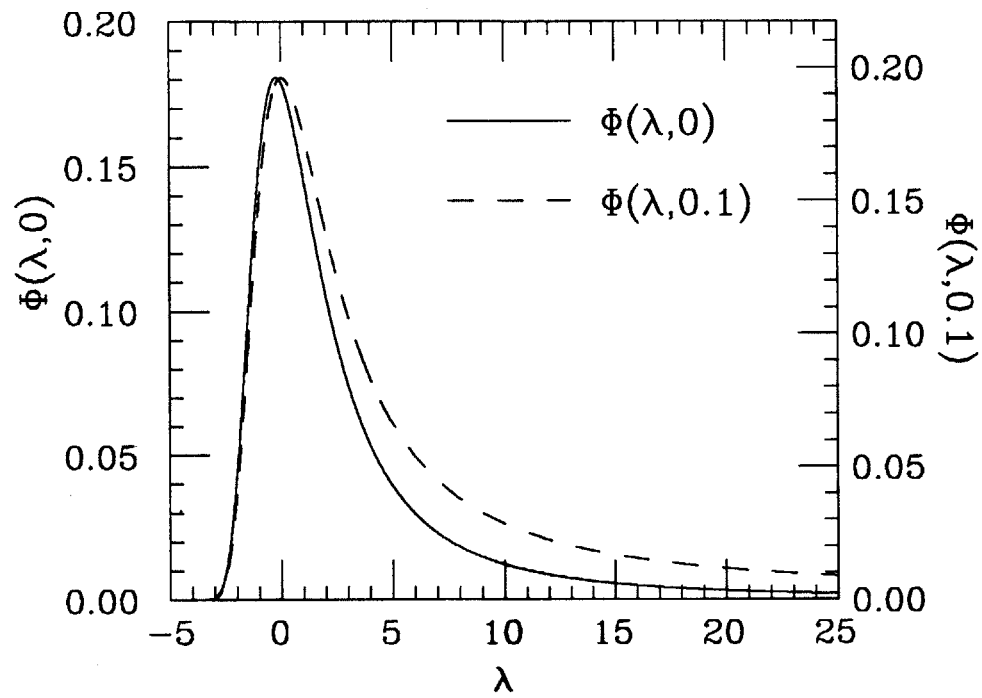


Figure 3-9: Comparing $\Phi(\lambda, T)$ for $T = 0$ and $T = 0.1$.

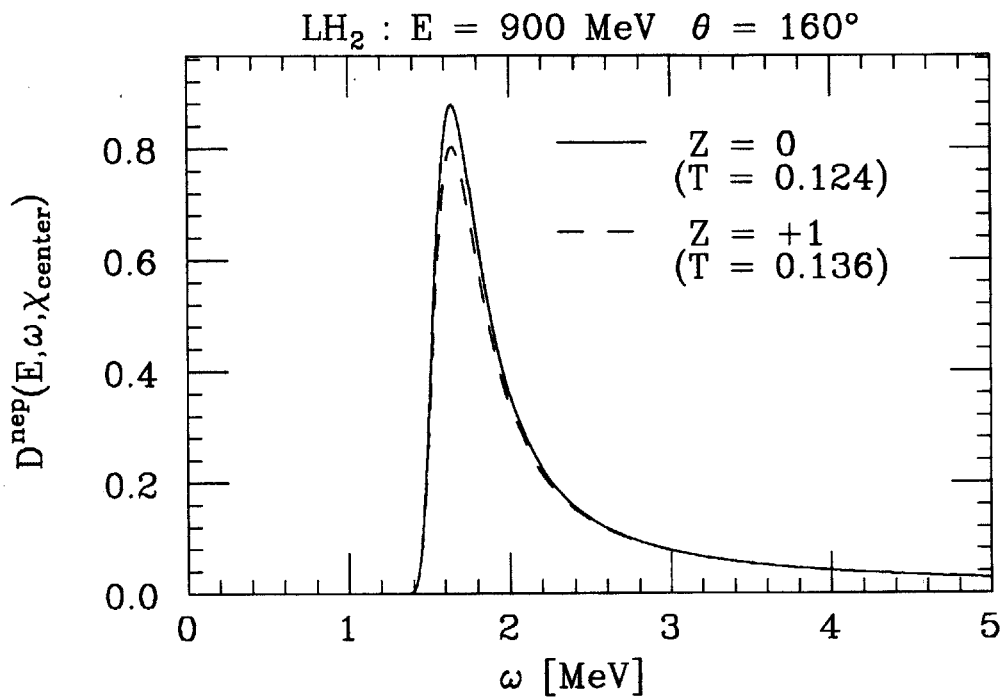


Figure 3-10: The line shape for elastic scattering from liquid hydrogen evaluated for $E = 900$ MeV, $\theta = 160^\circ$, and scattering from the center of the target cell, X_{center} .

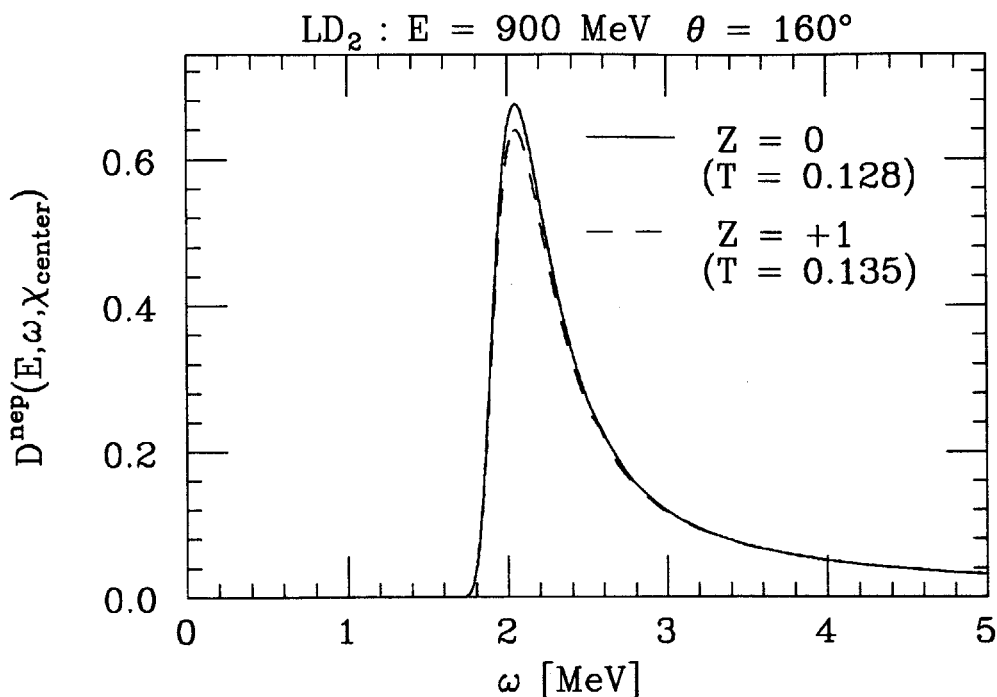


Figure 3-11: The line shape for elastic scattering from liquid deuterium evaluated for $E = 900$ MeV, $\theta = 160^\circ$, and scattering from the center of the target cell, $\mathcal{X}_{\text{center}}$.

The line shapes, $D^{\text{nep}}(E, \omega, \mathcal{X})$, for elastic scattering from liquid hydrogen (LH₂) and liquid deuterium (LD₂) are shown in Figures 3-10 and 3-11. These are evaluated for $E = 900$ MeV, $\theta = 160^\circ$, and scattering from the center of the target cell, $\mathcal{X}_{\text{center}}$, where $x_e = 0.1$, $x_i = 5.0$, $x_o = 3.0$, and $x_x = 0.2$ in centimeters. The solid curves ($Z = 0$) are the line shapes not including radiation from the nuclear current. The dashed curves ($Z = +1$) have this included. From the figures it can be seen that including the nuclear radiation terms puts more strength into the tail region. At the kinematics shown it is roughly a 9% effect for LH₂ and 5% for LD₂.

3.2.2.4 Most Probable Energy Loss

From Equation 3.110 we obtain the following formula for the most probable energy loss, ω_{mp} , which is a function of the parameter T :

$$\omega_{\text{mp}}(T) = F + G\lambda_{\text{peak}}(T), \quad (3.113)$$

where $\lambda_{\text{peak}}(T)$ corresponds to the maximum of the function $\Phi(\lambda, T)$. In Table 3.2, λ_{peak} is given for various values of T . For the case of pure Landau straggling, $T = 0$, we have $\lambda_{\text{peak}}(0) \approx$

T	$\lambda_{\text{peak}} \approx$
0	-0.225
0.05	-0.105
0.10	+0.025
0.15	+0.165
0.20	+0.315
0.25	+0.485
0.30	+0.665
0.35	+0.875
0.40	+1.105

Table 3.2: Values for λ_{peak} corresponding to the maximum of the function $\Phi(\lambda, T)$.

-0.225 since this corresponds to the peak of the Landau ϕ distribution (see Section 3.1.1). For $T \neq 0$, the change in λ_{peak} represents the effect of bremsstrahlung radiation on the most probable energy loss. To evaluate the importance of this effect, consider the following equation relating the pure Landau straggling most probable energy loss with the most probable energy loss for a finite value of T :

$$\omega_{\text{mp}}(T) - \omega_{\text{mp}}(0) = G [\lambda_{\text{peak}}(T) - \lambda_{\text{peak}}(0)] , \quad (3.114)$$

where G is given by Equation 3.102 and has units of energy. The magnitude of this shift is governed by the value of the variable G . Evaluating G for the conditions used in generating Figure 3-11 we find $G \approx 0.1$ MeV and $T = 0.135$. Therefore, the shift from pure Landau straggling is given by:

$$\omega_{\text{mp}}(T) - \omega_{\text{mp}}(0) \approx 0.1 [0.35] \text{ MeV} \approx 0.035 \text{ MeV} .$$

The small value of this shift indicates that to a good approximation the most probable energy loss is still given by Landau straggling alone.

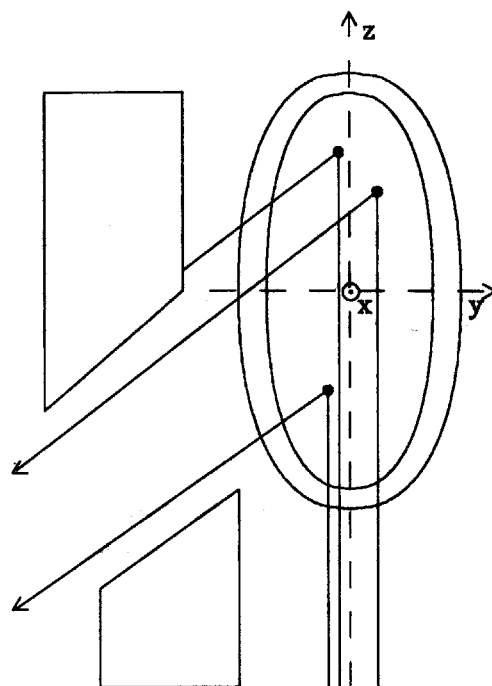


Figure 3-12: The target cell and collimating slits illustrating the target averaging that occurs.

3.2.3 Target-Averaged Elastic Line Shape

In the previous section, the elastic line shape for scattering at a particular point inside the target cell was derived. In this experiment the ELSSY spectrometer that was used to momentum analyze the scattered electrons was not able to reconstruct accurately the scattering point (see Section 4.3.2). Therefore, the experimentally observed elastic line shape represents an average over the target cell weighted with the solid angle acceptance and the incident electron beam spot size. Illustrated in Figure 3-12 is the geometry of the target cell and the collimating slits with three representative scattered electrons. The effect of this target averaging is to broaden the elastic line shape. This broadening is primarily due to the differences in path lengths which yields differences in the most probable energy losses for each of the individual distributions.

At each scattering point the solid angle acceptance, $\Omega(x, y, z)$, is determined not only by the ELSSY slit openings but also the location of the collimating slits. The electron beam spot size, $n_{inc}(x, y)$, describes the vertical and horizontal extent of the beam. The experimentally

observed elastic line shape is given by the following integral (see Section 5.3):

$$D^{\text{TA}}(E, \omega) = \frac{\iiint n_{\text{inc}}(x, y) \Omega(x, y, z) D^{\text{nep}}(E, \omega, x, y, z, \theta) dx dy dz}{\iiint n_{\text{inc}}(x, y) \Omega(x, y, z) dx dy dz}, \quad (3.115)$$

where in D^{nep} the entrance and exit thicknesses, \mathcal{X} , are now expressed as functions of the scattering coordinate (x, y, z) . This target-averaged line shape also has unit normalization since the line shapes, D^{nep} , are normalized to unity.

$$\int_0^{E/\eta} d\omega D^{\text{TA}}(E, \omega) = 1. \quad (3.116)$$

The multiple integral for the target-averaged line shape cannot be evaluated analytically as was done for D^{nep} . Instead, this was evaluated with a Monte Carlo calculation (see Section 4.3.3).

3.3 Approximate Formulas for the Line Shape Near the Elastic Peak

In the previous section we derived the following formula for the line shape near the elastic peak (Equation 3.108)

$$D^{\text{nep}}(E, \omega, \mathcal{X}) = \frac{H}{G} \Phi(\lambda, T),$$

where $\Phi(\lambda, T)$ is given by the inverse Laplace transform integral

$$\Phi(\lambda, T) = \frac{1}{2\pi i} \int_{c-i\infty}^{c+i\infty} du e^{[\lambda u - (T-u) \ln u]},$$

which can be evaluated to give the following real integral

$$\Phi(\lambda, T) = \frac{1}{\pi} \int_0^\infty e^{-[\lambda r + (T+r) \ln r]} \sin \pi(r+T) dr \quad T < 1.$$

In this section approximate formulas for the function $\Phi(\lambda, T)$ are developed for large values of λ , both positive and negative, and small values of T . The goal is to be able to calculate accurately the line shape using these approximations eliminating the need for a numerical evaluation which is more time consuming. For the large positive λ expansion an improvement is made in the

present development that gives accurate results for even moderate values of λ ($\lambda \sim 5$) as well as the tail region where the accuracy is even better.

3.3.1 Large Negative λ Expansion

For large negative values of λ the method describe by Landau [22] will be used to obtain an approximate expression for $\Phi(\lambda, T)$. Rewriting λ as $-|\lambda|$ we then have the following expression for $\Phi(\lambda, T)$ (see Equation 3.109):

$$\Phi(\lambda, T) = \frac{1}{2\pi i} \int_{c-i\infty}^{c+i\infty} du e^{f(u)}, \quad (3.117)$$

where

$$f(u) = (u - T) \ln u - |\lambda|u. \quad (3.118)$$

The saddle point method [31] will be used to evaluate this integral. Expanding the function $f(u)$ in a Taylor series about its extremum, u_o , we obtain:

$$f(u) = f(u_o) + f'(u_o)(u - u_o) + \frac{1}{2}f''(u_o)(u - u_o)^2 + \dots, \quad (3.119)$$

where $f'(u_o) = 0$ gives us the following equation for u_o

$$T = u_o [1 - |\lambda| + \ln u_o], \quad (3.120)$$

and

$$f''(u_o) = (T + u_o)/u_o^2. \quad (3.121)$$

Choosing the line of integration to be along this extremum, u_o , we obtain the following expression:

$$\Phi(\lambda, T) \approx \frac{1}{2\pi i} \int_{u_o-i\infty}^{u_o+i\infty} du \exp[f(u_o) + \frac{1}{2}f''(u_o)(u - u_o)^2]. \quad (3.122)$$

Making the change of variable

$$iw = u - u_o,$$

the integral then becomes

$$\Phi(\lambda, T) \approx \frac{1}{2\pi} \int_{-\infty}^{+\infty} dw \exp[f(u_o) - \frac{1}{2}f''(u_o)w^2], \quad (3.123)$$

which can be evaluated to give the following expression

$$\Phi(\lambda, T) \approx \frac{1}{\sqrt{2\pi}} \frac{e^{f(u_o)}}{\sqrt{f''(u_o)}} \quad \lambda \ll 0. \quad (3.124)$$

This equation can be rewritten in the following form

$$\Phi(\lambda, T) \approx \sqrt{\frac{u_o^2}{2\pi(T + u_o)}} e^{-[u_o - T(1 - \ln u_o)]}, \quad \lambda \ll 0, \quad (3.125)$$

where u_o is a function of λ and given by Equation 3.120. For $T = 0$ we reproduce the Landau [22] result for the large negative λ approximation of $\phi(\lambda)$.

From Equation 3.120 we can conclude the following about the value of u_o : $u_o \geq e^{|\lambda|-1}$ since $T \geq 0$. Therefore, using Equation 3.125 we have the result that $\Phi(\lambda, T)$ vanishes rapidly as $e^{-e^{|\lambda|-1}}$ for $\lambda \ll 0$.

3.3.2 Small T Expansion

For $T \ll 1$, Bergstrom [18] expanded $\Phi(\lambda, T)$ in a power series of T :

$$\Phi(\lambda, T) = \Phi(\lambda, 0) + \Phi'(\lambda, 0)T + \Phi''(\lambda, 0)T^2/2 + \dots \quad (3.126)$$

Using Equation 3.111 for $\Phi(\lambda, T)$ the coefficients can be evaluated and expressed in terms of the Landau ϕ and ψ distributions (see Section 3.1.1). The results are as follows:

$$\Phi(\lambda, 0) = \phi(\lambda), \quad (3.127)$$

$$\Phi'(\lambda, 0) = (\lambda + 1)\phi(\lambda). \quad (3.128)$$

$$\Phi''(\lambda, 0) = -1 + (\lambda + 1)^2\alpha(\lambda) + \psi(\lambda). \quad (3.129)$$

This gives us the following expansion through second order for $\Phi(\lambda, T)$:

$$\Phi(\lambda, T) \approx \phi(\lambda)[1 + T(1 + \lambda)] + [-1 + (\lambda + 1)^2\alpha(\lambda) + \psi(\lambda)]T^2/2. \quad (3.130)$$

Since each coefficient brings in a power of λ , the accuracy of this is limited to values of T and λ such that $\lambda T < 1$.

3.3.3 Large Positive λ Expansion

We seek a large positive λ ($\lambda \gg 0$) expansion for the function $\Phi(\lambda, T)$ which is given by Equation 3.111 and reproduced below:

$$\Phi(\lambda, T) = \frac{1}{\pi} \int_0^{\infty} e^{-[\lambda r + (T+r) \ln r]} \sin \pi(r+T) dr, \quad T < 1.$$

Bergstrom [18] derived such an expansion for $\Phi(\lambda, T)$ by following the method Landau [22] used to obtain a large λ expansion for his straggling function $\phi(\lambda)$. In the present development, a modification is made to this technique that yields more accurate results for smaller values of λ ($\lambda \sim 5$). This modification is to not expand the $\sin \pi(r+T)$ term in a Taylor series about $r = 0$ as was done previously*.

Defining the function $\Upsilon(\lambda, T)$ as follows:

$$\Upsilon(\lambda, T) = \frac{1}{\pi} \int_0^{\infty} e^{-[\lambda r + (T+r) \ln r]} e^{i\pi(r+T)} dr, \quad (3.131)$$

we have the equality

$$\Phi(\lambda, T) = \text{Im} [\Upsilon(\lambda, T)] = (\Upsilon - \Upsilon^*)/2i, \quad (3.132)$$

where $\text{Im}(\Upsilon)$ is the imaginary part of Υ . Making the following transformation[†]

$$\lambda = \kappa + A, \quad (3.133)$$

where A is a parameter to be chosen later, we obtain the following expression:

$$\Upsilon(\lambda, T) = \frac{1}{\pi} e^{i\pi T} \int_0^{\infty} r^{-T} e^{-(\kappa - i\pi)r} e^{-r(\ln r + A)} dr. \quad (3.134)$$

Assuming the parameter A is not too large, for $\lambda \gg 0$ we then also have $\kappa \gg 0$. In this case, the integrand vanishes quickly as $e^{-\kappa r}$ which confines the strength of the integral near the origin.

*Börsch-Supan [32] derived a large λ expansion formula for the Landau function ϕ where he kept $\sin \pi r$ in the first order λ expansion term but then expanded it in the second order term.

[†]Landau actually suggested the transformation $\lambda = \kappa + \ln \kappa + A$. However using this transformation with this new approximation scheme, A contained the term $-\ln \kappa$. Therefore it cancels out in the calculation of λ and is omitted.

Since the exponent, $-r(\ln r + A)$, of the second exponential term is small near the origin, it is useful to expand this term in the following power series:

$$\begin{aligned} e^{-r(\ln r + A)} &= \sum_{n=0}^{\infty} \frac{[-r(\ln r + A)]^n}{n!} \\ &= 1 - r(\ln r + A) + \dots, \end{aligned} \quad (3.135)$$

where an accurate value for the integral can be obtained by using only a few terms in the expansion. Defining the function Υ_n as follows

$$\Upsilon_n(\lambda, T) = \frac{1}{\pi} e^{i\pi T} \int_0^{\infty} r^{-T} e^{-(\kappa - i\pi)r} \frac{[-r(\ln r + A)]^n}{n!} dr, \quad (3.136)$$

we then have

$$\Upsilon = \sum_{n=0}^{\infty} \Upsilon_n = \Upsilon_0 + \Upsilon_1 + \Upsilon_2 + \dots, \quad (3.137)$$

and

$$\Phi(\lambda, T) = \text{Im}(\Upsilon_0) + \text{Im}(\Upsilon_1) + \text{Im}(\Upsilon_2) + \dots. \quad (3.138)$$

The parameter A is chosen to make the second term, $\text{Im}(\Upsilon_1)$, vanish in the expansion leading to a more accurate first order term, $\text{Im}(\Upsilon_0)$.

$$\text{Im}(\Upsilon_1) = 0 \quad \text{defines } A. \quad (3.139)$$

Evaluating Υ_0 we obtain [33]:

$$\begin{aligned} \Upsilon_0 &= \frac{1}{\pi} e^{i\pi T} \int_0^{\infty} r^{-T} e^{-(\kappa - i\pi)r} dr, \\ &= \frac{1}{\pi} \Gamma(1 - T) e^{i\pi T} (\kappa - i\pi)^{T-1}. \end{aligned} \quad (3.140)$$

The complex number, $\kappa - i\pi$, can be rewritten in the more convenient form

$$\begin{aligned} z &= \kappa - i\pi = |z|e^{i\zeta} \\ &= \sqrt{\kappa^2 + \pi^2} e^{i\zeta}, \end{aligned} \quad (3.141)$$

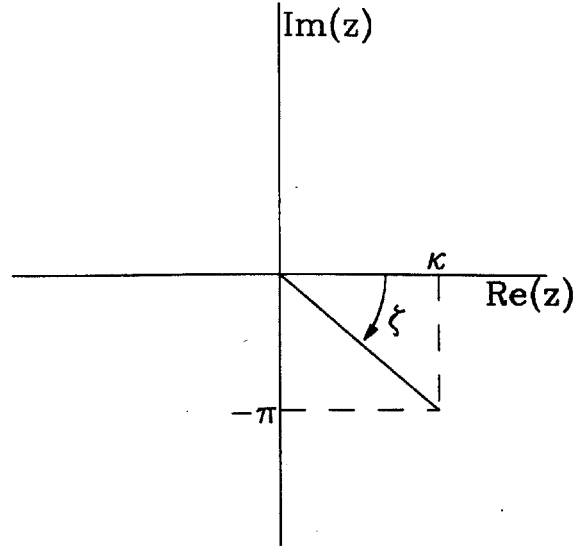


Figure 3-13: The angle, ζ , used in the large positive λ expansion.

where the angle, ζ , is defined in Figure 3-13 and given by

$$\sin \zeta = \frac{-\pi}{\sqrt{\kappa^2 + \pi^2}}. \quad (3.142)$$

The expression for Υ_0 then becomes:

$$\Upsilon_0 = \frac{1}{\pi} \Gamma(1 - T) (\kappa^2 + \pi^2)^{(T-1)/2} e^{i[\pi T + \zeta(T-1)]}. \quad (3.143)$$

Evaluating Υ_1 we obtain [33]:

$$\begin{aligned} \Upsilon_1 &= \frac{1}{\pi} e^{i\pi T} \int_0^\infty r^{-T} e^{-(\kappa - i\pi)r} [-r(\ln r + A)] dr \\ &= -\frac{1}{\pi} \Gamma(2 - T) e^{i\pi T} (\kappa - i\pi)^{T-2} [\psi(2 - T) - \ln(\kappa - i\pi) + A] \end{aligned} \quad (3.144)$$

where $\psi(x)$ is the Digamma function defined by

$$\psi(x) = \frac{d}{dx} \ln \Gamma(x), \quad (3.145)$$

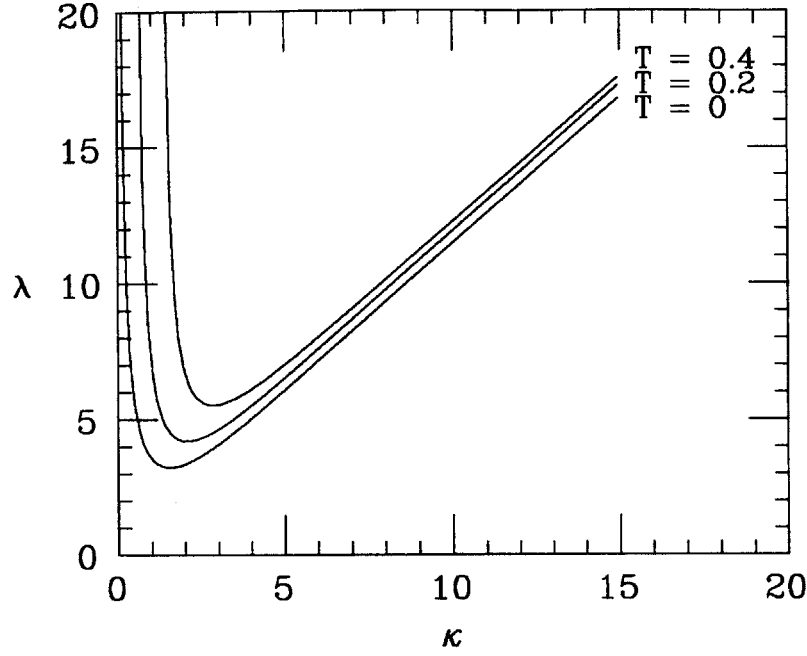


Figure 3-14: Plots of the equation relating λ and κ for $T = 0$, $T = 0.2$, and $T = 0.4$.

not the Landau $\psi(\lambda)$ function. This can be rewritten using Equation 3.141 to express the complex number, $\kappa - i\pi$.

$$\Upsilon_1 = -\frac{1}{\pi} \Gamma(2-T) (\kappa^2 + \pi^2)^{(T-2)/2} e^{i[\pi T + \zeta(T-2)]} [\psi(2-T) - \ln \sqrt{\kappa^2 + \pi^2} + A - i\zeta]. \quad (3.146)$$

Setting $\text{Im}(\Upsilon_1) = 0$, we obtain the formula for the parameter A :

$$A = \zeta \cot[\pi T + \zeta(T-2)] + \frac{1}{2} \ln(\kappa^2 + \pi^2) - \psi(2-T). \quad (3.147)$$

Therefore, the function $\Phi(\lambda, T)$ is approximated by the first order term $\text{Im}(\Upsilon_0)$:

$$\begin{aligned} \Phi(\lambda, T) &\approx \text{Im}(\Upsilon_0) \\ &\approx \frac{1}{\pi} \Gamma(1-T) (\kappa^2 + \pi^2)^{(T-1)/2} \sin[\pi T + \zeta(T-1)], \end{aligned} \quad (3.148)$$

where κ is given by the following equation

$$\lambda = \kappa + \zeta \cot[\pi T + \zeta(T - 2)] + \frac{1}{2} \ln(\kappa^2 + \pi^2) - \psi(2 - T), \quad (3.149)$$

and ζ is given by

$$\zeta = \sin^{-1} \left[\frac{-\pi}{\sqrt{\kappa^2 + \pi^2}} \right]. \quad (3.150)$$

In Figure 3-14 the equation relating λ and κ (Equation 3.149) is plotted for positive values of λ and κ and three values of T . From the figure it can be seen that there exists a lower limit for λ below which no solution to the equation can be found for positive values of κ and above which two positive κ solutions exist. For the later case, the larger value is always chosen for the expansion since the starting assumption was for $\lambda \gg 0$ we also have $\kappa \gg 0$ and A is not too large. This gives us $\lambda \sim \kappa$.

In Table 3.3 the accuracy of this new expansion for $\Phi(\lambda, T)$ is compared with the Landau result [22] for $T = 0$ where the exact values are found by numerical integration. From the table it can be seen that this new expansion is more accurate over a wider range of λ compared with the Landau expansion. Even for finite values of T this expansion remains accurate to within one percent for $\lambda > 5$.

3.3.4 Comparison with Numerical Evaluation

Shown in Figure 3-15 is a plot of the function $\Phi(\lambda, T)$ for $T = 0.2$ and for $\lambda \geq -3$. The solid curve is the result of the numerical evaluation of Equation 3.111 for $\Phi(\lambda, T)$. The squares are the values from the approximate formulas derived in the preceding sections. For $-3 \leq \lambda < 5$ the small T expansion was used to evaluate $\Phi(\lambda, T)$ and for $\lambda \geq 5$ the large positive λ expansion was used. The change at $\lambda = 5$ was chosen to give the best representation of the function $\Phi(\lambda, T)$ since extending either expansion beyond this point would lose the desired accuracy. In the small T expansion the values for the Landau ϕ and ψ distributions came from a lookup table and is presented in Appendix C. For $\lambda < -3$ the function $\Phi(\lambda, T)$ becomes vanishingly small and therefore ignored. The overall accuracy of calculating the function $\Phi(\lambda, T)$ for $T = 0.2$ using these two approximations is better than one percent except for $\lambda \sim -3$ and near the change over, $\lambda \sim 5$, where the accuracy is a few percent. For values of $T < 0.2$ the overall accuracy is even better.

$\Phi(\lambda, T)$ for $T = 0$					
λ	New		Landau		Exact
	Expansion	Accuracy	Expansion	Accuracy	
4.0	5.463×10^{-2}	2.5%	7.257×10^{-2}	36.%	5.327×10^{-2}
5.0	3.915×10^{-2}	-.04%	4.935×10^{-2}	26.%	3.916×10^{-2}
6.0	2.933×10^{-2}	-.77%	3.531×10^{-2}	19.%	2.956×10^{-2}
7.0	2.265×10^{-2}	-.95%	2.631×10^{-2}	15.%	2.287×10^{-2}
8.0	1.791×10^{-2}	-.99%	2.025×10^{-2}	12.%	1.809×10^{-2}
9.0	1.446×10^{-2}	-.93%	1.601×10^{-2}	9.7%	1.459×10^{-2}
10.0	1.188×10^{-2}	-.84%	1.294×10^{-2}	8.0%	1.198×10^{-2}
15.0	5.375×10^{-3}	-.48%	5.604×10^{-3}	3.8%	5.401×10^{-3}
20.0	2.996×10^{-3}	-.30%	3.069×10^{-3}	2.1%	3.005×10^{-3}
25.0	1.892×10^{-3}	-.19%	1.922×10^{-3}	1.4%	1.896×10^{-3}
30.0	1.297×10^{-3}	-.14%	1.311×10^{-3}	.95%	1.299×10^{-3}
40.0	7.139×10^{-4}	-.08%	7.182×10^{-4}	.54%	7.144×10^{-4}
50.0	4.494×10^{-4}	-.05%	4.512×10^{-4}	.34%	4.496×10^{-4}

Table 3.3: Comparison of large positive λ expansions with the exact result for the function $\Phi(\lambda, T)$ when $T = 0$.

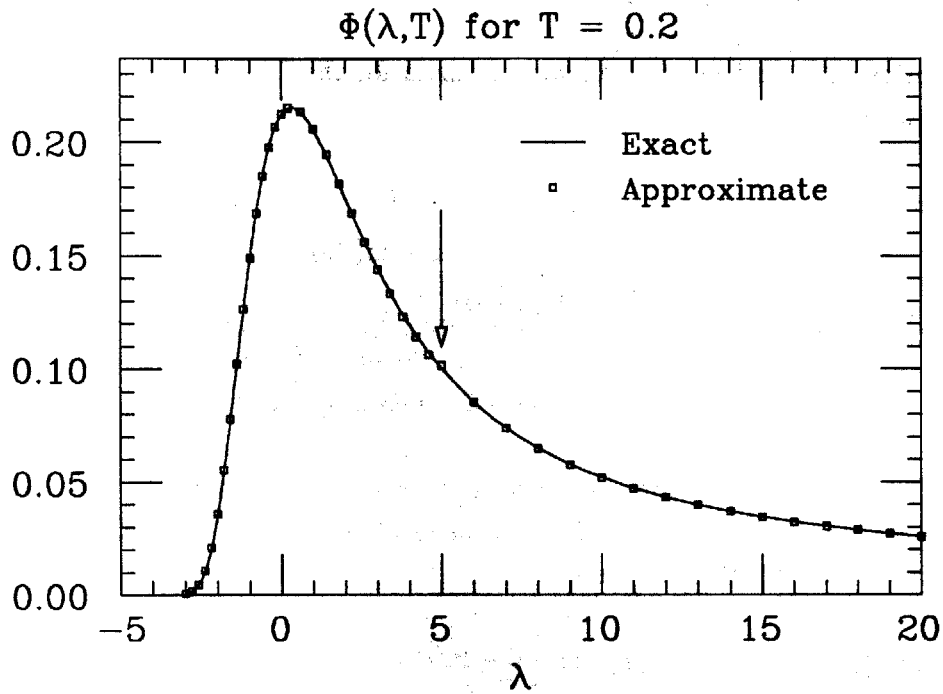


Figure 3-15: Comparison of the numerical evaluation of $\Phi(\lambda, T)$ with the approximate expansion formulas. For $-3 \leq \lambda < 5$ the small T expansion was used and for $\lambda \geq 5$ the large positive λ expansion was used. The arrow indicates where the change occurs.

3.4 Equivalent Radiator Method

In this section we derive an equivalent radiator method [21] for the line shape derived in Section 3.2.2. The method of equivalent radiators is to account for the effect of internal bremsstrahlung by placing additional radiators (equivalent radiators) before and after scattering in the external bremsstrahlung distributions. This then eliminates the need for including the internal bremsstrahlung distribution directly. We derive an expression for the appropriate equivalent radiator by working backwards.

From Equation 3.99 we have the following formula for the Laplace transform of the line shape, $D^{\text{nep}}(E, \omega, \mathcal{X})$:

$$\begin{aligned} d^{\text{nep}}(E, s, \mathcal{X}) = & \exp[-\xi_e s / \eta^2 (1 - C - \ln(\epsilon'_e s / \eta^2))] (Es / \eta^2)^{-bt_e} & (3.151) \\ & \times \exp[-\xi_i s / \eta^2 (1 - C - \ln(\epsilon'_i s / \eta^2))] (Es / \eta^2)^{-bt_i} \\ & \times \Gamma(\delta_1 + 1) (Es / \eta)^{-\delta_1} \\ & \times \exp[-\xi_o s (1 - C - \ln(\epsilon'_o s))] (Es / \eta)^{-bt_o} \\ & \times \exp[-\xi_x s (1 - C - \ln(\epsilon'_x s))] (Es / \eta)^{-bt_x}, \end{aligned}$$

where b_e , b_i , b_o , and b_x have been replaced with the average value, b , shown in Table 3.1. Combining the internal bremsstrahlung term, $\Gamma(\delta_1 + 1) (Es / \eta)^{-\delta_1}$, with the external bremsstrahlung term, $(Es / \eta)^{-bt_o}$, we obtain the following[‡]:

$$\begin{aligned} d^{\text{nep}}(E, s, \mathcal{X}) = & \exp[-\xi_e s / \eta^2 (1 - C - \ln(\epsilon'_e s / \eta^2))] (Es / \eta^2)^{-bt_e} & (3.152) \\ & \times \exp[-\xi_i s / \eta^2 (1 - C - \ln(\epsilon'_i s / \eta^2))] (Es / \eta^2)^{-bt_i} \\ & \times \exp[-\xi_o s (1 - C - \ln(\epsilon'_o s))] \Gamma(\delta_1 + 1) (Es / \eta)^{-b[t_o + \delta_1 / b]} \\ & \times \exp[-\xi_x s (1 - C - \ln(\epsilon'_x s))] (Es / \eta)^{-bt_x}. \end{aligned}$$

To be more suggestive we re-express this formula in terms of the individual Laplace transforms:

[‡]This is arbitrary. The internal bremsstrahlung term could have been grouped elsewhere or divided arbitrarily by any amount before and after scattering.

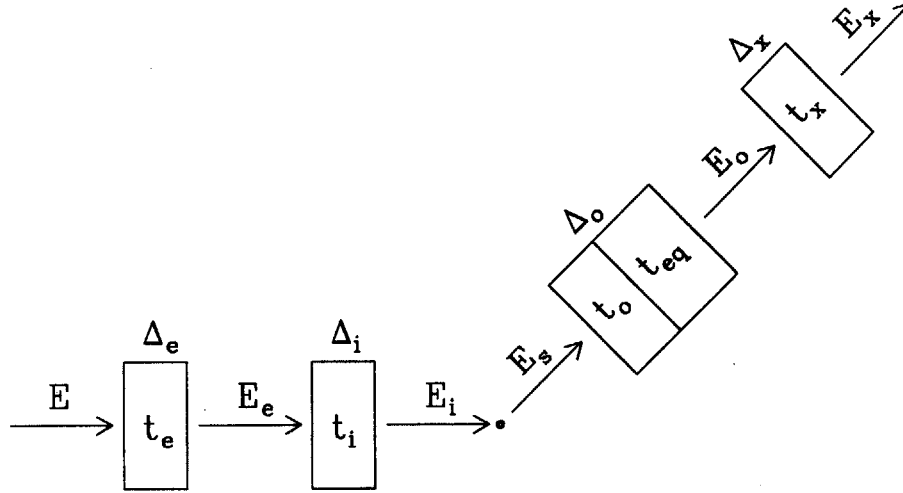


Figure 3-16: Schematic diagram indicating the placement of the equivalent radiator, t_{eq} , used to account for internal bremsstrahlung.

$$\begin{aligned}
 d^{nep}(E, s, \mathcal{X}) &= \Gamma(\delta_1 + 1) & (3.153) \\
 &\times d_I(E, s/\eta^2, x_e) d_{B_{ext}}^{nep}(E, s/\eta^2, t_e) \\
 &\times d_I(E, s/\eta^2, x_i) d_{B_{ext}}^{nep}(E, s/\eta^2, t_i) \\
 &\times d_I(E/\eta, s, x_o) d_{B_{ext}}^{nep}(E/\eta, s, t_o + t_{eq}) \\
 &\times d_I(E/\eta, s, x_x) d_{B_{ext}}^{nep}(E/\eta, s, t_x),
 \end{aligned}$$

where t_{eq} is defined to be the equivalent radiator and given by

$$t_{eq} = b^{-1} \delta_1. \quad (3.154)$$

In the above expression the effect of internal bremsstrahlung has been absorbed into an external bremsstrahlung term except for a multiplicative factor, $\Gamma(\delta_1 + 1)$ which for $\delta_1 \ll 1$, $\Gamma(\delta_1 + 1) \approx 1$. The convolution which corresponds to this is given by the following expression:

$$\begin{aligned}
D^{\text{nep}}(E, \omega, \mathcal{X}) &= \Gamma(\delta_1 + 1) \int_0^{\eta^2 \omega} d\Delta_e \int_0^{\eta^2 \omega - \Delta_e} d\Delta_i \int_0^{\omega - (\Delta_e + \Delta_i)/\eta^2} d\Delta_o \quad (3.155) \\
&\times F_{IB_{\text{ext}}}^{\text{nep}}(E, \Delta_e, t_e) F_{IB_{\text{ext}}}^{\text{nep}}(E, \Delta_i, t_i) \\
&\times \left\{ \int_0^{\Delta_o} D_I(E/\eta, \epsilon, x_o) D_{B_{\text{ext}}}^{\text{nep}}(E/\eta, \Delta_o - \epsilon, t_o + t_{\text{eq}}) d\epsilon \right\} \\
&\times F_{IB_{\text{ext}}}^{\text{nep}}(E/\eta, \omega - \Delta_o - (\Delta_e + \Delta_i)/\eta^2, t_x),
\end{aligned}$$

where Figure 3-16 shows a schematic diagram indicating the energy losses and the placement of the equivalent radiator, t_{eq} . This new expression for $D^{\text{nep}}(E, \omega, \mathcal{X})$ is not obviously equivalent to the one presented in Section 3.2.2 (Equation 3.92). However since their Laplace transforms are the same they are necessarily equal. Therefore, the effect of internal bremsstrahlung has been accounted for by adding an equivalent radiator t_{eq} after scattering as shown in Figure 3-16 and multiplying by the renormalizing factor $\Gamma(\delta_1 + 1)$.

Chapter 4

Monte Carlo Model

With the advent of fast computers, Monte Carlo techniques have become a powerful tool for analyzing and solving problems that would otherwise be very difficult to solve analytically. The basis of these techniques involves first modeling of some problem with a computer code and then “throwing darts” to evaluate it with randomly chosen parameters. The problem could be a complicated integral that needs to be evaluated or a distribution that needs to be simulated. The randomly evaluated functions are summed and histogrammed to obtain the desired result. Since this technique is statistical in nature, many darts will need to be thrown in order to obtain accurate results. For this experiment a Monte Carlo model was written primarily for two reasons: First, to compute the target-averaged elastic line shape presented in Section 3.2.3 and secondly for spectrometer modeling and generating the reverse matrix elements.

This chapter is divided into three sections. The first section describes the computer code that was written to simulate the experiment. The second section deals with generating the reverse matrix elements for the ELSSY spectrometer that were used in this experiment. And finally, section three presents some of the Monte Carlo results.

4.1 Event Modeling

This section describes the methodology used in simulating the experiment. This simulation can be decomposed into many independent stages, and each electron event which is modeled passes

through each of these stages. In Appendix G the main program of the Monte Carlo code is presented.

1. Event Generation

Illustrated in Figure 2-2 is the geometry of the target cell, collimating slits, and ELSSY's solid angle defining slits. This geometry was programed into the Monte Carlo code. Electrons are chosen randomly within a square beam spot size, x and y , to start the simulation. The incident electron energy is given by the following expression,

$$E_{inc} = E_{Beam} + \frac{x E_{Beam}}{100 (x|\delta)_{Beam}}, \quad (4.1)$$

where E_{Beam} is the beam energy and $(x|\delta)_{Beam}$ is the dispersion on target. When the system is fully dispersed matched this is given by the following expression for elastic scattering [5],

$$(x|\delta)_{Beam} = -\frac{1}{\eta} \frac{(x|\delta)_{ELSSY}}{(x|x)_{ELSSY}} = \frac{6.70}{\eta} [\text{cm}/\%], \quad (4.2)$$

where the ELSSY matrix elements are tabulated in Appendix F and η is the recoil factor:

$$\eta = 1 + \frac{2E_{Beam}}{M_t} \sin^2(\beta/2), \quad (4.3)$$

with M_t being the target mass and β the spectrometer angle; For this experiment $\beta = 160^\circ$. The scattering point inside of the target, z , is also chosen.

The polar scattering angle, θ , and azimuthal angle, ϕ , are chosen randomly within the limits $[\theta_{min}, \theta_{max}]$ and $[\phi_{min}, \phi_{max}]$ respectively where these limits are chosen to be larger than the physical acceptance. This defines a solid angle wedge used in the simulation, $\Delta\Omega$, given by the formula

$$\Delta\Omega = \iint \sin \theta d\theta d\phi = \Delta\phi (\cos \theta_{min} - \cos \theta_{max}). \quad (4.4)$$

2. Multiple Scattering

The multiple scattering that occurs in the target is calculated from the entrance and exit thicknesses that the electron passes through. The deviations in the projected scattering angles, θ_p

and ϕ_p , were calculated randomly from a gaussian distribution describing the multiple scattering. This was accomplished using the following method [34]. Given a distribution function, $P(z)$, which is normalized to unity, the variable y defined by the integral,

$$R = \int_{-\infty}^y P(z) dz, \quad (4.5)$$

where R is a random number between (0,1), will be distributed randomly according to the distribution $P(z)$. For multiple scattering the distribution to use is for the polar multiple scattering angle, Θ , and is given by the following approximate formula [12] [35]:

$$P(\Theta)d\Theta = \frac{2\Theta}{\Theta_{\text{rms}}^2} \exp\left(\frac{-\Theta^2}{\Theta_{\text{rms}}^2}\right) d\Theta. \quad (4.6)$$

The root-mean-square polar angle, Θ_{rms} [radians], is given by the formula [12],

$$\Theta_{\text{rms}} = \frac{19.94}{p_{\text{inc}}\beta_{\text{inc}}} Z_{\text{inc}} \sqrt{t_r} \left[1 + \frac{1}{9} \log_{10} t_r \right], \quad (4.7)$$

where

- p_{inc} is the incident momentum [MeV/c],
- β_{inc} is the ratio v/c for the incident particle,
- Z_{inc} is the charge number of the incident particle and
- t_r is the thickness in radiation lengths.

Evaluating the integral,

$$R = \int_0^{\Theta} P(\Theta) d\Theta, \quad (4.8)$$

we obtain the result that Θ will be distributed according to the distribution $P(\Theta)$ when given by the expression,

$$\Theta = \Theta_{\text{rms}} \sqrt{\ln\left(\frac{1}{1-R}\right)}, \quad (4.9)$$

and R is a random number generated between (0,1). The projected multiple scattering angles are given by the following relations [36] [37]:

$$\theta_p^{\text{MS}} = \Theta \sin \alpha, \quad (4.10)$$

$$\phi_p^{\text{MS}} = \Theta \cos \alpha \quad (4.11)$$

where $\alpha = 2\pi R'$ and R' is a new random number. These angles are added to the projected scattering angles to include the effect of multiple scattering in the target. Since the rms multiple scattering angles are of the order of a milliradian and the target depth is less than ten centimeters, the lateral displacement of the incident electron due to multiple scattering is less than one millimeter. This small displacement is ignored in this simulation.

3. Acceptance of the ELSSY Spectrometer

The resultant electron is then checked to make sure that it will enter the ELSSY spectrometer. This involves checking to make sure that it is not obstructed by the collimating slits and passes through the ELSSY solid angle defining slits. If this is true the event continues, otherwise it is discarded and a new event is started.

4. Picking an Energy Loss

We need to assign the electron a final energy, E_f . When simulating the elastic line shape this is obtained from the energy loss distribution, $D^{\text{nep}}(E_{\text{inc}}, \omega, \mathcal{X})$, presented in Chapter 3. Equation 3.62 gives us the final energy expressed as a function of the energy loss variable, ω :

$$E_f = \frac{E_{\text{inc}}}{\eta} - \omega . \quad (4.12)$$

The energy loss, ω , is then chosen randomly according to the energy loss distribution $D^{\text{nep}}(E_{\text{inc}}, \omega, \mathcal{X})$:

$$R = \int_0^\omega D^{\text{nep}}(\omega') d\omega' , \quad (4.13)$$

where R is a random number between (0,1). This integral is evaluated numerically to obtain a solution for the energy loss, ω .

When simulating a white spectrum (assumed uniform), E_f is picked randomly within some chosen limits.

5. Forward Transport Through ELSSY

A magnetic field, B , for the spectrometer is chosen from an experimental data run that we are simulating. The scattered electron is then transported to the focal plane using the matrix elements presented in Appendix F. Before this can be done the electron coordinates at the target need to be converted into the prime coordinate system illustrated in Figure 2-2 and the final momentum, P_f , converted into δ :

$$\delta = 100 \frac{P_f - P_{\text{cent}}}{P_{\text{cent}}} . \quad (4.14)$$

The spectrometer central momentum, P_{cent} , is given by the expression (see Section 2.4.1),

$$P_{\text{cent}} [\text{MeV}] = 66.85 B , \quad (4.15)$$

where B is expressed in kilogauss. Shown in Figure 2-4 is the focal plane coordinate system (X_f, Y_f, Z_f) used to describe the electron in the rear of the spectrometer. The electron is then checked to see if it passes through the active areas of each of the detectors. This is to ensure that this simulated electron would make a real experimental trigger. If this is true the event continues, otherwise it is discarded and a new event is started. The focal plane coordinates, x_f , θ_f , y_f , and ϕ_f are then converted into the coordinates, x_{VDC} , θ_{VDC} , y_{VDC} , and ϕ_{VDC} which are located at the VDC (see Figure 4-1). These are the coordinates that experimentally are measured. The transformation is given by the following formulas:

$$x_{\text{VDC}} = x_f \left[\frac{\cos \theta_f}{\cos(\theta_f + 45^\circ)} \right] , \quad (4.16)$$

$$\theta_{\text{VDC}} = \theta_f , \quad (4.17)$$

$$y_{\text{VDC}} = y_f + x_f \left[\frac{\sin 45^\circ \tan \phi_f \cos \theta_f}{\cos(\theta_f + 45^\circ)} \right] , \quad (4.18)$$

$$\phi_{\text{VDC}} = \phi_f , \quad (4.19)$$

where the VDC is inclined at a nominal angle of 45° . These coordinates are then smeared using the intrinsic detector resolutions for the VDC and HDC's (see Section 2.4.2). The focal plane angles are also smeared due to multiple scattering which occurs while the electron passes through the focal plane detection system.

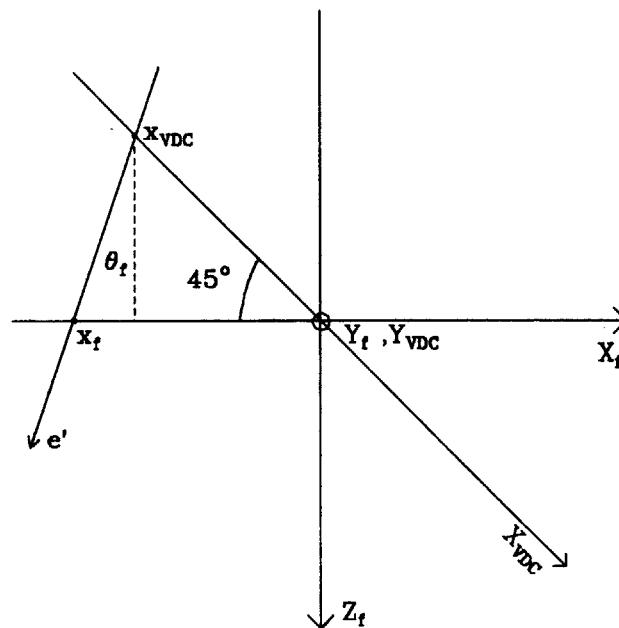


Figure 4-1: The focal plane coordinate system for the forward matrix elements and the VDC coordinate system which is inclined at a nominal angle of 45° .

6. Analyzing The Simulated Event

The final electron is then analyzed and histogrammed as a real data event would be in the data analysis replay software. The target variables, θ_t , y_t , ϕ_t , and δ are reconstructed from x_{VDC} , θ_f , y_{VDC} , and ϕ_f using the reverse matrix elements presented in Appendix F. The true polar scattering angle, θ , is computed from the target angles as follows:

$$\cos \theta = \frac{\tan \phi_t \sin \beta + \cos \beta}{\sqrt{1 + \tan^2 \theta_t + \tan^2 \phi_t}}, \quad (4.20)$$

where β is the ELSSY spectrometer angle and is 160° for this experiment. The final electron energy, E_f , is given by the following formula:

$$E_f \simeq P_f = P_{cent}(1 + \delta). \quad (4.21)$$

The excitation energy, E_{exc} , for the scattered electron is calculated from the expression:

$$E_f = \frac{E_{inc} - E_{exc} - E_{exc}^2/(2M_t)}{\eta}, \quad (4.22)$$

$$\eta = 1 + \frac{2E_{inc}}{M_t} \sin^2(\theta/2), \quad (4.23)$$

where M_t is the target mass and θ is the calculated polar scattering angle. At this point a new electron event is chosen and the process repeated for many simulated events.

4.2 Reverse Matrix Elements

The reverse matrix elements that were used in this Monte Carlo and in the experimental analysis were generated from a ray fitting procedure. This involved having the Monte Carlo write out many electron rays to a file where each ray contained the information of the target and VDC coordinates (see Figure 4-1 and Equations 4.16- 4.19).

An individual Ray: $(x_t, \theta_t, y_t, \phi_t, \delta, x_{VDC}, \theta_f, y_{VDC}, \phi_f)$

A program called RAY [11] used this file and found the best fit coefficients for a polynomial expression of the target variables and δ in terms of the VDC coordinates. Using median-plane symmetry the general polynomial expression can be written as follows [4]:

$$\chi = \sum (\chi | x^i \theta^j y^k \phi^l) x_{\text{VDC}}^i \theta_f^j y_{\text{VDC}}^k \phi_f^l, \quad (4.24)$$

where

$$\chi = \delta, \theta_t \Rightarrow k + l = \text{even}, \quad (4.25)$$

$$= y_t, \phi_t \Rightarrow k + l = \text{odd}. \quad (4.26)$$

These best fit coefficients become the inverse matrix elements which are presented in Appendix F.

4.3 Results

In the following subsections some of the Monte Carlo results are presented. Before interpreting such results one must be aware of possible sources of error in the calculations [34]. Specifically, these calculations depend on random numbers, and computer algorithms for generating random numbers are not perfect. For example, a computer generated random sequence will eventually repeat itself. However, good random number generators will have long periods greater than 10^8 random numbers. All of the Monte Carlo calculations presented in this thesis used less than 10^7 random numbers.

This is not the only problem associated with computer generated random numbers. In fact it is probably of lesser importance. Correlations between computer generated random numbers do exist and can have a large affect on the results. For example, if one plots pairs of computer generated random numbers, these points would tend to lie along a finite number of lines and not fill the space uniformly. Therefore, a calculation that uses two random numbers at a time would not sample the entire region uniformly. As one increases the number of random numbers used at a time in a calculation the problem gets even worse.

The errors associated with such non-randomness was checked for one Monte Carlo calculation: the integrated solid angle. This was evaluated numerically and the result compared

with the Monte Carlo calculation. Both calculations agreed with each other to within one percent (see below). Therefore, any systematic error in the Monte Carlo calculations due to such non-randomicity is expected to be negligible.

4.3.1 Integrated Solid Angle

The integrated solid angle is given by Equation 5.6 and reproduced below,

$$\langle \Omega z \rangle = \frac{\iiint n_{inc}(x, y) \Omega(x, y, z) dx dy dz}{\iint n_{inc}(x, y) dx dy}, \quad (4.27)$$

where $n_{inc}(x, y)$ describes the vertical and horizontal extent of the beam spot size and $\Omega(x, y, z)$ is the solid angle acceptance at each point in the target cell. This is evaluated in the Monte Carlo using the relation,

$$\frac{\iiint n_{inc}(x, y) \Omega(x, y, z) dx dy dz}{\iint n_{inc}(x, y) dx dy} = \left[\frac{N_f}{N_i} \pm \delta \left(\frac{N_f}{N_i} \right) \right] \Delta \Omega, \quad (4.28)$$

where N_f is the number of electrons that were accepted into the ELSSY spectrometer, N_i is the total number of trials, $\Delta \Omega$ is the value of solid angle used in the Monte Carlo (given by Equation 4.4), and $\delta(N_f/N_i)$ is the statistical error in the calculation. The number of electrons that were not accepted into the ELSSY spectrometer, N'_f , is given simply by $N_i - N_f$. When calculating the statistical error, $\delta(N_f/N_i)$, one must be careful since N_f and N_i are correlated variables ($N_i = N_f + N'_f$). The two uncorrelated variables are N_f and N'_f . Therefore, the statistical error is calculated for $N_f/(N_f + N'_f)$ and re-expressed in terms of N_i and N_f . The result is as follows:

$$\delta \left(\frac{N_f}{N_i} \right) = \frac{\sqrt{N_i^2 N_f - N_i N_f^2}}{N_i^2}. \quad (4.29)$$

For this experiment the ELSSY horizontal and vertical slit opening were set at 1.7 and 13.0 inches respectively. These settings did not change over the course of the experiment. The target collimating slit positions also were not changed. Performing the Monte Carlo calculation with these parameters, the integrated solid angle was determined statistically to better than one percent:

$$\langle \Omega z \rangle = 13.5 \pm .1 \text{ [msr-cm]}. \quad (4.30)$$

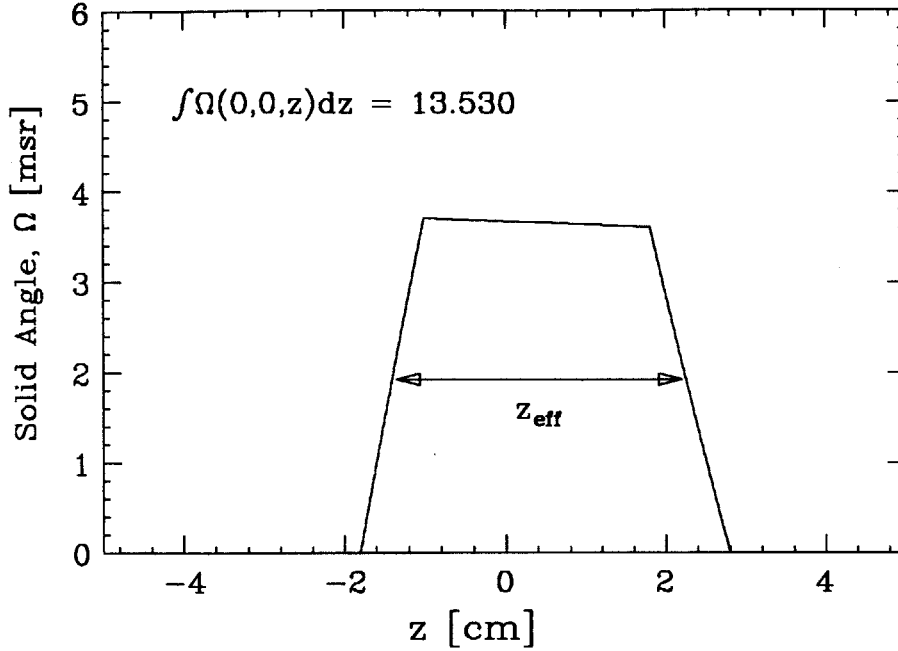


Figure 4-2: The solid angle acceptance function, $\Omega(z)$.

Uncertainties in this calculation due to collimating slit misalignment was estimated to be less than one percent. This result was also checked against a numerical evaluation of the integral, $\int \Omega(0,0,z) dz$. Shown in Figure 4-2 is a plot of the solid angle acceptance function, $\Omega(0,0,z)$. Since the extent of the target along the beam line is the most important part of the integral, this should be approximately equal to the full calculation. This evaluation was found to agree with the Monte Carlo result to better than one percent. The effective target length, z_{eff} , is given by the following relation:

$$z_{\text{eff}} = \frac{\int \Omega(0,0,z) dz}{\Omega(0,0,0)} = 3.69 \text{ [cm]}. \quad (4.31)$$

4.3.2 Scattering Vertex Reconstruction

An important property for any spectrometer is its ability to reconstruct the scattering vertex accurately. This involves not only determining the kinematics at the scattering point, the polar scattering angle θ and the scattered energy E' , but also the scattering position inside the target, y_t (see Figure 2-2, $y_t \equiv y'_t$). The reverse matrix elements presented in Appendix F give us this

reconstruction with the following resolutions: $\sigma_{\theta_t} \sim 1$ mr, $\sigma_{y_t} \sim 0.04$ cm, $\sigma_{\phi_t} \sim 0.1$ mr, and $\sigma_{\delta} \sim 0.01$ %. These resolutions represent the ultimate limit with perfect focal plane measurements of x_f , θ_f , y_f , and ϕ_f . This is not a realistic case since detectors have finite resolutions. Also multiple scattering occurs as the electron traverses the focal plane detection system and affects the measurements.

The reconstruction of δ and ϕ_t depends primarily on the focal plane positions, x_f and y_f respectively. Their resolutions are limited mostly by the accuracy of the focal plane position measurements. However, the reconstruction of y_t and θ_t depends primarily on the focal plane angles, θ_f and ϕ_f respectively, and they are limited mostly by the accuracy of the focal plane angle measurements. Since the ELSSY spectrometer was designed for high resolution work with thin targets, the kinematic reconstruction can still be done accurately from the focal plane coordinate measurements. However, the extended target position, y_t , is poorly determined, mostly due to the multiple scattering at the focal plane which affects the measurement of ϕ_f .

Shown in Figure 4-3 is a Monte Carlo result for reconstructing the target angles, θ_t and ϕ_t . The solid histograms are the actual distribution of target angles chosen in the simulation and the dashed histograms are the reconstructed angles. The resolution obtained in reconstructing θ_t was of the order of 20 milliradians (FWHM) whereas ϕ_t was better than 2 milliradians (FWHM). The poor resolution in θ_t was mainly due to the VDC's intrinsic θ_f resolution. In Figure 4-4 is shown the Monte Carlo result for the target position, y_t . In this case, the poor resolution was primarily due to focal plane multiple scattering which was evaluated with an electron energy of 300 MeV at the focal plane. For energies larger than this the resolution improves proportionally, but even at our highest scattered energy (450 MeV) it was still inadequate for determining target position, y_t . The resolution obtained for δ was of the order of 0.01 %.

4.3.3 Target-Averaged Line Shape, $D^{\text{TA}}(E, \omega)$

The expression for the target-averaged elastic line shape, $D^{\text{TA}}(E, \omega)$, is given by (see Equation 3.115)

$$D^{\text{TA}}(E, \omega) = \frac{\iiint n_{\text{inc}}(x, y) \Omega(x, y, z) D^{\text{nep}}(E, \omega, x, y, z, \theta) dx dy dz}{\iiint n_{\text{inc}}(x, y) \Omega(x, y, z) dx dy dz} \quad (4.32)$$

and was evaluated in the Monte Carlo. Shown in Figure 4-5 is a histogram of the result for LD₂ with an incident electron energy of 900 MeV and scattering angle of 160°. The dashed curve in

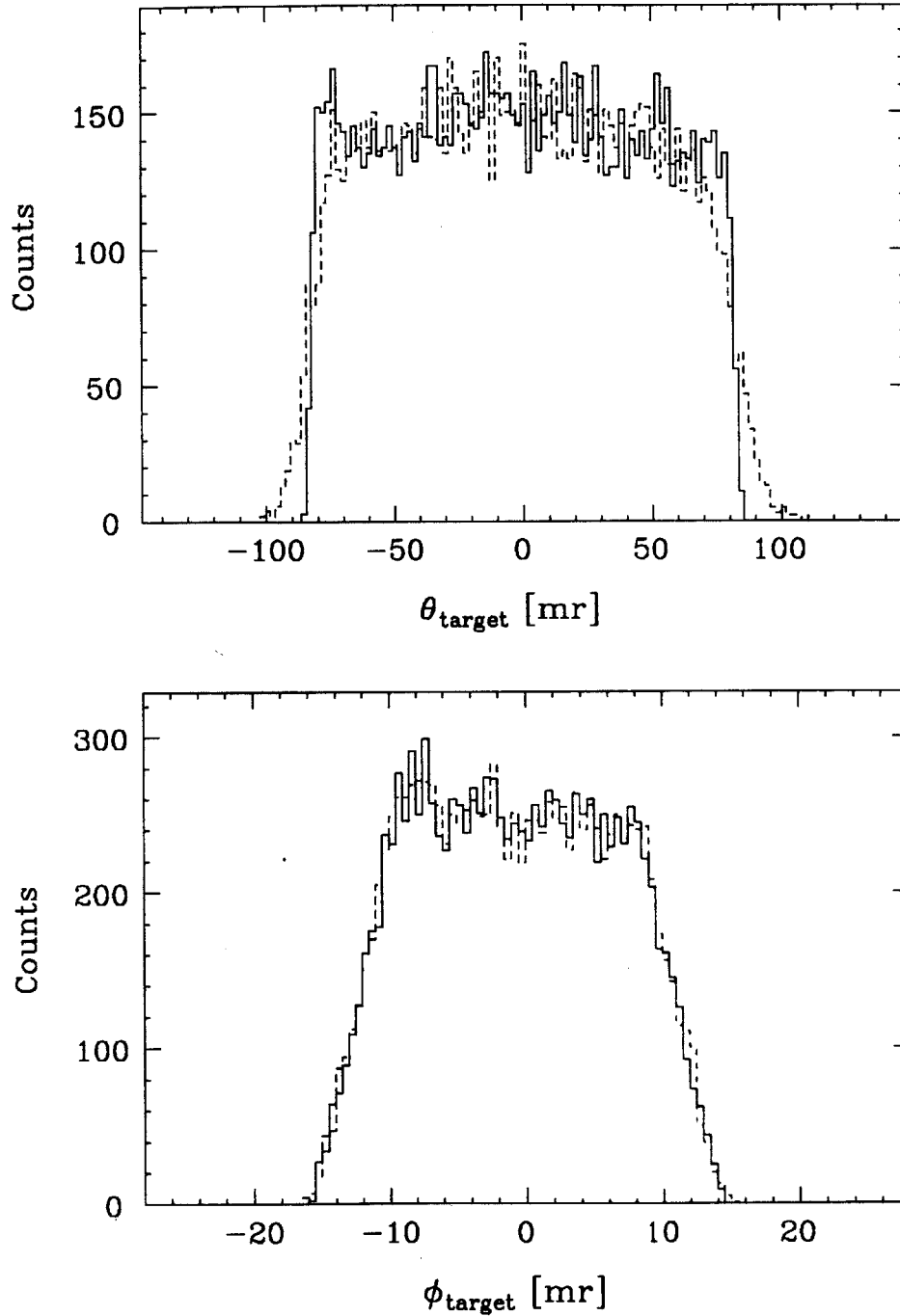


Figure 4-3: The ELSSY target angle reconstructions. The solid histograms are the actual distributions and the dashed histograms are the reconstructions.

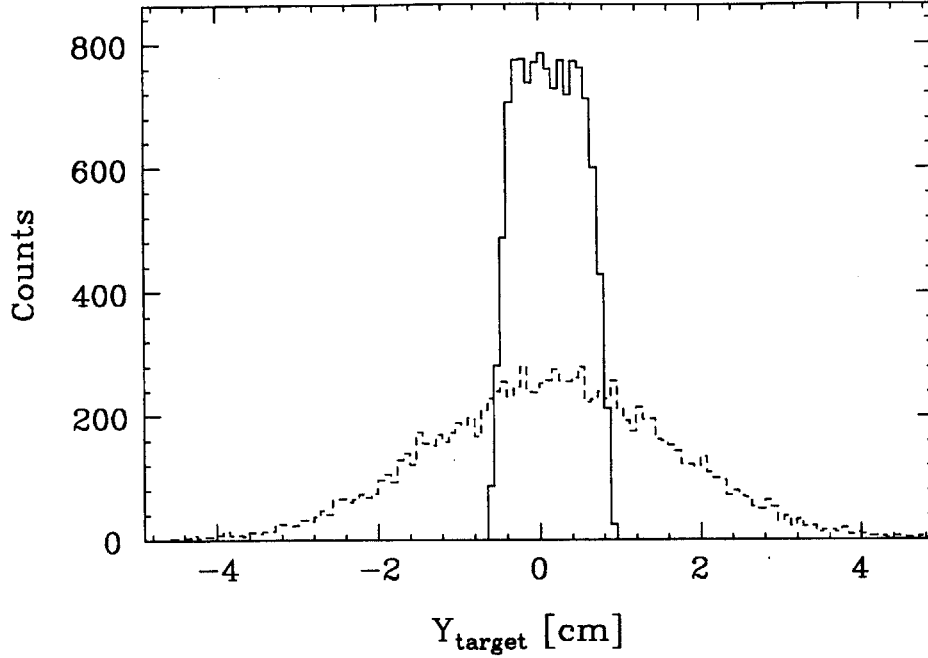


Figure 4-4: The ELSSY target position reconstruction. The solid histogram is the actual distribution and the dashed histogram is the reconstruction.

the figure represents the elastic line shape for scattering at the center of the target cell. Both spectra were centered to place the elastic peak at zero excitation. Notice that the width of the target-averaged line shape is much broader than the individual line shape. This is due to the differences in the most probable energy losses when averaging over the target length. If the ELSSY spectrometer were able to reconstruct the scattering position these differences could be removed and our elastic line shape would be given very closely by the dashed curve in the figure.

4.3.4 Inelastic Radiative Correction Factor, \mathcal{R}_{inel}

As derived in Section 5.3, the inelastic radiative correction factor is given by the following formula,

$$\mathcal{R}_{inel}(\Delta_c) = \left[\int_{-\infty}^{\Delta_c} D^{TA}(E, \Delta) dw \right]^{-1}, \quad (4.33)$$

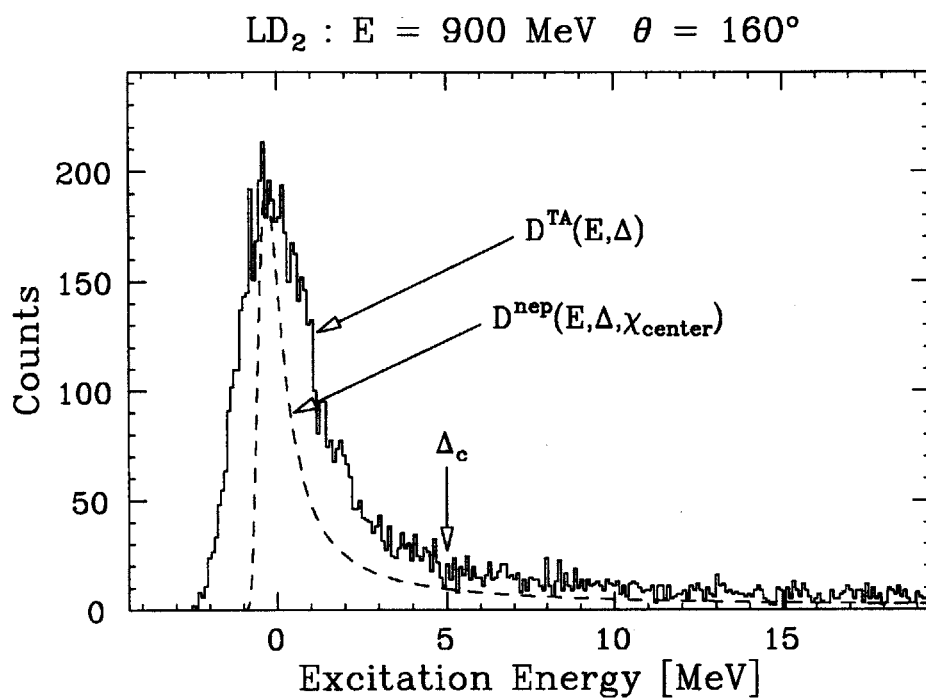


Figure 4-5: Monte Carlo calculation of the target-averaged line shape for elastic scattering from liquid deuterium evaluated for $E = 900 \text{ MeV}$, $\theta = 160^\circ$. The dashed curve is the line shape, D^{nep} , for scattering at the center of the target cell, χ_{center} .

and is a function of the experimental cutoff energy, Δ_c . This correction is evaluated in the Monte Carlo using the following relation,

$$\mathcal{R}_{inel}(\Delta_c) = \left[\int_{-\infty}^{\Delta_c} D^{TA}(E, \Delta) d\Delta \right]^{-1} = \frac{N_{tot}}{N(\Delta_c)} \pm \delta \left(\frac{N_{tot}}{N(\Delta_c)} \right), \quad (4.34)$$

where N_{tot} is the total number of electrons that were accepted into the ELSSY spectrometer and $N(\Delta_c)$ is the total number of electrons up to the cutoff energy; $N(\Delta_c) \leq N_{tot}$. The statistical error in the calculation, $\delta(N_{tot}/N(\Delta_c))$, is given by the following formula:

$$\delta \left(\frac{N_{tot}}{N(\Delta_c)} \right) = \frac{\sqrt{N_{tot}^2 N(\Delta_c) - N_{tot} N^2(\Delta_c)}}{N^2(\Delta_c)}. \quad (4.35)$$

For the case illustrated in Figure 4-5 the result was evaluated statistically to better than one percent,

$$\mathcal{R}_{inel}(\Delta_c = 5 \text{ MeV}) = 1.97 \pm 0.02,$$

where $N_{tot} = 12741$ and $N(\Delta_c = 5 \text{ MeV}) = 6467$.

Chapter 5

Data Analysis

5.1 Overview

The analysis of the data consisted of 3 separate stages. The first stage involved calculating the raw data spectra for scattered electrons from the wire chamber information and particle identification cuts. This is discussed in Chapter 2. The second stage involved writing a Monte Carlo code to simulate the experiment. This was used for modeling spectrometer acceptances and obtaining the elastic line shape and is discussed in Chapter 4. A detailed comparison between the Monte Carlo spectra and the raw experimental data spectra was also made and some of the results are presented in this chapter. The final stage of the analysis consisted of converting the raw data to absolute cross section measurements so that they could be compared with theoretical predictions. This part of the analysis is presented in this chapter.

5.2 Monte Carlo Comparisons

Shown in Figure 5-1 are two plots of θ_{target} versus x_{VDC} . The plot at the top of the page was generated from a quasi-elastic deuterium run with 12 inch (± 76 mr) vertical slits. The other plot was generated from a Monte Carlo simulation of this run. In each case the overall θ_{target} acceptance is consistent with vertical angle acceptance, ± 76 mr, smeared with the θ_f angular resolution of the VDC. As also can be seen in the figure both plots show a reduction in angular acceptance at the ends of the VDC. This reduction implies that the focal plane acceptance is not uniform at the ends of the VDC. This reduction can be understood from the geometry of the focal plane detection system (see Figure 2-4). For example, at the low momentum end it is possible that some values of θ_f could geometrically miss the lead-glass array while triggering the scintillators and gas Cherenkov. In this case the trigger would not constitute a valid electron event. This seemed to be the case for the low momentum end. The reduction at the high momentum end is also due to a similar scenario but involved electron tracks that geometrically missed the scintillators. Since the positions of the focal plane detectors were put into the Monte Carlo code the angular acceptance displayed in the data is also reproduced. The good agreement between the two plots indicates that the θ_{target} angular acceptance was well understood.

One of the primary calculations of the Monte Carlo was the elastic line shape. The calculation is discussed in Section 4.3.3. In Figures 5-2 and 5-3 the Monte Carlo results for the elastic line shapes are compared with data. In both figures the histograms are the experimental data and the solid circles are the results of the Monte Carlo calculation. In Figure 5-2 the comparison is made with the spectrum of 347 MeV electrons scattered from deuterium at 160° . The elastic line shapes agree well. Since the data spectrum contains inelastic strength along with the elastic peak a direct comparison of the tail shapes is not possible for deuterium. In Figure 5-3 the comparison is made with the spectrum of 913 MeV electrons scattered from hydrogen at 160° . Both the elastic peak and tail agree well. Therefore, the Monte Carlo determined elastic line shapes can be subtracted with confidence from the data to yield the threshold inelastic spectra.

5.3 Experimental Cross Sections

Illustrated in Figure 5-4 is our extended target geometry along with an electron scattering within the small volume element, $dx dy dz$. The number of scattering events per unit volume

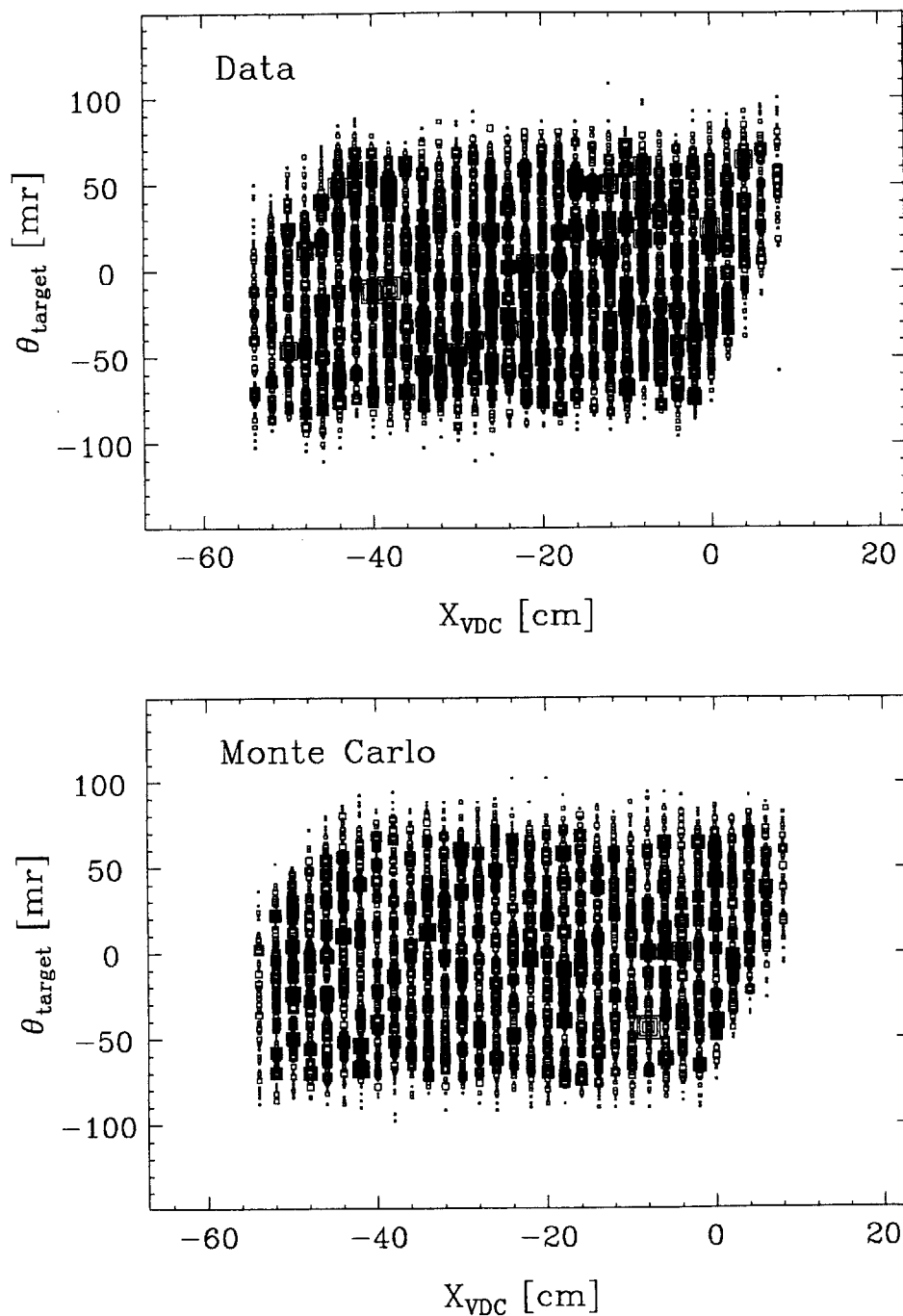


Figure 5-1: The plot θ_{target} versus x_{VDC} for a quasi-elastic data run with 12 inch vertical slits and a similar Monte Carlo run.

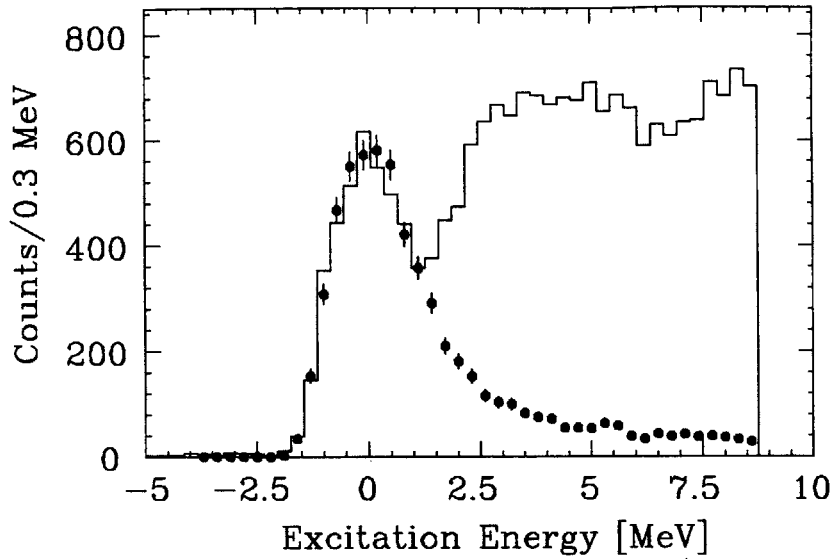


Figure 5-2: Spectrum of 347 MeV scattered electrons from deuterium at 160° . The histogram is the experimental data and the solid circles are the Monte Carlo calculation for the elastic line shape.

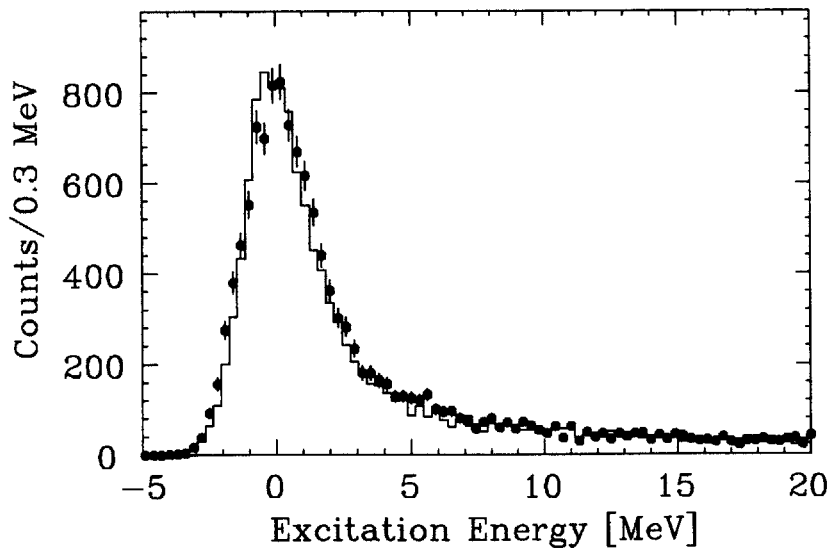


Figure 5-3: Spectrum of 913 MeV scattered electrons from hydrogen at 160° . The histogram is the experimental data and the solid circles are the Monte Carlo calculation for the elastic line shape.

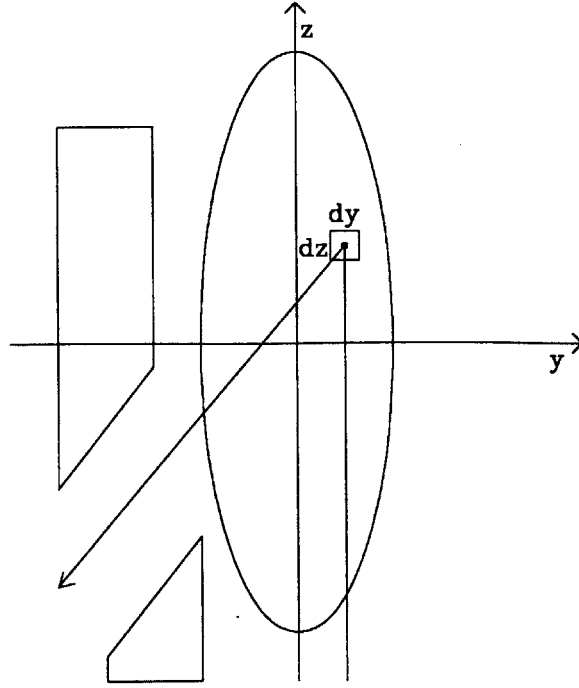


Figure 5-4: Scattering within a small volume element of the extended target.

of the target and per unit scattered energy, $dn_{scat}/d\omega$, is given by the well-known formula,

$$\frac{dn_{scat}}{d\omega} d\omega dx dy dz = \left(\frac{d^2\sigma}{d\Omega d\omega} \right)_{meas.} d\omega \Omega(x, y, z) [n_{inc}(x, y) dx dy] [n_{tar} dz], \quad (5.1)$$

where

$$\omega = E/\eta - E',$$

$\Omega(x, y, z)$ is the solid angle acceptance at x, y, z ,

$n_{inc}(x, y)$ is the number of incident particles per unit area and

n_{tar} is the number of scattering centers per unit target volume.

For elastic scattering the doubly differential measured cross section, $d^2\sigma/d\Omega/d\omega$, is expressed by Equation 3.70 and reproduced here.

$$\left(\frac{d^2\sigma}{d\Omega d\omega} \right)_{meas.} = \left(\frac{d\sigma}{d\Omega} \right)_{1\gamma} e^{\delta_2} D^{nep}(E, \omega, x, y, z, \theta). \quad (5.2)$$

In order to compare with theoretical calculations the one-photon exchange cross section, $d\sigma_{1\gamma}/d\Omega$, needs to be extracted from the measurement.

Experimentally what is measured is the total number of elastic counts, N_{scat} , integrated up to some cutoff energy, ω_c . Mathematically this is expressed as the following,

$$\begin{aligned} N_{scat}(\omega_c) &= \int_0^{\omega_c} d\omega \int dx \int dy \int dz \frac{dn_{scat}}{d\omega} \\ &= n_{tar} \int_0^{\omega_c} d\omega \int dx \int dy \int dz n_{inc}(x, y) \Omega(x, y, z) \left. \frac{d^2\sigma}{d\Omega d\omega} \right)_{\text{meas.}}, \end{aligned} \quad (5.3)$$

where we also have also integrated over the volume of the target. Performing some algebraic manipulations, this equation can be rewritten in a more suitable form:

$$\begin{aligned} N_{scat}(\omega_c) &= \frac{d\sigma}{d\Omega}_{1\gamma} e^{\delta_2} n_{tar} \\ &\times \int_0^{\omega_c} d\omega \frac{\iiint n_{inc}(x, y) \Omega(x, y, z) D^{\text{nep}}(E, \omega, x, y, z, \theta) dx dy dz}{\iiint n_{inc}(x, y) \Omega(x, y, z) dx dy dz} \\ &\times \frac{\iiint n_{inc}(x, y) \Omega(x, y, z) dx dy dz}{\iint n_{inc}(x, y) dx dy} \\ &\times \iint n_{inc}(x, y) dx dy, \end{aligned} \quad (5.4)$$

where Equation 5.2 has been used. In the second line of this equation the ratio,

$$\frac{\iiint n_{inc}(x, y) \Omega(x, y, z) D^{\text{nep}}(E, \omega, x, y, z, \theta) dx dy dz}{\iiint n_{inc}(x, y) \Omega(x, y, z) dx dy dz}, \quad (5.5)$$

is the target-averaged line shape (see Section 3.2.3). This is the line shape that is observed experimentally and is denoted by $D^{\text{TA}}(E, \omega)$. The third line contains the expression for the integrated solid angle,

$$\langle \Omega z \rangle = \frac{\iiint n_{inc}(x, y) \Omega(x, y, z) dx dy dz}{\iint n_{inc}(x, y) dx dy} \quad (5.6)$$

and represents a product between the effective solid angle and the effective target thickness. The last line of the equation is simply total number of incident electrons, N_{inc} .

The one-photon exchange cross section can then be extracted from the measurement by inverting the above formula:

$$\left. \frac{d\sigma}{d\Omega} \right)_{1\gamma} = \frac{N_{scat}(\omega_c)}{n_{tar} \langle \Omega z \rangle N_{inc}} \times \left[e^{-\delta_2} \frac{1}{\int_0^{\omega_c} D^{TA}(E, \omega) d\omega} \right]. \quad (5.7)$$

The term inside of the bracket represents the radiative correction to the measured data. This correction can be separated into two pieces: an elastic radiative correction and an inelastic radiative correction. The elastic radiative correction is given by

$$\mathcal{R}_{el} = e^{-\delta_2} \quad (5.8)$$

and is only a function of the kinematics. This term corrects for the change in the overall magnitude of the measured cross section due to higher order elastic processes (see Figure 3-4). The inelastic radiative correction is given by,

$$\mathcal{R}_{inel}(\omega_c) = \left[\int_0^{\omega_c} D^{TA}(E, \omega) d\omega \right]^{-1} \quad (5.9)$$

and is a function of the experimental energy cutoff, ω_c . This factor corrects the measurement of $N_{scat}(\omega_c)$ for the fraction of events which fell outside of the experimental cutoff energy due to the radiative tail. The product, $N_{scat}(\omega_c) \mathcal{R}_{inel}(\omega_c)$, is the total number of counts under the elastic peak and must be independent of the energy cutoff.

The equation used to extract the elastic cross section measurements can then be written as follows,

$$\left. \frac{d\sigma}{d\Omega} \right)_{1\gamma} = \frac{N_{scat}(\omega_c)}{N_{inc} n_{tar} \langle \Omega z \rangle \varepsilon} \mathcal{R}(\omega_c), \quad (5.10)$$

where

$$\mathcal{R}(\omega_c) = \mathcal{R}_{el} \mathcal{R}_{inel}(\omega_c), \quad (5.11)$$

and the efficiency for detecting electrons, ε , has also been included.

For the threshold inelastic data we would like to compute the cross section averaged over some range in E_{np} . Since previous measurements have averaged the cross sections over 0 to 3 MeV and 0 to 10 MeV in E_{np} the same is done here so that a direct comparison can be made. Two separate methods have been used to accomplish this averaging. The first method is explained below where it is shown explicitly for the 0 to 3 MeV average. The second method

computes this average directly from the radiatively unfolded threshold spectrum. The radiative unfolding procedure is presented in Section 5.4. Both methods used the elastic line shape as the resolution function for the inelastic region. Since the threshold region is close to the elastic peak this is a reasonable approximation. The results from both methods were found to be consistent within statistical errors.

Mathematically, the averaged threshold cross section differential in E_{np} can be written as follows:

$$\left\langle \frac{d^2\sigma}{d\Omega dE_{np}} \right\rangle_{0-3} = \frac{\int_0^3 d^2\sigma/d\Omega/dE_{np} dE_{np}}{\int_0^3 dE_{np}} = \frac{\int_0^3 \sigma(E_{np}) dE_{np}}{\int_0^3 dE_{np}}, \quad (5.12)$$

where for brevity the threshold cross section is written simply as $\sigma(E_{np})$. Rewriting the above expression we obtain the following,

$$\left\langle \frac{d^2\sigma}{d\Omega dE_{np}} \right\rangle_{0-3} = \frac{\int_0^3 \sigma(E_{np}) dE_{np}}{\int_{-\infty}^3 \sigma^{\text{meas}}(E_{np}) dE_{np}} \times \frac{\int_{-\infty}^3 \sigma^{\text{meas}}(E_{np}) dE_{np}}{\int_0^3 dE_{np}}, \quad (5.13)$$

where σ^{meas} is the experimentally measured threshold spectrum. This expression can be interpreted as follows: The first term is the radiative correction factor for the 0 to 3 MeV average and the second factor is the average measured cross section. Using Equation 5.10 this can be written as follows:

$$\left\langle \frac{d^2\sigma}{d\Omega dE_{np}} \right\rangle_{0-3} = \frac{\int_{-\infty}^3 N_{\text{scat}}(E_{np}) dE_{np}}{\int_0^3 dE_{np}} \frac{1}{N_{\text{inc}} n_{\text{tar}} \langle \Omega z \rangle \varepsilon} \mathcal{R}^{0-3}, \quad (5.14)$$

where

$$\mathcal{R}^{0-3} = \frac{\int_0^3 \sigma(E_{np}) dE_{np}}{\int_{-\infty}^3 \sigma^{\text{meas}}(E_{np}) dE_{np}}. \quad (5.15)$$

To convert this into an average threshold cross section differential in the scattered electron energy E' , the following equation was used:

$$\left\langle \frac{d^2\sigma}{d\Omega dE'} \right\rangle_{0-3} = \frac{dE_{np}}{dE'} \left\langle \frac{d^2\sigma}{d\Omega dE_{np}} \right\rangle_{0-3} \simeq \eta \left\langle \frac{d^2\sigma}{d\Omega dE_{np}} \right\rangle_{0-3}, \quad (5.16)$$

where η is the recoil factor.

In the expression for the radiative correction factor the denominator is the total measured strength up to 3 MeV in E_{np} . This can be re-expressed using the relation:

$$\int_{-\infty}^3 \sigma^{\text{meas}}(E_{np}) dE_{np} = \int_0^{\infty} \frac{\sigma(E_{np})}{\mathcal{R}_{el} \mathcal{R}_{inel}(3 - E_{np})} dE_{np}, \quad (5.17)$$

where $\mathcal{R}_{inel}(3 - E_{np}) \geq 1$ and given by Equation 5.9. Therefore, the formula for the radiative correction factor, \mathcal{R}^{0-3} , can be written as follows:

$$\mathcal{R}^{0-3} = \mathcal{R}_{el} \mathcal{R}_{inel}^{0-3} = \mathcal{R}_{el} \times \frac{\int_0^3 \sigma(E_{np}) dE_{np}}{\int_0^{\infty} \sigma(E_{np}) / \mathcal{R}_{inel}(3 - E_{np}) dE_{np}}. \quad (5.18)$$

Unfortunately, this correction factor depends on the shape of the threshold spectrum which is assumed unknown. However, since it appears in the numerator and denominator the dependence is weak and can be tested by calculating the radiative correction factors for different threshold shapes. The results of the radiative unfolding procedure can also be used to test for consistency between the two methods.

5.3.1 Integrated Solid Angle

The integrated solid angle, $\langle \Omega z \rangle$, was evaluated with a Monte Carlo calculation and discussed in Section 4.3.1. The result of the calculation was $\langle \Omega z \rangle = 13.5$ msr-cm. The uncertainty in this was estimated as 1%.

5.3.2 Incident Electron Flux

Two toroid current monitors measure the incident electron beam charge. This system has been discussed in detail elsewhere [38] and is known to be accurate to better than 0.5%.

5.3.3 Target Density

The target temperature was monitored by two diode temperature sensors one mounted above and the other below the target cell. These allowed accurate determination of the liquid temperature during data acquisition. For each energy the average target temperatures were then used

detector	ϵ [%]
VDC	~ 97
HDC1	~ 96
HDC2	~ 96
gas Cer.	> 99.5
Pb glass	> 99.9

Table 5.1: Detector efficiencies.

to obtain target densities. For each energy these differed by no than than 1%. For deuterium the average density was 0.166 g/cm^3 with an uncertainty of 1%. And for hydrogen the average density was 0.073 g/cm^3 with an uncertainty of 1%.

The effects of target boiling were also considered. However, since a dispersed beam was used the power densities achieved at the target cell were never large. Therefore, the effect of target boiling was estimated to be negligible.

5.3.4 Detection Efficiencies

The total detection efficiency for the focal plane detector array is given by a product of the individual detection efficiencies.

$$\epsilon = \epsilon_{\text{VDC}} \epsilon_{\text{HDC1}} \epsilon_{\text{HDC2}} \epsilon_{\text{Scint}} \epsilon_{\text{Cer}} \epsilon_{\text{PbG}} . \quad (5.19)$$

In the off-line analysis of the data each of these efficiencies can be determined except for the scintillator since this was a required part of the trigger. However, this is known to better than 99% efficient. For the rest of the detectors the following method was used.

If we label the VDC as detector A, the HDC1 as B, the HDC2 as C, the gas Cherenkov as D and the Pb glass as E, then the efficiency of the VDC can be expressed as the following ratio,

$$\epsilon_A = \frac{N_{A \cdot B \cdot C \cdot D \cdot E}}{N_{B \cdot C \cdot D \cdot E}} , \quad (5.20)$$

\mathcal{R}_{el}	E_i	θ	target
0.931	347	160°	^2H
0.921	576	160°	^2H
0.916	754	160°	^2H
0.914	817	160°	^2H
0.911	913	160°	^2H
0.900	913	160°	^1H

Table 5.2: \mathcal{R}_{el} radiative correction factors.

where $N_{A.B.C.D.E}$ is the number of events where the VDC and the rest of the detectors had a good signal and $N_{B.C.D.E}$ is taken as the number of good events. Similar expressions hold for the other detectors. Extra tests were used in order to guard against geometric misses contaminating the above ratio. For example, when computing the VDC's efficiency only events which passed through the central lead glass block were considered. Geometrically, any event which passed through this block had to pass through the active area of the VDC (see Figure 2-4). Similarly, when computing the lead-glass array efficiency only events which passed through the center of the VDC were used. The rest of the detectors were not as sensitive to these effects. The efficiencies found for each of the detectors is tabulated in Table 5.1. The total detection efficiency used in the cross section measurements was determined by this method to be 88% with an uncertainty of 2%.

5.3.5 Radiative Correction Factor

For both the elastic and threshold cross section measurements the radiative correction factor was written in the following form:

$$\mathcal{R} = \mathcal{R}_{el} \mathcal{R}_{inel} . \quad (5.21)$$

The first term is only a function of the kinematics and is the same for both measurements. The values that were used in the cross sections are tabulated in Table 5.2. For the elastic cross section measurements the second term is a function of the energy cutoff. This was calculated from the Monte Carlo elastic line shapes, and the method is discussed in Section 4.3.4. For the

threshold measurements the following integral was evaluated in the Monte Carlo:

$$\mathcal{R}_{inel}^{0-3} = \frac{\int_0^3 \sigma(E_{np}) dE_{np}}{\int_0^\infty \sigma(E_{np}) / \mathcal{R}_{inel}(3 - E_{np}) dE_{np}} = \frac{\int_0^3 \sigma(E_{np}) dE_{np}}{\int_{-\infty}^3 \sigma^{\text{meas}}(E_{np}) dE_{np}}. \quad (5.22)$$

The model dependence of this factor enters through the assumed shape for the threshold breakup cross section. However, the dependence is weak since it appears both in the numerator and in the denominator and can be explicitly evaluated. For cases where the radiative unfolding procedure did not yield adequate information for the detailed shape of the threshold cross section spectrum, model dependencies for reasonable shapes were estimated as 5%.

5.4 Radiative Unfolding

The observed spectrum of scattered electrons, σ^{meas} , is related to the true threshold spectrum, σ , by the following convolution,

$$\sigma^{\text{meas}}(E_{np}) = \mathcal{R}_{el} \int_{-\infty}^{\infty} \sigma(\epsilon) R(E_{np} - \epsilon) d\epsilon, \quad (5.23)$$

where \mathcal{R}_{el} is the elastic radiative correction factor which adjusts the overall magnitude of the measurement and $R(\epsilon)$ is the experimental resolution function. For this experiment the resolution was dominated by the energy loss processes in the target. Therefore, the experimental resolution function is given by the elastic line shape $D^{\text{TA}}(E, \Delta)$ (see Section 4.3.3).

$$R(\epsilon) = D^{\text{TA}}(E, \epsilon). \quad (5.24)$$

Defining σ^R as the cross section folded with the resolution function we then have,

$$\sigma^R(E_{np}) = \int_{-\infty}^{\infty} \sigma(\epsilon) R(E_{np} - \epsilon) d\epsilon, \quad (5.25)$$

where $\sigma^{\text{meas}} = \mathcal{R}_{el} \sigma^R$.

It is desirable to unfold the measured spectrum, σ^R , to obtain the true spectrum, σ , allowing a direct comparison with theoretical calculations. Mathematically, this can be done uniquely

and is given by the following expression,

$$\sigma = \mathcal{L}^{-1} \left[\frac{\mathcal{L}[\sigma^R]}{\mathcal{L}[R]} \right]. \quad (5.26)$$

However, the spectrum σ^R is not known exactly but only statistically as presented in the data. This also affects the uniqueness of the unfolded result. In the following paragraphs the iterative method that was used to unfold the threshold data is described.

We seek to find the true spectrum σ which generated the observed spectrum σ^R .

$$\sigma^R(E_{np}) = \int_{-\infty}^{\infty} \sigma(\epsilon) R(E_{np} - \epsilon) d\epsilon. \quad (5.27)$$

We start with an initial guess for the true distribution and label it σ' .

$$\sigma^{R'}(E_{np}) = \int_{-\infty}^{\infty} \sigma'(\epsilon) R(E_{np} - \epsilon) d\epsilon. \quad (5.28)$$

Manipulating the above equation we obtain the following expression:

$$\sigma^R(E_{np}) = \int_{-\infty}^{\infty} \frac{\sigma^R(E_{np})}{\sigma^{R'}(E_{np})} \sigma'(\epsilon) R(E_{np} - \epsilon) d\epsilon. \quad (5.29)$$

Since $R(E_{np} - \epsilon)$ is peaked around $E_{np} \simeq \epsilon$ we can make the following replacement introducing a small error,

$$\sigma^R(E_{np}) \simeq \int_{-\infty}^{\infty} \frac{\sigma^R(\epsilon)}{\sigma^{R'}(\epsilon)} \sigma'(\epsilon) R(E_{np} - \epsilon) d\epsilon. \quad (5.30)$$

Therefore, our next guess for the true spectrum is given by the expression,

$$\sigma''(\epsilon) = F(\epsilon) \sigma'(\epsilon), \quad (5.31)$$

where the correction factor, F , is given by

$$F(\epsilon) = \frac{\sigma^R(\epsilon)}{\sigma^{R'}(\epsilon)}. \quad (5.32)$$

This procedure is repeated until the folded spectrum, $\sigma^{R'}$, becomes statistically equivalent to the data spectrum, σ^R . When this is the case the result for the unfolded spectrum becomes σ' .

One must now examine the question of the uniqueness of this result. Mathematically, unfolding is a unique transformation. However, the spectrum we are unfolding is only statistically known. Therefore, the question of uniqueness becomes the following statement: Any function \mathcal{N} which when added to the unfolded result σ' and then folded with the resolution function whose effect does not statistically change the result is also a statistically acceptable solution. Stated another way, given any function \mathcal{N} which when folded with the resolution is statistically equivalent to zero, the function $\sigma' + \mathcal{N}$ will also be a solution. Mathematically, this can be expressed as follows:

$$\int_{-\infty}^{\infty} \mathcal{N}(\epsilon) R(E_{np} - \epsilon) d\epsilon \stackrel{\text{stat}}{\equiv} 0, \quad (5.33)$$

where we also have

$$\int_{-\infty}^{\infty} \mathcal{N}(\epsilon) d\epsilon \stackrel{\text{stat}}{\equiv} 0. \quad (5.34)$$

Therefore, these functions also have the property of not affecting the integrated result. A class of functions which have these properties are periodic functions. For example, a square wave whose period is smaller than the width of the resolution function could satisfy these requirements. The space of these functions is related to the width of the resolution function. For example, the broader the resolution width the larger the period for these functions can become. The resolution widths in this experiment were of the order of 2 MeV FWHM. Therefore, when unfolding the threshold spectrum with bin widths less than 2 MeV many statistically acceptable solutions exist. However, the addition of these solutions make the unfolded result appear jittery. Since we expect the threshold spectrum to be a smoothly varying function we can eliminate such solutions on physical grounds.

In practice the iterative method as described above yields unfolded spectra with unreasonably large amounts of jitter in the data points. This occurs because the statistical jitter in the original data spectrum gets magnified every iteration when the next guess is calculated (see Equation 5.31). Although these jittery spectra are solutions, on physical grounds we reject them. The following additions [39] were then made to the iterative procedure to yield spectra free from excessive jitter.

The correction factor $F(\epsilon_i)$ was smoothed before it was used to obtain the next guess [40]. (The index i labels the channel number.) This is reasonable since we expect the ratio to be a smoothly varying function. Then the smoothed correction factor $F^{sm}(\epsilon_i)$ was only applied to the spectrum $\sigma'(\epsilon_i)$ if it was deemed statistically significant. Otherwise, $F^{sm}(\epsilon_i)$ was set equal to one. The criterion used to determine if it were statistically significant comes from an application

of Chauvenet's criterion [41]. For a given channel the number of standard deviations, z_i , the folded spectrum $\sigma^{R'}(\epsilon_i)$ differed from the data spectrum $\sigma^R(\epsilon_i)$ was calculated.

$$z_i = \left| \frac{\sigma^R(\epsilon_i) - \sigma^{R'}(\epsilon_i)}{\delta\sigma^R(\epsilon_i)} \right|. \quad (5.35)$$

Based on a normal distribution we expect to see $[1 - \text{erf}(z_i/\sqrt{2})]N$ data points to be z_i or more away where N is the total number of data points in the spectrum. If this amount is less than one half the number actually observed then it is considered to be statistically significant. Mathematically, this is expressed as

$$[1 - \text{erf}(z_i/\sqrt{2})]N < \frac{1}{2} \sum_{j=1}^N u(z_j - z_i), \quad (5.36)$$

where $u(z)$ is the unit step function and $u(0) = 1$. Solving for z_i we obtain the following criterion for the difference between the folded spectrum and the data spectrum in the i 'th channel to be statistically significant.

$$z_i > \sqrt{2} \text{erf}^{-1} \left\{ 1 - \frac{1}{2N} \sum_{j=1}^N u(z_j - z_i) \right\}. \quad (5.37)$$

When this is true the smoothed correction factor is applied.

For the initial guess a flat distribution was chosen which started at the breakup threshold. This ensured that the following iterative guesses would also start abruptly at the breakup threshold (see Equation 5.31). This is reasonable since the true inelastic spectrum is expected to start at the breakup threshold.

The iterative procedure converged when the number of channels that were deemed statistically significant was either zero or did not change from the previous iteration. A reduced χ^2 was also calculated:

$$\chi_r^2 = \frac{1}{N} \sum_{j=1}^N \left(\frac{\sigma^R(\epsilon_j) - \sigma^{R'}(\epsilon_j)}{\delta\sigma^R(\epsilon_j)} \right)^2. \quad (5.38)$$

In all cases no more than 4 iterations were needed for convergence with reduced χ^2 of the order of one.

In Figure 5-5 the affect of including smoothing and Chauvenet's criterion in the unfolding procedure is shown explicitly for the 347 MeV deuterium threshold data. The first plot is the

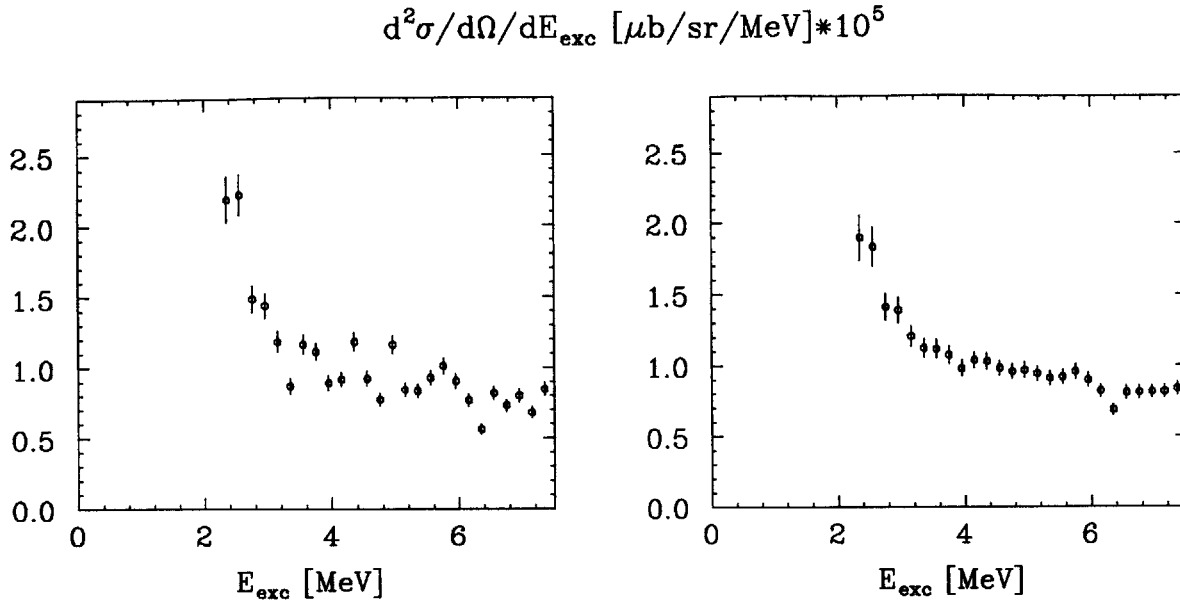


Figure 5-5: Comparison of two methods used to unfold the 347 MeV threshold data. The first plot was generated without using either smoothing or Chauvenet's criterion. The second plot included these additions and is the final result.

unfolded result without these additions. This was stopped after 3 iterations when χ_r^2 dropped below one. This appears unacceptably jittery. The second plot was generated with these additions and is the final result.

5.5 Beam Energy

The electron beam energy was given by the Beck calibration formula, [42]

$$E_{\text{true}} = \frac{E_{\text{nom}}}{0.987 + E_{\text{nom}}(5.6 \times 10^{-5})}, \quad (5.39)$$

where E_{nom} is the beam switchyard nominal value. Based on a more recent energy calibration [43] the accuracy of this formula was taken as 1%.

E [MeV]	$(\frac{d\sigma}{d\Omega})_{el}$	$\langle \frac{d^2\sigma}{d\Omega dE'} \rangle_{0-3}$	$\langle \frac{d^2\sigma}{d\Omega dE'} \rangle_{0-10}$
347	4%	4%	
576	9%	9%	
754	14%	14%	4%
820	30%	30%	10%
913	4%	4%	1%

Table 5.3: Estimated systematic errors.

5.6 Systematic Errors

The cross section formulas for the elastic and threshold measurements are given by Equations 5.10 and 5.14, respectively. The estimated systematic error in each of the cross section measurements was determined from the individual systematic uncertainties in each of the factors that gives the cross section. For this experiment the largest source of systematic error was due to the uncertainty in the elastic peak positions which was caused by the poor knowledge of the beam energy. This uncertainty affected the measured cross sections by introducing an uncertainty into the cutoff energies associated with the radiative correction factors. For energies where the statistics were poor and a well-defined elastic peak did not exist, this represented a large error. However, at the highest energy elastic scattering data from hydrogen was also measured, and this allowed an accurate calibration for the deuterium elastic peak position at that energy. Another source of systematic error was our uncertainty in target thickness due to target boiling effects. The estimated systematic errors associated with each measurement and energy are tabulated in Table 5.3. These errors are smaller than the statistical errors involved except at the lowest energy.

Chapter 6

Results and Discussion

In this chapter the unfolded threshold spectra and cross sections average over 0 to 3 and 0 to 10 MeV are presented. Measurements of elastic electron-deuteron scattering and electron-proton scattering (the latter at 913 MeV only) are also presented. The average threshold measurements are plotted versus Q^2 and compared with previous measurements as well as various theoretical calculations. The unfolded spectra are also compared with theoretical predictions of the threshold breakup spectrum.

6.1 Results

In Table 6.1 all the measured cross sections of this thesis work are presented. The table contains the threshold cross sections averaged over 0 to 3 and 0 to 10 MeV as well as the measurements of elastic scattering from deuterium and hydrogen. The quoted error bars are statistical only. In Table 5.3 the estimated systematic errors for the elastic and threshold measurements are given. Tables for the unfolded threshold differential cross sections are given in Appendix H. The elastic measurements for deuterium and hydrogen were found to be in agreement with existing data [44] [45] [46] [47] [48]. The averaged threshold cross sections also agree well with the Saclay data ($E_{np} = \langle 0 - 3 \rangle$) [1] and the SLAC data ($E_{np} = \langle 0 - 10 \rangle$) [2] in the region of overlap. These data are plotted along with the new measurements of this thesis in the next section.

E MeV	target	Q_μ^2 fm^{-2}	$(\frac{d\sigma}{d\Omega})_{el}$ $\mu\text{b/sr}$	$\langle \frac{d^2\sigma}{d\Omega dE'} \rangle_{0-3}$ $\mu\text{b/sr/MeV}$	$\langle \frac{d^2\sigma}{d\Omega dE'} \rangle_{0-10}$ $\mu\text{b/sr/MeV}$
347	^2H	8.75	$1.71 \pm 0.03 \times 10^{-5}$	$1.14 \pm 0.02 \times 10^{-5}$	
576	^2H	20.6	$2.02 \pm 0.18 \times 10^{-7}$	$4.27 \pm 0.75 \times 10^{-8}$	
754	^2H	31.7	$1.53 \pm 0.26 \times 10^{-8}$	$4.52 \pm 1.34 \times 10^{-9}$	$5.09 \pm 0.61 \times 10^{-9}$
820	^2H	36.1	$3.78 \pm 1.26 \times 10^{-9}$	$2.07 \pm 0.83 \times 10^{-9}$	$2.65 \pm 0.43 \times 10^{-9}$
913	^2H	42.6	$2.00 \pm 1.16 \times 10^{-9}$	$2.30 \pm 1.06 \times 10^{-9}$	$2.05 \pm 0.46 \times 10^{-9}$
913	^1H	28.7	$2.40 \pm 0.03 \times 10^{-4}$		

Table 6.1: Experimental cross sections measured in the thesis.

6.2 Comparison with Existing Data

In Figure 6-1 the new measurements are plotted along with existing data as a function of Q^2 . The open squares are data from Saclay average over $E_{np} = 0 - 3$ MeV [1] and the open diamonds from SLAC averaged over $E_{np} = 0 - 10$ MeV [2]. We present our data also averaged over both ranges for direct comparison. The open circles are the data averaged over $E_{np} = 0 - 3$ MeV and the crosses are the data averaged over $E_{np} = 0 - 10$ MeV. As can be seen in the figure the agreement between the three data sets is good. The two lowest Bates Q^2 points averaged over $E_{np} = 0 - 3$ MeV Bates agree quite well with the Saclay measurement averaged over the same interval. The three highest Bates Q^2 points averaged over $E_{np} = 0 - 10$ MeV also agree well with the SLAC measurement averaged over this interval. The three highest Q^2 points are also plotted averaged over $E_{np} = 0 - 3$ MeV. As can be seen in the figure there is little difference between the results for the two averages. This indicates that the breakup threshold spectrum must on the average remain relatively flat up to E_{np} of 10 MeV at these three values of Q^2 .

6.3 Comparison with Theory

In Figure 6-2 the data averages over $E_{np} = 0 - 3$ MeV are plotted against nonrelativistic Paris potential [49] calculations evaluated at $E_{np} = 1.5$ MeV [50]. These calculations include contributions to the cross section up to $L = 4$ in the final n-p scattering states. The open squares represent data from Saclay [1] and the open circles represent the data presented in

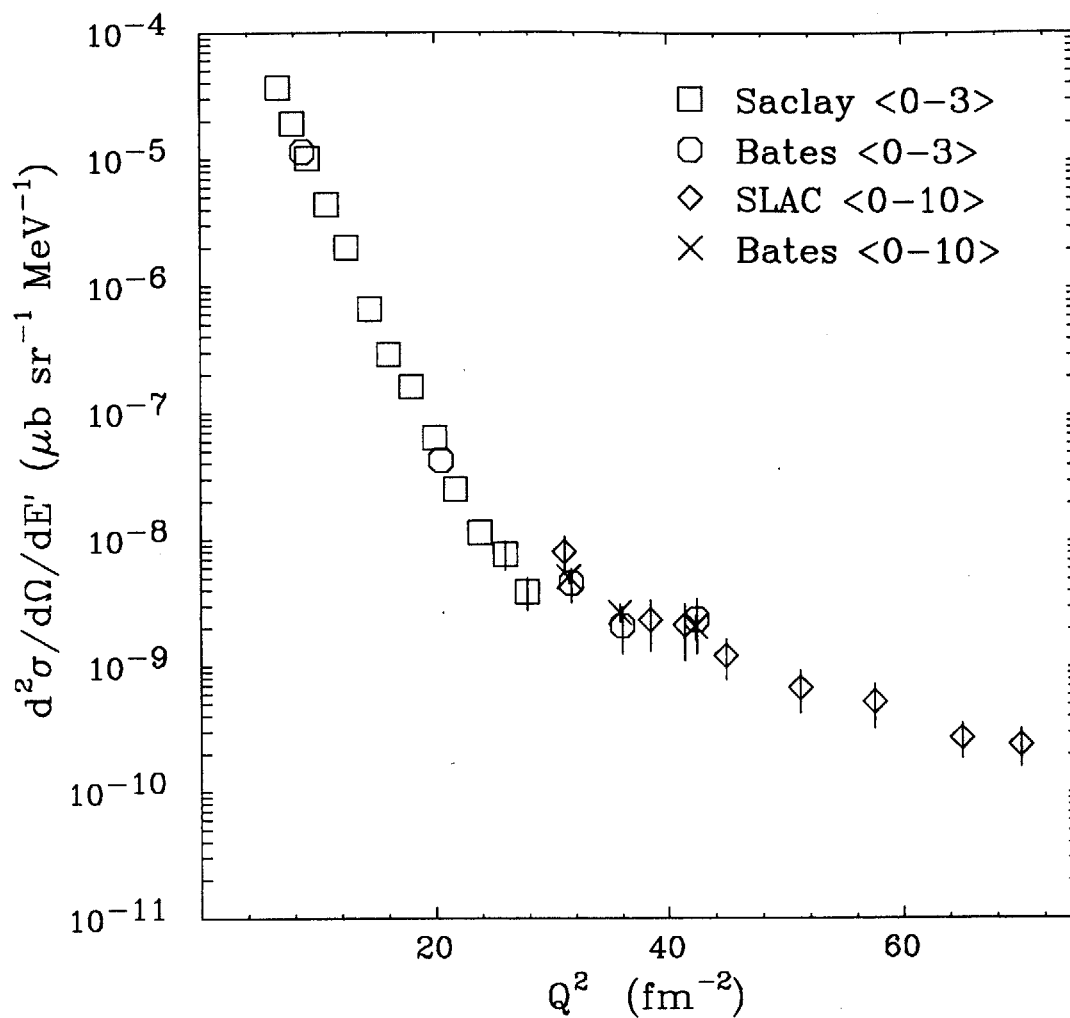


Figure 6-1: Comparison of the new threshold electrodisintegration cross section measurements with existing data. The open squares represent data from Saclay that were averaged over $E_{np} = 0 - 3$ MeV [1]. The open diamonds represent data from SLAC that were averaged $E_{np} = 0 - 10$ MeV [2].

this thesis. The dotted curve is the impulse approximation and the other four curves represent MEC calculations. Since there is theoretical uncertainty (in a nonrelativistic framework) as to the choice of the appropriate MEC form factor [51] [50] [52], the isovector Sachs G_E^V or the isovector Dirac F_1^V , both are plotted for comparison with two different electromagnetic nucleon form factors: the dipole (D) and Gari-Krümpelmann (GK) parameterization. This ambiguity can be thought of as the systematic error in the theoretical calculations since a fully relativistic theory is not yet available.

As can be seen in figure the impulse approximation disagrees with the trend of the data for the range of Q^2 shown. Including MEC brings the theoretical predictions in closer agreement with the data. The most dramatic effect is the filling in of the deep minimum predicted by the IA. At Higher Q^2 the MEC calculations qualitatively describe the trend of the data where the best overall agreement in these calculations comes from using the isovector Dirac form factor F_1^V for the MEC. This should not be interpreted too seriously since calculations with different nucleon-nucleon potentials can reverse the situation [53]. The most interesting trend in the data is the definite change in slope at $Q^2 \sim 27 \text{ fm}^{-2}$. This was also seen in the SLAC data although with poorer energy resolution ($E_{np} = \langle 0 - 10 \rangle \text{ MeV}$).

In Figure 6-3 the SLAC data are included along with the present measurements and the Saclay results. Where the present measurements overlapped with the SLAC data the cross sections were averaged over $E_{np} = \langle 0 - 10 \rangle \text{ MeV}$ and represented by crosses in the figure. The theoretical curves are nonrelativistic Argonne v_{14} potential [54] calculations averaged over E_{np} to allow a direct comparison with experiment [55]. The break in the figure indicates the differences between the two theoretical averages. Below 30 fm^{-2} the curves were averaged over $E_{np} = 0 - 3 \text{ MeV}$ and above 30 fm^{-2} $E_{np} = 0 - 10 \text{ MeV}$. The apparent discontinuities in the curves reflect the differences between the two averaging. The SLAC data show the trend of a change in slope as mentioned above for the threshold cross sections up to 72 fm^{-2} . The MEC calculations agree with the trend of the data up to the highest Q^2 shown. Again in these calculations using F_1^V instead of G_E^V in the MEC gives a substantially better fit to the data.

For Q^2 above 40 fm^{-2} the spatial resolution of the virtual photon exchanged becomes of the order of the size of a nucleon, $\sim 1 \text{ fm}$. Therefore, the question of the validity of the meson-exchange picture in this regime becomes important since the description of the nucleon-nucleon interaction might give way to the more fundamental description in terms of quarks and gluons. The point at which quark degrees of freedom become important is not yet known, and these degrees of freedom are also suppressed by the nuclear hard core. This inhibits short range interactions between the nucleons. However, hybrid quark-hadron model calculations have

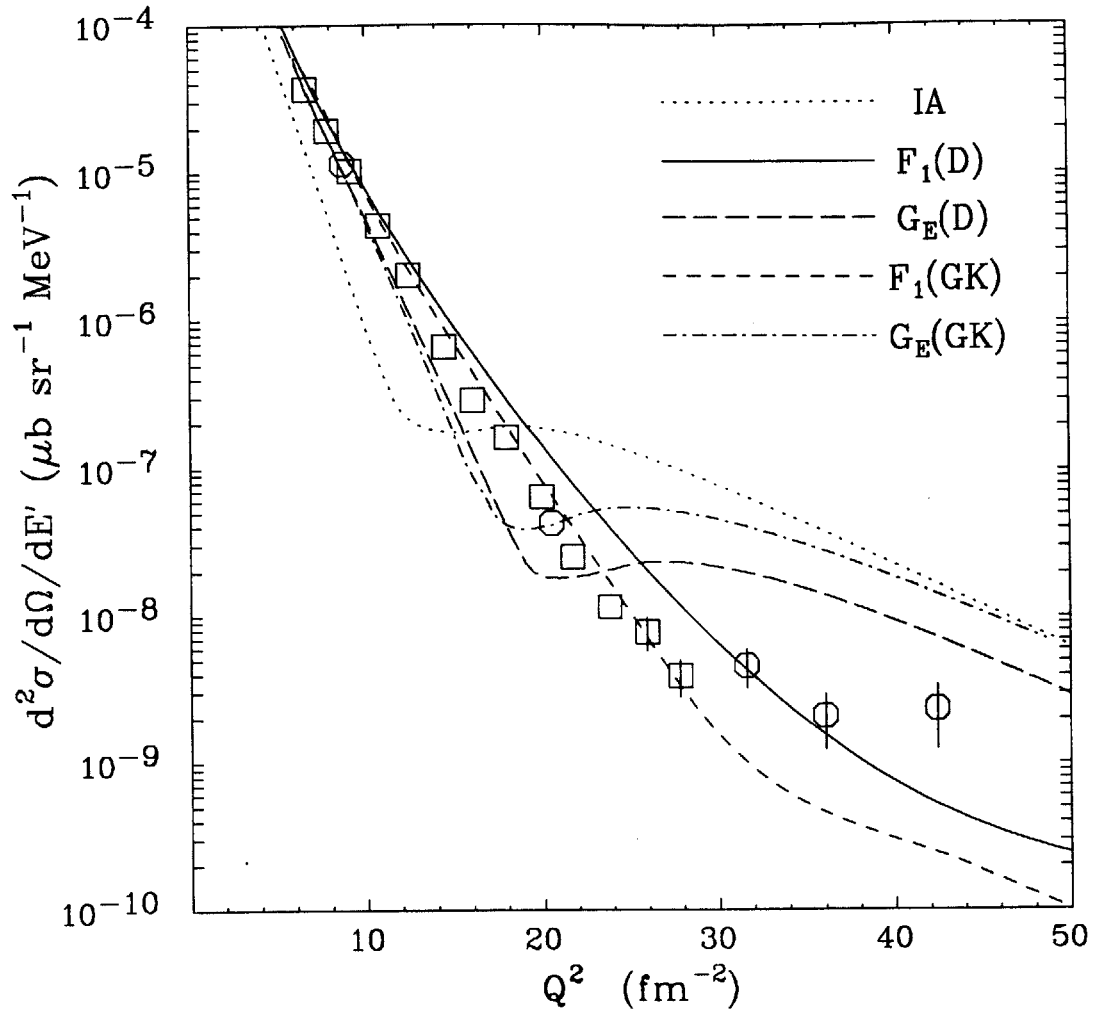


Figure 6-2: Threshold electrodisintegration cross sections averaged over $E_{np} = 0 - 3$ MeV compared with Paris potential calculations evaluated at $E_{np} = 1.5$ MeV [50]. The open squares represent data from Saclay [1] and the open circles represent the data presented in this thesis. The dotted curve is the impulse approximation. The solid curve is for F_1^V with the dipole EM form factors. The long-dash curve is for G_E^V . The short-dash curve is for F_1^V with GK EM form factors. The dot-dash curve is for G_E^V .

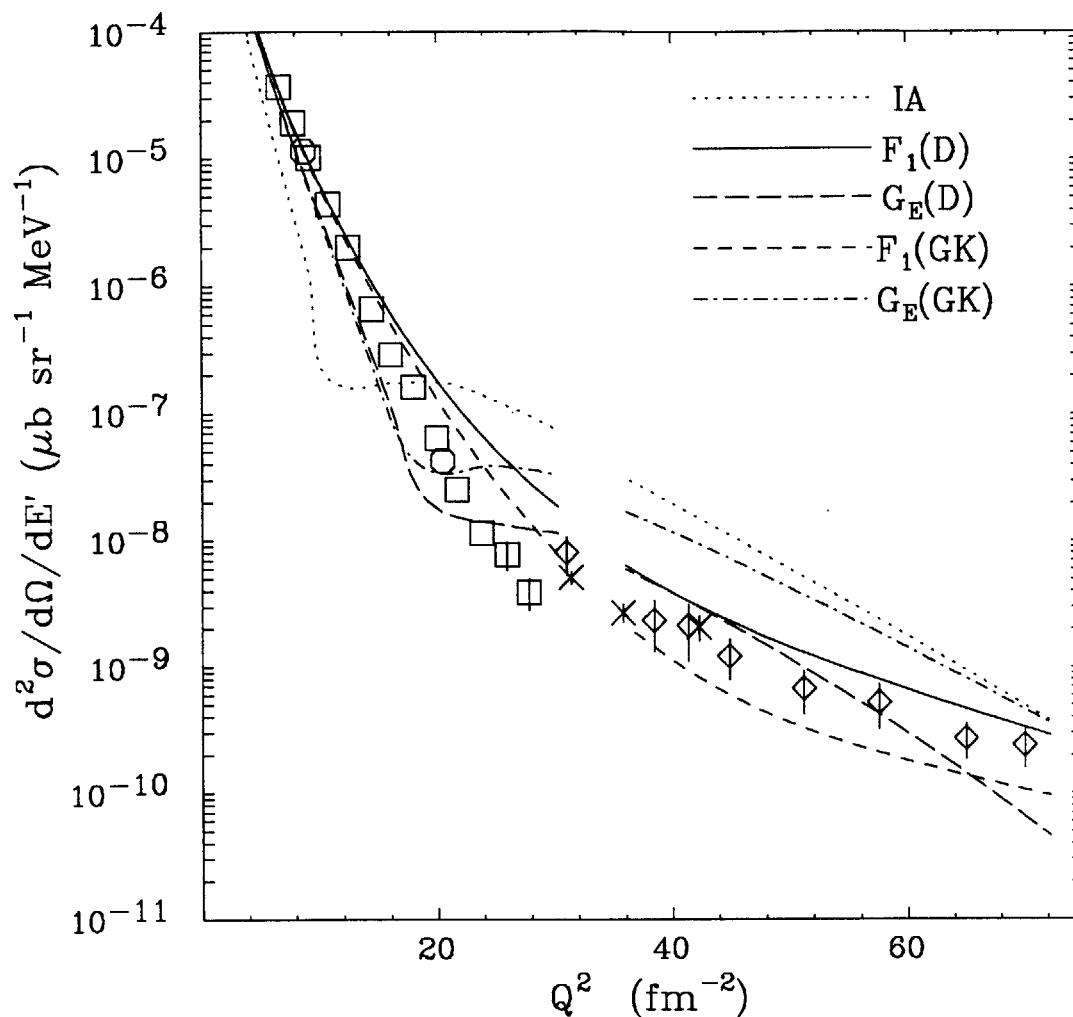


Figure 6-3: Threshold electrodisintegration cross sections compared with Argonne v_{14} potential calculations [55]. For $Q^2 < 27 \text{ fm}^{-2}$ both theory and experiment were averaged over $E_{np} = 0 - 3 \text{ MeV}$. For $Q^2 > 27 \text{ fm}^{-2}$ both were averaged over $E_{np} = 0 - 3 \text{ MeV}$. The break in the curves indicated the change in the averaging. The open squares represent data from Saclay [1], the open circles and crosses data from this measurement and the open diamonds data from SLAC [2]. The labels for the curves are the same given for Figure 6-2

been performed for deuteron electrodisintegration to test these ideas. These models match the long and medium range meson-exchange potentials with six-quark cluster potentials at short distances. In Figure 6-4 two hybrid quark-hadron models for deuteron electrodisintegration are plotted along with the data [56] [57]. Both calculations predict a weak second maximum in the threshold cross which is not seen in the data. However, these models do predict the general magnitude of the data about as well as the potential models.

In Figure 6-5 the radiatively unfolded doubly differential threshold cross sections are presented for the four lowest energies. The statistical accuracy of the data at the highest bombarding energy of 913 MeV was too poor to allow meaningful unfolding. These cross sections are compared with Paris and Bonn potential MEC calculations for the threshold excitation spectrum[58]. The solid curve is the Bonn potential calculation using G_E^V for the MEC. The dashed curve is the corresponding calculation with F_1^V . The dotted curve is for the Paris potential using G_E^V for the MEC. The dot-dashed curve is the corresponding calculation with F_1^V . At $E = 347$ MeV the four calculations describe the overall shape of the spectrum quite well. All calculations predict the presence of a resonance cusp at threshold with an increasing cross section at higher excitations. For the next highest energy, $E = 576$ MeV, the shape of the resonance cusp becomes more model dependent. In particular, the Bonn potential using G_E^V does not predict the presence of a cusp at threshold. However, the data clearly indicate the presence of resonance cusp at threshold. For the higher energies the trend of the various calculations diverges even more widely and some of the calculations appear off the plotting scale.

6.4 Conclusions

The threshold measurements presented in this thesis extend the range of data out to 42 fm^{-2} with good resolution. Comparisons of the data averaged over $E_{np} = 0 - 3$ MeV with data from Saclay show excellent agreement in the region of overlap. Good agreement is also obtained when the data is averaged over $E_{np} = 0 - 10$ MeV and compared with the lower resolution SLAC data.

Comparisons of the data were also made with nonrelativistic meson-exchange potential calculations. In the range $27 \text{ fm}^{-2} < Q^2 < 42 \text{ fm}^{-2}$ there exists much model sensitivity to the choice of the MEC potential and form factors. This reflects the delicate cancellation between one-body and two-body amplitudes for $Q^2 > 27 \text{ fm}^{-2}$ and in principle makes this an ideal place

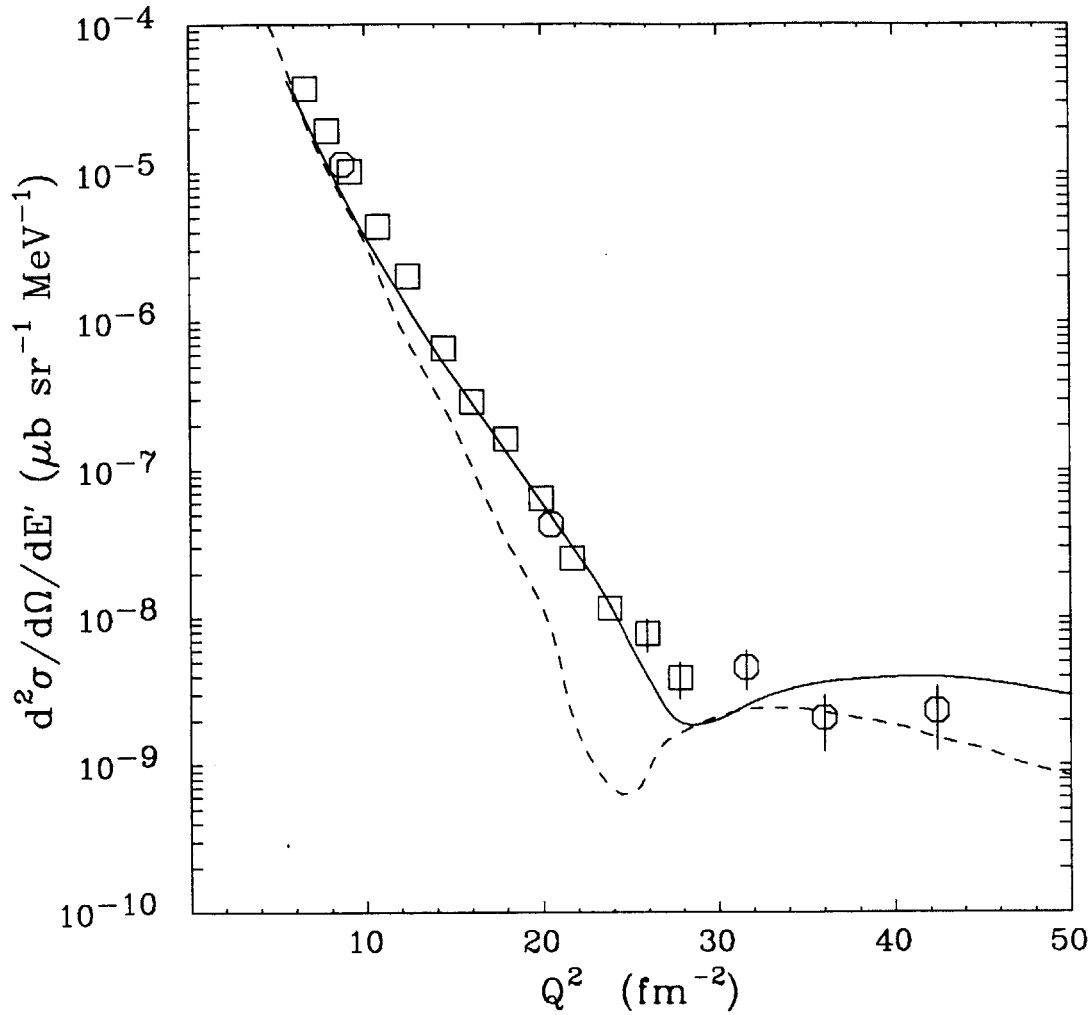


Figure 6-4: Threshold electrodisintegration cross sections averaged over $E_{np} = 0 - 3$ MeV compared with hybrid quark-hadron models evaluated at $E_{np} = 1.5$ MeV. The solid curve is by Cheng and Kisslinger [57]. The dashed curve is by Yamauchi, Buchmann, and Faessler [56]. The open squares represent data from Saclay [1] and the open circles represent the data presented in this thesis.

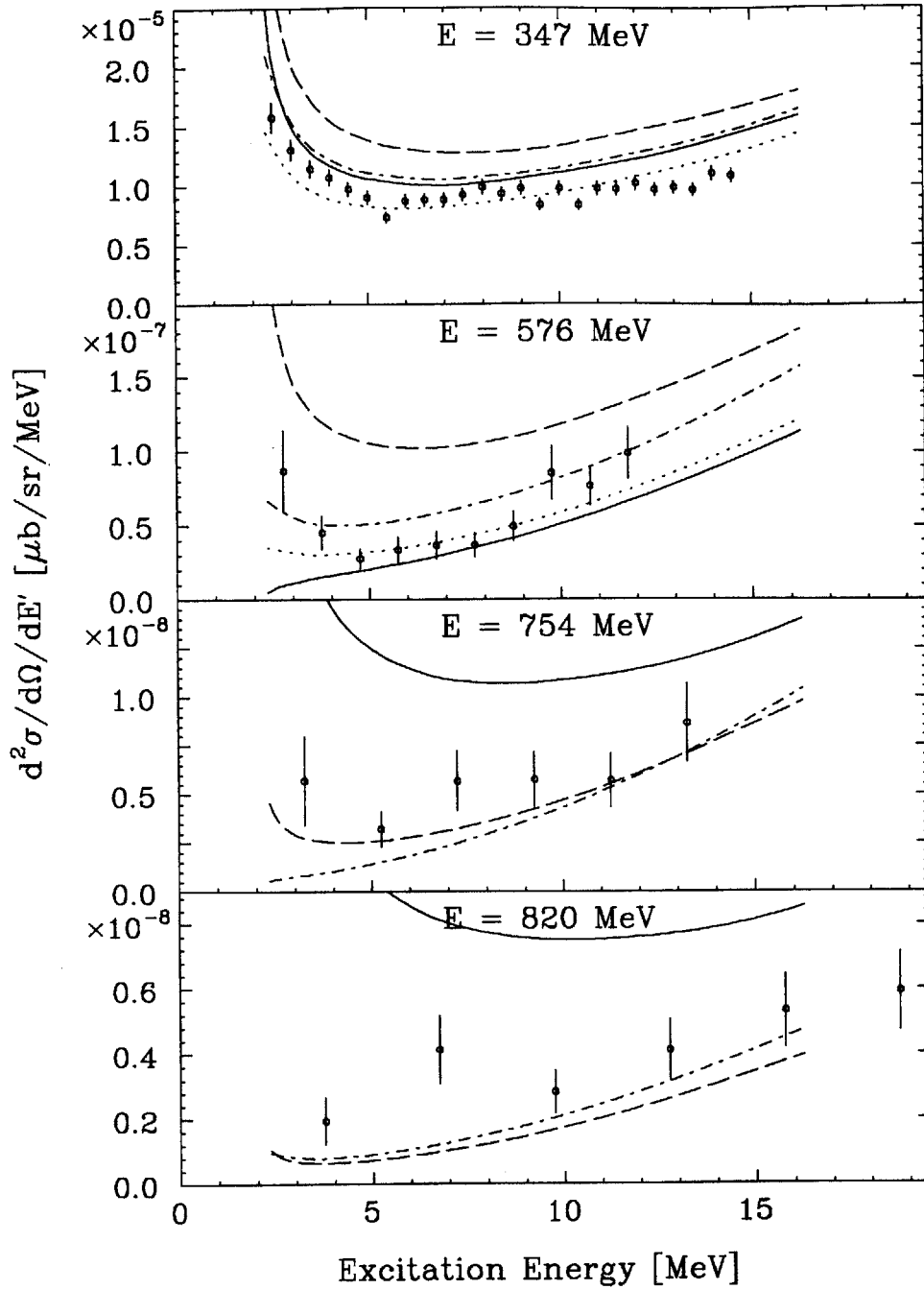


Figure 6-5: Radiative unfolded threshold spectra for $E = 347, 576, 754$ and 820 MeV at $\theta = 160^\circ$ compared with Bonn and Paris potential calculations [58]. The solid curve is the Bonn potential using G_E^V for the MEC. The dashed curve is the corresponding calculation with F_1^V . The dotted curve is the Paris potential using G_E^V for the MEC. The dot-dashed curve is the corresponding calculation with F_1^V . The dipole parameterization was used for the nucleon EM form factor.

to test competing models. However, since a fully relativistic theory of interacting particles with structure does not at present exist, one does not know the proper nonrelativistic reduction. At the energy transfers achieved in this experiment relativistic effects are very likely to be important. Hence, sharp conclusions cannot be drawn about the detailed structure of the MEC until relativistic corrections have been incorporated. The fact that calculations using Dirac isovector form factor, F_1^V , or the Sachs isovector form factor, G_E^V , for the MEC form factor differ at high momentum transfer is a possible indication that relativistic effects are becoming important.

For the calculations that the data are compared to it appears that, for the Paris, Bonn, and Argonne v_{14} potentials, the Dirac isovector form factor fits the data better in our Q^2 range. However, it must be recognized that this is a highly model dependent conclusion since different model dependent parameters could exist that would favor the Sachs form factor.

Comparisons of the data to hybrid quark-hadrons models were also presented. These models describe the system as a six-quark cluster for distances less than an arbitrary chosen radius and a two-nucleon system interacting through meson-exchanges outside of this radius. These models predict a weak second maximum at $Q^2 \sim 25 \text{ fm}^{-2}$ which is not present in the data. However, they do seem to predict the relative magnitude and trend of the data quite well. This is a hopeful sign that a complete quark model calculation might predict the data quite well.

The future holds great promise for extending the current Q^2 range to values greater than 100 fm^{-2} at the CEBAF. At such high values of Q^2 relativistic effects will indeed become more important and a quantitative understanding of the data may only be possible within such a relativistic framework. Also the effects of quark degrees of freedom may play a prominent role at these Q^2 . These are difficult tasks to undertake for theorists but it must be done in order to understand fully the nature of matter in the QCD confinement limit.

Appendix A

The ELSSY Focal Surface

The shape of the ELSSY focal surface [4] can be obtained by considering separately the shape in the dispersion plane and the shape perpendicular to the dispersion plane. The dispersion plane is defined by taking a slice in the X-Z focal plane coordinate system illustrated in Figure A-1. A slice in Y-Z gives us the transverse shape illustrated in Figure A-2. In this Appendix these shapes are derived from the relevant matrix elements. The coordinate system and units used are that of RAYTRACE [59]. All distances are in centimeters and angles in milliradians. We start first by deriving the shape in the dispersion plane.

Shown in Figure A-1 is a cross sectional slice of the focal surface at $y_f = 0$. The rays shown all originate at the target with x_t , y_t , and ϕ_t equal to zero. The central ray, $\delta = 0$, defines the Z_f axis and has θ_t equal to zero. Ray 1 and 2 have the same value of δ but different θ_t 's. Their intersection defines a point on the focal surface. Since there are no magnetic fields present at the focal surface, the trajectories of the rays are straight lines. From Figure A-1, we construct the following relations,

$$\tan \psi = -\frac{h}{x_{f1}}, \quad (\text{A.1})$$

$$h = 1000 \frac{x_{f2} - x_{f1}}{\theta_{f2}}, \quad (\text{A.2})$$

where small angles have been assumed in the latter equation. To first order in each of the target variables, the focal plane coordinates for ray 1 and 2 can be expressed as follows,

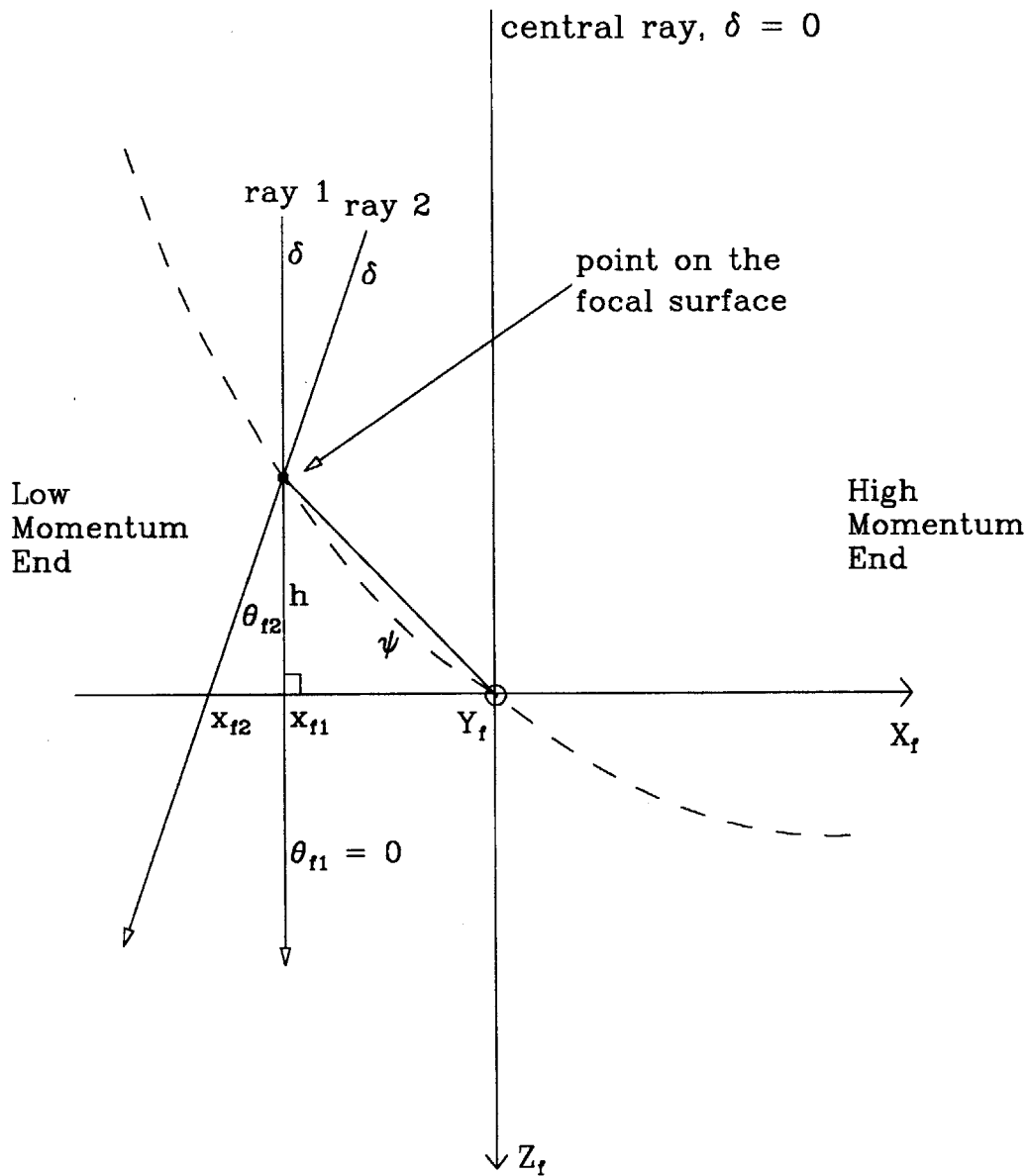


Figure A-1: Sketch of the focal surface curvature in the dispersion plane. The central ray is shown along with two rays with the same δ but different θ 's at the target. Their intersection defines a point on the focal surface.

Ray 1 ($x_t, y_t, \phi_t = 0$):

$$x_{f1} = (x|\delta)\delta + (x|\theta\delta)\theta_{t1}\delta, \quad (\text{A.3})$$

$$\theta_{f1} = (\theta|\theta)\theta_{t1} + (\theta|\delta)\delta + (\theta|\theta\delta)\theta_{t1}\delta = 0; \quad (\text{A.4})$$

Ray 2 ($x_t, y_t, \phi_t = 0$):

$$x_{f2} = (x|\delta)\delta + (x|\theta\delta)\theta_{t2}\delta, \quad (\text{A.5})$$

$$\theta_{f2} = (\theta|\theta)\theta_{t2} + (\theta|\delta)\delta + (\theta|\theta\delta)\theta_{t2}\delta; \quad (\text{A.6})$$

where the matrix elements are for a focal plane tilt angle of zero degrees and tabulated in Appendix F. Using these relations, the equation for $\tan \psi$ can be rewritten solely as a function of the variable δ :

$$\tan \psi = -1000 \frac{x_{f2} - x_{f1}}{x_{f1}\theta_{f2}} \quad (\text{A.7})$$

$$= \frac{-1000 (x|\theta\delta)}{(x|\delta)(\theta|\theta) + [(x|\delta)(\theta|\theta\delta) - (\theta|\delta)(x|\theta\delta)]\delta}. \quad (\text{A.8})$$

Evaluating this at $\delta = 0$ gives us the tangent angle of the focal surface at the central ray:

$$\tan \psi_{\delta=0} = -1000 \frac{(x|\theta\delta)}{(x|\delta)(\theta|\theta)}, \quad (\text{A.9})$$

$$\psi_{\delta=0} \cong 43.5^\circ,$$

which agrees with the quoted nominal value of 45° [4].

The equation for the height, h , can also be rewritten to obtain the following formula:

$$h = 1000 \frac{(x|\theta\delta)\delta}{(\theta|\theta) + (\theta|\theta\delta)\delta}. \quad (\text{A.10})$$

From Equations A.3 and A.4, δ can be solved as a function of x_{f1} . The result is a quadratic expression:

$$a\delta^2 + b\delta + c = 0, \quad (\text{A.11})$$

with

$$a = (x|\delta)(\theta|\theta\delta) - (\theta|\delta)(x|\theta\delta), \quad (\text{A.12})$$

x_{f1} [cm]	h [cm]	$h(43.5^\circ)$ [cm]
-25	26.2	23.7
-20	20.5	19.0
-15	15.1	14.2
-10	9.9	9.5
-5	4.8	4.7
0	0	0
5	-4.7	-4.7
10	-9.2	-9.5
15	-13.5	-14.2
20	-17.8	-19.0
25	-21.9	-23.7

Table A.1: The curvature of the ELSSY focal surface in the dispersion plane compared with a flat focal surface at an angle of 43.5° .

$$b = (x|\delta)(\theta|\theta) - (\theta|\theta\delta)x_{f1}, \quad (\text{A.13})$$

$$c = -(\theta|\theta)x_{f1}, \quad (\text{A.14})$$

and

$$\delta = \frac{-b - \sqrt{b^2 - 4ac}}{2a}. \quad (\text{A.15})$$

The sign choice comes from the constraint that $\delta = 0$ at $x_{f1} = 0$. In Table A.1 the results for $h(x_{f1})$ are tabulated along with $h(43.5^\circ)$ which assumes a flat focal surface at an angle of 43.5° (from Equation A.9). Qualitatively these results are in agreement with the curvature sketch in Figure A-1. Over the instrumented length of the focal plane detection system, $|x_{f1}| < 25$ centimeters, the focal surface curvature in the dispersion plane is not too severe. At $|x_{f1}| \sim 25$, the planar deviations are of the order of two centimeters.

To obtain the curvature of the focal surface perpendicular to the dispersion plane, the rays illustrated in Figure A-2 are used. For simplicity we first derive this curvature for central rays, $\delta = 0$, and then later discuss the curvature for noncentral rays, $\delta \neq 0$. As shown in the figure, ray 1 and 2 represent “off-axis” central rays. Ray 1 and 2 originate at the target with x_t, y_t , and $\delta = 0$ but $\phi_{t1} = \phi_{t2} = \phi_t \neq 0$. Their intersection defines a point on the focal surface. From

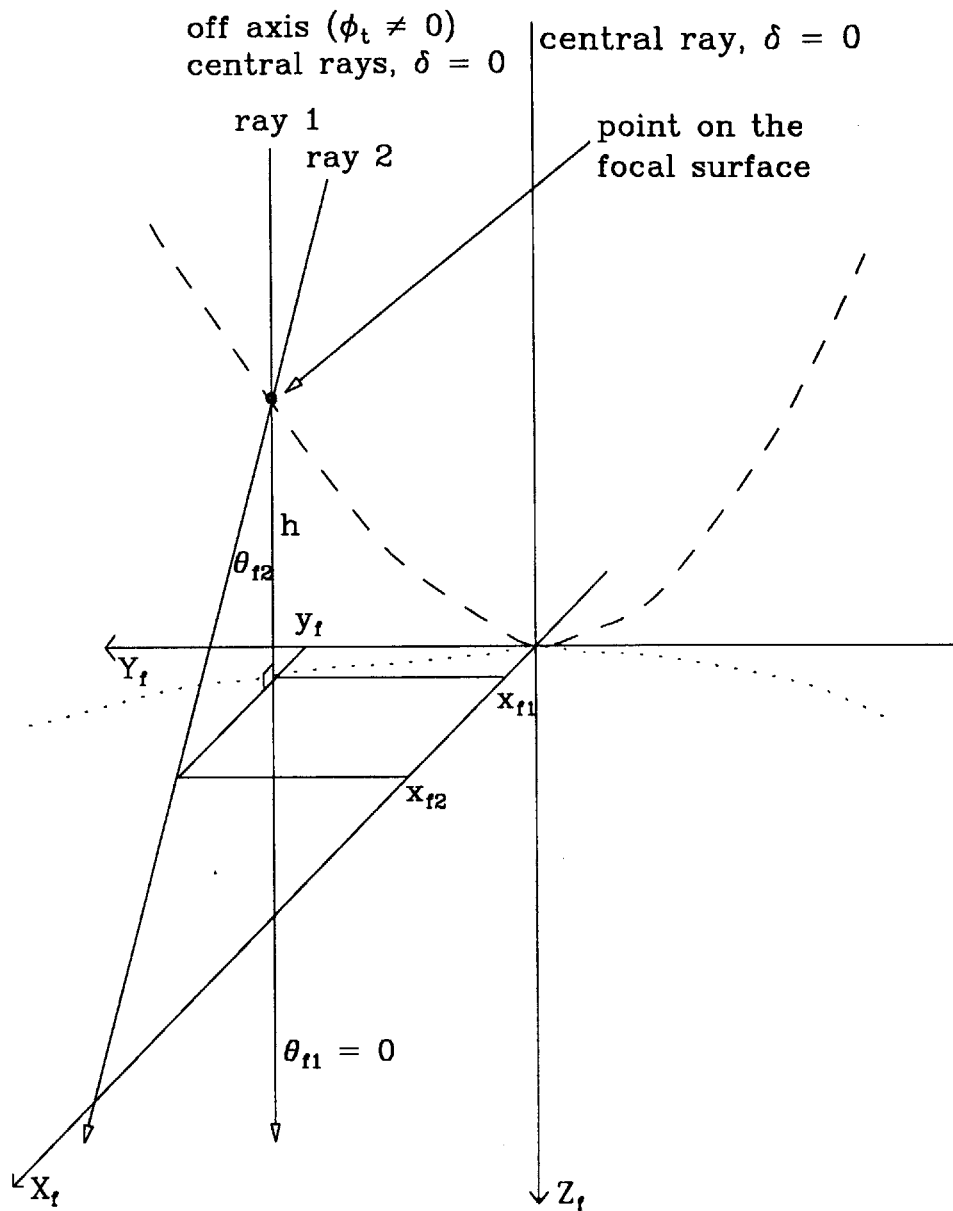


Figure A-2: Sketch of the focal surface curvature perpendicular to the dispersion plane. Two off-axis ($\phi_t \neq 0$) central rays are shown with different θ_t . Their intersection defines a point on the focal surface.

Figure A-2 we construct the following relation for the height, h :

$$h = 1000 \frac{x_{f2} - x_{f1}}{\theta_{f2}}, \quad (\text{A.16})$$

where small angles have been assumed. The focal plane coordinates for ray 1 and 2 can be expressed in terms of their target variables. Keeping only the most significant terms we have,

Ray 1 ($x_t, y_t, \delta = 0$):

$$x_{f1} = (x|\phi^2)\phi_t^2 + (x|\theta\phi^2)\theta_{t1}\phi_t^2, \quad (\text{A.17})$$

$$\theta_{f1} = (\theta|\theta)\theta_{t1} = 0, \quad (\text{A.18})$$

$$y_{f1} = (y|\phi)\phi_t; \quad (\text{A.19})$$

Ray 2 ($x_t, y_t, \delta = 0$):

$$x_{f2} = (x|\phi^2)\phi_t^2 + (x|\theta\phi^2)\theta_{t2}\phi_t^2, \quad (\text{A.20})$$

$$\theta_{f2} = (\theta|\theta)\theta_{t2}, \quad (\text{A.21})$$

$$y_{f2} = (y|\phi)\phi_t; \quad (\text{A.22})$$

where the matrix elements are for a focal plane tilt angle of zero degrees and tabulated in Appendix F. Using these relations the equation for the height, h , can be rewritten solely as a function of the variable y_f (notice that the matrix element $(x|\theta\phi^2)$ is mostly responsible for this curvature):

$$h = 1000 \frac{(x|\theta\phi^2)}{(\theta|\theta)(y|\phi)^2} y_f^2. \quad (\text{A.23})$$

This equation is parabolic in y_f and describes only part of the transverse shape of the focal surface. As shown in Figure A-2 the dashed curve, which represents the $\delta = 0$ slice, also has a finite x_f component. This is illustrated by the dotted curve in the X-Y plane. This curvature is described by the coordinate x_{f1} . From Equation A.17 we obtain the following shape written as a function of y_f :

$$x_{f1} = \frac{(x|\phi^2)}{(y|\phi)^2} y_f^2, \quad (\text{A.24})$$

which is also parabolic in y_f . Qualitatively these results are in agreement with the curvature illustrated in Figure A-2. Using the matrix elements presented in Appendix F the expressions for $h(y_f)$ and $x_{f1}(y_f)$ can be evaluated to obtain the following:

$$h = 6.8 \times 10^{-2} y_f^2, \quad (\text{A.25})$$

$$x_{f1} = 3.0 \times 10^{-5} y_f^2. \quad (\text{A.26})$$

The transverse length used by the ELSSY focal plane detection system extends from roughly y_f equal to -10 to $+10$ centimeters. The curvature in x_{f1} is then very small and negligible, but the curvature represented by the height, h , is significant. At $|y_f| = 10$, the curvature is of the order of seven centimeters and lies almost completely in the Y-Z focal plane.

It is also possible to derive this shape for noncentral rays, $\delta \neq 0$. When this is done the entire focal surface will be described within the accuracy of our Raytrace expansions for the focal plane coordinates: x_f , θ_f , and y_f . Keeping only the most significant terms we have,

Ray ($x_t, y_t = 0$):

$$x_f = (x|\delta)\delta + (x|\theta\delta)\theta_t\delta + (x|\phi^2)\phi_t^2 + (x|\theta\phi^2)\theta_t\phi_t^2 + (x|\phi^2\delta)\phi_t^2\delta + (x|\delta^3)\delta^3, \quad (\text{A.27})$$

$$\theta_f = (\theta|\theta)\theta_t + (\theta|\delta)\delta + (\theta|\theta\delta)\theta\delta, \quad (\text{A.28})$$

$$y_f = (y|\phi)\phi_t + (y|\phi\delta)\phi\delta, \quad (\text{A.29})$$

where for ray 1, $\theta_t = \theta_{t1}$ and $\theta_{f1} \equiv 0$, and ray 2, $\theta_t = \theta_{t2}$. Using Equation A.16 and these relations the equation for the height, h , can be written as follows:

$$h = 1000 \frac{(x|\theta\delta)\delta + (x|\theta\phi^2)\phi_t^2}{(\theta|\theta) + (\theta|\theta\delta)\delta}, \quad (\text{A.30})$$

and from Equation A.29 we have

$$\phi_t = \frac{y_f}{(y|\phi) + (y|\phi\delta)\delta}. \quad (\text{A.31})$$

This solution for h can be decomposed and rewritten in a more convenient form.

$$h(\delta, y_f) = 1000 \frac{(x|\theta\delta)\delta}{(\theta|\theta) + (\theta|\theta\delta)\delta} + 1000 \frac{(x|\theta\phi^2)}{(\theta|\theta)(y|\phi)^2} \left[1 + \frac{(\theta|\theta\delta)}{(\theta|\theta)}\delta \right]^{-1} \left[1 + \frac{(y|\phi\delta)}{(y|\phi)}\delta \right]^{-2} y_f^2. \quad (\text{A.32})$$

The first term describes the curvature in the dispersion plane as was found earlier (see Equation A.10). The second term describes the transverse curvature as a function of δ and for $\delta = 0$ this term reproduces the previous result. For $\delta \neq 0$ the curvature is still parabolic with the origin lying along the dashed curve sketched in Figure A-1, but the amount of curvature

changes due to the δ -dependent factors. Using the matrix elements from Appendix F these can be evaluated to yield (note that the matrix element $(y|\phi\delta)$ is mostly responsible for this effect):

$$\left[1 + 0.013 \delta\right]^{-1} \left[1 + 0.050 \delta\right]^{-2}.$$

The effect of these terms is then to flatten out the parabola, decreasing the curvature, for increasing values of δ . Relative to the transverse curvature for the central ray given by Equation A.25 the size of this effect is +45% at $\delta = -3\%$ and -25% at $\delta = +3\%$. The curvature represented by Equation A.26 is also very small for noncentral rays. Therefore, these parabolas lie almost completely in a plane perpendicular to the X_f axis which for ELSSY is a vertical plane.

Appendix B

The Target Collimating Slits

The purpose of the target collimating slits is to prevent the electrons which scatter from the aluminum entrance and exit windows of the target cell from entering the acceptance of the spectrometer. This is accomplished by requiring these electrons to traverse some specified collimator slit thickness. During this traversal the electrons lose their energy by ionization and radiation. Since this is a statistical process not all electrons lose the same amount of energy. Hence, there is a finite fraction of the initial electrons which will pass through the slits and be accepted into the spectrometer. The challenge that had to be met was to design a system that would reduce this background to a negligible level.

Shown in Figure 2-2 is a schematic diagram of the collimating slit geometry in relation to the target cell. The slit thickness that needs to be determined is the electron traversal thickness, l , and is the distance between the points labeled in the figure as a and b or c and d. This is the distance an electron would have to traverse in the slit in order to be accepted into the spectrometer.

The largest source of background at the kinematics of this experiment was determined to be quasi-elastic scattering from the aluminum target cell. In Table B.1 the estimated cross sections are presented for the range of energies used in this experiment. The counting rate estimates per beam burst were then made for each reaction with the following assumptions:

$$\begin{aligned}\text{Beam pulse duration} &= 10 \mu\text{s} , \\ \text{Peak current} &= 5 \text{ mA} , \\ \text{Spectrometer solid angle} &= 3.5 \text{ msr} ,\end{aligned}$$

Energy [MeV]	Deuterium Threshold [cm ² /sr/MeV]	Aluminum QE [cm ² /sr/MeV]
320	2.2×10^{-35}	1.18×10^{-33}
532	1.5×10^{-37}	1.04×10^{-34}
762	1.9×10^{-39}	1.07×10^{-35}
823	1.3×10^{-39}	6.29×10^{-36}
942	6×10^{-40}	2.37×10^{-36}

Table B.1: Estimated cross sections for the deuterium threshold electrodisintegration and aluminum quasi-elastic reactions at the kinematics of this experiment.

Energy [MeV]	Deuterium Threshold [counts/bb]	Aluminum QE [counts/bb]
320	3.5×10^{-2}	9.0×10^{-2}
532	3.4×10^{-4}	1.05×10^{-2}
762	5.4×10^{-6}	1.28×10^{-3}
823	3.8×10^{-6}	7.5×10^{-4}
942	1.9×10^{-6}	3.0×10^{-4}

Table B.2: Count rate estimates per beam burst for the deuterium threshold electrodisintegration and aluminum quasi-elastic reactions at the kinematics of this experiment.

$$\text{Aluminum thickness} = 0.1 \text{ cm ,}$$

$$\text{LD}_2 \text{ thickness} = 4 \text{ cm .}$$

and the results are in Table B.2.

The methodology used in determining the optimum slit traversal thickness is as follows. For a given incident beam energy the scattered electron energy associated with the peak of the quasi-elastic spectrum was calculated. The width of the quasi-elastic peak is given by the expression

$$\text{width QE} = 2 \times q \times P_f / m , \quad (\text{B.1})$$

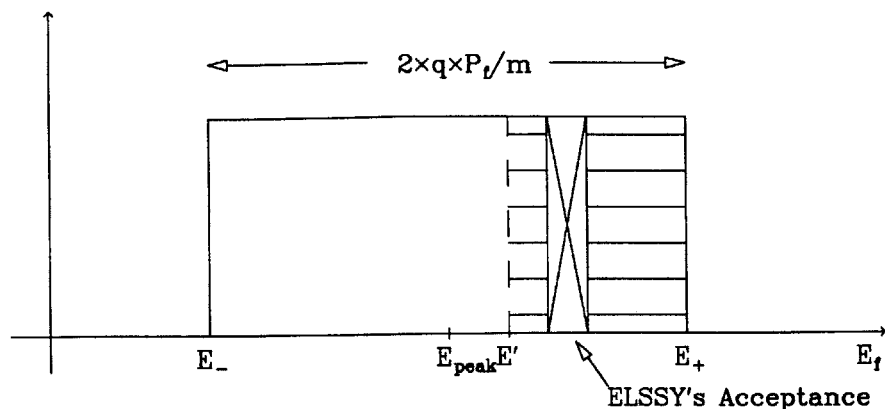


Figure B-1: A flat quasi-elastic response.

where

q is the 3-momentum transfer,

P_f is the Fermi momentum = 200 MeV/c,

m is the mass of a nucleon.

The strength of the quasi-elastic peak was taken as uniform across this width. Therefore, the peak has the form of a square box. This is plotted in Figure B-1 along with the momentum acceptance of ELSSY spectrometer.

The intersection between the quasi-elastic peak and the ELSSY acceptance is the source of background that needs to be reduced by the slits. Consider the region defined by the energy range $[E', E_+]$, where E' is the lowest accepted energy of ELSSY minus 20 MeV (this is arbitrary) and E_+ is the highest energy in the flat quasi-elastic spectrum. In calculating what the optimum slit thickness, l , should be, the total counting rate from this region $[E', E_+]$ is taken to occur at the highest energy E_+ . Then the criterion used in determining the thickness of the slits is as follows:

$$\Pi(E', E_+, l) \times (\text{Al count rate from } [E', E_+]) \leq ({}^2\text{H threshold count rate})/1000, \quad (\text{B.2})$$

Energy [MeV]	Traversal Thickness [radiation lengths]
320	8.0
532	10.3
762	13.4
823	13.1
942	13.1

Table B.3: The minimum electron slit traversal thicknesses needed effectively to eliminate the quasi-elastic aluminum background.

where l is the thickness in radiation lengths, and $\Pi(E', E_+, l)$ is the average number of electrons at a depth t in a material with energy greater than E' , given initially an incident electron with energy E_+ at $l = 0$ [15]. Therefore, the slit thickness, l , is chosen such that the attenuation factor Π reduces the counting rate from the aluminum to be one thousandth of the deuteron threshold counting rate. The results for the minimum slit thicknesses, expressed in radiation lengths, at each energy are tabulated in Table B.3.

From the table it can be seen that the minimum slit thickness to adequately reduce the aluminum background at all energies is 13.4 radiation lengths. Since the slits were made from a machineable tungsten alloy (Hevi-Met) this corresponded to a physical thickness of roughly 5 centimeters (1 r.l. \cong .35 cm). For this experiment the collimating slits were made with a traversal thickness of 7.4 centimeters (approximately 21 r.l.).

Appendix C

Table of the Landau Functions $\phi(\lambda)$ and $\psi(\lambda)$

Both of the Landau functions, $\phi(\lambda)$ and $\psi(\lambda)$, were evaluated numerically and the results are presented in Table C.1. Börsch-Supan [32] gives a more extensive tabulation for the Landau straggling function, $\phi(\lambda)$.

λ	$\phi(\lambda)$	$\psi(\lambda)$	λ	$\phi(\lambda)$	$\psi(\lambda)$	λ	$\phi(\lambda)$	$\psi(\lambda)$
-4.0	3.390×10^{-9}	1.0000	0.7	1.576×10^{-1}	0.5944	5.4	3.489×10^{-2}	0.2122
-3.9	2.181×10^{-8}	1.0000	0.8	1.536×10^{-1}	0.5789	5.5	3.391×10^{-2}	0.2087
-3.8	1.170×10^{-7}	1.0000	0.9	1.494×10^{-1}	0.5637	5.6	3.298×10^{-2}	0.2054
-3.7	5.323×10^{-7}	1.0000	1.0	1.452×10^{-1}	0.5490	5.7	3.207×10^{-2}	0.2022
-3.6	2.087×10^{-6}	1.0000	1.1	1.410×10^{-1}	0.5347	5.8	3.121×10^{-2}	0.1990
-3.5	7.152×10^{-6}	1.0000	1.2	1.367×10^{-1}	0.5208	5.9	3.037×10^{-2}	0.1959
-3.4	2.169×10^{-5}	1.0000	1.3	1.325×10^{-1}	0.5073	6.0	2.956×10^{-2}	0.1929
-3.3	5.893×10^{-5}	1.0000	1.4	1.283×10^{-1}	0.4943	6.1	2.878×10^{-2}	0.1900
-3.2	1.449×10^{-4}	1.0000	1.5	1.242×10^{-1}	0.4817	6.2	2.803×10^{-2}	0.1872
-3.1	3.255×10^{-4}	1.0000	1.6	1.202×10^{-1}	0.4694	6.3	2.730×10^{-2}	0.1844
-3.0	6.737×10^{-4}	0.9999	1.7	1.162×10^{-1}	0.4576	6.4	2.660×10^{-2}	0.1817
-2.9	1.295×10^{-3}	0.9998	1.8	1.124×10^{-1}	0.4462	6.5	2.592×10^{-2}	0.1791
-2.8	2.329×10^{-3}	0.9996	1.9	1.086×10^{-1}	0.4351	6.6	2.527×10^{-2}	0.1765
-2.7	3.943×10^{-3}	0.9993	2.0	1.049×10^{-1}	0.4245	6.7	2.464×10^{-2}	0.1740
-2.6	6.319×10^{-3}	0.9988	2.1	1.014×10^{-1}	0.4142	6.8	2.403×10^{-2}	0.1716
-2.5	9.637×10^{-3}	0.9980	2.2	9.791×10^{-2}	0.4042	6.9	2.344×10^{-2}	0.1692
-2.4	1.405×10^{-2}	0.9969	2.3	9.457×10^{-2}	0.3946	7.0	2.287×10^{-2}	0.1669
-2.3	1.968×10^{-2}	0.9952	2.4	9.134×10^{-2}	0.3853	7.1	2.232×10^{-2}	0.1646
-2.2	2.657×10^{-2}	0.9929	2.5	8.822×10^{-2}	0.3763	7.2	2.178×10^{-2}	0.1624
-2.1	3.470×10^{-2}	0.9898	2.6	8.522×10^{-2}	0.3676	7.3	2.127×10^{-2}	0.1603
-2.0	4.399×10^{-2}	0.9859	2.7	8.232×10^{-2}	0.3593	7.4	2.077×10^{-2}	0.1582
-1.9	5.426×10^{-2}	0.9810	2.8	7.953×10^{-2}	0.3512	7.5	2.029×10^{-2}	0.1561
-1.8	6.531×10^{-2}	0.9750	2.9	7.684×10^{-2}	0.3433	7.6	1.982×10^{-2}	0.1541
-1.7	7.689×10^{-2}	0.9679	3.0	7.425×10^{-2}	0.3358	7.7	1.937×10^{-2}	0.1522
-1.6	8.873×10^{-2}	0.9596	3.1	7.176×10^{-2}	0.3285	7.8	1.893×10^{-2}	0.1502
-1.5	1.006×10^{-1}	0.9502	3.2	6.936×10^{-2}	0.3214	7.9	1.850×10^{-2}	0.1484
-1.4	1.121×10^{-1}	0.9395	3.3	6.706×10^{-2}	0.3146	8.0	1.809×10^{-2}	0.1465
-1.3	1.231×10^{-1}	0.9278	3.4	6.485×10^{-2}	0.3080	8.1	1.769×10^{-2}	0.1447
-1.2	1.335×10^{-1}	0.9149	3.5	6.272×10^{-2}	0.3016	8.2	1.730×10^{-2}	0.1430
-1.1	1.429×10^{-1}	0.9011	3.6	6.068×10^{-2}	0.2955	8.3	1.693×10^{-2}	0.1413
-1.0	1.514×10^{-1}	0.8864	3.7	5.871×10^{-2}	0.2895	8.4	1.656×10^{-2}	0.1396
-0.9	1.588×10^{-1}	0.8709	3.8	5.682×10^{-2}	0.2837	8.5	1.621×10^{-2}	0.1380
-0.8	1.651×10^{-1}	0.8547	3.9	5.501×10^{-2}	0.2781	8.6	1.587×10^{-2}	0.1364
-0.7	1.703×10^{-1}	0.8379	4.0	5.327×10^{-2}	0.2727	8.7	1.553×10^{-2}	0.1348
-0.6	1.743×10^{-1}	0.8206	4.1	5.159×10^{-2}	0.2675	8.8	1.521×10^{-2}	0.1333
-0.5	1.773×10^{-1}	0.8031	4.2	4.999×10^{-2}	0.2624	8.9	1.490×10^{-2}	0.1318
-0.4	1.793×10^{-1}	0.7852	4.3	4.844×10^{-2}	0.2575	9.0	1.459×10^{-2}	0.1303
-0.3	1.804×10^{-1}	0.7672	4.4	4.695×10^{-2}	0.2527	9.1	1.430×10^{-2}	0.1288
-0.2	1.806×10^{-1}	0.7492	4.5	4.552×10^{-2}	0.2481	9.2	1.401×10^{-2}	0.1274
-0.1	1.801×10^{-1}	0.7311	4.6	4.415×10^{-2}	0.2436	9.3	1.373×10^{-2}	0.1260
0.0	1.788×10^{-1}	0.7132	4.7	4.283×10^{-2}	0.2393	9.4	1.346×10^{-2}	0.1247
0.1	1.770×10^{-1}	0.6954	4.8	4.156×10^{-2}	0.2350	9.5	1.319×10^{-2}	0.1234
0.2	1.747×10^{-1}	0.6778	4.9	4.034×10^{-2}	0.2309	9.6	1.294×10^{-2}	0.1220
0.3	1.719×10^{-1}	0.6604	5.0	3.916×10^{-2}	0.2270	9.7	1.269×10^{-2}	0.1208
0.4	1.687×10^{-1}	0.6434	5.1	3.803×10^{-2}	0.2231	9.8	1.244×10^{-2}	0.1195
0.5	1.652×10^{-1}	0.6267	5.2	3.694×10^{-2}	0.2194	9.9	1.221×10^{-2}	0.1183
0.6	1.615×10^{-1}	0.6104	5.3	3.590×10^{-2}	0.2157	10.0	1.198×10^{-2}	0.1171

Table C.1: Table of the Landau functions $\phi(\lambda)$ and $\psi(\lambda)$.

Appendix D

Density Effect Correction

When a charged particle traverses matter, the amount of ionization loss given by the well known Bethe-Bloch formula will be reduced due to the effect of the polarization of the medium. This polarization, induced by the electric field of the charged particle, will reduce the field strength at larger distances, hence buffering the effect of the passing particle. For this correction we used the Sternheimer parameterization [23] [24] [60]. The correction, denoted by δ , is given by

$$\begin{aligned}\delta(X) &= \delta_o 10^{2(X-X_o)}, & X \leq X_o, \\ &= 4.6052X + a(X_1 - X)^m + C, & X_o < X \leq X_1, \\ &= 4.6052X + C, & X > X_1,\end{aligned}\tag{D.1}$$

where

$$X \equiv \log_{10}(pc/m_o c^2) = \frac{1}{\ln 10} \ln(pc/m_o c^2) \approx \frac{1}{1.6052} \ln(pc/m_o c^2),$$

p is the momentum of the particle,

and $m_o c^2$ is its rest energy.

In Table D.1 the values that were used for the parameters X_o , X_1 , m , and δ_o are listed.

	X_o	X_1	m	δ_o
Al	0.1708	3.0127	3.6345	0.12
LH ₂	0.4759	1.9215	5.6249	0
LD ₂	0.4759	1.9215	5.6249	0

Table D.1: The independent density effect correction parameters [60]. Values for LD₂ were taken to be the same as LH₂.

The parameter C is a function of the electron density of the traversed material. This was evaluated using the formulas:

$$h\nu_p = \sqrt{\frac{ne^2}{\pi m_e}}, \quad (\text{D.2})$$

$$C = -2\ln(I/h\nu_p) - 1, \quad (\text{D.3})$$

where

n is the electron density of the traversed material,

e is the charge of the electron,

m_e is the mass of the electron,

$h\nu_p$ is the plasma energy, and

I is the mean ionization potential of the electrons in the medium.

From the boundary condition at $\delta(X_o)$, a formula can be derived for a in terms of the other parameters:

$$a = \frac{\delta_o - C - 4.6052X_o}{(X_1 - X_o)^m}. \quad (\text{D.4})$$

	I [eV]	ρ [g/cm ³]	C	a
Al	166.0	2.70	-4.2395	0.08024
LH ₂	21.8	0.073	-3.0692	0.1104
LD ₂	21.8	0.165	-2.9419	0.0944

Table D.2: Density effect correction parameters.

In Table D.2 are listed the values of the parameters used for aluminum. However, for liquid hydrogen and deuterium the densities varied slightly during the course of the experiment. Shown are the values for the parameters evaluated for a typical average density.

Appendix E

Elastic Line Shape with Cross Section Dependence

In Section 3.2.2, Equation 3.69 gives us the elastic line shape for electrons traversing the target cell. An approximation was then made that ignored the energy dependence of the scattering cross section which allowed us to relate the elastic line shape with the energy loss distribution, Equation 3.70. It was asserted that this would be valid near the elastic peak where the change in the scattering cross section is expected to be small. In this Appendix the validity of this assertion is explored directly by computing the elastic line shape near the elastic peak assuming a linear change in the scattering cross section. We will not attempt to solve this problem using the line shape of Section 3.2.2, but a simpler example which can be solved exactly will be treated.

Consider the scattering process illustrated in Figure E-1. An incident electron passes through some initial amount of target of thickness, x , before scattering, then scatters from the target nucleus and passes through same amount of thickness, x , as it exits the target. $D_1(\Delta)$ is the distribution for an energy loss Δ due to ionization and external bremsstrahlung (see Equation 3.49). The fact that the distances, x , before and after the scattering are the same implies that their energy loss distributions are the same, $D_1(\Delta)$. This assumption is made to make the problem exactly solvable. Also, recoil will be ignored ($\eta = 1$). $D_2(\Delta)$ is the distribution for an energy loss Δ due to internal bremsstrahlung at the time of scattering (see Equation 3.44). The equation for the elastic line shape is given by the following expression,

$$\left. \frac{d^2\sigma}{d\Omega d\Delta} \right)_{\text{meas.}} = \int_0^\Delta d\Delta_1 \int_0^{\Delta-\Delta_1} d\Delta_2 D_1(\Delta_1) \frac{d\sigma(E - \Delta_1 - \Delta_2/2)}{d\Omega} D_2(\Delta_2) D_1(\Delta - \Delta_1 - \Delta_2), \quad (\text{E.1})$$

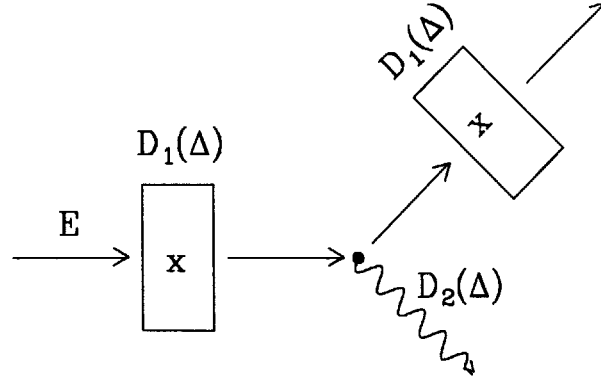


Figure E-1: Schematic diagram illustrating the scattering process.

where half of the energy loss due to internal bremsstrahlung, Δ_2 , is taken to occur before the scattering.

If we are only interested in the line shape near the elastic peak, the cross section can be expanded in a power series. Only the first order terms need to be kept for sufficient accuracy:

$$\begin{aligned} \frac{d\sigma(E - \Delta_1 - \Delta_2/2)}{d\Omega} &= \frac{d\sigma(E)}{d\Omega} + \left. \frac{d^2\sigma}{d\Omega d\Delta_b} \right|_{\Delta_b=0} (\Delta_1 + \Delta_2/2) + \dots \\ &\cong \sigma(E)[1 + \xi(\Delta_1 + \Delta_2/2)] \end{aligned} \quad (\text{E.2})$$

where

$$\xi = \left. \frac{d^2\sigma}{d\Omega d\Delta_b} \right|_{\Delta_b=0} / \frac{d\sigma(E)}{d\Omega}, \quad (\text{E.3})$$

and

$$\Delta_b = \Delta_1 + \Delta_2/2. \quad (\text{E.4})$$

For a cross section which increases with lower scattering energies, $\xi > 0$. Our expression for the line shape near the elastic peak then becomes ($\Delta_b/E \ll 1$):

$$\begin{aligned}
\left. \frac{d^2\sigma}{d\Omega d\Delta} \right)_{\text{meas.}} &= \sigma(E) \int_0^\Delta d\Delta_1 \int_0^{\Delta-\Delta_1} d\Delta_2 D_1(\Delta_1) D_2(\Delta_2) D_1(\Delta-\Delta_1-\Delta_2) \quad (\text{E.5}) \\
&+ \xi\sigma(E) \left\{ \int_0^\Delta d\Delta_1 \int_0^{\Delta-\Delta_1} d\Delta_2 \Delta_1 D_1(\Delta_1) D_2(\Delta_2) D_1(\Delta-\Delta_1-\Delta_2) \right. \\
&\left. + \frac{1}{2} \int_0^\Delta d\Delta_1 \int_0^{\Delta-\Delta_1} d\Delta_2 D_1(\Delta_1) \Delta_2 D_2(\Delta_2) D_1(\Delta-\Delta_1-\Delta_2) \right\}.
\end{aligned}$$

The first convolution in the expression is the energy loss distribution function, $D(\Delta)$, which gives the probability for an energy loss, Δ , due to the various energy loss processes. The second and third convolution represent the effect of the energy dependence of the cross section to first order and must be evaluated. To evaluate the second convolution term we consider its Laplace transform:

$$\mathcal{L}[\text{2nd conv}] = \mathcal{L}[\Delta D_1(\Delta)] \mathcal{L}[D_2(\Delta)] \mathcal{L}[D_1(\Delta)], \quad (\text{E.6})$$

where the property that the Laplace transform of a convolution is the product of the individual Laplace transforms has been used. We can re-express the term, $\mathcal{L}[\Delta D_1(\Delta)]$, using the following property:

$$\mathcal{L}[xF(x)] = -\frac{d}{ds} \mathcal{L}[F]. \quad (\text{E.7})$$

Our expression then can be rewritten as follows.

$$\mathcal{L}[\text{2nd term}] = -\frac{1}{2} \frac{d}{ds} \left(\mathcal{L}^2[D_1] \mathcal{L}[D_2] \right) + \frac{1}{2} \mathcal{L}^2[D_1] \frac{d}{ds} \mathcal{L}[D_2]. \quad (\text{E.8})$$

Doing the same for the third convolution we have the result:

$$\mathcal{L}[\text{3rd conv}] = -\frac{1}{2} \mathcal{L}^2[D_1] \frac{d}{ds} \mathcal{L}[D_2]. \quad (\text{E.9})$$

Adding the two terms together we have,

$$\mathcal{L}[\text{2nd conv}] + \mathcal{L}[\text{3rd conv}] = -\frac{1}{2} \frac{d}{ds} \mathcal{L}[D], \quad (\text{E.10})$$

where $\mathcal{L}[D] = \mathcal{L}[D_1] \mathcal{L}[D_2] \mathcal{L}[D_1]$. Using the inverse relation of Equation E.7 this correction can then be evaluated in terms of $D(\Delta)$. This yields the following expression for the elastic line shape near the elastic peak ($\Delta/E \ll 1$),

$$\left. \frac{d^2\sigma}{d\Omega d\Delta} \right)_{\text{meas.}} = \sigma(E) \left[1 + \xi \frac{\Delta}{2} \right] D(\Delta), \quad (\text{E.11})$$

which can be written as follows (see Equation E.2),

$$\left. \frac{d^2\sigma}{d\Omega d\Delta} \right)_{\text{meas.}} \cong \sigma(E - \Delta/2) D(\Delta). \quad (\text{E.12})$$

This result could have been guessed on intuitive grounds, since $\sigma(E - \Delta/2)$ is the cross section for scattering assuming that half of the energy loss occurs before scattering. Based on this result we expect the change in the line shape presented in Section 3.2.2 also to be given by a similar expression but modified by recoil in the following manner:

$$\left. \frac{d^2\sigma}{d\Omega d\omega} \right)_{\text{meas.}} \sim \sigma(E - \eta^2\omega/2) D^{\text{nep}}(E, \omega, \mathcal{X}), \quad \frac{\omega}{E} \ll 1. \quad (\text{E.13})$$

In Figure E-2 this line shape is plotted for scattering at the center of the target cell ($\mathcal{X}_{\text{center}}$) from LH₂ with an energy of 900 MeV and angle of 160°. The dipole fit [61] for the proton electromagnetic form factors was used to obtain the hydrogen cross sections. Also shown is the elastic line shape assuming a constant cross section evaluated at the most probable energy loss before scattering, ω_{mp} . At $\omega = 10$ the effect of including the dependence of the cross section increases the strength of the tail by roughly 20%. This simply reflects the percentage change of the hydrogen cross section evaluated at $\omega = 10$ with respect to ω_{mp} . This error is not critical for hydrogen since the detailed shape of the tail need not be known. But for the deuterium data this is not the case. An underestimation of the elastic tail increases the measurement of the threshold cross section since this tail is subtracted in order to obtain the inelastic spectrum. The size of the systematic error introduced into the threshold measurements can be estimated. For the threshold cross sections averaged from 0-3 MeV in E_{np} , the error is given by the percentage change in the deuterium elastic cross section evaluated at $E_{\text{np}} = 1.5$ MeV:

$$\text{Systematic Error} \sim \frac{\sigma(E) - \sigma(E - \eta E_{\text{exc}}/2)}{\sigma(E)}, \quad (\text{E.14})$$

where Equation 3.66 has been used to re-express ω in terms of the excitation energy, E_{exc} , and $E_{\text{exc}} = 2.23 + 1.5$ MeV. Using previous measurements for the deuterium elastic cross sections [46] [48] [47] [45] and interpolating the results at different energies, a systematic error of the order of -5% for the threshold data averaged from 0-3 MeV in E_{np} was obtained for the energies that were used in this experiment. For all the threshold measurements, except at the lowest

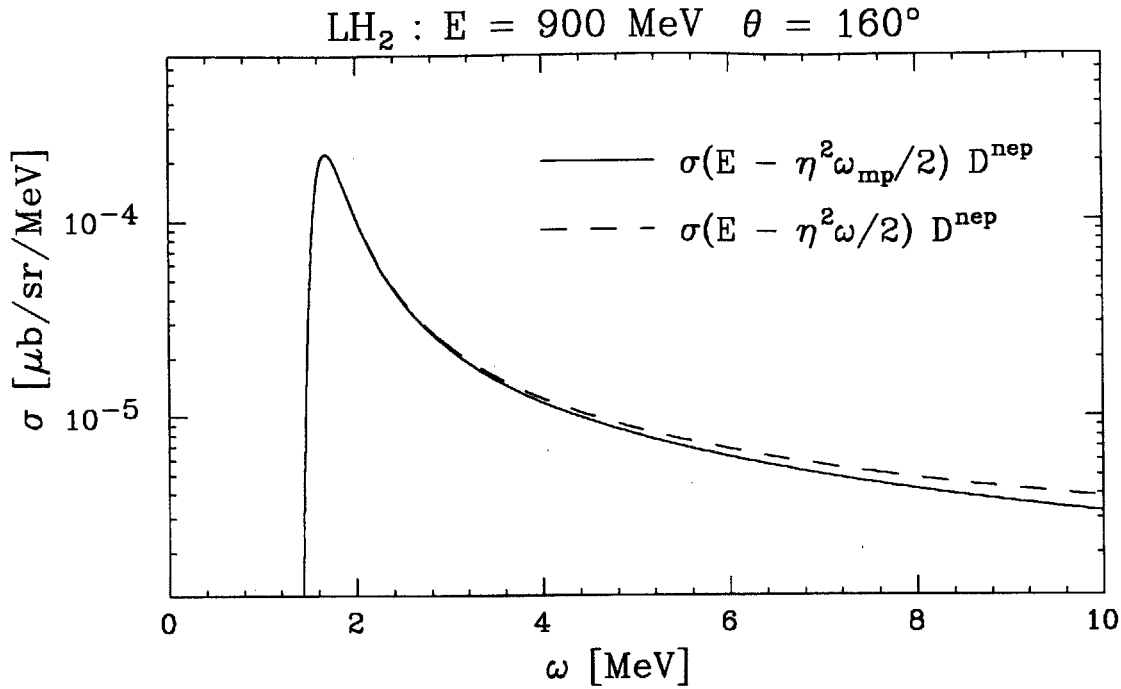


Figure E-2: Elastic line shapes for scattering from ¹H showing the effect of including the energy dependence of the elastic cross section.

Q^2 point, this error is much smaller than the statistical errors involved. For the 0-10 MeV averaged threshold data an error of the order of -10% was obtained. This systematic error is comparable to or larger than the statistical errors except at the highest Q^2 point.

Appendix F

The ELSSY Matrix Elements

In this Appendix the matrix elements that were used to describe the ELSSY spectrometer in the Monte Carlo for this experiment are given. The forward matrix elements were obtained from a Raytrace calculation [62], and the Raytrace file that was used to describe the ELSSY spectrometer is also included for completeness. These forward matrix elements are for a focal plane tilt angle of zero degrees. This is not the same as that given by Bertozzi *et al.* [4]. In the latter the forward matrix elements were calculated along the focal plane angle of 45°, hence their $(x|\theta\delta)$ matrix element is identically zero. The reverse matrix elements were generated from the Monte Carlo model and relates the target coordinates in terms of the VDC coordinates (see Section 4.2). The VDC coordinate system is the focal plane coordinate system with a tilt angle of 45°.

ELSSY Raytrace file with R = 1 meter.

MIT - DD (45. - 45.) MIT-128,135 F.F. COEFF.

46,201,0,0,0,46,0

300.,0.,1.,0.,1.

DIPOLE

1.0,2.0,1.0,2.0,2.,0.

152.57,18.0,9.0,100.0,1.

45.0,13.5,3.0

0.,0.,0.,0.

30. , -20. , -20. , 18.

0.1224 , 1.9724 , -0.5005 , 0.8462 , 0.1174 , -0.0524

0.1403 , 2.1325 , -0.5835 , 0.7657 , 0.1148 , -0.0521

0.,0.,0.,0.,0.,0.

-0.030675,0.014450,0.0,0.0

0.0,-0.80433,2.304,0.0,0.0,0.0,0.0

0.0,0.026550,-0.252,0.0,0.0,0.0,0.0

DIPOLE

1.0,2.0,1.0,2.0,2.,0.

18.0,200.0,9.0,100.0,1.

45.0,3.0,13.50

0.,0.,0.,0.

18. , -20. , -20. , 30.

0.1403 , 2.1325 , -0.5835 , 0.7657 , 0.1148 , -0.0521

0.1224 , 1.9724 , -0.5005 , 0.8462 , 0.1174 , -0.0524

0.,0.,0.,0.,0.,0.

0.014450,-0.022026,0.0,0.0

0.0,-0.02655,-0.2520,0.0,0.0,0.0,0.0

0.0,0.379980,-0.0828,0.0,0.0,0.0,0.0

SENTINEL

0.0 , 0.0 , 0.034,90.,0.034,15.0,5.0

	(x)	(θ)	(y)	(ϕ)	(δ)
(x)	-0.9947	0	0	0	6.669
(θ)	-3.484	-1.006	0	0	11.648
(y)	0	0	-4.920×10^{-3}	0.6148	0
(ϕ)	0	0	-1.611	1.137×10^{-2}	0

Table F.1: The first order ELSSY forward matrix elements for $R = 2.23$ meters. Units are that of Raytrace: distances in [cm], angles in [mr], and δ in %.

	x	θ	y	ϕ	δ	
(x)	-4.973×10^{-3}					(x)
(x)	-9.783×10^{-4}	1.473×10^{-6}				(θ)
(x)	0	0	2.540×10^{-3}			(y)
(x)	0	0	3.860×10^{-4}	1.138×10^{-5}		(ϕ)
(x)	3.555×10^{-2}	6.373×10^{-3}	0	0	-0.1051	(δ)
(θ)	7.193×10^{-3}					(x)
(θ)	8.274×10^{-3}	4.993×10^{-4}				(θ)
(θ)	0	0	-9.642×10^{-3}			(y)
(θ)	0	0	-2.731×10^{-3}	2.999×10^{-3}		(ϕ)
(θ)	5.511×10^{-2}	-1.271×10^{-2}	0	0	-0.2925	(δ)
(y)	0					(x)
(y)	0	0				(θ)
(y)	2.314×10^{-2}	7.523×10^{-4}	0			(y)
(y)	1.938×10^{-3}	2.964×10^{-4}	0	0		(ϕ)
(y)	0	0	2.213×10^{-2}	3.075×10^{-2}	0	(δ)
(ϕ)	0					(x)
(ϕ)	0	0				(θ)
(ϕ)	7.816×10^{-3}	-6.036×10^{-4}	0			(y)
(ϕ)	-1.037×10^{-2}	-4.187×10^{-5}	0	0		(ϕ)
(ϕ)	0	0	8.027×10^{-2}	0.100	0	(δ)

Table F.2: The second order ELSSY forward matrix elements for $R = 2.23$ meters. These are for a focal plane tilt angle of 0° . Units are that of Raytrace: distances in [cm], angles in [mr], and δ in %.

matrix element	value
$(x \theta^3)$	-7.308×10^{-8}
$(x \theta^2 \delta)$	-5.151×10^{-6}
$(x \theta \phi^2)$	-2.585×10^{-5}
$(x \theta \delta^2)$	-2.670×10^{-4}
$(x \phi^2 \delta)$	-1.107×10^{-4}
$(x \delta^3)$	4.989×10^{-3}
$(\theta \delta^3)$	1.516×10^{-2}
$(y \theta^2 \phi)$	-2.676×10^{-5}
$(y \phi^3)$	-6.422×10^{-5}
$(x \theta^4)$	-8.269×10^{-11}
$(x \theta^2 \phi^2)$	-3.407×10^{-8}
$(x \phi^4)$	-5.698×10^{-9}
$(x \phi^2 \delta^2)$	1.163×10^{-5}
$(x \delta^4)$	-2.346×10^{-4}
$(\theta \delta^4)$	-7.214×10^{-4}
$(y \theta^3 \phi)$	8.140×10^{-9}
$(y \theta \phi^3)$	-4.794×10^{-7}

Table F.3: Some important third and fourth order ELSSY forward matrix elements for $R = 2.23$ meters. These are for a focal plane tilt angle of 0° . Units are that of raytrace: distances in [cm], angles in [mr], and δ in %.

matrix element	value	matrix element	value
Theta target		Phi target	
(θx)	1.229	(ϕy)	1.621
$(\theta \theta)$	-0.9996	(ϕxy)	-9.474×10^{-3}
(θx^2)	-3.756×10^{-3}	$(\phi x\phi)$	1.644×10^{-3}
$(\theta x\theta)$	2.034×10^{-4}	$(\phi \theta y)$	7.270×10^{-4}
$(\theta \theta^2)$	5.360×10^{-4}	$(\phi \theta\phi)$	-9.554×10^{-4}
(θx^3)	1.898×10^{-5}	$(\phi x^2 y)$	1.371×10^{-4}
Y target		$(\phi x\theta y)$	-2.350×10^{-4}
$(y y)$	1.832×10^{-2}	$(\phi \theta^2 y)$	1.022×10^{-4}
$(y \phi)$	-0.6191	$(\phi x^3 y)$	-4.095×10^{-6}
$(y xy)$	9.498×10^{-3}	$(\phi x^3 \phi)$	1.313×10^{-6}
$(y x\phi)$	-1.029×10^{-3}	$(\phi x^2 \theta y)$	4.910×10^{-6}
$(y \theta\phi)$	2.037×10^{-4}	$(\phi x^2 \theta\phi)$	-1.792×10^{-6}
$(y x^2 y)$	-1.152×10^{-4}	$(\phi x\theta^2 y)$	-1.517×10^{-6}
$(y x^2 \phi)$	4.698×10^{-5}	$(\phi x\theta^2 \phi)$	5.625×10^{-7}
$(y y^2 \phi)$	2.112×10^{-4}	Delta	
$(y x^2 \theta y)$	-2.774×10^{-6}	(δx)	0.1075
$(y x\theta^2 y)$	9.527×10^{-7}	$(\delta \theta)$	-6.359×10^{-4}
		(δx^2)	7.547×10^{-5}

Table F.4: The ELSSY reverse matrix elements generated from the Monte Carlo Model. These express the target coordinates in terms of the VDC coordinates. Units are that of Raytrace: distances in [cm], angles in [mr], and δ in %.

Appendix G

Monte Carlo Code

The Monte Carlo code written for the Deuteron Electrodisintegration Experiment (DEE) consists of a main shell program, DEE_MC, and a main shell subroutine DEE_MC_MAIN. The program DEE_MC simply executes the subroutine DEE_MC_MAIN as many times as there are electron events to simulate. The subroutine DEE_MC_MAIN is where the real part of the simulation occurs for each event and executes many more subroutines used in the simulation process. For brevity, only the main program, DEE_MC, and the main subroutine, DEE_MC_MAIN, are included in their entirety. The other user written subroutines are well documented within the code and should be self explanatory as to their purpose. All of the computer code was written in Fortran except for DEE_MC_MAIN. This was written in FLECS [63]. In this code the flow of execution is given by the "task execution list" where each entry represents a subroutine call which can be found at the bottom in a "TO" statement. This Monte Carlo also utilizes the Q data acquisition system's histogramming, test, and dynamic parameter array packages [64] and some MP-10 routines [11]. These subroutine programs are highlighted in the Monte Carlo code by being typed in all capital letters whereas the user written subroutines in lower case.

```

CCCCCCCCCCCCCCCCCCCCCCCCCCCCCCCCCCCCCCCCCCCCCCCCCCCCCCCCCCCCCCCC
C
PROGRAM DEE_MC
C
C This program is the Monte Carlo code for the Deuteron Electro-
C disintegration Experiment (DEE). This experiment ran at the
C Bates laboratory in the spring of 1990.
C
C FILE: DEE_MC.FOR
C LANG: fortran
C AUTHOR: W. M. Schmitt
C DATE: May 12, 1991
C
C My programming convention is that all Q subroutines are
C capitalized, whereas user written are not.
C COMMONBLK,LINK,NOTES....
C
CCCCCCCCCCCCCCCCCCCCCCCCCCCCCCCCCCCCCCCCCCCCCCCCCCCCCCCCCCCCCCCC
C----- Local Variables -----
C----- Global Variables -----
include 'prm.inc/list'
C----- First we must initialize and map the appropriate Q stuff! -----
call dee_mc_qinit
C----- Do all the user initializations -----
call target_init
call elssy_init
call phi_psi_init
call Eloss_init
if (WrtRayflg .eq. 123) then ! Initialize Ray writing
  call WrtRay_init
endif
C----- Code -----
do icount = 1, Nelectron ! Total number of electrons
call dee_mc_main ! Main code
enddo
if (WrtRayflg .eq. 123) then ! Close up shop
  close(unit=Rayoutlun)
  write(lunmes,*) '==> Rays written to MC.ray'
endif
stop 'DEE_MC has completed successfully'
end

```



```
CCCCCCCCCCCCCCCCCCCCCCCCCCCCCCCCCCCCCCCCCCCCCCCCCCCCCCCCCCCCCCCCCCCCCCCC
```

```
C
```

```
SUBROUTINE dee_mc_main
```

```
C
```

```
C This is the main code for the DEE Monte Carlo. All user create
C routines are called from this task. The logical flow of the
C Monte Carlo is given in the task execution list.
```

```
C
```

```
C My programming convention is that all Q subroutines are
C capitalized, whereas user written are not. (most of the time)
```

```
C
```

```
C FILE: DEE_MC_MAIN.FLX
```

```
C LANG: flecs
```

```
C AUTHOR: W. M. Schmitt
```

```
C DATE: May 22, 1991
```

```
C CHN BLOCKS: /REGION/, /event/, /target/, /Eloss/, /Elsy/,
```

```
C /WrtRay/
```

```
C
```

```
C
```

```
C MODIFICATIONS:
```

```
C 1. Added the trigger check subroutine to be more realistic.
```

```
C 8-26-91 (WMS)
```

```
C 2. Added the option of doing a Quasi-Elastic Monte Carlo.
```

```
C 9-2-91 (WMS)
```

```
C 3. Adding theta rear, x rear, y rear smearing.
```

```
C 9-23-91 (WMS)
```

```
C 4. Changed MC to use 66.85 as the spectrometer constant!
```

```
C I had to change more things than I first thought.
```

```
C 11-21-91 (WMS)
```

```
C 5. Changed the way I was do the focal plane Mult Scat and
```

```
C Phi rear smearing.
```

```
C 12-1-91 (WMS)
```

```
C 6. Added Ray writing routines!
```

```
C 12-2-91 (WMS)
```

```
C 7. Added calculation of (true-multis)^2 if flag is set.
```

```
C 12-9-91 (WMS)
```

```
C 8. Made an overhall of my derivation of my line shape!
```

```
C 6-5-92 (WMS)
```

```
C Implimented the following corrections:
```

```
C 8.1 Change from using  $1/\ln(2)$  as the bremsstrahlung exponent
```

```
C to  $b_{ave}$ . Where  $b_{ave}$  was determined to be 1.355.
```

```
C 8.2 Put in more GAMMA(1 +  $b_{ave}$ ) factors. called this W_EL.
```

```
C 8.3 Added proton radiation terms to delta1. i.e.  $2Z\ln(rf)$ ...
```

```
C 8.4 Removed the extra GAMMA(1 +  $b_{ave}$ ) factors because
```

```
C I went back to my old Brems. dist.  $W_{EL} = 1$ 
```

```
C (WMS) 6-23-92
```

```
C
```

```
CCCCCCCCCCCCCCCCCCCCCCCCCCCCCCCCCCCCCCCCCCCCCCCCCCCCCCCCCCCCCCCCCCCCCCCC
```

```
.IMPLICIT NONE ! flag undeclared variables as error
```

```
C----- External functions -----
```

```
EXTERNAL GAMMA ! IMSL special function
```

```
EXTERNAL GAUSSIAN ! My function for gaussian rnd #s
```

```
C----- Global Variables -----
```

```
.INCLUDE PRM.INC/LIST
```

```
.INCLUDE EVENT.INC/LIST
```

```
.INCLUDE TARGET.INC/LIST
.INCLUDE ELOSS.INC/LIST
.INCLUDE ELSSY.INC/LIST
.INCLUDE WRTRAY.INC/LIST
```

```
C----- Local Variables -----
```

```
integer*2 ierr(2) ! error array for Q tasks
integer*2 icnt ! = icount for write-out-ray

logical*2 tarchkflg ! .true. when scat. point inside target

logical*2 elschkflg1 ! .true. when e' makes it into ELSSY's
! solid angle acceptance
logical*2 elschkflg2 ! .true. when e' makes it into ELSSY's
! momentum acceptance

real*4 GAMMA
real*4 gaussian
real*4 tmp1,tmp2,tmp3
real*4 tmp4
real*4 tmp7,tmp8
real*4 tmp9,tmp10
real*4 tmp11,tmp12,tmp13,tmp14
real*4 tmp20
real*4 Rndnum
real*4 MS_rms_Ang_tmp1
real*4 MS_Space_Ang_tmp1
real*4 MS_the_tmp1
real*4 MS_phi_tmp1
```

```
C-----<>----- Code -----<>-----
C----- Task execution list -----
```

```
C--- Are we writing rays?
```

```
WHEN (WrtRayflg .EQ. 123) ! write out rays.
  initialize-all-quantities
  generate-RAY-event-at-target
  transport-scattered-electron-thru-ELSSY
  rotate-from-rear-transport-to-focal-plane-coords
  convert-into-detector-rear-coords
  write-out-ray
FIN !WHEN
ELSE ! do DEE MONTE CARLO
  initialize-all-quantities
  generate-incident-electron
  pick-a-scattering-point
  check-if-inside-target-cell
  IF (tarchkflg) ! only if inside target cell
    calculate-entrance-thicknesses
    IF (IFLAG(1) .EQ. 123) calculate-entrance-mult-scat
    calculate-incident-electron-angle
    pick-a-scattering-angle
    calculate-exit-thicknesses
    IF (IFLAG(2) .EQ. 123) calculate-exit-mult-scat
    check-if-it-is-going-to-make-it-into-ELSSY
    IF (elschkflg1) ! only if made it into ELSSY Sol Ang
      pick-an-energy-loss
      IF (elschkflg2) ! only if made it into ELSSY Mom Acc
```

```

convert-into-ray-for-transporting-thru-ELSSY
calculate-perfect-spectrometer-quantities
transport-scattered-electron-thru-ELSSY
check-if-it-is-going-to-make-a-trigger
rotate-from-rear-transport-to-focal-plane-coords
IF (IFLAG(3) .EQ. 123) calculate-focal-plane-mult-scat
convert-into-detector-rear-coords
IF (IFLAG(4) .EQ. 123) smear-x-rear
IF (IFLAG(5) .EQ. 123) smear-theta-rear
IF (IFLAG(6) .EQ. 123) smear-y-rear
IF (IFLAG(7) .EQ. 123) smear-phi-rear
do-first-MULTIS-calculations
do-calkin-calculations
IF (IFLAG(8) .EQ. 123) compute-variance-in-ELSSY-calc
FIN ! IF for elschkflg2
FIN ! IF for elschkflg1
FIN ! IF for tarchkflg
integerize-everything
execute-all-tests
do-histogramming
FIN !ELSE

RETURN

C-----<>----- Subroutine calls -----<>-----
C====>
TO initialize-all-quantities

call VALSET( idw(1), 400, 0 ) ! set idw(*) = 0
call VALSET( rdw(1), 800, 0 ) ! same except a trick!
call TSCLFA(ierr) ! Zero out all test flag results
IF ( ierr(1) .ne. 1 )
  write(lunmes,11)ierr
11  format(1x,
  & 'dee_mc_main -- F-- TSCLFA: Error Zeroing test flags ',2i7)
  stop 'ABORTING'
FIN ! IF

FIN ! TO
C====>
TO generate-RAY-event-at-target

xt_ray = 0.0 !when dispersion matched, not relavent
thet_ray = thetRalo + ran(iiseed)*(thetRahi - thetRalo)
yt_ray = ytRalo + ran(iiseed)*(ytRahi - ytRalo)
phit_ray = phitRalo + ran(iiseed)*(phitRahi - phitRalo)
Delta = deltRalo + ran(iiseed)*(deltRahi - deltRalo)

FIN ! TO
C====>
TO generate-incident-electron

call beam

FIN ! TO
C====>
TO pick-a-scattering-point

z_tar = zlimlo + ran(iiseed)*(zlimhi - zlimlo)

```

```

FIN ! TO
C====>
TO check-if-inside-target-cell

call tar_cell_eqn( tarchkflg )

FIN ! TO
C====>
TO calculate-entrance-thicknesses

C first calculate the line vector components u_inc,v_inc,
C w_inc for the incident electron. See my "The Beam" write up on this.

u_inc = tan(beam_the/1000.) ! x component
v_inc = tan(beam_phi/1000.) ! y component
w_inc = 1. ! e is traveling along pos. z direction

call calc_intercepts(u_inc,v_inc,w_inc,
    & xint_ent,yint_ent,zint_ent)

call calc_thick(xint_ent,yint_ent,zint_ent,
    & Al_thk_ent,tar_thk_ent,Rad_bef)

FIN ! TO
C====>
TO calculate-entrance-mult-scat

call Mult_Scat( Einc, Rad_bef, MS_rms_Ang_ent,
    & MS_Space_Ang_ent, MS_the_ent, MS_phi_ent)

FIN ! TO
C====>
TO calculate-incident-electron-angle

CCC See this write up!!!
the_tar = MS_the_ent
phi_tar = MS_phi_ent

FIN ! TO
C====>
TO pick-a-scattering-angle

scat_ang = scatlimlo + ran(iiseed)*(scatlimhi-scatlimlo)
azim_scat_ang = azimlimlo + ran(iiseed)*(azimlimhi-azimlimlo)

C Now Compute the recoil factor and the energy, Erec, for elastic
C scattering including only recoil losses.
C Assume we are doing Elastic unless flag is set for Inelastic.

Excit = 0.0 ! Elastic [MeV]
IF ( Rznflg .eq. 321 ) ! Pick Inelastic randomly

C Pick random number [0,1]
Rndnum = ran(iiseed)
WHEN ( Rndnum .le. Rconst )
    tmp20 = 1.0 + 2.0*Rm1*Rndnum/(Rb1*Rb1*Rnorm)
    Excit = (Rb1/Rm1)*(-1.0 + SQRT(tmp20) )
FIN !WHEN
ELSE
    Excit = (Rndnum - Rconst)/(Rnorm*Rb2) + Enp_1

```

```

FIN !ELSE

Excit = Excit + dee_thr ! need to add 2.23 MeV
FIN ! IF

rf = 1. + (2.*Einc/M_t)*(sind(scat_ang/2.))**2.
Erec = (Einc - Excit)/rf ! Neglect 2nd order term

C Compute the scat. vector components (in the rotated frame)

Szp = -1. ! Back Scattering
Sxp = Szp*tand(scat_ang)*cosd(azim_scat_ang)
Syp = Szp*tand(scat_ang)*sind(azim_scat_ang)

C Now compute the scat. vector components. in the pivot point coords
C First get the rotation angles!!!!

tmp2 = phi_tar/1000. ! Rotation Angles in radians
tmp1 = (the_tar/1000.)*cos(tmp2) ! Rotation Angles in radians

call inv_rotate(Sxp,Syp,Szp,tmp1,tmp2,Sx,Sy,Sz)

FIN ! TO
C====>
TO calculate-exit-thicknesses

C first calculate the line vector components u_scat,v_scat,
C w_scat for the scattered electron. Notice I reverse the
C direction!!!! I have to do this to get the correct signs
C for the exit intercept coordinates.

u_scat = -Sx ! x component
v_scat = -Sy ! y component
w_scat = -Sz ! z component

call calc_intercepts(u_scat,v_scat,w_scat,
& xint_ext,yint_ext,zint_ext)

call calc_thick(xint_ext,yint_ext,zint_ext,
& Al_thk_ext,tar_thk_ext,Rad_aft)

FIN ! TO
C====>
TO calculate-exit-mult-scat

call Mult_Scat( Erec, Rad_aft, MS_rms_Ang_ext,
& MS_Space_Ang_ext, MS_the_ext, MS_phi_ext)

FIN ! TO
C====>
TO check-if-it-is-going-to-make-it-into-ELSSY

C The first thing I have to do is compute the components
C of the multiple scattered out going electron in the
C pivot point coordinate system.

Smsxp = tan(MS_the_ext/1000.)
Smsyp = tan(MS_phi_ext/1000.)
Smszp = 1.

```

```

C Now compute the rotation angles

tmp3 = atan(Sy/Sz)
tmp2 = tmp3 - pi ! Rotation Angles in radians
tmp1 = atan( (-Sx/Sz)*cos(tmp3) ) ! Rotation Angles in radians

call inv_rotate(Smsxp,Smsyp,Smszp,tmp1,tmp2,Smsx,Smsy,Smsz)

call slit_checks( elschkflg1 )

FIN ! TO
C====>
TO pick-an-energy-loss

C Are we doing an Elastic or Quasi-Elastic run?

WHEN ( Rxnflg .eq. 123 ) ! => QE
  call QE_energy_loss( elschkflg2 )
FIN ! WHEN
ELSE ! => Elastic or Inelastic

C First, calculate all the quantities needed to define
C the energy loss distribution.

C Compute the "effective" thickness T

Q2 = -4.*Einc*Erec*sind(scat_ang/2.)**2

C Include terms that deal with the radiation from the
C struck target nucleus. Erec_tar is the total energy of the
C recoiling nucleus. be_tar is the beta of that nucleus.

Erec_tar = Einc + M_t - Erec
be_tar = sqrt(Erec_tar*Erec_tar - M_t*M_t)/Erec_tar
tmp20 = log( (1.+be_tar)/(1.-be_tar) )

delta1 = (2.*alp/pi)*( log(-Q2/(me*me)) - 1.0
&                + 2.0*float(Z_Tsai)*log(rf)
&                + float(Z_Tsai*Z_Tsai)*(tmp20/(2.0*be_tar) - 1.0) )

T_EL = ( Al_thk_ent + Al_thk_ext)*rho_Al/Rad_Al +
&      ( tar_thk_ent + tar_thk_ext)*rho_t/Rad_t )*b_ave + delta1

C Compute incident and final beta**2

bei2 = 1. - (me*me)/(Einc*Einc)
bef2 = 1. - (me*me)/(Erec*Erec)

C Compute other quantities

A_EL = (Al_thk_ent/(rf*rf))*(const/bei2)*(rho_Al*Z_Al/MW_Al)
B_EL = (tar_thk_ent/(rf*rf))*(const/bei2)*(rho_t*Z_t/MW_t)
C_EL = (tar_thk_ext)*(const/bef2)*(rho_t*Z_t/MW_t)
D_EL = (Al_thk_ext)*(const/bef2)*(rho_Al*Z_Al/MW_Al)
G_EL = A_EL + B_EL + C_EL + D_EL

C Compute density effect corrections

call Dens_eff_corr

```

C Now compute more quantities

```

ee = (I_A1*I_A1*1.e-12/(2.0*me*bei2))*
    & ((me/Einc)**2)*exp(bei2+defe)
ei = (I_t*I_t*1.e-12/(2.0*me*bei2))*
    & ((me/Einc)**2)*exp(bei2+defi)
eo = (I_t*I_t*1.e-12/(2.0*me*bef2))*
    & ((me/Erec)**2)*exp(bef2+defo)
ex = (I_A1*I_A1*1.e-12/(2.0*me*bef2))*
    & ((me/Erec)**2)*exp(bef2+defx)

```

W_EL = 1.0

CC decided that this was not correct!!!!

CC

```

CC W_EL = GAMMA(1. + b_ave*Al_thk_ent*rho_A1/Rad_A1)*
CC & GAMMA(1. + b_ave*tar_thk_ent*rho_t/Rad_t)*
CC & GAMMA(1. + b_ave*tar_thk_ext*rho_t/Rad_t)*
CC & GAMMA(1. + b_ave*Al_thk_ext*rho_A1/Rad_A1)
CC

```

```

H_EL = W_EL*GAMMA(delta1 + 1.)*((Erec)**(-T_EL))*rf**
    & ((Al_thk_ent*rho_A1/Rad_A1+tar_thk_ent*rho_t/Rad_t)*b_ave)

```

C I've calculated every thing I need !!!

```

call E_energy_loss( elschkflg2 )

```

FIN ! ELSE

FIN ! TO

C====>

TO convert-into-ray-for-transporting-thru-ELSSY

C First, we need to convert the scattered electron into a Rotated
C coordinate system at the pivot point suitable for transport.

```

xint_ext_R = xint_ext(2)
yint_ext_R = yint_ext(2)*cosd(ELSSY_ang)
    & + zint_ext(2)*sind(ELSSY_ang)
zint_ext_R = -yint_ext(2)*sind(ELSSY_ang)
    & + zint_ext(2)*cosd(ELSSY_ang)

```

```

Smsx_R = Smsx
Smsy_R = Smsy*cosd(ELSSY_ang) + Smsz*sind(ELSSY_ang)
Smsz_R = -Smsy*sind(ELSSY_ang) + Smsz*cosd(ELSSY_ang)

```

C Now we can compute the transport ray at the target!!!!

```

xt_ray = xint_ext_R - Smsx_R*zint_ext_R/Smsz_R
thet_ray = 1000.*atan(Smsx_R/Smsz_R)
yt_ray = yint_ext_R - Smsy_R*zint_ext_R/Smsz_R
phit_ray = 1000.*atan(Smsy_R/Smsz_R)

```

FIN ! TO

C====>

TO calculate-perfect-spectrometer-quantities

C calculate the "fake" scat angle due to Mult. Scat.
C There is no way of knowing what the actual scattering was.

```

C All we know is the angle between the exiting electron and
C the incident beam direction.

scat_ang_MS = atand(sqrt(Smsx+Smsx+Smsy+Smsy)/Smsz)+180.

C Compute MM coming out of target, if ELSSY was a perfect Spectr.
C tmp4 is the first order missing mass calculation [MeV]

tmp4 = (1. + (2.*Einc/M_t)*sind(scat_ang_MS/2.))**2)*Eloss
      & - (1. + (2.*Einc/M_t)*sind(scat_ang_MS/2.))**2)*Einc/xf
      & + Einc

MM_tar = -M_t + M_t*sqrt( 1. + 2.*tmp4/M_t )

FIN ! TO
C====>
TO transport-scattered-electron-thru-ELSSY

call transfer

FIN ! TO
C====>
TO check-if-it-is-going-to-make-a-trigger

call trig_checks

FIN ! TO
C====>
TO rotate-from-rear-transport-to-focal-plane-coords

call rot_to_focal

FIN ! TO
C====>
TO calculate-focal-plane-mult-scat

C Note, I am using the number of radiation lengths traversed up
C to the focal plane which should be the VDC's center, RadL_rear(1).

call Mult_Scat( Efin, RadL_rear(1), MS_rms_Ang_foc,
              & MS_Space_Ang_foc, MS_the_foc, MS_phi_foc)

phif_ray = phif_ray + MS_phi_foc
thef_ray = thef_ray + MS_the_foc

FIN ! TO
C====>
TO convert-into-detector-rear-coords

C Notice: The 66.85 central momentum ray defines the origin of our
C rear coordinate system. No longer the scribe mark!

x_rear = xf_ray
the_rear = thef_ray
y_rear = yf_ray
phi_rear = phif_ray

FIN ! TO
C====>
TO write-out-ray

```



```

icnt = icount

write(Rayoutlun'ivar) icnt,xt_ray,thet_ray,yt_ray,phit_ray,
&
x_rear,the_rear,y_rear,phi_rear,Delta

FIN ! TO
C====>
TO smear-x-rear

C Due to the finite resolution of the VDC I need to smear x_rear
C by the appropriate sigma for the VDC, sigma_x.

x_rear = x_rear + gaussian( sigma_x )

FIN ! TO
C====>
TO smear-theta-rear

C Due to the finite resolution of the VDC I need to smear the_rear
C by the appropriate sigma for the VDC, sigma_the.

the_rear = the_rear + gaussian( sigma_the )

FIN ! TO
C====>
TO smear-y-rear

C Due to the finite resolution of the TA I need to smear y_rear
C by the appropriate sigma for the TA, sigma_y.

y_rear = y_rear + gaussian( sigma_y )

FIN ! TO
C====>
TO smear-phi-rear

C This smearing is mainly due to Mult. Scat. First, we have to add
C the Mult. Scat. that occurs before TA plane 1, i.e. RadL_rear(2).

call Mult_Scat( Efin, RadL_rear(2), MS_rms_Ang_tmp1,
& MS_Space_Ang_tmp1, MS_the_tmp1, MS_phi_tmp1 )

phi_rear = phi_rear + MS_phi_tmp1

C Now we need to calculate the Mult. Scat. contribution inside
C the chambers themselves. This is crucial! Since the TA's measure
C phi thru displacements I need the rms lateral displacement divided
C by the length. This is simply: rms_plane_ang/sqrt(3) !!!!!!!!!!!

sigma_phi_MS = (14.1/Efin)*sqrt(RadL_rear(3))*
& (1.0 + log10(RadL_rear(3))/9.0)*1000.0/1.7320508

C Sum in quadrature with sigma_phi, TA resolution w/o MS
sigma_phi_TA = sqrt(sigma_phi**2 + sigma_phi_MS**2)

phi_rear = phi_rear + gaussian( sigma_phi_TA )

FIN ! TO
C====>

```

```

TO do-first-MULTIS-calculations

C Using rear coordinates, calculate target quantities and Delta
C for this event. This is the calculation my experimental
C analyzer does to calculate these quantities. Hopefully, they
C won't be much different from the actual values otherwise POL.dat
C isn't that good.

call MULTIS( rdw(1), rdw(1), ierr )

FIN ! TO
C====>
TO do-calkin-calculations

C I'm not including the experimental analyzer code for calkin.
C It's klugey so I'm just going to use my own formulas.

C First, calculate what the polar scattering angle would be from
C thet_pol and phit_pol.

tmp7 = 1. + tan(thet_pol/1000.):**2 + tan(phit_pol/1000.):**2
tmp8 = tan(phit_pol/1000.)*sind(ELSSY_ang) + cosd(ELSSY_ang)

scat_ang_calkin = acosd( tmp8/sqrt(tmp7) )

C Now calculate Missing Mass.
C tmp9 is the recoil factor
C tmp10 is the first order missing mass [MeV]

tmp9 = 1.+(2.*beam_energy/M_t)*sind(scat_ang_calkin/2.):**2
tmp10 = beam_energy - tmp9*P_cent*(1. + .01*Delta_pol)
MM_calkin = -M_t + M_t*sqrt( 1. + 2.*tmp10/M_t )

FIN ! TO
C====>
TO compute-variance-in-ELSSY-calc

CCC These will be histogrammed.

Var_tht = 10.0*(thet_ray - thet_pol)**2
Var_yt = 1000.0*(yt_ray - yt_pol)**2
Var_pht = 100.0*(phit_ray - phit_pol)**2

tmp11 = 1. + (2.*beam_energy/M_t)*(sind(scat_ang/2.))**2.
tmp12 = beam_energy/tmp11
tmp13 = tmp12 - Eloss
tmp14 = 100.*(tmp13 - P_cent)/P_cent

Var_del = 1000.0*(tmp14 - Delta_pol)**2
Var_SA = 1000.0*(scat_ang_MS - scat_ang_calkin)**2
Var_MM = 100.0*(MM_tar - MM_calkin)**2

FIN ! TO
C====>
TO integerize-everything

CCC First calculate auxiliary stuff for histogramming purposes

hist_scat_ang = (scat_ang - 160.)
hist_azim_scat_ang = (azim_scat_ang - 270.)*.1

```

```

hist_scat_ang_MS = (scat_ang_MS - 160.)
hist_scat_ang_calkin = (scat_ang_calkin - 160.)*10.

CCC Now Kluge/Unkluge variables so they come out right
CCC when histogramming and executing tests.

x_tar = 10.*x_tar
y_tar = 10.*y_tar
MS_rms_ang_ent = 10.*MS_rms_ang_ent
MS_rms_ang_ext = 10.*MS_rms_ang_ext
call INTGZ( rdw(1), idw(1), 27, 10., 0. )
x_tar = .1*x_tar
y_tar = .1*y_tar
MS_rms_ang_ent = .1*MS_rms_ang_ent
MS_rms_ang_ext = .1*MS_rms_ang_ext

Al_thk_ent = 10.*Al_thk_ent
Rad_bef = 10.*Rad_bef
Al_thk_ext = 10.*Al_thk_ext
Rad_aft = 10.*Rad_aft
MM_tar = .1*MM_tar
Excit = .1*Excit
thet_ray = .01*thet_ray
phit_ray = .1*phit_ray
call INTGZ( rdw(30), idw(30), 150, 100., 0. )
Al_thk_ent = .1*Al_thk_ent
Rad_bef = .1*Rad_bef
Al_thk_ext = .1*Al_thk_ext
Rad_aft = .1*Rad_aft
MM_tar = 10.*MM_tar
Excit = 10.*Excit
thet_ray = 100.*thet_ray
phit_ray = 10.*phit_ray

therf_ray = .1*therf_ray
thef_ray = .1*thef_ray
the_rear = .1*the_rear
thet_pol = .1*thet_pol
yt_pol = 10.*yt_pol
Delta_pol = 10.*Delta_pol
call INTGZ( rdw(180), idw(180), 100, 10., 0. )
therf_ray = 10.*therf_ray
thef_ray = 10.*thef_ray
the_rear = 10.*the_rear
thet_pol = 10.*thet_pol
yt_pol = .1*yt_pol
Delta_pol = .1*Delta_pol

FIN ! TO
C====>
TO execute-all-tests

call TSTEXE( 1, idw(1), ierr ) ! Executes First Block of Tests
IF ( ierr(1) .ne. 1 )
  write(lunmes,21)ierr
  21  format(1x,
    & 'dee_mc_main -- F-- TSTEXE: Error In Exec. First Block',2i7)
  stop 'ABORTING'
FIN ! IF

```

```
FIN ! TO
C====>
TO do-histogramming

call HSTBLK( 1, idw, 1, 1, ierr )
IF ( ierr(1) .ne. 1 )
  write(lunmes,201)ierr
201  format(1x,
  &  'dee_mc_main -- F-- HSTBLK: Error Making Histograms ',2i7)
  stop 'ABORTING'
FIN ! IF

FIN ! TO

END
```

Appendix H

Threshold Cross Sections

In this appendix the results for the unfolded threshold spectra are given in tabulated form for the energies 347, 576, 754 and 820 MeV.

$E = 347 \text{ MeV } \theta = 160^\circ$	
E_{exc} [MeV]	$\frac{d\sigma^2}{d\Omega dE'}$ [$\mu\text{b}/\text{sr}/\text{MeV}$]
2.50	$1.583 \pm 0.127 \times 10^{-5}$
3.00	$1.309 \pm 0.086 \times 10^{-5}$
3.50	$1.148 \pm 0.071 \times 10^{-5}$
4.00	$1.074 \pm 0.067 \times 10^{-5}$
4.50	$0.974 \pm 0.058 \times 10^{-5}$
5.00	$0.903 \pm 0.055 \times 10^{-5}$
5.50	$0.737 \pm 0.046 \times 10^{-5}$
6.00	$0.873 \pm 0.054 \times 10^{-5}$
6.50	$0.879 \pm 0.052 \times 10^{-5}$
7.00	$0.882 \pm 0.052 \times 10^{-5}$
7.50	$0.922 \pm 0.053 \times 10^{-5}$
8.00	$0.985 \pm 0.060 \times 10^{-5}$
8.50	$0.928 \pm 0.052 \times 10^{-5}$
9.00	$0.976 \pm 0.057 \times 10^{-5}$
9.50	$0.837 \pm 0.046 \times 10^{-5}$
10.00	$0.973 \pm 0.056 \times 10^{-5}$
10.50	$0.835 \pm 0.044 \times 10^{-5}$
11.00	$0.973 \pm 0.056 \times 10^{-5}$
11.50	$0.972 \pm 0.054 \times 10^{-5}$
12.00	$1.021 \pm 0.057 \times 10^{-5}$
12.50	$0.969 \pm 0.053 \times 10^{-5}$
13.00	$0.989 \pm 0.053 \times 10^{-5}$
13.50	$0.972 \pm 0.050 \times 10^{-5}$
14.00	$1.112 \pm 0.062 \times 10^{-5}$
14.50	$1.093 \pm 0.059 \times 10^{-5}$

Table H.1: Unfolded threshold cross sections.

$E = 576 \text{ MeV } \theta = 160^\circ$	
E_{exc} [MeV]	$\frac{d\sigma^2}{d\Omega dE'}$ [$\mu\text{b}/\text{sr}/\text{MeV}$]
2.75	$0.868 \pm 0.275 \times 10^{-7}$
3.75	$0.451 \pm 0.110 \times 10^{-7}$
4.75	$0.275 \pm 0.064 \times 10^{-7}$
5.75	$0.335 \pm 0.084 \times 10^{-7}$
6.75	$0.366 \pm 0.091 \times 10^{-7}$
7.75	$0.366 \pm 0.081 \times 10^{-7}$
8.75	$0.493 \pm 0.099 \times 10^{-7}$
9.75	$0.852 \pm 0.180 \times 10^{-7}$
10.75	$0.765 \pm 0.131 \times 10^{-7}$
11.75	$0.985 \pm 0.174 \times 10^{-7}$

Table H.2: Unfolded threshold cross sections.

$E = 754 \text{ MeV } \theta = 160^\circ$	
E_{exc} [MeV]	$\frac{d\sigma^2}{d\Omega dE'}$ [$\mu\text{b}/\text{sr}/\text{MeV}$]
3.25	$0.571 \pm 0.228 \times 10^{-8}$
5.25	$0.322 \pm 0.092 \times 10^{-8}$
7.25	$0.569 \pm 0.153 \times 10^{-8}$
9.25	$0.576 \pm 0.140 \times 10^{-8}$
11.25	$0.571 \pm 0.136 \times 10^{-8}$
13.25	$0.864 \pm 0.202 \times 10^{-8}$

Table H.3: Unfolded threshold cross sections.

$E = 820 \text{ MeV } \theta = 160^\circ$	
E_{exc} [MeV]	$\frac{d\sigma^2}{d\Omega dE'}$ [$\mu\text{b}/\text{sr}/\text{MeV}$]
3.75	$0.194 \pm 0.072 \times 10^{-8}$
6.75	$0.412 \pm 0.105 \times 10^{-8}$
9.75	$0.283 \pm 0.065 \times 10^{-8}$
12.75	$0.411 \pm 0.094 \times 10^{-8}$
15.75	$0.533 \pm 0.113 \times 10^{-8}$
18.75	$0.592 \pm 0.121 \times 10^{-8}$

Table H.4: Unfolded threshold cross sections.

Bibliography

- [1] S. Auffret et al. "Evidence for Nonnucleonic Effects in the Threshold Electrodisintegration of the Deuteron at High Momentum Transfer," *Physical Review Letters*, **55**, 1362–1365 (1985).
- [2] M. Frodyma et al. "Measurements of Transverse Electron Scattering from the Deuteron in the Threshold Region at High Momentum Transfers," *Physical Review C*, **47**, 1599–1614 (1993).
- [3] J. Mathiot. "What Do We Learn From Deuteron Electrodisintegration Near Threshold and Thermal np Capture?," *Nuclear Physics*, **A412**, 201–227 (1984).
- [4] W. Bertozzi et al. "High Resolution Spectrometers for Electron Scattering," *Nuclear Instruments and Methods*, **162**, 211 (1979).
- [5] K. I. Blomqvist, *Considerations for Application of the Energy Loss Principle to Single Arm Scattering Experiments*, Bates Internal Report 82-3 (unpublished) (1982).
- [6] C.F. Williamson, **VADE MECUM: Bates High Power Liquid Hydrogen/Deuterium Target System**, Version April 1990, Bates Internal Report 88-01 (unpublished) (1988).
- [7] W.M. Schmitt and C.F. Williamson, *Boiloff Rates of Cryogenic Targets Subjected to a Catastrophic Vacuum Failure*, Bates Internal Report 90-02 (unpublished) (1990).
- [8] W. Bertozzi et al. "Focal Plane Instrumentation: A Very High Resolution MWPC System For Inclined Tracks," *Nuclear Instruments and Methods*, **141**, 457 (1977).
- [9] A. Breskin et al. "Further Results on the Operations of High-Accuracy Drift Chambers," *Nuclear Instruments and Methods*, **119**, 9 (1974).
- [10] K. S. Lee. PhD thesis, University of Massachusetts-Amherst, 1993. (unpublished).
- [11] LAMPF MP-10 Support Software, J. F. Amann (1986).

- [12] "Particle Properties Data Booklet," *Physics Letters*, **B204** (1988).
- [13] W. Leo. *Techniques for Nuclear and Particle Physics Experiments*. Springer-Verlag, New York, NY, 1987.
- [14] K. Kleinknecht. *Detectors for Particle Radiation*. Cambridge University Press, Cambridge, England, 1987.
- [15] B. Rossi and K. Greisen. "Cosmic-Ray Theory," *Reviews of Modern Physics*, **13**, 240 (1941).
- [16] LAMPF Internal Report MP-1-3401-3, *Introduction to Q* (1985).
- [17] LAMPF Internal Report MP-1-3414-2, *LAMPF Computer Information Directory* (1986).
- [18] J. Bergstrom. 1967. MIT 1967 Summer Study: Medium Energy Nuclear Physics with Electron Linear Accelerators, pg. 251 (unpublished).
- [19] R. Perrin and E. L. Lomon. "Infrared Contributions to Intermediate State Sums in Quantum Electrodynamics," *Annals of Physics*, **33**, 328-359 (1965).
- [20] Y. S. Tsai. "Radiative Corrections to Electron-Proton Scattering," *Physical Review*, **122**, 1898 (1961).
- [21] L. Mo and Y. Tsai. "Radiative Corrections to Elastic and Inelastic ep and μp Scattering," *Reviews of Modern Physics*, **41**, 205 (1969).
- [22] L. Landau. "On The Energy Loss of Fast Particles by Ionization," *Journal of Physics*, **VIII**, 201 (1944).
- [23] R. Sternheimer. "The Density Effect for the Ionization Loss in Various Materials," *Physical Review*, **88**, 851-859 (1952).
- [24] R. Sternheimer and R. Peierls. "General Expression for the Density Effect for the Ionization Loss of Charged Particles," *Physical Review*, **3B**, 3681 (1971).
- [25] H. Maccabee and D. Papworth. "Correction to Landau's Energy Loss Formula," *Physics Letters*, **30A**, 241 (1969).
- [26] Y. S. Tsai. "Radiative Corrections to Electron Scatterings". Technical report, Stanford Linear Accelerator Center, 1971. SLAC-PUB-848 (unpublished).

- [27] Y. S. Tsai. "Pair Production and Bremsstrahlung of Charged Leptons," *Reviews of Modern Physics*, **46**, 815 (1974).
- [28] W. Heitler. *The Quantum Theory of Radiation, 3rd Ed.* Oxford University Press, London, pg. 378, 1954.
- [29] J. Schwinger. "Quantum Electrodynamics. III. The Electromagnetic Properties of the Electron-Radiative Corrections to Scattering," *Physical Review*, **76**, 790 (1949).
- [30] F. B. Hildebrand. *Advanced Calculus for Applications, 2nd Ed.* Prentice-Hall, Inc., Englewood Cliffs, New Jersey, pg. 626, 1976.
- [31] G. Arfken. *Mathematical Methods for Physicists, 3rd Ed.* Academic Press, Inc., Orlando, Florida, pg. 428, 1985.
- [32] W. Börsch-Supan. "On the Evaluation of the Function $\phi(\lambda) = \frac{1}{2\pi i} \int_{\sigma-i\infty}^{\sigma+i\infty} du e^{\lambda u + u \ln u}$ for Real Values of λ ," *Journal of Research of the National Bureau of Standards.*, **65B**, 245 (1961).
- [33] I. Gradshteyn and I. Ryzhik. *Table of Integrals, Series, and Products.* Academic Press, Inc., Orlando, Florida, pg. 310 and 576, 1980.
- [34] W. Press, B. Flannery, S. Teukolsky, and W. Vetterling. *Numerical Recipes.* Cambridge University Press., New York, NY, 1986.
- [35] D. Perkins. *Introduction to High Energy Physics, 2nd Ed.* Addison-Wesley Publishing Company, Inc., Reading, MA, 1983.
- [36] A. Katramatou, American University Ph.D. Thesis, unpublished (1988).
- [37] W. Scott. "The Theory of Small-Angle Multiple Scattering of Fast Charged Particles," *Reviews of Modern Physics*, **35**, 231 (1963).
- [38] P. Dunn, Harvard University Ph.D. Thesis, unpublished (1980).
- [39] D. Potterveld, California Institute of Technology Ph.D. Thesis, unpublished (1989).
- [40] P. Bevington. *Data Reduction and Error Analysis for the Physical Sciences.* McGraw-Hill, New York, 1969.
- [41] H. Young. *Statistical Treatment of Experimental Data.* McGraw-Hill, New York, 1962.
- [42] D. Beck, Massachusetts Institute of Technology Ph.D. Thesis, unpublished (1986).

- [43] V. Bhushan, Massachusetts Institute of Technology M.S. Thesis, unpublished (1992).
- [44] R. Walker et al. "Measurement of the Proton Elastic Form Factors for $Q^2 = 1-3$ (GeV/c)²," *Physics Letters B*, **224**, 353-358 (1989).
- [45] P. Bosted et al. "Measurements of the Deuteron and Proton Magnetic Form Factors at Large Momentum Transfers," *Physical Review C*, **42**, 38-64 (1990).
- [46] R. G. Arnold et al. "Measurement of the Electron-Deuteron Elastic-Scattering Cross Section in the Range $0.8 \leq q^2 \leq 6$ GeV₂," *Physical Review Letters*, **35**, 776-779 (1975).
- [47] S. Platchkov et al. "The Deuteron $A(Q^2)$ Structure Function and the Neutron Electric Form Factor," *Nuclear Physics*, **A510**, 740-758 (1990).
- [48] S. Auffret et al. "Magnetic Form Factor of the Deuteron," *Physical Review Letters*, **54**, 649-652 (1985).
- [49] M. Lacombe et al. "Parametrization of the Paris N-N Potential," *Physical Review C*, **21**, 861-873 (1980).
- [50] S.K. Singh and W. Leidemann and H. Arenhövel. "The Role of Electromagnetic Form Factors in Meson Exchange Currents," *Z. Physics A*, **331**, 509-518 (1988).
- [51] W. Leidemann and H. Arenhövel. "Deuteron Electrodisintegration Near Threshold at High Momentum Transfer," *Nuclear Physics*, **A393**, 385-398 (1983).
- [52] R. Dymarz and F. Khanna. "Reaction ${}^2\text{H}(e,e')\text{pn}$ Near Breakup Threshold at Backward angles," *Physical Review C*, **41**, 828-833 (1990).
- [53] W. Leidemann and K.-M. Schmitt and H. Arenhövel. "Bonn Potential and Electron-Deuteron Scattering at High Momentum Transfer," *Physical Review C*, **42**, R826-R829 (1990).
- [54] R. Wiringa, R. Smith, and T. Ainsworth. "Nucleon-Nucleon Potentials With and Without $\Delta(1232)$ Degrees of Freedom," *Physical Review C*, **29**, 1207-1221 (1984).
- [55] R. Schiavilla and D. Riska. "Threshold Electrodisintegration and Electromagnetic Form Factors of the Deuteron," *Physical Review C*, **43**, 437-451 (1991).
- [56] Y. Yamauchi, A. Buchmann, and A. Faessler. "Deuteron Threshold Electrodisintegration in a Microscopic Meson-Quark Cluster Model," *Nuclear Physics*, **A494**, 401-437 (1989).

- [57] T. Cheng and L. Kisslinger. "Possible Role of Six-Quark Clusters in Deuteron Electrodisintegration," *Nuclear Physics*, **A457**, 602–620 (1986).
- [58] H. Arenhövel, private communication.
- [59] S. Kowalski and H. Enge. 1985. *RAYTRACE* manual (unpublished).
- [60] R. Sternheimer, M. Berger, and S. Seltzer. "Density Effect for the Ionization Loss of Charged Particles in Various Substances," *Atomic Data and Nuclear Data Tables*, **30**, 261–271 (1984).
- [61] F. Halzen and A. Martin. *Quarks and Leptons*. John Wiley and Sons, Inc., New York, NY, pg. 178, 1984.
- [62] This calculation and the ELSSY Raytrace file was provided to me by Stephen M. Dolfini (Univ. of Illinois).
- [63] LAMPF Internal Report MP-1-3415, *FLECS and ALECS User's Manual* (1984).
- [64] LAMPF Internal Report MP-1-3409-1, *User Information Manual* (1985).

Biographical Note

William Michael Schmitt was born on April 7, 1965 in Saint Louis, Missouri. He lived there for 22 years where he attended Saint Mary's High School and the University of Missouri at Saint Louis. There he completed the degree Bachelor of Arts in Physics and Chemistry in the spring of 1987. He continued his education at the Massachusetts Institute of Technology in the fall of 1987, where he was a full-time research assistant. While a graduate student he participated in experiments at the Bates Linear Accelerator center in Middleton, Massachusetts. He completed the requirements for the degree Doctor of Philosophy in June 1993. In the summer of 1993 he will begin a two-year postdoctoral appointment at the Indiana University Cyclotron Facility.